

NORTHWESTERN UNIVERSITY

Homogeneous Organocalcium and Organolanthanide Catalysis for the
Formation of C–N Bonds and Selective C–O Bond Cleavage

A DISSERTATION

SUBMITTED TO THE GRADUATE SCHOOL
IN PARTIAL FULFILLMENT OF THE REQUIREMENTS

for the degree

DOCTOR OF PHILOSOPHY

Field of Chemistry

By

Rachel Dowrey Dicken

EVANSTON, ILLINOIS

September 2021

ABSTRACT

Homogeneous Organocalcium and Organolanthanide Catalysis for the
Formation of C–N Bonds and Selective C–O Bond Cleavage.

Rachel Dowrey Dicken

Among the most valuable applications of organometallic chemistry is its implementation in the field of catalysis. Many industrial processes rely heavily on catalysis, employing organometallic complexes in the production of commodity chemicals, fine chemicals, materials, and even in the discovery and development of pharmaceuticals. Through decades of intense study, homogeneous catalysis using the precious metals has allowed for tremendous advances in modern synthesis by providing access to robust, reliable, and often predictable chemistry. However, given that there are also a number of limitations associated with the use of precious metals (i.e., Pt, Pd, Ir, Rh, Ru, Au, and Ag) including high cost and environmental impact, and limited availability, the use of more sustainable metal catalysts and the new reactivity and selectivity that they may offer has gained increasing attention.

Relative to the late transition metals, the catalytic chemistry of the more sustainable alkaline earth and rare earth elements is less well understood, as their reactivity is fundamentally different than that of the transition metals. The work described herein details the investigation of two catalysts which make use of the abundant and environmentally benign metals calcium and lanthanum. The first project involves the development of a direct enantioselective conjugate addition of unprotected alkyl amines to maleimides using a chiral calcium(II)-phosphate complex to generate chiral aminosuccinimides. The second project presents a chemoselective

organolanthanide amide-catalyzed deoxygenative reduction of amides with pinacolborane to provide access to a diverse set of amines. Investigation into the kinetics, thermodynamics, and mechanism of the latter is also described.

Thesis Advisor: Prof. Tobin J. Marks

ACKNOWLEDGMENTS

Throughout my time at Northwestern I have received a great deal of support and assistance. I would first like to thank my advisor, Professor Tobin Marks, whose constant support and guidance during my time here has been invaluable. I would also like to thank my committee members, Professors Thomson and Nguyen, as their support has meant a great deal to my personal and scientific development.

I am incredibly grateful for all of the wonderful mentors that I have had during my time at Northwestern. In particular I would like to thank Dr. Tracy Lohr, Dr. Brice Uno, and Dr. Michael Blayney.

I could not have completed this dissertation without the support of my friends. In particular I would like to thank Dr. Shanfu Liu, Dr. Anna Invergo, Dr. Ben Williams, Christian Contreras, Cole Carter, Jake Rothbaum, Joe Accardo, Oliver Hayes, and Nic Watkins.

I am immensely lucky to have such a loving and supportive family. While I haven't gotten to visit as much as I would have liked over the past 5 years, I am thankful for every birthday, holiday, phone and video call that I have gotten to share with them. To my parents, Dave and Fran, I would not be where I am today without your love, support, and countless sacrifices. To my brother and sister-in-law, Matt and Em, thank you for cheering me on and always keeping your door open for me.

LIST OF ABBREVIATIONS

Ac	acetyl
AcO	acetate
ATR	attenuated total reflectance
Bn	benzyl
Bu or ⁿ Bu	butyl
BuLi	<i>n</i> -butyl lithium
Bz	benzoyl
Cp	cyclopentadienyl
Cp*	pentamethylcyclopentadienyl
Cy	cyclohexane
DCB	dichlorobenzene
DCE	dichloroethane
DCM	dichloromethane
DIBAL	diisobutylaluminum hydride
DMF	dimethylformamide
DMSO	dimethyl sulfoxide
dr	diastereomeric ratio
ee	enantiomeric
EI	electron impact
er	enantiomeric ratio
ESI	electrospray ionization
Et	ethyl

EtOAc	ethyl acetate
equiv	equivalent(s)
FT	Fourier transform
GC	gas chromatography
GWP	global warming potential
HRMS	high-resolution mass spectrometry
HPLC	high-performance liquid chromatography
ⁱ Pr	isopropyl
IR	infrared spectroscopy
<i>J</i>	coupling constant
KHMDS	potassium bis(trimethylsilyl) amide
LAH	lithium aluminum hydride
LDA	lithium diisopropylamide
LiHMDS	lithium bis(trimethylsilyl) amide
LRMS	low-resolution mass spectrometry
Me	methyl
Mes	mesitylene
MOM	methoxymethyl
Ms	methanesulfonyl
NaHMDS	sodium bis(trimethylsilyl) amide
NaK	sodium potassium alloy
Nap	naphthyl

NMR	nuclear magnetic resonance spectroscopy
Ph	phenyl
Pr	propyl
^t Bu	<i>tert</i> -butyl
TFA	trifluoroacetic acid
THF	tetrahydrofuran
TLC	thin layer chromatography
TMS	trimethyl silyl

Dedication

To my parents.

TABLE OF CONTENTS

ABSTRACT	2
ACKNOWLEDGMENTS	4
LIST OF ABBREVIATIONS	5
TABLE OF CONTENTS	9
LIST OF FIGURES	11
LIST OF SCHEMES	15
LIST OF TABLES	16
Chapter 1 Introduction to the Catalytic Behavior of Group 2 and 3	17
1.1 Introduction	18
1.2 Catalytic Behavior of Group 3 Elements.....	21
1.3 Catalytic Behavior of Group 2 Elements.....	26
1.4 Thesis Scope and Organization	28
Chapter 2 Ca(II)-Catalyzed Enantioselective Conjugate Additions of Amines	29
2.1 Introduction	30
2.2 Background and Motivation	31
2.3 Development of the Enantioselective Conjugate Additions of Amines	34
2.4 Substrate Scope	36
2.5 Rationalization of the Observed Stereoselectivity	39
2.6 Substrate Diversification	41
2.7 Conclusion	42
2.8 Experimental.....	43
Chapter 3 La[N(SiMe₃)₂]₃-Catalyzed Deoxygenative Reduction of Amides with	

	10
Pinacolborane. Scope and Mechanism.	71
3.1 Introduction	72
3.2 Background and Motivation	73
3.3 Hydroboration Scope	76
3.4 Kinetics and Mechanism	80
3.5 Computational Mechanistic Analysis	85
3.6 Conclusion	91
3.7 Experimental.....	92
Chapter 4 Thesis Overview	121
4.1 Overview and Outlook	122
REFERENCES	124
APPENDICES	148
Appendix A Supplementary to Chapter 2	149
Appendix B Supplementary to Chapter 3	195

LIST OF FIGURES

Figure 1.1	Comparison of the crustal abundance of various metals used in catalysis. Original data adapted from ref 5.	19
Figure 1.2	Contributions of various metals to Global Warming. (A) Comparison of Global Warming Potential (GWP) of the precious metals; (B) Comparison of the GWP of Ca, La, and the base metals to Pd. Original data adapted from ref 6.	20
Figure 1.3	General reactivity pathways characteristic of organolanthanide complexes (X = H or main group element fragment) including (A) [1,2]-insertion and (B) σ -bond metathesis steps.	22
Figure 1.4	Examples of ligands used in lanthanide chemistry. (A) Metallocenes; (B) Constrained Geometry Catalysts (CGC); (C) Post-metallocenes. (Ln = lanthanide, TMS = $-\text{SiMe}_3$, OTf = $-\text{OSO}_2\text{CF}_3$).	24
Figure 1.5	Examples of well-defined organocalcium catalysts. TMS = $-\text{SiMe}_3$, NTf ₂ = $-\text{N}(\text{CF}_3\text{SO}_2)_2$.	27
Figure 2.1	Enantioselective conjugate additions of amines.	31
Figure 2.2	(A) Crystal structure of the proposed hydrated precatalyst at 80% probability and (B) ³¹ P NMR spectra of reaction components.	40
Figure 3.1	Observed Reaction of La ^{NTMS} with Secondary Amides. (A) ¹ H NMR (500 MHz) spectrum of benzanilide in C ₆ D ₆ ; (B) ¹ H NMR (500 MHz) spectrum of <i>in situ</i> formed lanthanum tris-amidate catalyst obtained from benzanilide and La ^{NTMS} (3:1 molar ratio) in C ₆ D ₆ .	79
Figure 3.2	(A) Pseudo-first-order plots for reaction order in <i>N,N</i> -dimethylbenzamide (HBpin in 10-fold excess). ^a The zeroth-order plot ([Amine] vs. time) is linear, while the other two plots are not. (B) Ln vs. ln plot for the determination of the reaction order of La ^{NTMS} for reduction of <i>N,N</i> -dimethylbenzamide (see Section 3.7.5 for details). ^a Reaction conditions: La ^{NTMS} (6.25 μmol), <i>N,N</i> -dimethylbenzamide (0.125 mmol), HBpin (1.25 mmol), C ₆ Me ₆ (0.0330 mmol), C ₆ D ₆ (V _{total} = 1.00 mL).	81
Figure 3.3	(A) Pseudo-first-order plots for reaction order in HBpin for amide reduction (10-fold excess of amide). ^a None of the plots are linear, indicating HBpin consumption is likely mixed-order for amide reduction. (B) Ln vs. ln plot for the determination of reaction order of HBpin in	82

amide reduction. A mixed-order system is observed, wherein at [HBpin] < 1.67 M, the order in HBpin = 1 (slope = 0.910 \approx 1, vide infra for derivation and explanation). At [HBpin] \geq 1.67 M, the order in HBpin = 0 (slope = 0.0268 \approx 0). ^a Reaction conditions: La^{NTMS} (6.25 μ mol), *N,N*-dimethylbenzamide (1.25 mmol), HBpin (0.125 mmol), C₆Me₆ (0.0330 mmol), C₆D₆ (V_{total} = 1.00 mL).

- Figure 3.4** Eyring (blue) and Arrhenius (red) plots for the reduction of *N,N*-dimethylbenzamide. (A) low [HBpin] (5 equiv); (B) high [HBpin] (10 equiv). 83
- Figure 3.5** (A) Hammett plot generated from the reduction of *para*-substituted *N*-benzoylpiperidines with HBpin.^a (B) Plots for the determination of the kinetic isotope effect for reduction of *N,N*-dimethylbenzamide using HBpin and DBpin. ^a Rates determined via integration of product ¹H NMR signals relative to a hexamethylbenzene internal standard. 84
- Figure 3.6** (A) Off-cycle product observed in stoichiometric studies of both amide and ester hydroboration catalyzed by La^{NTMS}. (B) Comparable deactivation product reported for [Cp*₂LaH]₂-catalyzed pyridine dearomatization characterized by single-crystal X-ray diffraction; Cp* = η^5 -pentamethylcyclopentadienyl. 87
- Figure 3.7** Proposed DFT-computed catalytic cycle and transition states for the catalytic hydroboration/reduction of *N,N*-dimethylbenzamide catalyzed by La^{NTMS}. 88
- Figure 3.8** DFT-computed Gibbs free energy profile/catalytic cycle for the hydroboration/reduction of *N,N*-dimethylbenzamide catalyzed by La^{NTMS}. 89
- Figure 3.9** Proposed monomeric or oligomeric La-hemiaminalate complex [(Me₃Si)₂N]₂La{ η^2 -OC(NH)Ph} obtained from the reaction of La^{NTMS} with the primary amide benzamide. 105
- Figure 3.10** Top: ¹H NMR (500 MHz) spectrum of a proposed La-hemiaminalate complex [(Me₃Si)₂N]₂La{ η^2 -OC(NH)Ph} obtained as a precipitate from the reaction of benzamide and La^{NTMS} (1:1 molar ratio) in C₆D₆. Spectrum obtained from a solution of precipitate in THF with a sealed capillary containing DMSO-*d*₆. (HN(SiMe₃)₂: δ 0.03 ppm); Bottom: ¹H NMR (500 MHz) spectrum of the D₂O-quenched proposed La-hemiaminalate complex [(Me₃Si)₂N]₂La{ η^2 -OC(NH)Ph} obtained as a precipitate from the reaction of benzamide and La^{NTMS} (1:1 molar ratio) in C₆D₆. Spectrum obtained from a solution of precipitate in THF with a sealed capillary 106

containing DMSO-*d*₆. (HN(SiMe₃)₂: δ 0.03 ppm).

- Figure 3.11** Top: ²⁹Si NMR (125 MHz) spectrum of a proposed La-hemiaminalate complex [(Me₃Si)₂N]₂La{η²-OC(NH)Ph} obtained as a precipitate from the reaction of benzamide and La^{NTMS} (1:1 molar ratio) in C₆D₆. Spectrum obtained from a solution of precipitate in THF with a sealed capillary containing DMSO-*d*₆. (HN(SiMe₃)₂: δ 1.23 ppm); Bottom: ²⁹Si NMR (125 MHz) spectrum of the D₂O-quenched proposed La-hemiaminalate complex [(Me₃Si)₂N]₂La{η²-OC(NH)Ph} obtained as a precipitate from the reaction of benzamide and La^{NTMS} (1:1 molar ratio) in C₆D₆. Spectrum obtained from a solution of precipitate in THF with a sealed capillary containing DMSO-*d*₆. (HN(SiMe₃)₂: δ 1.23 ppm). 107
- Figure 3.12** ¹H NMR (500 MHz) spectrum of the reduction of benzanilide with HBpin using an *in situ* formed lanthanum tris-amidate catalyst. 108
- Figure 3.13** ¹H NMR (500 MHz) spectrum of *N,N*-dimethylbenzamide in C₆D₆ included for reference. 110
- Figure 3.14** ¹³C NMR (125 MHz) spectrum of *N,N*-dimethylbenzamide in C₆D₆ included for reference. 110
- Figure 3.15** ¹H NMR (500 MHz) spectrum of the proposed catalyst activation intermediate **I-act-1** in C₆D₆. 111
- Figure 3.16** ¹³C NMR (125 MHz) spectrum of the proposed catalyst activation intermediate **I-act-1** in C₆D₆. 111
- Figure 3.17** ¹H NMR (500 MHz) spectrum of the catalyst deactivation product (Figure 3.6) obtained from 1:3 mixture of La^{NTMS} and HBpin in C₆D₆. 112
- Figure 3.18** ¹¹B NMR (128 MHz) spectrum of the catalyst deactivation product (Figure 3.6) obtained from 1:3 mixture of La^{NTMS} and HBpin in C₆D₆. * = Unidentified side product, possibly weakly and reversibly coordinated pinB-N(SiMe₃)₂ or B₂pin₃. The peak at δ 31.6 ppm is a broad doublet, likely due to coordination of the B-H to the metal center or exchange with RBH₃⁻. The downfield shift is similar to previously reported coordinated boranes. 113
- Figure 3.19** ¹³C NMR (125 MHz) spectrum of the catalyst deactivation product (Figure 3.6) obtained from 1:3 mixture of La^{NTMS} and HBpin in C₆D₆. 114

- Figure 3.20** Gibbs free energy profile/catalytic cycle for the hydroboration/reduction of amides catalyzed by La^{NTMS} , and conversion of active catalyst **B** to species **D**. 116
- Figure 3.21** Gibbs free energy profile for a La-silylamide group ($\text{La-N}(\text{SiMe}_3)_2$) insertion of the La^{NTMS} precatalyst into the benzamide C=O bond and subsequent silyl migration to yield a La-siloxide complex. 119
- Figure 3.22** DFT-computed Gibbs free energy profile associated with the decomposition pathway of La^{NTMS} precatalyst induced by HBpin. 120

LIST OF SCHEMES

Scheme 2.1	1,2- vs 1,4-additions of amines to maleimides.	30
Scheme 2.2	Ni(II)-catalyzed addition of alkyl amines to activated alkenes reported by Togni and co-workers.	33
Scheme 2.3	NHC Brønsted base-catalyzed conjugate addition of primary alkyl amines to activated β -aryl β -trifluoromethyl nitroolefins reported by Huang and co-workers.	33
Scheme 2.4	Reaction scale-up.	38
Scheme 2.5	Synthesis and <i>in situ</i> activation of Ca[B] ₂ and proposed stereinduction model.	41
Scheme 2.6	Substrate diversification and target synthesis.	42
Scheme 3.1	General reaction pathways in the reduction of amides.	73
Scheme 3.2	Examples of large-scale deoxygenative reductions of amides in the pharmaceutical industry.	74
Scheme 3.3	(A) Ln ^{NTMS} -Catalyzed Hydroboration of Ketones and Aldehydes with HBpin; (B) Ln ^{NTMS} -Catalyzed Hydroboration of Esters with HBpin.	75
Scheme 3.4	Selective Reduction of <i>N,N</i> -Dimethylbenzamide in the Presence of 1-Octene (A) and 1-Octyne (B).	78
Scheme 3.5	Proposed catalyst activation process for the hydroboration/reduction of amides catalyzed by La ^{NTMS} .	86

LIST OF TABLES

Table 1.1	Comparison of ionic radii, electronegativity, and M—C bond ionicity across the alkaline earth metals.	26
Table 2.1	Optimization of the amino-conjugate addition reaction.	35
Table 2.2	Scope of the Ca(II)-Catalyzed Enantioselective Conjugate Additions of Amines.	37
Table 3.1	Scope of the La ^{NTMS} -Catalyzed Amide Reduction with Pinacolborane.	77
Table 3.2	Stabilization energy (kcal/mol) obtained using different basis sets computed at the SCF level of theory.	117

Chapter 1

Introduction to the Catalytic Behavior of Group 2 and 3.

Portions of this chapter appear in the following publication:

Rachel D. Dicken, Alessandro Motta, and Tobin J. Marks, Homoleptic Lanthanide Amide Catalysts for Organic Synthesis: Experiment and Theory. *ACS Catal.* **2021**, *11* (5), 2715-2734.

1 Chapter 1

1.1 Introduction

Though the phenomenon of catalysis has played a central role in much of society throughout the course of human history, the modern concept of catalysis was introduced only 185 years ago,¹ defining a catalyst as a substance that accelerates a chemical reaction without being consumed in the process. Today, catalysis has become essential to our everyday lives, with over 90% of all industrial chemical processes involving at least one catalytic step, many of which would not proceed in the absence of a catalyst.² Intense research into new and increasingly specialized catalysts continues to transform a variety of industries while decreasing global energy demand and providing society with access to more environmentally benign fuels, life-saving medicines, and higher quality, more easily recycled plastics.

In 2019, the global catalyst demand was valued at \$33.9 billion and is currently projected to reach \$48 billion by 2027.³ Much of this demand has been driven by an increased awareness of the environmental impact of our current industrial processes, causing many industries to shift towards more sustainable (or “green”) chemical processes. At present, the most widely employed catalysts are those based on the transition metals.⁴ Of the transition metals, the catalytic chemistry of the precious metals (i.e., Pt, Pd, Ir, Rh, Ru, Au, and Ag) is particularly well-developed, and has allowed for tremendous advances in modern organic synthesis. This is largely due to their high stability, unique selectivity, and the relative ease with which their associated catalytic cycles can be studied and characterized. Additionally, in many cases, air, moisture, and a variety of functional groups are well-tolerated by precious metal catalysts, and their high catalytic activity allows for exceedingly low catalyst loadings.

Though catalysis is superior to the use of stoichiometric reagents from a sustainability standpoint, not all metal catalysts are created equal in terms of sustainability. Despite the clear advantages afforded by the use of precious metal catalysts, there are also a number of disadvantages associated with their continued use in catalytic processes, including high cost and environmental impact, and limited availability. Precious metals are among the least abundant elements in the earth's crust (Figure 1.1),⁵ resulting in dramatically higher economic and enviro-

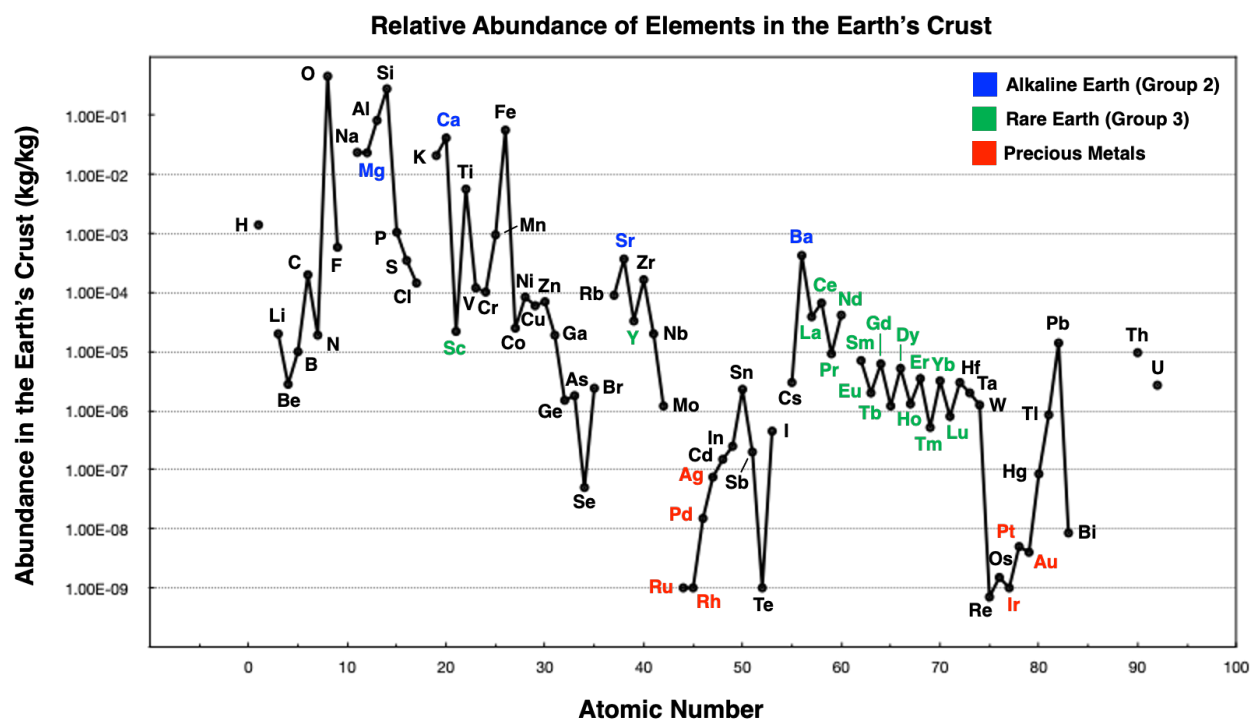


Figure 1.1 Comparison of the crustal abundance of various metals used in catalysis. Original data adapted from ref 5.

mental impact from their use compared to more abundant metals. For example, regarding environmental impact, life cycle analyses estimate that the combined environmental effects for each kilogram of palladium metal produced is equivalent to releasing 3,380 kg of carbon dioxide

into the atmosphere (Figure 1.2A).⁶ In contrast, Group 2 and Group 3 metals are far more abundant in the earth's crust compared to the precious metals (Figure 1.1), allowing for significantly reduced energy requirements when it comes to their mining, refining, and overall production. As such, lanthanum is estimated to have a global warming potential (GWP) of only 11 kg CO₂-eq/kg, and many other metals (including calcium) possess even lower GWPs (Figure 1.2B).

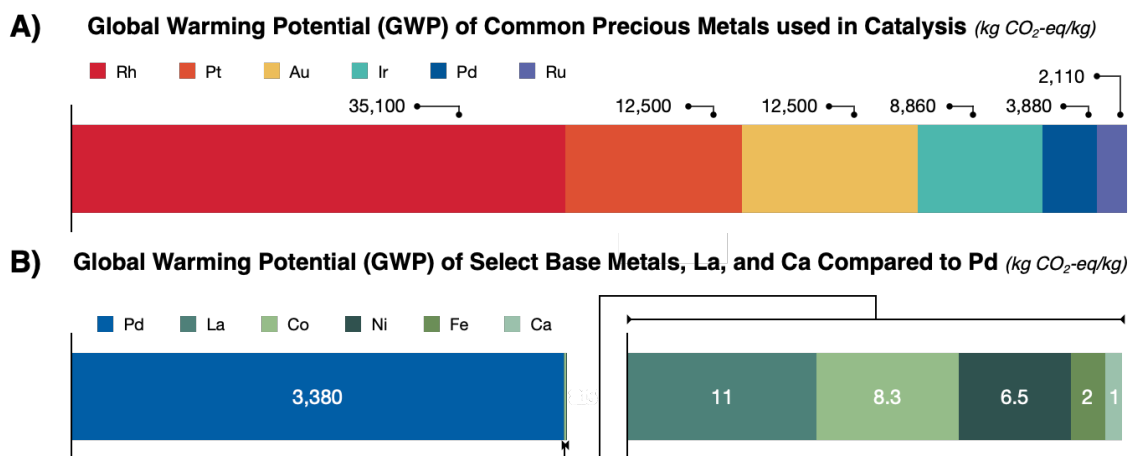


Figure 1.2 Contributions of various metals to Global Warming. (A) Comparison of Global Warming Potential (GWP) of the precious metals; (B) Comparison of the GWP of Ca, La, and the base metals to Pd.⁶ Original data adapted from ref 6.

In addition to this increased environmental impact, the scarcity of the precious metals has resulted in their high and often volatile prices, as well as uncertainty regarding their future availability. Since 2016, the cost of palladium has increased over 300%, and at the time of writing, palladium metal is currently 4 orders of magnitude more expensive than lanthanum on a per mol basis.⁷⁻⁹ Moreover, if consumption continues at the present rate, the known reserves of many of these precious metals (including Pt, Ir, Rh, Ru, Au, and Ag) are projected to be depleted within the next 50 years.¹⁰

In light of the limitations associated with the use of precious metals, the development of more sustainable catalysts based on earth-abundant metals has gained increasing attention. While the use of these more abundant metals is clearly advantageous from an environmental as well as an economical perspective compared to the transition metals, their overall reactivity is often markedly different. This precludes the direct substitution of more abundant metals into many catalytic processes currently dominated by the precious metals. Further, the catalytic behavior of most abundant metals remains understudied, and more research is needed in order to better characterize their unique reactivities and further improve their utility.

This thesis outlines the investigation of two earth-abundant metal catalysts based on the alkaline earth (Group 2) and lanthanide (Group 3) metals. The purpose of this chapter is to provide the reader with the necessary background regarding the catalytic chemistry of these metals. It is worth emphasizing that, while the concept of developing more sustainable chemical processes has so far focused solely on metal selection, in reality, sustainability is exceptionally complicated, with numerous factors to consider, just one of which is the identity of the catalytic metal center. The purpose of this discussion is not to suggest that precious metal catalysis can or should be completely eliminated from our synthetic toolbox; rather, it is to suggest that substituting more abundant metals for precious metals (where both possible and practical) could make a significant difference in moving toward more sustainable chemical processes.

1.2 Catalytic Behavior of Group 3 Elements

1.2.1 Properties and Reactivity of the Lanthanides

Lanthanide elements are used in numerous applications in areas including materials science,¹¹⁻¹³ clean energy technologies,^{14, 15} medical imaging,¹⁶⁻¹⁸ and catalysis.¹⁹⁻²² Their ubiquity

and success in these areas are undoubtedly due (at least in part) to their relatively high abundance in the earth's crust, low cost, and low toxicity.²³ Lanthanides exhibit unique chemical characteristics, many of which directly result from the presence of 4f orbitals. These f orbitals (relative to the 5s and 5p orbitals) have a limited radial extension, and as a result, 4f electrons are core-like in their behavior, imbuing lanthanide complexes with significantly attenuated covalent bonding character and extremely labile and nondirectional metal–ligand interactions.^{19, 23-25} Consequently, the ligand environment is highly tunable, and organolanthanide catalysis is heavily dominated by steric factors.

Whereas transition metals can access a number of different oxidation states, organolanthanide chemistry is largely that of a single oxidation state (+3), and while exceptions are known (+4 Ce, Tb; +2 Sm, Eu, Yb), lanthanide redox processes are uncommon. This inability to readily traverse multiple oxidation states also prevents 4f metals from participating in the elementary catalytic steps typically observed in transition metal chemistry, including oxidative addition and reductive elimination. Instead, the lanthanides primarily participate in [1,2]-insertion and σ -bond metathesis pathways (Figure 1.3).²³⁻²⁶ Useful mechanistic details rega-

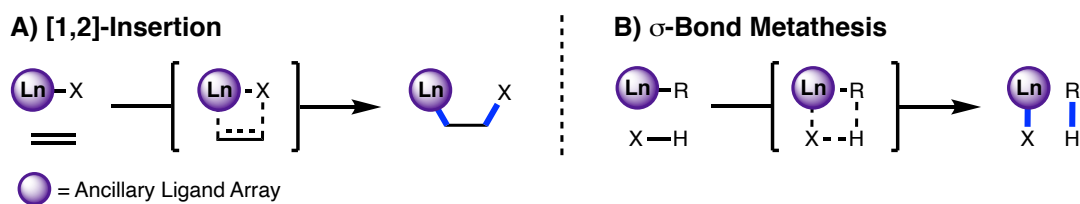


Figure 1.3 General reactivity pathways characteristic of organolanthanide complexes (X = H or main group element fragment) including (A) [1,2]-insertion and (B) σ -bond metathesis steps.

rding organolanthanide reactivity have emerged from theoretical modeling applied to several atom-efficient, environmentally benign catalytic processes including carbonyl hydroboration,^{27, 28}

ring-opening polymerization,^{29, 30} etheric C–O bond cleavage,³¹ olefin polymerization,³² olefin hydrosilylation,³³ and hydroamination^{34,35} as well as hydroalkoxylation processes.³⁶

The combination of these unique characteristics means that the organometallic chemistry of the lanthanides is fundamentally different from that of the d-block transition metals and exempts organolanthanide complexes from the generally accepted rules and principles that govern transition metal chemistry, including the 18 electron rule. This enables the viability of many reaction pathways not observed in typical transition metal catalysis. The large, flexible coordination numbers observed for 4f metal ions allow substrates to approach the metal center in a variety of orientations. This, along with their labile polar/ionic bonding, enables even sterically hindered substrates to coordinate and dissociate rapidly, allowing for extremely high catalytic turnover rates. Additionally, the lanthanide contraction,³⁷ along with the lack of orbital interactions, allows for the lanthanides to contract in ionic radius across the series while their fundamental chemistry and reactivity remain unchanged, allowing for catalysts to be fine-tuned for a particular transformation by simply substituting different lanthanide metals.

1.2.1.1 Organolanthanide Catalysis

Considering much of lanthanide chemistry is determined by steric factors, fine-tuning and modification of the metal-ligand environment is essential in order to control and explore catalytic reactivity and selectivity. In general, most organolanthanide catalysts employ sterically demanding, anionic ligands in order to saturate the coordination sphere, thereby stabilizing the metal center and preventing common catalyst decomposition pathways (i.e., oligomerization, ligand redistribution, etc.). Examples of common ligand frameworks employed in organolanthanide catalysis are shown in Figure 1.4.

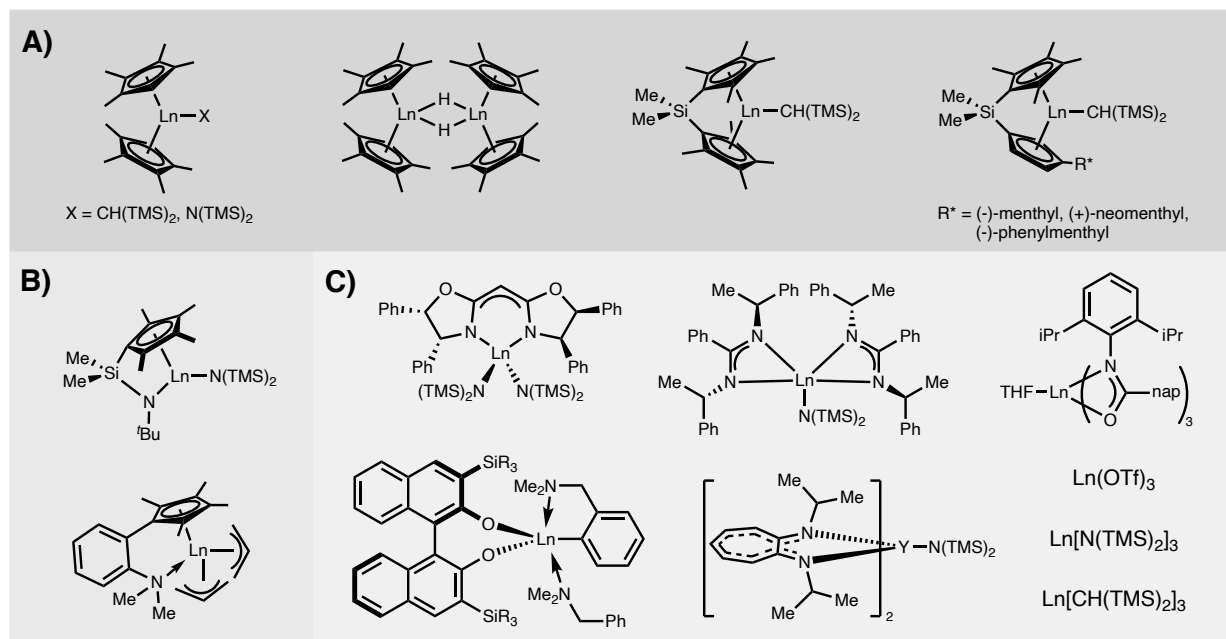


Figure 1.4 Examples of well-defined organolanthanide catalysts. (A) Metallocenes; (B) Constrained Geometry Catalysts (CGC); (C) Post-metallocenes. (Ln = lanthanide, TMS = $-\text{SiMe}_3$, OTf = $-\text{OSO}_2\text{CF}_3$).

Much of the catalytic chemistry of the lanthanides has been uncovered through the study of lanthanide metallocene, *ansa*-metallocene, and constrained geometry (CGC) catalysts (Figure 1.4A and 1.4B). While these metallocene-based complexes are known to be highly effective and reliable catalysts for a variety of transformations, the pursuit of organolanthanide complexes that do not depend on cyclopentadienyl-type ligands has played an important role in advancing organo-f-element catalysis. Much work has gone into the development of these alternative ligand sets, many of which have enabled completely new modes of lanthanide reactivity (Figure 1.4C). However, accessing many of these metallocene and post-metallocene complexes requires complex multistep syntheses and the resulting catalysts are often highly sensitive to air and moisture, limiting their use by non-lanthanide chemists. Recently, there has been increased

interest in more simple and accessible lanthanide catalysts such as the lanthanide trisamides. This will be explored in further detail in the next section.

1.2.1.2 Lanthanide Amides

Homoleptic lanthanide trisamides of the type $\text{Ln}[\text{N}(\text{TMS})_2]_3$ ($\text{TMS} = -\text{SiMe}_3$) have been known for nearly 50 years.³⁸⁻⁴¹ These complexes were recognized as useful synthetic precursors for organolanthanide catalysts and materials early on due to the high reactivity of the silylamide group.⁴² However, their intrinsic catalytic potential has been largely unrecognized. Over the past two decades, while these complexes have continued to serve as reliable precursors for a growing number of organolanthanide catalysts, they have also proven to be efficient, selective, and environmentally benign homogeneous catalysts in their own right.

Homoleptic lanthanide amides provide a simple and highly accessible bridge between organolanthanide chemistry and the organic methodology community. While many organolanthanide catalysts require laborious, multistep anaerobic syntheses and rigorous exclusion of air and moisture, the homoleptic lanthanide amide catalysts are generally commercially available and typically less sensitive to air and moisture in syntheses, making their experimental use far more straightforward.⁴³ To date, these complexes have proven to be extremely active for a wide variety of atom-efficient homogeneous catalytic transformations, including C–H functionalization,^{44, 45} insertion reactions,⁴⁶⁻⁵⁰ hydroelementations,⁵¹⁻⁵⁸ as well as reductions of diverse C=O and C–C unsaturated systems.⁵⁹⁻⁶⁴ This exceptional versatility demonstrated by the homoleptic lanthanide amides, paired with their ability to participate in a wide variety of reactions and mechanisms, makes these catalysts attractive candidates for further exploration, as their reactivity is understudied relative to lanthanide metallocenes, and even more so relative to d-block catalysts.

1.3 Catalytic Behavior of Group 2 Elements

1.3.1 Properties and Reactivity of the Alkaline Earth Metals

The catalytic behavior of Group 2 and Group 3 are quite similar in that the chemistry of the alkaline earth metals (i.e., Mg, Ca, Sr, and Ba*) is largely determined by steric factors and primarily that of one oxidation state (+2). This redox inactivity again prohibits the catalytic chemistry typical of many transition metals such as oxidative addition and reductive elimination. Instead, catalytic cycles of the alkaline earth metals are based on [1,2]-insertion and σ -bond metathesis steps (Figure 1.3). Though much of the overall chemistry of Group 2 and 3 is the same, compared to the lanthanides, the reactivity of the alkaline earth metals is more varied from metal to metal. This is due to significant changes in both electronegativity and ionic radii as Group 2 is descended (Table 1.1).^{37, 65} As a result, though organomagnesium complexes tend to display some degree of covalency in metal–ligand interactions, the metal–ligand bonding observed in organometallic complexes of calcium and the heavier alkaline earth elements is almost exclusively ionic in nature.⁶⁶

Table 1.1 Comparison of ionic radii, electronegativity, and M–C bond ionicity across the alkaline earth metals.

	Mg²⁺	Ca²⁺	Sr²⁺	Ba²⁺
^a ionic radius	0.78 Å	1.06 Å	1.27 Å	1.43 Å
^b Pauling electronegativity	1.31	1.00	0.95	0.89
^c M–C bond ionicity	77%	87%	91%	94%

^a Original data adapted from ref 37; ^b Original data adapted from ref 65; ^c Original data adapted from ref 66.

*Be and Ra are excluded here due to their difference in reactivity and lack of modern applications in catalysis.

nally, well-defined calcium complexes have been reported as competent catalysts for a variety of enantioselective transformations.⁸³⁻⁸⁸ Examples of well-defined organocalcium catalysts are shown in Figure 1.5.

1.4 Thesis Scope and Organization

The work described herein explores the use of more sustainable metals for catalysis through the investigation of two catalytic systems which make use of the abundant and environmentally benign metals calcium and lanthanum. Chapter 2 focuses on the development of a direct enantioselective chiral calcium(II)-phosphate complex (Ca[CPA]₂)-catalyzed conjugate addition of unprotected alkyl amines to maleimides. This mild catalytic system represents a significant advance towards the general convergent asymmetric amination of α,β -unsaturated electrophiles, providing medicinally relevant chiral aminosuccinimide products in high yields and enantioselectivities. Chapter 3 then discloses an efficient and selective method for the reduction of tertiary and secondary amides with pinacolborane using a tris[*N,N*-bis(trimethylsilyl)amide]lanthanum (La^{NTMS}) catalyst. Kinetic and thermodynamic studies, isotopic labeling, and DFT calculations using energetic span analysis suggest a unique active catalytic species and mechanism which is also discussed. The final chapter summarizes the key findings disclosed in this thesis and briefly mentions possible future directions.

Chapter 2

Ca(II)-Catalyzed Enantioselective Conjugate Additions of Amines.

Portions of this chapter appear in the following publication:

Brice E. Uno, Rachel D. Dicken, Louis R. Redfern, Charlotte M. Stern, Greg G. Krzywicki, and Karl A. Scheidt, Calcium(II)-catalyzed enantioselective conjugate addition of amines. *Chem. Sci.*

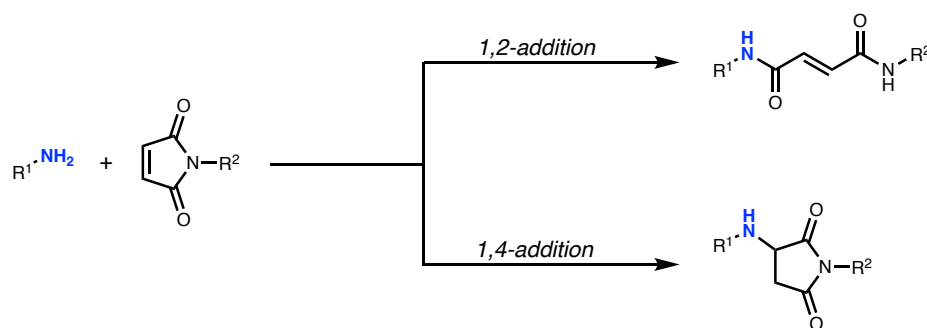
2018, 9, 1634-1639.

2 Chapter 2

2.1 Introduction

The conjugate addition of nucleophilic amines to α,β -unsaturated systems is recognized as a simple and atom-economical synthetic strategy for the formation of C–N bonds. While much work has been done in the development of reactions involving nitrogen nucleophiles and a wide range of conjugate acceptors, very few methods make use of maleimides. Additions to maleimides often require elevated temperatures, high pressures, and extended reaction times. Aside from the obvious impracticalities that these reaction conditions can present, the tendency for maleimides to polymerize or hydrolyze under such conditions presents yet another challenge and limits their application. Current methods for addition of amines to maleimides also frequently encounter selectivity issues, resulting in mixtures of both 1,2- and 1,4-addition products (Scheme 2.1). As a result, amine nucleophiles are currently underutilized in reactions with maleimides.

Scheme 2.1 1,2- vs 1,4-additions of amines to maleimides.



This chapter outlines the development of the direct enantioselective chiral calcium(II)-phosphate complex ($Ca[CPA]_2$)-catalyzed conjugate addition of unprotected alkyl amines to maleimides. This mild catalytic system represents a significant advance towards the general

convergent asymmetric amination of α,β -unsaturated electrophiles, providing medicinally relevant chiral aminosuccinimide products in high yields and enantioselectivities. Furthermore, the catalyst can be reused directly from a previously chromatographed reaction and still maintain both high yield and selectivity.

2.2 Background and Motivation

Chiral amines are a ubiquitous motif in pharmaceuticals and natural products (Figure 2.1).⁸⁹ The conjugate addition of amine nucleophiles to various α,β -unsaturated systems is a well-established transformation to access the corresponding β -amino carbonyl products.⁹⁰⁻⁹³ However, catalytic enantioselective methods for the construction of C–N bonds directly from amines remain a challenge in synthetic organic chemistry. Direct conjugate additions of amines with α,β -unsaturated electrophiles have been shown to proceed at high temperatures and pressur-

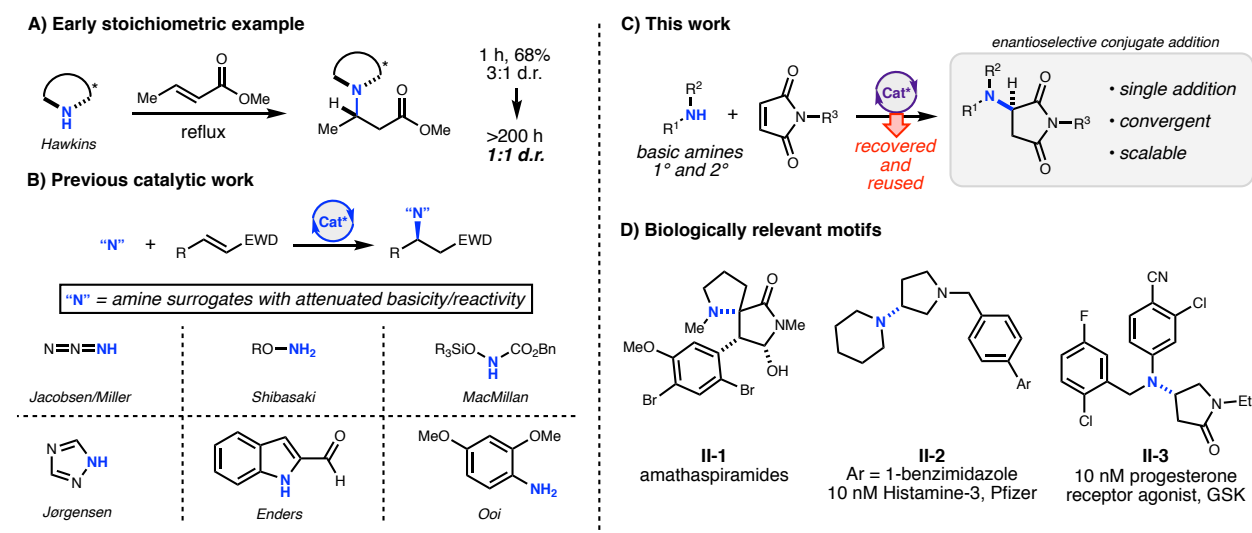


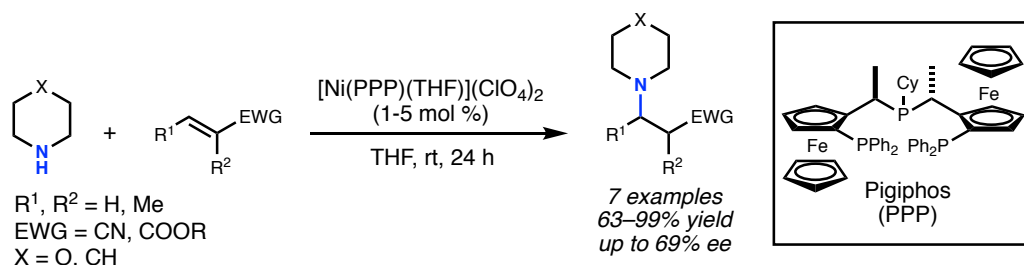
Figure 2.1 Enantioselective conjugate addition of amines.

es;⁹⁴⁻⁹⁶ however the reversibility of the initial attack by the amine eventually leads to racemic products (Figure 2.1A).⁹⁷⁻¹⁰⁰ Stoichiometric homochiral lithium amides can be successfully deployed under kinetic control, achieving high yield and selectivity. However, these sensitive, strongly basic reagents are further limited by the need to remove the chiral α -methylbenzyl moiety to carry the products forward to useful targets.^{101, 102} To circumvent these issues, current catalytic methods have relied upon the use of non-basic nitrogen nucleophiles as amine surrogates to avoid catalyst poisoning (Figure 2.1B),¹⁰³⁻¹⁰⁵ which is common when basic amines are used as reagents in the presence of chiral Lewis or Brønsted acidic catalysts.^{106, 107} Therefore, numerous examples of non-basic nitrogen nucleophiles including azides,¹⁰⁸⁻¹¹³ hydroxylamines,¹¹⁴⁻¹¹⁷ *O*-functionalized carbamates,¹¹⁸⁻¹²⁰ 1,2,4-triazoles,¹²¹⁻¹²³ indoles,¹²⁴ and anilines^{125, 126} have been strategically deployed to avoid Lewis acid complexation,^{127, 128} Brønsted acid neutralization, or unselective iminium activation.¹¹⁸ However, in all of these cases, a protected nitrogen atom is installed which requires multiple steps to elaborate further. Thus, a more convergent approach would be enabled by the direct asymmetric amination of basic primary and secondary amines without the use of protecting groups.

Apparently, there are only three examples of catalytic asymmetric amino-conjugate additions that have successfully employed alkyl amines.¹²⁹⁻¹³¹ In 2003, Togni briefly explored asymmetric aminoconjugate additions to activated olefins as the initial step in a catalytic asymmetric hydroamination reaction catalyzed by a novel chiral Ni(II) phosphine complex (Scheme 2.2).¹²⁹ Morpholine and piperidine produced modestly enantioenriched products when reacted with methacrylonitrile (69% and 20% ee, respectively), which represents the first significant example of an effective, enantioselective intermolecular hydroamination reaction employing alkyl amines. Despite this promising proof-of-concept study, general asymmetric

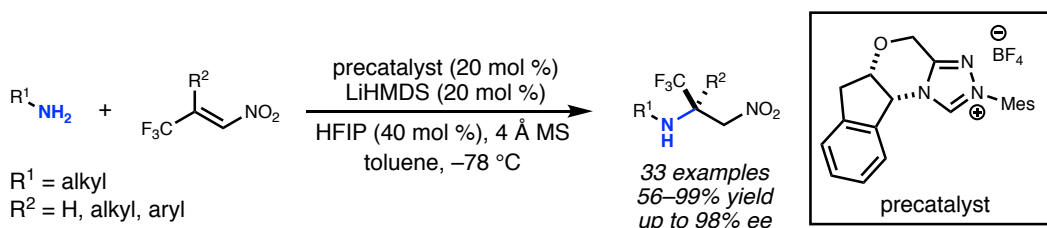
aminoconjugate additions with unfunctionalized/masked amines remain unrealized, which underscores the fundamental challenge associated with the use of highly basic and sterically un-

Scheme 2.2 Ni(II)-catalyzed addition of alkyl amines to activated alkenes reported by Togni and co-workers.¹²⁹



numbered reagents in conjunction with Lewis acidic metal catalysts. In 2015, Huang and co-workers reported an efficient, highly enantioselective conjugate addition of primary alkyl amines to activated β -aryl β -trifluoromethyl nitroolefins (Scheme 2.3).¹³¹ Unlike most catalytic examples, their strategy uses a chiral *N*-heterocyclic carbene (NHC) Brønsted base catalyst.¹³²

Scheme 2.3 NHC Brønsted base-catalyzed conjugate addition of primary alkyl amines to activated β -aryl β -trifluoromethyl nitroolefins reported by Huang and co-workers.¹³¹



However, a major limitation of this method is the lack of secondary amines as nucleophiles. Additionally, strongly basic and cryogenic conditions are required, which potentially limit the generality of this transformation.¹³¹ Therefore, we sought mild catalytic conditions capable of providing enantioenriched amino-conjugate addition products from a general set of readily

available alkyl amines with maleimides, which were chosen as an ideal substrate for catalyst identification and optimization due to their ready availability and excellent conjugate acceptor properties (Figure 2.1C). Additionally, enantioenriched aminosuccinimide products serve as an easily functionalized scaffold to generate aminolactams and aminopyrrolidines.¹³³⁻¹³⁶ Aminosuccinimides and their derivatives are also a common motif in bioactive small molecules, pharmaceuticals, and natural products (Figure 2.1D).¹³⁷⁻¹⁴² Access to these products from achiral starting materials can facilitate the rapid generation of diverse small molecule libraries aimed at probing new chemical spaces.

2.3 Development of the Enantioselective Conjugate Additions of Amines

We began our studies with a reaction between equimolar quantities of *N*-benzylmaleimide and *p*-tolylamine. Our primary focus was to enhance the enantioselectivity of the title reaction (Table 2.1). An initial exhaustive screen of various asymmetric catalyst families including hydrogen bond donors (HBD), metal-TADDOL complexes, metal-BINOL complexes, and chiral phosphoric acids (CPA), identified that CPA **A-H** possessing 1-naphthyl substitution at the 3,3'-positions has the capability to produce the title compound in modest yield and selectivity (Table 2.1, entry 1). Subsequently, we investigated the role of water in the reaction and observed that the addition of 4 Å MS had a moderate but reproducible impact on selectivity (Table 2.1, entry 2).

We then investigated a wide range of desiccants¹¹⁷ and found that calcium oxide had a greater than anticipated positive effect on the selectivity of the reaction (Table 2.1, entry 3).^{67, 143-}

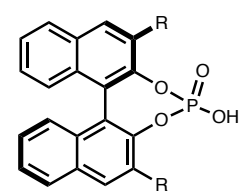
¹⁵¹ Additionally, we observed a moderate increase in e.r. over time to 80:20 e.r. (Table 2.1, entry 4). We therefore hypothesized that the reaction of calcium oxide with **A-H** led to the formation

of a more enantioselective calcium phosphate catalyst. Our hypothesis was enlightened by combining the prior elegant work of Ishihara, Antilla, and Rueping who demonstrated the role of

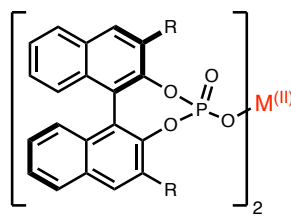
Table 2.1 Optimization of the amino-conjugate addition reaction.

entry	catalyst	temp (°C)	additive	% yield ^b	er
1.	A-H	4	–	35	64:36
2.	A-H	4	4 Å MS	37	69:31
3.	A-H	4	CaO	39	76:24
4.	A-H	4	CaO	55	80:20 ^c
5.	Ca[A]₂	4	4 Å MS	63	86:14
6.	Ca[B]₂	4	4 Å MS	76	95:5
7.	Ca[B]₂	4	–	45	87:13
8.	Ca[B]₂	–20	4 Å MS	80	98:2
9.	Ca[B]₂	–40	4 Å MS	21	80:20
10.	Ca[C]₂	–20	4 Å MS	84	60:40
11.	Ca[D]₂	–20	4 Å MS	73	73:27
12.	Ca[E]₂	–20	4 Å MS	65	72:28
13.	Mg[B]₂	–20	4 Å MS	65	74:26
14. ^d	Ca[B]₂	–20	4 Å MS	94	94:6
15. ^e	Ca[B]₂	–20	4 Å MS	95	94:6

catalyst structures



A-H; R = 1-naphthalene



M[CPA]₂

CPAs:

- A**, R = 1-naphthalene
- B**, R = 9-phenanthracene
- C**, R = 2-naphthalene
- D**, R = SiPh₃
- E**, R = C₆F₅

^a 0.025 mmol scale, toluene 0.02 M, 18 h. ^b ¹H NMR yields with 1,3,5-trimethoxybenzene as an internal standard. ^c Time point taken at 48 h. ^d Toluene 0.05 M. ^e Toluene 0.05 M, 5 mol % catalyst loading of Ca[B]₂.

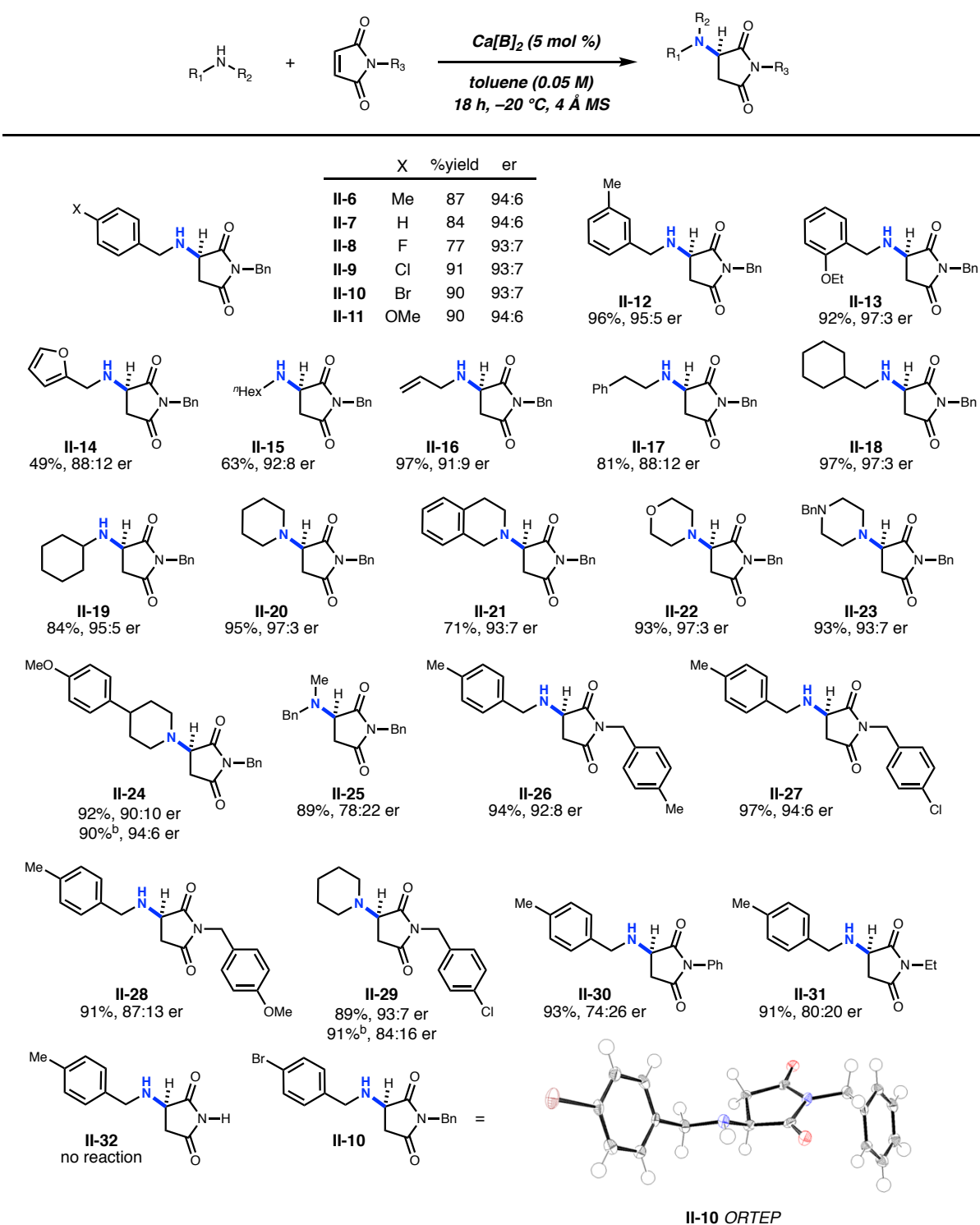
catalytic chiral alkali metal and alkaline earth metal-phosphate salts in various reactions.^{87, 88, 152-}

¹⁶² Thus, we investigated two pre-formed calcium phosphate complexes (Table 2.1, entries 5 &

6) and observed that the calcium CPA complex possessing 9-phenanthracenyl substitution on the phosphate 3,3'-positions, Ca[**B**]₂ (Table 2.1), facilitated the title reaction in 76% yield and 95:5 e.r. (Table 2.1, entry 6). Strikingly, removal of the 4 Å MS diminished both yield and selectivity (Table 2.1, entry 7). After investigating selectivity as a function of temperature (entries 8 & 9), we looked at other CPA salts (Table 2.1, entries 10–12) and determined that Ca[**B**]₂ was indeed optimal. We then compared calcium and magnesium phosphate complexes, and demonstrated again that Ca[**B**]₂ was optimal (Table 2.1, entry 13). Furthermore, increasing its concentration to 0.05 M and lowering the catalyst loading to 5 mol% increased the yield to 95% with 94:6 e.r. (Table 2.1, entries 14 & 15).

2.4 Substrate Scope

With the optimized conditions in hand, we next investigated the scope of the reaction with a range of aliphatic amines and maleimides (Table 2.2). *Para*-substituted primary benzylamines with a range of electron donating and withdrawing groups afforded the conjugate addition products (**II-6–II-11**) in 93:7–94:6 e.r. and 77–91% yield. *Meta*- and *ortho*-substituted benzyl amines afforded **II-12** and **II-13** in similar yields and selectivities. The products derived from less sterically bulky amines and linear amines were obtained with lower enantioselectivity (**II-14–II-17**) and moderate yields. In contrast, bulkier amines gave products **II-18** and **II-19** in high yield and selectivity. Notably, secondary cyclic amines provided conjugated products **II-20–II-24** in 93:7–97:3 e.r. These substrates would be difficult to access via other methodologies or from an enantiopure amino acid derived starting material.¹⁶³ The enantioselectivity for the arylpiperidine-derived **II-24** uniquely improved at –40 °C which was not general for the other substrates.

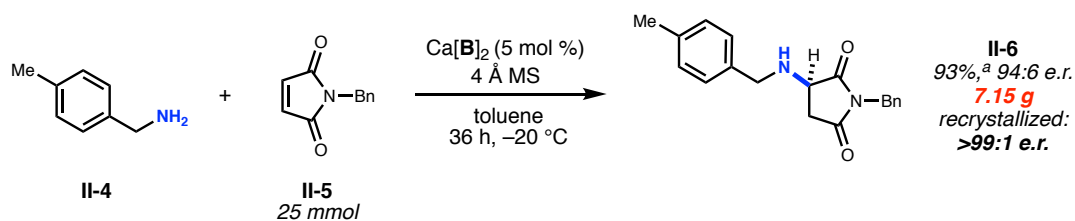
Table 2.2 Scope of the Ca(II)-Catalyzed Enantioselective Conjugate Additions of Amines.

^a Isolated yields on 0.2 mmol scale. ^b Reaction run at $-40\text{ }^{\circ}\text{C}$ for 24 h.

Acyclic secondary amines showed the lowest selectivity among the nucleophiles (**II-25**). Also, substitutions on the benzyl maleimide were tolerated (**II-26–II-28**). The cross-reaction between piperidine and a substituted benzyl maleimide generated product **II-29** in good yield and selectivity. *N*-phenyl maleimide was a poor substrate with regard to selectivity (74:26 e.r.); however, the desired 1,4-addition product **II-30** was synthesized in 93% yield with no observed 1,2-addition product (a common side-reaction with *N*-aryl maleimides).^{164, 165} Maleimide substrates with smaller appendages were observed to react with lower selectivities (**II-31**). The unsubstituted maleimide product **II-32** was not observed, presumably due to a lack of solubility.

The title reaction was successfully scaled up by 1000-fold from the initial screening conditions (Scheme 2.4). Taking into account the observed dependence of enantioselectivity on concentration, the amine nucleophile was added slowly to the other reaction components via a cannula. These conditions afforded 7.15 g of the product (93% yield) in 94:6 e.r. The product was successfully recrystallized to >99:1 e.r. Additionally, >95% of the catalyst Ca[B]₂ was recovered via column purification. The recovered Ca[B]₂ was subsequently able to reproduce the title reaction without loss of yield or selectivity. The ability to directly recover and reuse Ca[B]₂

Scheme 2.4 Reaction scale-up.



^a Isolated yield on 25 mmol scale using 1.1 equivalents of **II-4**. Active catalyst was recovered after chromatography (96%, 1.6 g).

from each reaction at >95% efficiency gives this methodology more utility, especially given the high molecular weight of the catalyst.

2.5 Rationalization of the Observed Stereoselectivity

In an effort to rationalize the observed enantioselectivity, we obtained X-ray crystal structure and ^{31}P NMR spectroscopy data for the pre-formed calcium phosphate complex used in our optimization and scope studies (Figure 2.2). Surprisingly, the observed structure shows a 4:2 ratio of **B** to Ca^{2+} , not a $\text{Ca}[\text{B}]_2$ complex. Additionally, both calcium atoms are coordinatively saturated, with each cation bound to five molecules of water, which creates a hydrogen-bonding network. Although it is possible that the observed ORTEP structure is the actual catalytic species we hypothesize that it is more likely a precatalyst that is activated via dehydration in the presence of molecular sieves. This observation is supported by the significant change in the ^{31}P NMR spectrum in the presence of 4 Å MS (Figure 2.2). The yield and selectivity of the reaction also diminished in the absence of the 4 Å MS (Table 2.1, entry 7), which supports that dehydration of the $\text{Ca}_2[\text{B}]_4 \cdot (\text{H}_2\text{O})_{10}$ complex is necessary. Interestingly, when all of the reaction components are present, the ^{31}P NMR data is reminiscent of the precatalyst (Figure 2.2). This data indicates that the presence of the amine re-establishes the hydrogen-bonding network that is lost upon dehydration of the $\text{Ca}_2[\text{B}]_4 \cdot (\text{H}_2\text{O})_{10}$ complex. Understanding this Lewis base/Lewis acid interaction between the active catalyst and a coordinated maleimide substrate will require further investigation.

Based on the obtained spectroscopic data, we hypothesize that the $\text{Ca}_2[\text{B}]_4 \cdot (\text{H}_2\text{O})_{10}$ complex is activated via dehydration in the presence of 4 Å MS, inducing it to reorganize to form

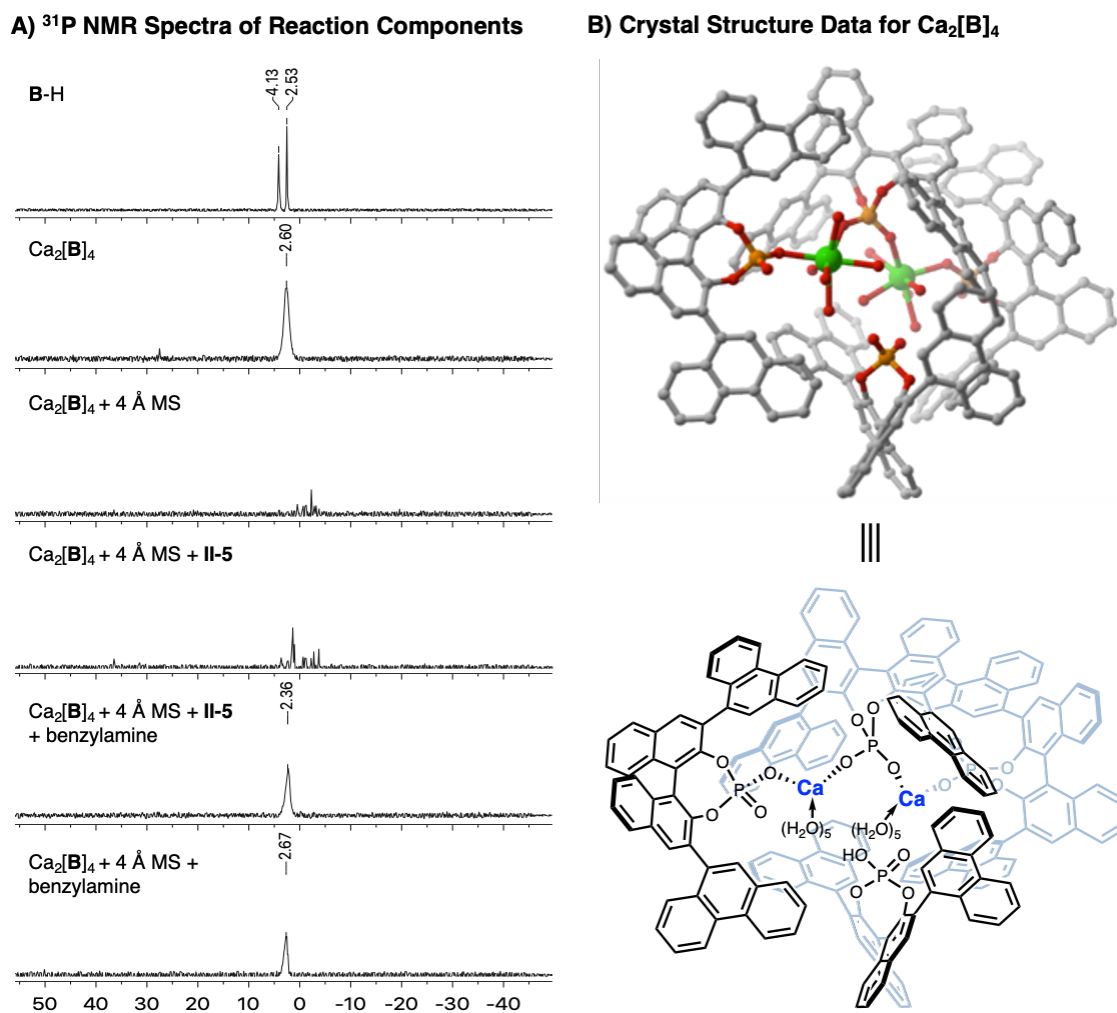
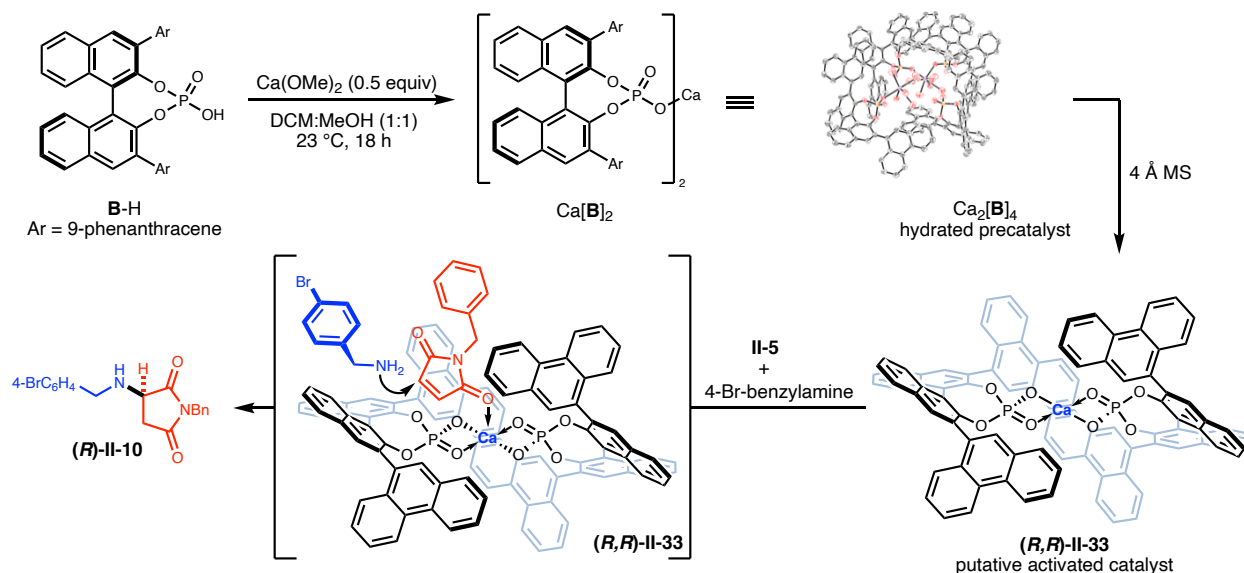


Figure 2.2 (A) Crystal structure of the proposed hydrated precatalyst at 80% probability and (B) ^{31}P NMR spectra of reaction components.

$\text{Ca}[\text{B}]_2$ complex **II-33** (observed by HRMS). The extent of dehydration of $\text{Ca}_2[\text{B}]_4 \cdot (\text{H}_2\text{O})_{10}$ required to form the active catalyst cannot be quantified by these experiments; however, it is reasonable to postulate that the loss of some coordinating water ligands from the $\text{Ca}_2[\text{B}]_4 \cdot (\text{H}_2\text{O})_{10}$ complex should open up Lewis acidic sites on the calcium atom, which are then able to coordinate the amine nucleophile. Based on structure **II-33**, we propose a model for enantioselective

Scheme 2.5 Synthesis and *in situ* activation of Ca[B]₂ and proposed stereinduction model.

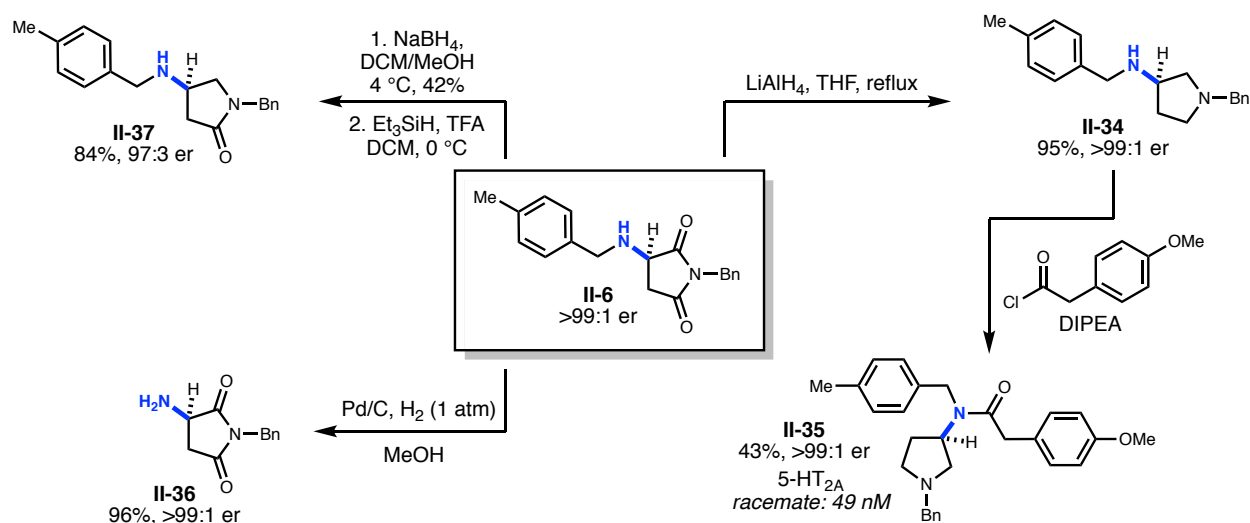
ctivity, where the *si*-face of maleimide **II-5** is blocked, which allows the *re*-face attack of the amine nucleophile (Scheme 2.5).

2.6 Substrate Diversification

After exploring the scope of our conjugate addition with a variety of amines and maleimides, we also applied our methodology to the synthesis of **II-35**, a potent novel 5-HT_{2A} agonist developed by Acadia Pharmaceuticals (Scheme 2.6).¹³⁷ Since the binding affinity of **II-35** was measured as a racemic mixture, we envisioned that our methodology could readily determine the more active enantiomer. Starting from recrystallized **II-6**, lithium aluminum hydride reduction cleanly produced **II-34** in 95% yield and >99:1 e.r. (Scheme 2.6). Selective acylation of **II-34** with 4-methoxyphenylacetic acid produced **II-35** in 43% yield and >99:1 e.r. To further demonstrate the utility of this methodology, we selectively removed the benzylic group

on the amine (**II-36**) via hydrogenation as well as selectively deoxygenated the position adjacent to the amine (**II-37**).

Scheme 2.6 Substrate diversification and target synthesis.



2.7 Conclusion

In summary, we have discovered an efficient and scalable catalytic asymmetric conjugate addition of unmasked and unfunctionalized amines to maleimides. This process accommodates both primary and secondary amines, which underscores the unusual compatibility of these Lewis basic nucleophiles with the Lewis acidic Ca²⁺ complex. Crystallographic studies indicate an initial Ca₂[B]₄ species is formed through the reaction of a chiral phosphoric acid and calcium(II) methoxide. Further spectroscopic studies indicate that a dynamic process is involved, where molecular sieves are required for the observed reactivity and selectivity, which are thought to play a role in the activation of the catalyst. The addition of amine nucleophiles can re-establish a

hydrogen bonding network similar to that found in the hydrated $\text{Ca}_2[\mathbf{B}]_4 \cdot (\text{H}_2\text{O})_{10}$ complex. Furthermore, although the calcium phosphate catalyst $\text{Ca}[\mathbf{B}]_2$ has a relatively high molecular weight, it can be effectively recovered in >95% yield. Future investigations involve continued analysis of the calcium-phosphate dynamics and applications of this reaction in the synthesis of bioactive compounds.

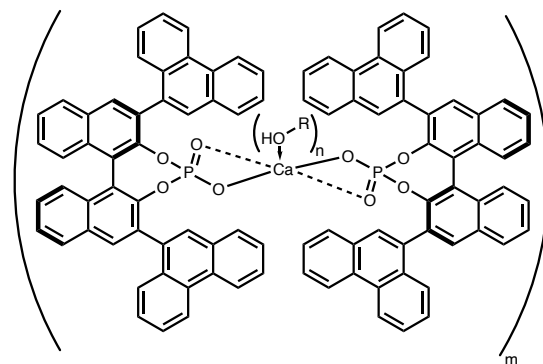
2.8 Experimental

2.8.1 Materials and Methods

All reactions were carried out under an ambient atmosphere in non-oven-dried glassware with magnetic stirring. THF, toluene, and DMF were purified by passage through a bed of activated alumina.¹⁶⁶ Reagents were purified prior to use unless otherwise stated following the guidelines of Perrin and Armarego.¹⁶⁷ *N*-tolylamine was distilled from CaH_2 . Purification of reaction products was carried out by flash chromatography using EM Reagent silica gel 60 (230-400 mesh). Analytical thin layer chromatography was performed on EM Reagent 0.25 mm silica gel 60-F plates. Visualization was accomplished with UV light and ceric ammonium nitrate stain or potassium permanganate stain followed by heating. Infrared spectra were recorded on a Bruker Tensor 37 FT-IR spectrometer. ^1H NMR spectra were recorded on AVANCE III 500 MHz with direct cryoprobe (500 MHz) spectrometer and are reported in ppm using solvent as an internal standard (CDCl_3 at δ 7.26 ppm). Data are reported as (ap = apparent, s = singlet, d = doublet, t = apparent triplet, q = quartet, m = multiplet, b = broad; coupling constant(s) in Hz; integration). Proton-decoupled ^{13}C NMR spectra were recorded on an AVANCE III 500 MHz with direct cryoprobe (125 MHz) spectrometer and are reported in ppm using solvent as an internal standard (CDCl_3 at δ 77.00 ppm). ^{31}P NMR spectra were acquired at 26 °C on a 400

MHz Agilent 400MR-DD2 spectrometer equipped with a OneNMR probe and a 7600AS autosampler; this system was funded by NSF CRIF grant CHE-104873. Mass spectra were obtained on a WATERS Acquity-H UPLC-MS with a single quad detector (ESI) or on a Varian 1200 Quadrupole Mass Spectrometer and Micromass Quadro II Spectrometer (ESI). All optical rotation measurements were obtained on a Rudolph Research Analytical Autopol IV, Serial #82239. X-ray data were collected on the Kappa Apex 2 diffractometer.

2.8.2 Synthesis and Characterization of $\text{Ca}[\mathbf{B}]_2$

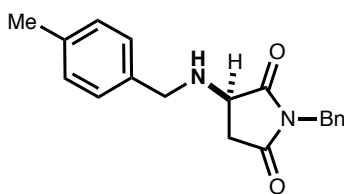


Calcium 2,6-di(phenanthren-9-yl)dinaphtho[2,1-d:1',2'-f][1,3,2]dioxaphosphepin-4-olate 4-oxide ($\text{Ca}[\mathbf{B}]_2$): To a flame-dried flask at 23 °C, charged with dichloromethane:MeOH (1:1, 12 mL), was added **B** [(*R*)-9,9'-bisphenanthryl-BINOL phosphoric acid (2.57 mmol, 1.80 g, 2.0 equiv)] and freshly powdered calcium methoxide (1.28 mmol, 0.131 g, 1.0 equiv). The reaction was stirred for 24 h at 23 °C at which point the slightly turbid solution was concentrated to dryness, azeotroped with toluene (3 x 15 mL), and placed under high vacuum (~ 0.1 Torr) to yield $\text{Ca}[\mathbf{B}]_2$ as an off white powder (1.28 mmol, 1.84 g, quantitative): ^1H NMR (500 MHz, $\text{DMSO-}d_6$) δ 8.90 (dd, $J = 14.0, 8.2$ Hz, 8H), 8.06 (m, 16H), 7.57 (m, 36H), 4.11 (q, $J = 5.2$ Hz, 1H, MeOH), 3.34 (s, 14H, H_2O), 3.17 (d, $J = 5.0$ Hz, 3H, MeOH); ^{13}C NMR (126 MHz, $\text{DMSO-}d_6$) δ 148.4, 148.3, 134.3, 133.3, 132.3, 131.4, 131.2, 130.1, 129.6, 129.6, 129.3, 129.0, 128.3,

126.8, 126.5, 126.3, 124.9, 123.0, 122.7, 122.4, 48.6 (MeOH); HRMS (ESI): Mass calculated for $C_{26}H_{27}CaO_5P_2$ $[M+H]^+$: 1439.3155; found: 1439.3149. For full 1H NMR and ^{13}C NMR spectra of $Ca[B]_2$, see Appendix A.

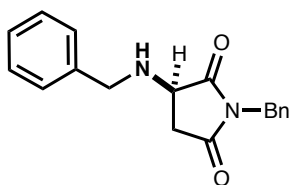
2.8.3 General Procedure and Characterization Data for the Synthesis of Aminosuccinimides

In a nitrogen-filled dry box, a screw-cap reaction tube equipped with a magnetic stir bar was charged with the corresponding maleimide (0.2 mmol, 1.0 equiv), calcium phosphate complex catalyst $Ca[B]_2$ (14.0 mg, 0.01 mmol, 0.05 equiv), and 4 Å MS (100 mg). The tube was capped with a septum cap, removed from the drybox, and put under positive N_2 pressure. Dry toluene (3.0 mL) was then added and the heterogeneous mixture was cooled to -20 °C. A solution of the corresponding amine (0.20 mmol, 1.0 equiv) in toluene (0.9 mL) was added dropwise, and the reaction was stirred at -20 °C for 14 h. At this point, an additional bolus of amine (0.02 mmol, 0.1 equiv) in toluene (0.1 mL) was added. After 18 h, the entire crude reaction mixture at -20 °C was directly transferred onto a SiO_2 column pre-equilibrated with 3:1 hexanes:EtOAc. Flash chromatography (gradient 3:1 hexanes:EtOAc \rightarrow 1:1 hexanes:EtOAc) afforded the aminosuccinimide product, followed by elution with 10:1 EtOAc:MeOH to recover $Ca[B]_2$. For full 1H NMR, ^{13}C NMR, and chiral HPLC spectra of all products, see Appendix A.

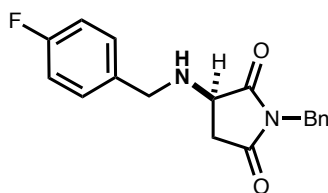


(R)-1-benzyl-3-[(4-methylbenzyl)amino]pyrrolidine-2,5-dione (Compound II-6): Prepared according to the general procedure using *p*-tolylmethylamine (0.027 g, 0.22 mmol, 1.1 equiv) to afford 0.062 g (87% yield) of product as a clear crystalline solid: 1H NMR (500 MHz,

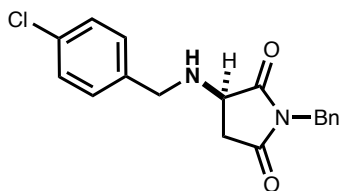
Chloroform-*d*) δ 7.24 (m, 10H), 4.65 (s, 2H), 3.79 (m, 3H), 2.85 (dd, $J = 18.0, 8.3$ Hz, 1H), 2.51 (dd, $J = 18.1, 4.8$ Hz, 1H), 2.33 (s, 3H), 2.16 (s, 1H) ppm; ^{13}C NMR (126 MHz, Chloroform-*d*) δ 177.6, 174.9, 137.2, 135.5, 135.5, 129.3, 128.8, 128.7; 128.2, 128.0, 55.4, 51.6, 42.4, 36.4, 21.1 ppm; HRMS (ESI): Mass calculated for $\text{C}_{19}\text{H}_{21}\text{N}_2\text{O}_2$ $[\text{M}+\text{H}]^+$: 309.1603; found: 309.1603; IR (thin film): 3302, 3291, 2913, 2846, 1763, 1690, 1514, 1495, 1453 cm^{-1} ; Enantiomeric ratio was measured by chiral phase HPLC (AD-H, 10% *i*PrOH/hexanes, 1.0 mL/min, 210 nm), t_{R} (major) = 18.07 min, t_{R} (minor) = 15.16 min; e.r. = 94:6.



(*R*)-1-benzyl-3-(benzylamino)pyrrolidine-2,5-dione (Compound II-7): Prepared according to the general procedure using benzylamine (0.024 g, 0.22 mmol, 1.1 equiv) to afford 0.049 g (84% yield) of product as a clear crystalline solid: ^1H NMR (500 MHz, Chloroform-*d*) δ 7.32 (m, 10H), 4.65 (d, $J = 2.4$ Hz, 2H), 3.86 (q, $J = 13.1$ Hz, 2H), 3.75 (dd, $J = 8.2, 5.0$ Hz, 1H), 2.87 (dd, $J = 17.9, 8.3$ Hz, 1H), 2.52 (dd, $J = 17.9, 5.0$ Hz, 1H), 2.21 (s, 1H) ppm; ^{13}C NMR (126 MHz, Chloroform-*d*) δ 177.6, 174.8, 138.6, 135.5, 128.8, 128.7 (x 2), 128.3, 128.0, 127.6, 55.5, 51.8, 42.4, 36.4 ppm; HRMS (ESI): Mass calculated for $\text{C}_{18}\text{H}_{19}\text{N}_2\text{O}_2$ $[\text{M}+\text{H}]^+$: 295.1447; found: 295.1445; IR (thin film): 3330, 3028, 2926, 2848, 1694, 1605, 1401, 1426, 1458, 1495 cm^{-1} ; Enantiomeric ratio was measured by chiral phase HPLC (AD-H, 10% *i*PrOH/hexanes, 1.0 mL/min, 210 nm), t_{R} (major) = 18.14 min, t_{R} (minor) = 14.78 min; e.r. = 94:6.

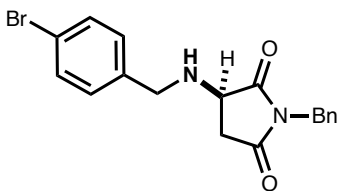


(R)-1-benzyl-3-[(4-fluorobenzyl)amino]pyrrolidine-2,5-dione (Compound II-8): Prepared according to the general procedure using (4-fluorophenyl)methanamine (0.028 g, 0.22 mmol, 1.1 equiv) to afford 0.048 g (77% yield) of product as a clear crystalline solid: ^1H NMR (500 MHz, Chloroform-*d*) δ 7.32 (m, 7H), 7.01 (m, 2H), 4.65 (d, $J = 2.0$ Hz, 2H), 3.83 (s, 2H), 3.75 (dd, $J = 8.3, 5.0$ Hz, 1H), 2.88 (dd, $J = 17.9, 8.3$ Hz, 1H), 2.50 (dd, $J = 17.9, 5.0$ Hz, 1H), 2.14 (s, 1H) ppm; ^{13}C NMR (126 MHz, Chloroform-*d*) δ 177.5, 174.7, 162.2 (d, $J_{\text{C,F}} = 245.7$ Hz), 135.5, 134.5 (d, $J_{\text{C,F}} = 3.2$ Hz), 129.9 (d, $J_{\text{C,F}} = 8.1$ Hz), 128.8, 128.7, 128.1, 115.5 (d, $J_{\text{C,F}} = 21.4$ Hz), 55.6, 51.1, 42.5, 36.4 ppm; HRMS (ESI): Mass calculated for $\text{C}_{18}\text{H}_{18}\text{FN}_2\text{O}_2$ [$\text{M}+\text{H}$] $^+$: 313.1352; found: 313.1347; IR (thin film): 3300, 3035, 2845, 2912, 1598, 1507, 1482, 1446, 1429, 1401, 1357 cm^{-1} ; Enantiomeric ratio was measured by chiral phase HPLC (AD-H, 10% i PrOH/hexanes, 1.0 mL/min, 210 nm), t_{R} (major) = 20.17 min, t_{R} (minor) = 15.66 min; e.r. = 93:7.

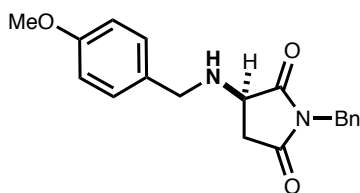


(R)-1-benzyl-3-[(4-chlorophenyl)amino]pyrrolidine-2,5-dione (Compound II-9): Prepared according to the general procedure using (4-chlorophenyl)methanamine (0.031 g, 0.22 mmol, 1.1 equiv) to afford 0.060 g (91% yield) of product as a clear crystalline solid: ^1H NMR (500 MHz, Chloroform-*d*) δ 7.28 (m, 9H), 4.62 (d, $J = 1.9$ Hz, 2H), 3.80 (s, 2H), 3.71 (dd, $J = 8.3, 5.0$ Hz, 1H), 2.84 (dd, $J = 17.9, 8.3$ Hz, 1H), 2.46 (dd, $J = 17.9, 5.0$ Hz, 1H), 2.11 (s, 1H) ppm; ^{13}C NMR

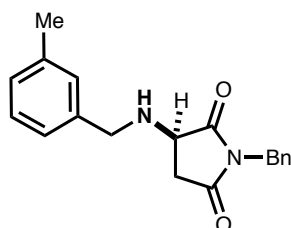
(126 MHz, Chloroform-*d*) δ 177.5, 174.7, 137.2, 135.4, 133.3, 129.6, 128.8, 128.8, 128.7, 128.1, 55.5, 51.1, 42.5, 36.4 ppm; HRMS (ESI): Mass calculated for C₁₈H₁₈ClN₂O₂ [M+H]⁺: 329.1057; found: 329.1051; IR (thin film): 3302, 3036, 2911, 2833, 1690, 1445, 1429, 1400, 1335 cm⁻¹; Enantiomeric ratio was measured by chiral phase HPLC (AD-H, 10% *i*PrOH/hexanes, 1.0 mL/min, 210 nm), t_R (major) = 22.05 min, t_R (minor) = 18.0 min; e.r. = 93:7.



(*R*)-1-benzyl-3-[(4-bromobenzyl)amino]pyrrolidine-2,5-dione (Compound II-10): Prepared according to the general procedure using (4-bromophenyl)methanamine (0.041 g, 0.22 mmol, 1.1 equiv) to afford 0.067 g (90% yield) of product as a clear crystalline solid: ¹H NMR (500 MHz, Chloroform-*d*) δ 7.45 (m, 2H), 7.37 (dd, J = 7.9, 1.7 Hz, 2H), 7.30 (m, 3H), 7.18 (d, J = 8.1 Hz, 2H), 4.65 (d, J = 2.1 Hz, 2H), 3.82 (s, 2H), 3.74 (dd, J = 8.3, 5.0 Hz, 1H), 2.87 (dd, J = 18.0, 8.3 Hz, 1H), 2.49 (dd, J = 18.0, 5.0 Hz, 1H), 2.13 (s, 1H) ppm; ¹³C NMR (126 MHz, Chloroform-*d*) δ 177.5, 174.6, 137.7, 135.4, 131.7, 129.9, 128.8, 128.7, 128.1, 121.4, 55.5, 51.2, 42.5, 36.4 ppm; HRMS (ESI): Mass calculated for C₁₈H₁₈BrN₂O₂ [M+H]⁺: 373.0552; found: 373.0546; IR (thin film): 3300, 3010, 2833, 1690, 1487, 1466, 1454, 1429, 1402, 1361 cm⁻¹; Enantiomeric ratio was measured by chiral phase HPLC (AD-H, 10% *i*PrOH/hexanes, 1.0 mL/min, 210 nm), t_R (major) = 22.34 min, t_R (minor) = 18.30 min; e.r. = 93:7.

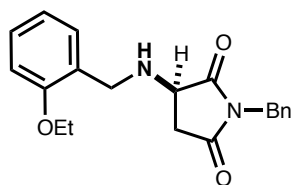


(R)-1-benzyl-3-[(4-methoxybenzyl)amino]pyrrolidine-2,5-dione (Compound II-11): Prepared according to the general procedure using (4-methoxyphenyl)methanamine (0.030 g, 0.22 mmol, 1.1 equiv) to afford 0.058 g (90% yield) of product as a clear crystalline solid: ^1H NMR (500 MHz, Chloroform-*d*) δ 7.36 (m, 2H), 7.30 (m, 4H), 7.21 (d, $J = 8.5$ Hz, 2H), 6.86 (d, $J = 8.6$ Hz, 2H), 4.65 (d, $J = 2.4$ Hz, 2H), 3.79 (m, 6H), 2.85 (dd, $J = 17.9, 8.3$ Hz, 1H), 2.50 (dd, $J = 18.0, 5.0$ Hz, 1H) ppm; ^{13}C NMR (126 MHz, Chloroform-*d*) δ 177.7, 174.9, 159.0, 135.5, 130.7, 129.5, 128.8, 128.7, 128.0, 114.0, 55.4, 55.3, 51.3, 42.4, 36.4 ppm; HRMS (ESI): Mass calculated for $\text{C}_{19}\text{H}_{20}\text{N}_2\text{O}_3\text{Na}$ $[\text{M}+\text{Na}]^+$: 347.1372; found: 347.1366; IR (thin film): 3301, 3050, 2836, 2957, 1689, 1607, 1401, 1428, 1445, 1482, 1513, 1581 cm^{-1} ; Enantiomeric ratio was measured by chiral phase HPLC (AD-H, 10% *i*PrOH/hexanes, 1.0 mL/min, 210 nm), t_{R} (major) = 26.30 min, t_{R} (minor) = 20.72 min; e.r. = 94:6.

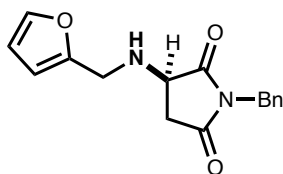


(R)-1-benzyl-3-[(3-methylbenzyl)amino]pyrrolidine-2,5-dione (Compound II-12): Prepared according to the general procedure using (3-methylphenyl)methanamine (0.027 g, 0.22 mmol, 1.1 equiv) to afford 0.059 g (96% yield) of product as a clear crystalline solid: ^1H NMR (500 MHz, Chloroform-*d*) δ 7.37 (m, 2H), 7.30 (m, 3H), 7.22 (t, $J = 7.5$ Hz, 1H), 7.09 (m, 3H), 4.65

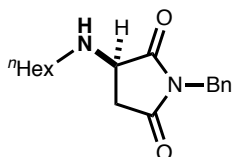
(d, $J = 2.4$ Hz, 2H), 3.77 (m, 3H), 2.87 (dd, $J = 18.0, 8.2$ Hz, 1H), 2.52 (dd, $J = 17.9, 5.0$ Hz, 1H), 2.34 (s, 3H), 2.21 (s, 1H) ppm; ^{13}C NMR (126 MHz, Chloroform-*d*) δ 177.6, 174.9, 138.5, 138.4, 135.5, 129.0, 128.8, 128.7, 128.5, 128.3, 128.0, 125.3, 55.5, 51.8, 42.4, 36.4, 21.4 ppm; HRMS (ESI): Mass calculated for $\text{C}_{19}\text{H}_{21}\text{N}_2\text{O}_2$ $[\text{M}+\text{H}]^+$: 309.1603; found: 309.1598; IR (thin film): 3289, 3009, 2810, 1689, 1607, 1432, 1453, 1496, 1513 cm^{-1} ; Enantiomeric ratio was measured by chiral phase HPLC (AD-H, 10% *i*PrOH/hexanes, 1.0 mL/min, 210 nm), t_{R} (major) = 14.20 min, t_{R} (minor) = 11.72 min; e.r. = 95:5.



(R)-1-benzyl-3-[(2-ethoxybenzyl)amino]pyrrolidine-2,5-dione (Compound II-13): Prepared according to the general procedure using (2-ethoxyphenyl)methanamine (0.033 g, 0.22 mmol, 1.1 equiv) to afford 0.062 g (92% yield) of product as a clear crystalline solid: ^1H NMR (500 MHz, Chloroform-*d*) δ 7.35 (m, 2H), 7.26 (m, 4H), 7.17 (dd, $J = 7.4, 1.7$ Hz, 1H), 6.88 (m, 2H), 4.64 (m, 2H), 4.08 (q, $J = 7.0$ Hz, 2H), 3.95 (d, $J = 13.5$ Hz, 1H), 3.73 (d, $J = 13.5$ Hz, 1H), 3.66 (dd, $J = 8.1, 4.8$ Hz, 1H), 2.88 (dd, $J = 17.8, 8.1$ Hz, 1H), 2.58 (m, 2H), 1.45 (t, $J = 6.9$ Hz, 3H) ppm; ^{13}C NMR (126 MHz, Chloroform-*d*) δ 177.7, 175.2, 157.2, 135.5, 130.2, 128.9, 128.7, 128.6, 127.9, 126.5, 120.4, 111.3, 63.5, 54.8, 47.4, 42.4, 36.3, 14.9 ppm; HRMS (ESI): Mass calculated for $\text{C}_{20}\text{H}_{23}\text{N}_2\text{O}_3$ $[\text{M}+\text{H}]^+$: 339.1709; found: 339.1906; IR (thin film): 2933, 1699, 1430, 1354, 1476, 1493, 1587, 1599 cm^{-1} ; Enantiomeric ratio was measured by chiral phase HPLC (AD-H, 10% *i*PrOH/hexanes, 0.5 mL/min, 210 nm), t_{R} (major) = 31.75 min, t_{R} (minor) = 33.25 min; e.r. = 97:3.

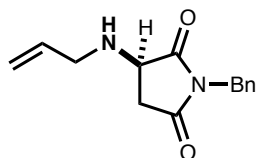


(R)-1-benzyl-3-[(furan-2-ylmethyl)amino]pyrrolidine-2,5-dione (Compound II-14): Prepared according to the general procedure using furan-2-ylmethanamine (0.021 g, 0.22 mmol, 1.1 equiv) to afford 0.028 g (49% yield) of product as a clear oil: ^1H NMR (500 MHz, Chloroform-*d*) δ 7.22 (m, 6H), 6.16 (m, 2H), 4.53 (d, $J = 1.9$ Hz, 2H), 3.77 (m, 2H), 3.62 (dd, $J = 8.2, 5.0$ Hz, 1H), 2.76 (dd, $J = 17.9, 8.2$ Hz, 1H), 2.36 (dd, $J = 18.0, 5.1$ Hz, 1H), 2.23 (m, 1H) ppm; ^{13}C NMR (126 MHz, Chloroform-*d*) δ 177.3, 174.7, 152.1, 142.4, 135.4, 128.8, 128.6, 128.0, 110.3, 108.0, 55.0, 44.1, 42.4, 36.2 ppm; HRMS (ESI): Mass calculated for $\text{C}_{16}\text{H}_{17}\text{N}_2\text{O}_3$ $[\text{M}+\text{H}]^+$: 285.1239; found: 285.1232; IR (thin film): 3291, 3010, 2982, 2850, 1690, 1604, 1505, 1494, 1456, 1432 cm^{-1} ; Enantiomeric ratio was measured by chiral phase HPLC (AD-H, 10% $^i\text{PrOH}$ /hexanes, 1.0 mL/min, 210 nm), t_{R} (major) = 19.49 min, t_{R} (minor) = 17.13 min; e.r. = 88:12.

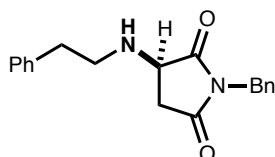


(R)-1-benzyl-3-(hexylamino)pyrrolidine-2,5-dione (Compound II-15): Prepared according to the general procedure using *n*-hexylamine (0.022 g, 0.22 mmol, 1.1 equiv) to afford 0.036 g (63% yield) of product as a clear oil: ^1H NMR (500 MHz, Chloroform-*d*) δ 7.32 (m, 5H), 4.65 (s, 2H), 3.75 (dd, $J = 8.3, 4.9$ Hz, 1H), 2.92 (dd, $J = 18.0, 8.3$ Hz, 1H), 2.65 (dt, $J = 11.1, 7.1$ Hz, 1H), 2.54 (m, 2H), 1.83 (s, 1H), 1.47 (q, $J = 7.3$ Hz, 2H), 1.29 (m, 7H), 0.88 (t, $J = 6.8$ Hz, 3H)

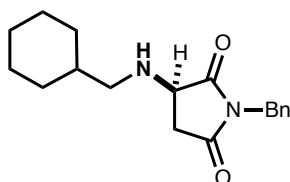
ppm; ^{13}C NMR (126 MHz, Chloroform-*d*) δ = 177.7, 175.0, 135.5, 128.8, 128.7, 128.0, 56.4, 47.7, 42.4, 36.3, 31.6, 29.9, 26.8, 22.5, 14.0 ppm; HRMS (ESI): Mass calculated for $\text{C}_{17}\text{H}_{25}\text{N}_2\text{O}_2$ $[\text{M}+\text{H}]^+$: 289.1916; found: 289.1911; IR (thin film): 3298, 3031, 2952, 2928, 2849, 1694, 1494, 1465, 1455, 1430 cm^{-1} ; Enantiomeric ratio was measured by chiral phase HPLC (AD-H, 10% *i*PrOH/hexanes, 1.0 mL/min, 210 nm), t_{R} (major) = 11.37 min, t_{R} (minor) = 9.12 min; e.r. = 92:8.



(R)-1-benzyl-3-(propylamino)pyrrolidine-2,5-dione (Compound II-16): Prepared according to the general procedure using allylamine (0.013 g, 0.22 mmol, 1.1 equiv) to afford 0.048 g (97% yield) of product as a clear solid: ^1H NMR (500 MHz, Chloroform-*d*) δ 7.37 (d, J = 6.8 Hz, 2H), 7.30 (m, 3H), 5.85 (ddt, J = 16.5, 10.3, 6.1 Hz, 1H), 5.18 (m, 2H), 4.65 (s, 2H), 3.79 (dd, J = 8.3, 5.0 Hz, 1H), 3.30 (m, 2H), 2.91 (dd, J = 17.9, 8.3 Hz, 1H), 2.53 (dd, J = 18.0, 5.0 Hz, 1H), 1.94 (s, 1H) ppm; ^{13}C NMR (126 MHz, Chloroform-*d*) δ 177.6, 174.8, 135.5, 135.4, 128.8, 128.7, 128.0, 117.3, 55.5, 50.3, 42.4, 36.5 ppm; HRMS (ESI): Mass calculated for $\text{C}_{14}\text{H}_{17}\text{N}_2\text{O}_2$ $[\text{M}+\text{H}]^+$: 245.1290; found: 245.1285; IR (thin film): 3301, 3035, 2928, 2855, 1690, 1497, 1455, 1430, 1397 cm^{-1} ; Enantiomeric ratio was measured by chiral phase HPLC (AD-H, 10% *i*PrOH/hexanes, 1.0 mL/min, 210 nm), t_{R} (major) = 13.87 min, t_{R} (minor) = 11.63 min; e.r. = 91:9.

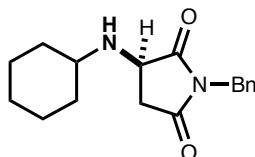


(R)-1-benzyl-3-(phenethylamino)pyrrolidine-2,5-dione (Compound II-17): Prepared according to the general procedure using phenethylamine (0.027 g, 0.22 mmol, 1.1 equiv) to afford 0.062 g (81% yield) of product as a clear solid: ^1H NMR (500 MHz, Chloroform-*d*) δ 7.33 (m, 7H), 7.21 (m, 3H), 4.64 (d, $J = 1.6$ Hz, 2H), 3.75 (dd, $J = 8.3, 4.9$ Hz, 1H), 2.88 (m, 5H), 2.50 (dd, $J = 18.0, 4.9$ Hz, 1H), 1.85 (s, 1H) ppm; ^{13}C NMR (126 MHz, Chloroform-*d*) δ 177.4, 174.8, 139.1, 135.5, 128.8, 128.7, 128.6, 128.6, 128.0, 126.5, 56.3, 48.8, 42.4, 36.2, 36.2 ppm; HRMS (ESI): Mass calculated for $\text{C}_{19}\text{H}_{21}\text{N}_2\text{O}_2$ $[\text{M}+\text{H}]^+$: 309.1603; found: 309.1598; IR (thin film): 3301, 3028, 2918, 2860, 1693, 1604, 1497, 1465, 1453, 1431 cm^{-1} ; Enantiomeric ratio was measured by chiral phase HPLC (AD-H, 10% *i*PrOH/hexanes, 1.0 mL/min, 210 nm), t_{R} (major) = 17.06 min, t_{R} (minor) = 14.05 min; e.r. = 88:12.

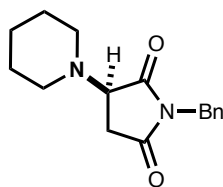


(R)-1-benzyl-3-[(cyclohexylmethyl)amino]pyrrolidine-2,5-dione (Compound II-18): Prepared according to the general procedure using cyclohexylmethanamine (0.025 g, 0.22 mmol, 1.1 equiv) to afford 0.058 g (97% yield) of product as a clear solid: ^1H NMR (500 MHz, Chloroform-*d*) δ 7.33 (m, 5H), 4.65 (d, $J = 1.9$ Hz, 2H), 3.73 (dd, $J = 8.3, 4.9$ Hz, 1H), 2.91 (dd, $J = 18.0, 8.3$ Hz, 1H), 2.50 (dt, $J = 17.8, 5.5$ Hz, 2H), 2.37 (dd, $J = 11.3, 6.7$ Hz, 1H), 1.83 (s, 1H), 1.71 (m, 5H), 1.41 (m, 1H), 1.20 (m, 3H), 0.90 (m, 2H) ppm; ^{13}C NMR (126 MHz, Chloroform-*d*) δ = 177.7, 175.0, 135.5, 128.8, 128.6, 128.0, 56.5, 54.2, 42.4, 38.0, 36.3, 31.2, 26.5, 25.9 ppm; HRMS (ESI): Mass calculated for $\text{C}_{18}\text{H}_{25}\text{N}_2\text{O}_2$ $[\text{M}+\text{H}]^+$: 301.1916; found: 301.1911; IR (thin film): 3303, 2916, 2850, 1694, 1494, 1461, 1431 cm^{-1} ; Enantiomeric ratio

was measured by chiral phase HPLC (AD-H, 10% *i*-PrOH/hexanes, 1.0 mL/min, 210 nm), t_R (major) = 9.75 min, t_R (minor) = 9.18 min; e.r. = 97:3.

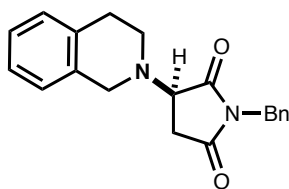


(R)-1-benzyl-3-(cyclohexylamino)pyrrolidine-2,5-dione (Compound II-19): Prepared according to the general procedure using cyclohexylamine (0.022 g, 0.22 mmol, 1.1 equiv) to afford 0.048 g (84% yield) of product as a clear solid: ^1H NMR (500 MHz, Chloroform-*d*) δ 7.32 (m, 5H), 4.65 (s, 2H), 3.86 (dd, J = 8.2, 5.0 Hz, 1H), 2.93 (dd, J = 17.9, 8.2 Hz, 1H), 2.54 (m, 2H), 1.86 (m, 2H), 1.60 (m, 3H), 1.18 (m, 5H) ppm; ^{13}C NMR (126 MHz, Chloroform-*d*) δ 178.2, 175.0, 135.5, 128.9, 128.7, 128.0, 55.7, 54.2, 42.5, 38.1, 34.1, 33.1, 25.8, 24.9, 24.9 ppm; HRMS (ESI): Mass calculated for $\text{C}_{17}\text{H}_{23}\text{N}_2\text{O}_2$ $[\text{M}+\text{H}]^+$: 287.1760; found: 287.1754; IR (thin film): 3520, 3248, 3035, 2920, 2849, 1688, 1630, 1520, 1498, 1470, 1455, 1439, 1401 cm^{-1} ; Enantiomeric ratio was measured by chiral phase supercritical fluid HPLC (IA, 2% MeOH/ CO_2 , 1.0 mL/min, 210 nm), t_R (major) = 2.16 min, t_R (minor) = 2.38 min; e.r. = 95:5.



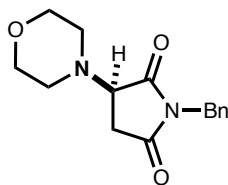
(R)-1-benzyl-3-(piperidin-1-yl)pyrrolidine-2,5-dione (Compound II-20): Prepared according to the general procedure using piperidine (0.019 g, 0.22 mmol, 1.1 equiv) to afford 0.052 g (95% yield) of product as a clear oil: ^1H NMR (500 MHz, Chloroform-*d*) δ 7.32 (m, 5H), 4.64 (m, 2H),

3.77 (dd, $J = 9.1, 4.7$ Hz, 1H), 2.82 (dd, $J = 18.6, 9.0$ Hz, 1H), 2.69 (m, 3H), 2.41 (dt, $J = 11.0, 5.3$ Hz, 2H), 1.59 (m, 4H), 1.43 (p, $J = 6.0$ Hz, 2H) ppm; ^{13}C NMR (126 MHz, Chloroform-*d*) δ 176.2, 175.0, 135.8, 128.8, 128.6, 127.9, 63.2, 50.2, 42.1, 31.6, 26.0, 24.0 ppm; HRMS (ESI): Mass calculated for $\text{C}_{16}\text{H}_{21}\text{N}_2\text{O}_2$ $[\text{M}+\text{H}]^+$: 273.1603; found: 273.1598; IR (thin film): 2934, 2846, 1691, 1499, 1470, 1454, 1441, 1422 cm^{-1} ; Enantiomeric ratio was measured by chiral phase HPLC (AD-H, 10% $^i\text{PrOH}$ /hexanes, 1.0 mL/min, 210 nm), t_{R} (major) = 23.70 min, t_{R} (minor) = 27.27 min; e.r. = 97:3.

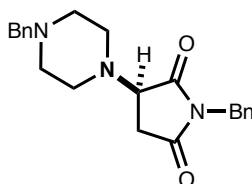


(*R*)-1-benzyl-3-[3,4-dihydroisoquinolin-2(1H)-yl]pyrrolidine-2,5-dione (Compound II-21):

Prepared according to the general procedure using 1,2,3,4-tetrahydroisoquinoline (0.029 g, 0.22 mmol, 1.1 equiv) to afford 0.045 g (71% yield) of product as a clear oil: ^1H NMR (500 MHz, Chloroform-*d*) δ 7.40 (m, 2H), 7.31 (m, 3H), 7.11 (m, 3H), 6.95 (m, 1H), 4.69 (m, 2H), 4.05 (d, $J = 14.3$ Hz, 1H), 3.97 (dd, $J = 9.0, 4.7$ Hz, 1H), 3.70 (d, $J = 14.3$ Hz, 1H), 2.87 (m, 6H) ppm; ^{13}C NMR (126 MHz, Chloroform-*d*) δ 175.9, 174.7, 135.7, 133.7, 133.6, 128.9, 128.8, 128.7, 128.0, 126.5, 126.3, 125.8, 62.2, 51.9, 47.0, 42.3, 32.3, 29.4 ppm; HRMS (ESI): Mass calculated for $\text{C}_{20}\text{H}_{21}\text{N}_2\text{O}_2$ $[\text{M}+\text{H}]^+$: 321.1603; found: 321.1598; IR (thin film): 3282, 3004, 2922, 1692, 1605, 1585, 1498, 1455, 1424, 1400 cm^{-1} ; Enantiomeric ratio was measured by chiral phase HPLC (AD-H, 10% $^i\text{PrOH}$ /hexanes, 1.0 mL/min, 210 nm), t_{R} (major) = 20.75 min, t_{R} (minor) = 13.99 min; e.r. = 93:7.

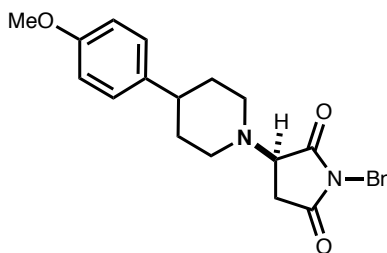


(R)-1-benzyl-3-morpholinopyrrolidine-2,5-dione (Compound II-22): Prepared according to the general procedure using morpholine (0.019 g, 0.22 mmol, 1.1 equiv) to afford 0.051 g (93% yield) of product as a clear oil: ^1H NMR (500 MHz, Chloroform-*d*) δ 7.28 (m, 5H), 4.60 (m, 2H), 3.66 (dt, $J = 19.5, 4.4$ Hz, 5H), 2.76 (m, 3H), 2.61 (dd, $J = 18.4, 4.9$ Hz, 1H), 2.43 (dt, $J = 10.3, 4.6$ Hz, 2H) ppm; ^{13}C NMR (126 MHz, Chloroform-*d*) δ 175.5, 174.5, 135.6, 128.8, 128.7, 128.0, 66.8, 62.5, 49.5, 42.2, 31.4 ppm; HRMS (ESI): Mass calculated for $\text{C}_{15}\text{H}_{19}\text{N}_2\text{O}_3$ $[\text{M}+\text{H}]^+$: 275.1396; found: 275.1390; IR (thin film): 2853, 1698, 1496, 1454, 1429 cm^{-1} ; Enantiomeric ratio was measured by chiral phase HPLC (AD-H, 10% *i*PrOH/hexanes, 0.5 mL/min, 210 nm), t_{R} (major) = 51.83 min, t_{R} (minor) = 49.28 min; e.r. = 97:3.



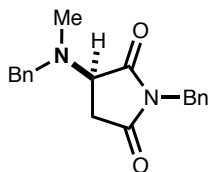
(R)-1-benzyl-3-(4-benzylpiperazin-1-yl)pyrrolidine-2,5-dione (Compound II-23): Prepared according to the general procedure using 1-benzylpiperazine (0.039 g, 0.22 mmol, 1.1 equiv) to afford 0.068 g (93% yield) of product as a clear oil: ^1H NMR (500 MHz, Chloroform-*d*) δ 7.32 (m, 10H), 4.65 (d, $J = 5.3$ Hz, 2H), 3.79 (dd, $J = 8.8, 4.9$ Hz, 1H), 3.51 (s, 2H), 2.80 (m, 3H), 2.67 (dd, $J = 18.4, 5.0$ Hz, 1H), 2.50 (s, 6H) ppm; ^{13}C NMR (126 MHz, Chloroform-*d*) δ 175.8, 174.7, 137.9, 135.7, 129.1, 128.8, 128.6, 128.2, 128.0, 127.1, 62.8, 62.4, 52.8, 49.0, 42.2, 31.2 ppm; HRMS (ESI): Mass calculated for $\text{C}_{22}\text{H}_{26}\text{N}_3\text{O}_2$ $[\text{M}+\text{H}]^+$: 364.2025; found: 364.2020; IR

(thin film): 2918, 2814, 1692, 1496, 1453, 1426, 1401 cm^{-1} ; Enantiomeric ratio was measured by chiral phase HPLC (AD-H, 10% *i*PrOH/hexanes, 1.0 mL/min, 210 nm), t_R (major) = 22.91 min, t_R (minor) = 15.41 min; e.r. = 93:7.

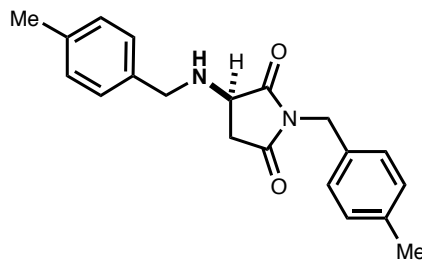


(R)-1-benzyl-3-[4-(4-methoxyphenyl)piperidin-1-yl]pyrrolidine-2,5-dione (Compound II-24): Prepared according to the general procedure using 4-(4-methoxyphenyl)piperidine (0.042 g, 0.22 mmol, 1.1 equiv) to afford 0.070 g (92% yield) of product as a colorless solid. An improved procedure was developed by only changing the temperature to $-40\text{ }^{\circ}\text{C}$ to afford 0.068 g (90% yield) of product as a colorless solid: ^1H NMR (500 MHz, Chloroform-*d*) δ 7.33 (m, 5H), 7.12 (m, 2H), 6.84 (m, 2H), 4.67 (m, 2H), 3.85 (ddd, $J = 9.4, 4.8, 1.9$ Hz, 1H), 3.78 (d, $J = 1.9$ Hz, 3H), 2.87 (td, $J = 13.3, 11.2, 7.6$ Hz, 4H), 2.69 (ddd, $J = 18.5, 4.9, 1.8$ Hz, 1H), 2.45 (m, 1H), 2.27 (td, $J = 11.3, 2.7$ Hz, 1H), 1.77 (m, 4H) ppm; ^{13}C NMR (126 MHz, Chloroform-*d*) δ 176.1, 174.9, 158.0, 138.0, 135.7, 128.8, 128.7, 128.0, 127.6, 113.8, 62.8, 55.2, 51.5, 48.5, 42.2, 41.4, 33.8, 33.5, 31.7 ppm; HRMS (ESI): Mass calculated for $\text{C}_{23}\text{H}_{27}\text{N}_2\text{O}_3$ $[\text{M}+\text{H}]^+$: 379.2022; found: 379.2016; IR (thin film): 3291, 2848, 2914, 1691, 1597, 1514, 1491, 1454, 1435 cm^{-1} ; For the standard reaction run at $-20\text{ }^{\circ}\text{C}$, enantiomeric ratio was measured by chiral phase HPLC (AD-H, 10% *i*PrOH/hexanes, 1.0 mL/min, 210 nm), t_R (major) = 31.84 min, t_R (minor) = 17.77 min; er = 90:10. For the same reaction run at $-40\text{ }^{\circ}\text{C}$, enantiomeric ratio was measured by chiral phase

HPLC (AD-H, 10% *i*PrOH/hexanes, 1.0 mL/min, 210 nm), t_R (major) = 32.26 min, t_R (minor) = 17.91 min; e.r. = 94:6.

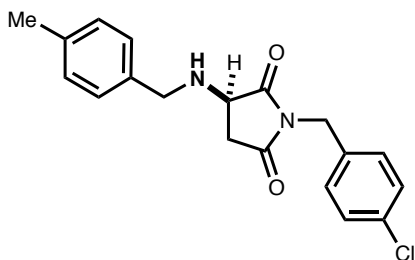


(*R*)-1-benzyl-3-[benzyl(methyl)amino]pyrrolidine-2,5-dione (Compound II-25): Prepared according to the general procedure using *N*-methyl-phenethylamine (0.024 g, 0.22 mmol, 1.1 equiv) to afford 0.055 g (89% yield) of product as a clear oil: ^1H NMR (500 MHz, Chloroform-*d*) δ 7.32 (m, 10H), 4.67 (m, 2H), 3.86 (m, 2H), 3.70 (d, J = 13.1 Hz, 1H), 2.80 (dd, J = 18.6, 9.1 Hz, 1H), 2.63 (dd, J = 18.6, 4.8 Hz, 1H), 2.25 (s, 3H) ppm; ^{13}C NMR (126 MHz, Chloroform-*d*) δ 176.6, 174.9, 137.9, 135.8, 128.9, 128.8, 128.6, 128.5, 128.0, 127.5, 60.3, 59.1, 42.2, 37.2, 31.8 ppm; HRMS (ESI): Mass calculated for $\text{C}_{19}\text{H}_{21}\text{N}_2\text{O}_2$ $[\text{M}+\text{H}]^+$: 309.1603; found: 309.1598; IR (thin film): 3069, 2955, 1701, 1493, 1467, 1417 cm^{-1} ; Enantiomeric ratio was measured by chiral phase HPLC (IA, 2% *i*PrOH/hexanes, 1.0 mL/min, 210 nm), t_R (major) = 19.75 min, t_R (minor) = 20.98 min; e.r. = 78:22.



(*R*)-1-(4-methylbenzyl)-3-[(4-methylbenzyl)amino]pyrrolidine-2,5-dione (Compound II-26): Prepared according to the general procedure using 1-(4-methylbenzyl)-1H-pyrrole-2,5-dione

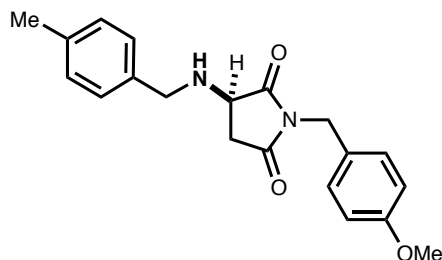
(0.040 g, 0.20 mmol, 1.0 equiv) and *p*-tolylmethanamine (0.027 g, 0.22 mmol, 1.1 equiv) to afford 0.060 g (94% yield) of product as a clear solid: ^1H NMR (500 MHz, Chloroform-*d*) δ 7.23 (s, 2H), 7.12 (m, 6H), 4.58 (d, $J = 2.9$ Hz, 2H), 3.75 (m, 3H), 2.81 (dd, $J = 17.9, 8.2$ Hz, 1H), 2.47 (dd, $J = 17.9, 5.0$ Hz, 1H), 2.30 (d, $J = 11.1$ Hz, 6H), 2.13 (s, 1H) ppm; ^{13}C NMR (126 MHz, Chloroform-*d*) δ 177.7, 174.9, 137.8, 137.2, 135.6, 132.6, 129.3, 129.3, 128.8, 128.2, 55.4, 51.6, 42.2, 36.5, 21.1, 21.1 ppm; HRMS (ESI): Mass calculated for $\text{C}_{20}\text{H}_{23}\text{N}_2\text{O}_2$ $[\text{M}+\text{H}]^+$: 323.1760; found: 323.1554; IR (thin film): 3289, 2980, 2918, 2852, 1691, 1615, 1514, 1454, 1437 cm^{-1} ; Enantiomeric ratio was measured by chiral phase HPLC (AD-H, 10% *i*PrOH/hexanes, 1.0 mL/min, 210 nm), t_{R} (major) = 16.75 min, t_{R} (minor) = 13.13 min; e.r. = 92:8.



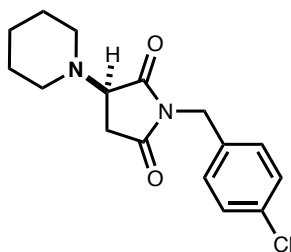
(*R*)-1-(4-chlorobenzyl)-3-[(4-methylbenzyl)amino]pyrrolidine-2,5-dione (Compound II-27):

Prepared according to the general procedure using 1-(4-chlorobenzyl)-1H-pyrrole-2,5-dione (0.044 g, 0.20 mmol, 1.0 equiv) and *p*-tolylmethanamine (0.027 g, 0.22 mmol, 1.1 equiv) to afford 0.066 g (97% yield) of product as a clear solid: ^1H NMR (500 MHz, Chloroform-*d*) δ 7.30 (m, 4H), 7.16 (m, 4H), 4.60 (d, $J = 1.9$ Hz, 2H), 3.78 (m, 3H), 2.85 (dd, $J = 18.0, 8.2$ Hz, 1H), 2.50 (dd, $J = 18.0, 4.9$ Hz, 1H), 2.33 (s, 3H), 2.15 (s, 1H) ppm; ^{13}C NMR (126 MHz, Chloroform-*d*) δ 177.5, 174.8, 137.3, 135.5, 134.0, 133.9, 130.3, 129.3, 128.8, 128.2, 55.4, 51.6, 41.7, 36.4, 21.1 ppm; HRMS (ESI): Mass calculated for $\text{C}_{19}\text{H}_{20}\text{ClN}_2\text{O}_2$ $[\text{M}+\text{H}]^+$: 343.1213; found: 343.1208; IR (thin film): 3291, 2917, 2847, 1691, 1597, 1514, 1491, 1454, 1435 cm^{-1} ;

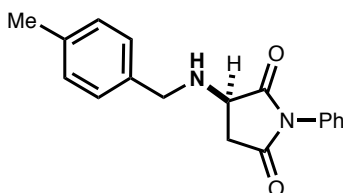
Enantiomeric ratio was measured by chiral phase HPLC (AD-H, 10% *i*PrOH/hexanes, 1.0 mL/min, 210 nm), t_R (major) = 17.92 min, t_R (minor) = 15.52 min; e.r. = 94:6.



(R)-1-(4-methoxybenzyl)-3-[(4-methylbenzyl)amino]pyrrolidine-2,5-dione (Compound II-28): Prepared according to the general procedure using 1-(4-methoxybenzyl)-1H-pyrrole-2,5-dione (0.040 g, 0.20 mmol, 1.0 equiv) and *p*-tolylmethanamine (0.027 g, 0.22 mmol, 1.1 equiv) to afford 0.062 g (91% yield) of product as a clear solid: ^1H NMR (500 MHz, Chloroform-*d*) δ 7.31 (m, 2H), 7.15 (m, 4H), 6.82 (m, 2H), 4.58 (d, $J = 2.8$ Hz, 2H), 3.78 (m, 5H), 3.71 (dd, $J = 8.3, 4.9$ Hz, 1H), 2.83 (dd, $J = 17.9, 8.3$ Hz, 1H), 2.48 (dd, $J = 17.9, 5.0$ Hz, 1H), 2.33 (s, 3H), 2.15 (s, 1H) ppm; ^{13}C NMR (126 MHz, Chloroform-*d*) δ 177.7, 174.9, 159.3, 137.2, 135.6, 130.3, 129.3, 128.2, 127.8, 114.0, 55.4, 55.3, 51.6, 41.9, 36.4, 21.1 ppm; HRMS (ESI): Mass calculated for $\text{C}_{20}\text{H}_{23}\text{N}_2\text{O}_3$ $[\text{M}+\text{H}]^+$: 339.1709; found: 339.1703; IR (thin film): 3284, 3018, 2913, 2857, 1687, 1614, 1585, 1513, 1437, 1398, 1353 cm^{-1} ; Enantiomeric ratio was measured by chiral phase HPLC (AD-H, 10% *i*PrOH/hexanes, 1.0 mL/min, 210 nm), t_R (major) = 31.8 min, t_R (minor) = 23.20 min; e.r. = 87:13.

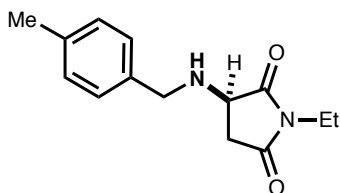


(R)-1-(4-chlorobenzyl)-3-(piperidin-1-yl)pyrrolidine-2,5-dione (Compound II-29): Prepared according to the general procedure using 1-(4-chlorobenzyl)-1H-pyrrole-2,5-dione (0.044 g, 0.20 mmol, 1.0 equiv) and piperidine (0.019 g, 0.22, 1.1 equiv) to afford 0.055 g (89% yield) of product as a clear solid: ^1H NMR (500 MHz, Chloroform-*d*) δ 7.30 (m, 4H), 4.62 (m, 2H), 3.77 (dd, $J = 9.1, 4.7$ Hz, 1H), 2.82 (dd, $J = 18.6, 9.0$ Hz, 1H), 2.67 (m, 3H), 2.40 (dt, $J = 10.8, 5.3$ Hz, 2H), 1.55 (d, $J = 5.5$ Hz, 4H), 1.44 (m, 2H) ppm; ^{13}C NMR (126 MHz, Chloroform-*d*) δ 176.1, 174.9, 134.2, 133.9, 130.3, 128.8, 63.2, 50.2, 41.4, 31.6, 26.0, 24.0 ppm; HRMS (ESI): Mass calculated for $\text{C}_{16}\text{H}_{20}\text{ClN}_2\text{O}_2$ $[\text{M}+\text{H}]^+$: 307.1213; found: 323.1208; IR (thin film): 2927, 2822, 1688, 1508, 1449, 1424, 1395 cm^{-1} ; For the standard reaction run at -20 $^\circ\text{C}$, enantiomeric ratio was measured by chiral phase HPLC (AD-H, 10% *i*PrOH/hexanes, 1.0 mL/min, 210 nm), t_{R} (major) = 10.68 min, t_{R} (minor) = 13.16 min; er = 93:7. For the same reaction run at -40 $^\circ\text{C}$, enantiomeric ratio was measured by chiral phase HPLC (AD-H, 10% *i*PrOH/hexanes, 1.0 mL/min, 210 nm), t_{R} (major) = 10.64 min, t_{R} (minor) = 13.13 min; e.r. = 84:16.



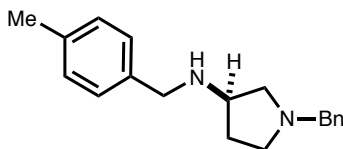
(R)-3-[(4-methylbenzyl)amino]-1-phenylpyrrolidine-2,5-dione (Compound II-30): Prepared according to the general procedure using *p*-tolylmethanamine (0.027 g, 0.22 mmol, 1.1 equiv)

and 1-phenyl-1H-pyrrole-2,5-dione (0.035 g, 0.2 mmol, 1.0 equiv) to afford 0.059 g (93% yield) of 30 as a white solid: ^1H NMR (500 MHz, Chloroform-*d*) δ 7.50 (dd, $J = 8.4, 7.0$ Hz, 2H), 7.43 (m, 1H), 7.29 (m, 4H), 7.20 (d, $J = 7.7$ Hz, 2H), 3.95 (m, 3H), 3.05 (dd, $J = 18.0, 8.4$ Hz, 1H), 2.73 (dd, $J = 18.0, 5.3$ Hz, 1H), 2.38 (s, 4H) ppm; ^{13}C NMR (126 MHz, Chloroform-*d*) δ 176.8, 174.1, 137.4, 135.3, 131.6, 129.4, 129.2, 128.7, 128.4, 126.3, 55.4, 51.6, 36.5, 21.1 ppm; HRMS (ESI): Mass calculated for $\text{C}_{18}\text{H}_{19}\text{N}_2\text{O}_2$ $[\text{M}+\text{H}]^+$: 295.1447; found: 295.1441; IR (thin film): 3299, 3047, 1698, 1594, 1513, 1495, 1453, 1395, 1370 cm^{-1} ; Enantiomeric ratio was measured by chiral phase HPLC (IA, 30% $^i\text{PrOH}$ /hexanes, 0.5 mL/min, 210 nm), t_{R} (major) = 28.33 min, t_{R} (minor) = 27.03 min; e.r. = 74:26.



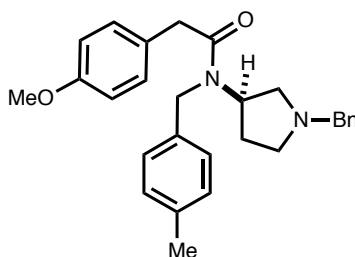
(R)-1-ethyl-3-[(4-methylbenzyl)amino]pyrrolidine-2,5-dione (Compound II-31): Prepared according to the general procedure using *p*-tolylmethanamine (0.027 g, 0.22 mmol, 1.1 equiv) and 1-ethyl-1H-pyrrole-2,5-dione (0.025 g, 0.20 mmol, 1.0 equiv) to afford 0.045 g (91% yield) of product 31 as a clear oil: ^1H NMR (500 MHz, Chloroform-*d*) δ 7.17 (m, 4H), 3.81 (m, 2H), 3.72 (dd, $J = 8.2, 4.9$ Hz, 1H), 3.55 (q, $J = 7.2$ Hz, 2H), 2.83 (dd, $J = 17.9, 8.2$ Hz, 1H), 2.49 (dd, $J = 17.9, 4.9$ Hz, 1H), 2.34 (s, 3H), 1.16 (t, $J = 7.2$ Hz, 3H) ppm; ^{13}C NMR (126 MHz, Chloroform-*d*) δ 177.8, 175.2, 137.3, 135.5, 129.3, 128.2, 55.4, 51.7, 36.5, 33.8, 21.1, 13.0 ppm; HRMS (ESI): Mass calculated for $\text{C}_{14}\text{H}_{19}\text{N}_2\text{O}_2$ $[\text{M}+\text{H}]^+$: 247.1447; found: 247.1441; IR (thin film): 3294, 2981, 2848, 1686, 1516, 1491, 1447, 1405 cm^{-1} ; Enantiomeric ratio was measured

by chiral phase HPLC (AD-H, 10% ⁱPrOH/hexanes, 1.0 mL/min, 210 nm), t_R (major) = 12.56 min, t_R (minor) = 11.21 min; e.r. = 80:20.



(R)-1-benzyl-N-(4-methylbenzyl)pyrrolidin-3-amine (Compound II-34): A flame-dried 25 mL round bottom flask equipped with a magnetic stirring bar and a nitrogen inlet was charged with THF (7.6 mL) and lithium aluminum hydride (0.215 g, 5.67 mmol, 5.0 equiv). To the resulting suspension was added (R)-1-benzyl-3-[(4-methylbenzyl)amino]pyrrolidine-2,5-dione **II-6** (0.350 g, 1.135 mmol) portion-wise as a solid. The reaction flask was equipped with a reflux condenser and heated to 60 °C for 14 h. The reaction mixture was then cooled to 23 °C and poured into ice cold 1.0 M NaOH (50 mL) and stirred for 10 min. The mixture was transferred to a separatory funnel and extracted with diethyl ether (3 x 100 mL). The organic layer was collected, dried over Na₂SO₄, filtered and concentrated on a rotary evaporator to give the product **II-34** as analytically pure pale yellow oil (0.305 g, 1.08 mmol, 95%): ¹H NMR (500 MHz, Chloroform-*d*) δ 7.31 (dt, *J* = 8.6, 4.1 Hz, 4H), 7.25 (m, 2H), 7.19 (m, 2H), 7.11 (m, 2H), 3.69 (d, *J* = 1.8 Hz, 2H), 3.60 (qd, *J* = 12.9, 1.8 Hz, 2H), 3.34 (ddtd, *J* = 8.8, 6.7, 4.8, 1.7 Hz, 1H), 2.75 (ddd, *J* = 8.8, 6.7, 1.7 Hz, 1H), 2.63 (tdd, *J* = 8.4, 6.0, 1.8 Hz, 1H), 2.53 (tdd, *J* = 9.4, 6.7, 1.7 Hz, 1H), 2.39 (ddd, *J* = 9.5, 5.0, 1.8 Hz, 1H), 2.33 (d, *J* = 1.7 Hz, 3H), 2.13 (m, 1H), 1.61 (dddt, *J* = 12.8, 10.9, 6.1, 3.0 Hz, 1H), 1.37 (s, 1H) ppm; ¹³C NMR (126 MHz, Chloroform-*d*) δ 139.1, 137.3, 136.4, 129.0, 128.8, 128.2, 128.1, 126.9, 60.8, 60.5, 56.7, 53.1, 52.1, 32.2, 21.1 ppm; HRMS (ESI): Mass calculated for C₁₉H₂₅N₂ [M+H]⁺: 281.2018; found: 281.2012; IR (thin

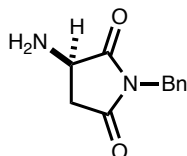
film): 3025, 2955, 2910, 2783, 1514, 1494, 1452 cm^{-1} ; Enantiomeric ratio was measured by chiral phase HPLC (OD-H, 5% *i*PrOH/hexanes, 1.0 mL/min, 210 nm), t_R (major) = 15.91 min, t_R (minor) = 11.56 min; e.r. = 99:1.



(*R*)-*N*-(1-benzylpyrrolidin-3-yl)-2-(4-methoxyphenyl)-*N*-(4-methylbenzyl)acetamide

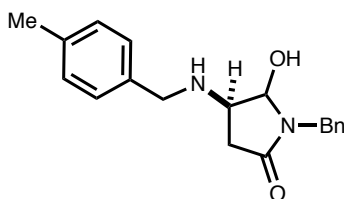
(Compound II-35): To a 25 ml flask charged with dichloromethane (10.9 ml) was added sequentially (*R*)-1-benzyl-*N*-(4-methylbenzyl)pyrrolidin-3-amine **II-34** (0.305 g, 1.088 mmol), Hünig's Base (2.280 mL, 13.05 mmol, 12 equiv), and 2-(4-methoxyphenyl)acetyl chloride (0.602 g, 3.26 mmol, 3.0 equiv) at 23 °C. The reaction was allowed to stir at 23 °C for 48 h, at which point it was poured into a separatory funnel containing saturated NaHCO_3 (10 mL) and extracted with dichloromethane (3 x 15 mL). The combined organic layers were washed with water (15 mL), saturated brine (15 mL), then dried over Na_2SO_4 , filtered, and concentrated on a rotary evaporator. The crude residue was purified via column chromatography (9:1 hexanes:acetone) to afford product **II-35** as a colorless oil (0.201 g, 0.469 mmol, 43%), which was characterized as a ~2:1 mixture of amide rotamers at 23 °C by NMR spectroscopy: ^1H NMR (500 MHz, Chloroform-*d*) δ 7.20 (m, 11H), 7.06 (q, $J = 8.5, 7.4$ Hz, 6H), 6.83 (dd, $J = 20.1, 8.1$ Hz, 3H), 5.17 (m, 1H), 4.65 (dt, $J = 32.4, 18.0$ Hz, 4H), 3.79 (d, $J = 7.3$ Hz, 6H), 3.54 (t, $J = 14.2$ Hz, 2H), 3.47 (m, 4H), 2.79 (t, $J = 7.5$ Hz, 1H), 2.59 (ddd, $J = 26.5, 10.4, 4.0$ Hz, 1H), 2.47 (t, $J = 9.1$ Hz, 1H), 2.30 (m, 8H), 1.90 (t, $J = 8.8$ Hz, 1H), 1.70 (dt, $J = 18.2, 6.2$ Hz, 2H) ppm; ^{13}C

NMR (126 MHz, Chloroform-*d*) δ 172.4, 171.4, 158.4, 138.9, 138.5, 136.7, 136.6, 136.0, 135.7, 129.7, 129.7, 129.5, 129.0, 128.6, 128.4, 128.3, 128.2, 127.3, 127.1, 127.0, 126.8, 126.8, 125.4, 114.1, 114.0, 60.0, 57.5, 57.4, 57.0, 56.0, 55.2, 53.6, 53.3, 53.3, 47.5, 45.5, 40.9, 40.6, 30.0, 29.9, 24.7, 21.0 ppm; HRMS (ESI): Mass calculated for C₂₈H₃₃N₂O₂ [M+H]⁺: 429.2542; found: 429.2537; IR (thin film): 3334, 3055, 2898, 2875, 1716, 1652, 1558, 1512, 1456, 1419, 1379 cm⁻¹.



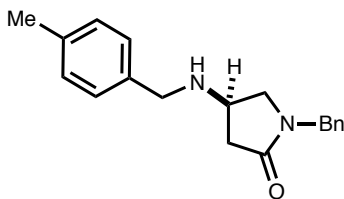
(R)-3-amino-1-benzylpyrrolidine-2,5-dione (Compound II-36): To a flame dried 10 mL round bottom flask under an inert atmosphere was added 10% Pd/C (21.28 mg, 0.020 mmol), (*R*)-1-benzyl-3-[(4-methylbenzyl)amino]pyrrolidine-2,5-dione **II-6** (61.7 mg, 0.2 mmol), followed by MeOH (4.0 mL). The flask was then equipped with a balloon of H₂ (1 atm) and stirred at 23 °C for 5 h, at which point the reaction mixture was filtered through a 0.5 cm plug of Celite™. The filter cake was rinsed with 20 mL of ethyl acetate, and the resulting clear homogeneous filtrate was concentrated in vacuo. The resulting crude residue was purified on SiO₂ in the following manner: a chloroform solution (0.5 mL) of the crude residue was loaded onto a dry pad of silica gel (2 x 2 cm), which was first flushed with hexanes (15 mL) then with MeCN (~15 mL) until all of **II-36** had been eluted (TLC monitoring). The MeCN eluent was concentrated in vacuo to give **II-36** as a colorless solid (39 mg, 0.192 mmol, 96% yield): ¹H NMR (500 MHz, Chloroform-*d*) δ 7.34 (m, 5H), 4.66 (s, 2H), 3.90 (dd, *J* = 8.7, 5.3 Hz, 1H), 3.05 (dd, *J* = 18.1, 8.7 Hz, 1H), 2.46 (dd, *J* = 18.1, 5.4 Hz, 1H) 1.68 (s, 2H) ppm; ¹³C NMR (126 MHz, Chloroform-*d*) δ 179.0, 174.5,

135.5, 128.9, 128.7, 128.1, 50.5, 42.5, 37.9 ppm; HRMS (ESI): Mass calculated for $C_{11}H_{13}N_2O_2$ $[M+H]^+$: 205.0977; found: 205.0972; IR (thin film): 3302, 3036, 2932, 2810, 1697, 1608, 1581, 1512, 1501, 1455, 1423, 1362 cm^{-1} ; Enantiomeric ratio was measured by chiral phase HPLC (OD-H, 2% i PrOH/hexanes, 1.0 mL/min, 210 nm), t_R (major) = 52.71 min, t_R (minor) = not observed; e.r. = >99:1.



(R)-1-benzyl-4-[(4-methylbenzyl)amino]-5-hydroxypyrrolidin-2-one (SI-1): To a flame dried 25 mL flask charged with 2:1 CH_2Cl_2 :MeOH (2 mL) was added (R)-1-benzyl-3-[(4-methylbenzyl)amino]pyrrolidine-2,5-dione **6** (61.7 mg, 0.2 mmol), and the resulting solution was cooled to 0 °C using an external ice bath. Sodium borohydride (7.6 mg, 0.2 mmol, 1.0 equiv) was added in a single bolus, after which the reaction was warmed to 4 °C and stirred at this temperature for 14 h. The crude reaction was quenched with 5 mL saturated aqueous $NaHCO_3$, washed into a separatory funnel with 5 mL of EtOAc, and extracted with EtOAc (3 x 5 mL). The combined organic layers were washed with saturated aqueous brine (5 mL), dried over Na_2SO_4 , filtered, and concentrated on a rotary evaporator. The crude oily product was triturated with ethyl acetate, resulting in precipitation of a white solid. The precipitate was filtered, washed with cold ethyl acetate (0.5 mL) and dried under high-vacuum (\sim 0.1 Torr) to give a white solid (0.026 g, 0.084 mmol, 42%) which was characterized as the *trans*-isomer of **SI-1**: 1H NMR (500 MHz, Chloroform-*d*) δ 7.32 (m, 6H), 7.13 (m, 4H), 4.83 (m, 2H), 4.25 (d, J = 14.9 Hz, 1H), 3.72 (m, 2H), 3.23 (m, 1H), 2.85 (dd, J = 17.1, 7.6 Hz, 1H), 2.33 (s, 3H), 2.22 (dd, J = 17.2, 4.1 Hz, 1H),

2.07 (s, 1H) ppm; ^{13}C NMR (126 MHz, Chloroform-*d*), δ 172.6, 137.0, 136.3, 136.2, 129.2, 128.8, 128.3, 128.1, 127.7, 87.7, 59.7, 51.5, 43.6, 37.1, 21.1 ppm.



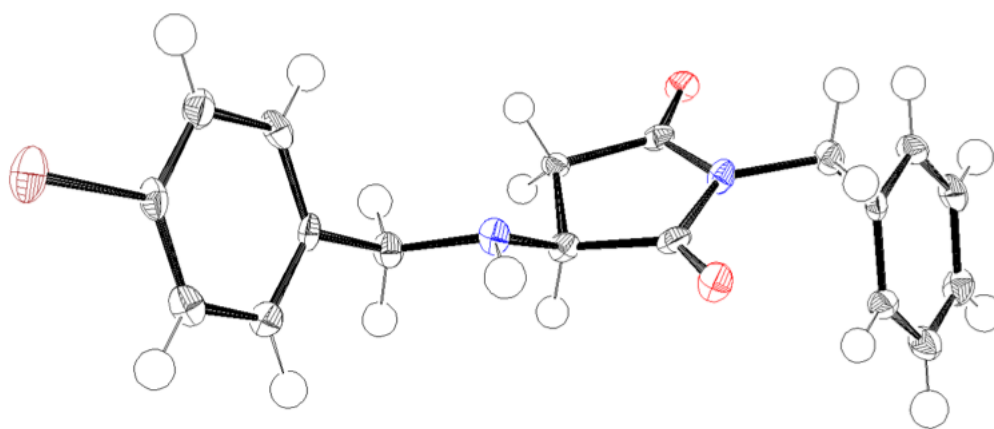
(*R*)-1-benzyl-4-[(4-methylbenzyl)amino]pyrrolidin-2-one (Compound II-37): To a 25 mL round bottom flask was added **SI-1** (49 mg, 0.158 mmol, 1.0 equiv), followed by dichloromethane (16 mL), and triethylsilane (0.252 mL, 1.58 mmol, 10.0 equiv). The resulting solution was cooled to $-78\text{ }^{\circ}\text{C}$ in an acetone/dry ice bath, whereupon $\text{BF}_3\cdot\text{OEt}_2$ (0.050 mL, 0.395 mmol, 2.5 equiv) was added dropwise via syringe. The cooling bath was removed after 15 min, and the reaction was stirred at $23\text{ }^{\circ}\text{C}$ for 16 h. The crude reaction was quenched by addition of 10 mL of saturated aqueous NaHCO_3 , and then transferred to a separatory funnel. The mixture was extracted with dichloromethane (3 x 15 mL), and the combined organic portions were washed with brine (15 mL), collected and dried over Na_2SO_4 , filtered, and concentrated to a crude oily residue. The crude product was purified via flash column chromatography (hexanes:acetone, gradient 10:1 \rightarrow 1:1) to yield **II-37** as a colorless oil (39 mg, 0.132 mmol, 84%): ^1H NMR (500 MHz, Chloroform-*d*) δ 7.31 (m, 4H), 7.24 (m, 2H), 7.12 (m, 4H), 4.46 (d, $J = 2.9$ Hz, 2H), 3.69 (m, 2H), 3.48 (tt, $J = 7.5, 5.0$ Hz, 1H), 3.42 (dd, $J = 9.8, 6.9$ Hz, 1H), 3.07 (dd, $J = 9.8, 4.4$ Hz, 1H), 2.69 (dd, $J = 16.9, 7.7$ Hz, 1H), 2.34 (m, 4H) ppm; ^{13}C NMR (126 MHz, Chloroform-*d*), δ 173.0, 136.9, 136.4, 136.3, 129.2, 128.7, 128.1, 128.0, 127.6, 53.0, 51.4, 50.3, 46.4, 38.9, 21.1 ppm; HRMS (ESI): Mass calculated for $\text{C}_{19}\text{H}_{23}\text{N}_2\text{O}$ $[\text{M}+\text{H}]^+$: 295.1810; found: 295.1805; IR (thin film): 3283, 3017, 2919, 2856, 1685, 1614, 1585, 1513, 1496, 1437, 1399, 1354 cm^{-1} ;

Enantiomeric ratio was measured by chiral phase HPLC (AD-H, 10% ⁱPrOH/hexanes, 1.0 mL/min, 210 nm), t_R (major) = 18.35 min, t_R (minor) = 20.53 min; e.r. = 97:3.

2.8.4 X-Ray Crystallography Data

Determination of the Absolute Configuration of Compound II-10: The absolute stereochemistry of **II-10** was determined by X-ray diffraction. **II-10** was recrystallized from ethyl acetate/hexane. X-ray diffraction was performed at 100.01 K and raw frame data were processed using SAINT. Molecular structure was solved using direct methods and refined on F^2 by full-matrix least-squares techniques. The GOF = 1.111 for 212 variables refined to R^1 = 0.0485 for 2336 reflections with $I > 2\sigma(I)$. A multi-scan absorption correction was performed and the Flack parameter was $-0.02(4)$. Further information can be found in the CIF file. This crystal was deposited in the Cambridge Crystallographic Data Centre and assigned as CCDC 1531303.

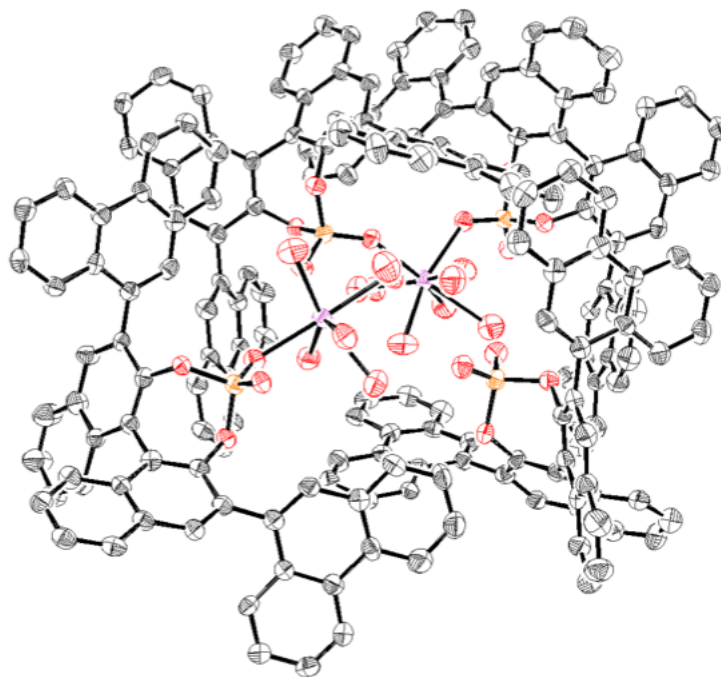
X-ray crystal structure of **II-10**:



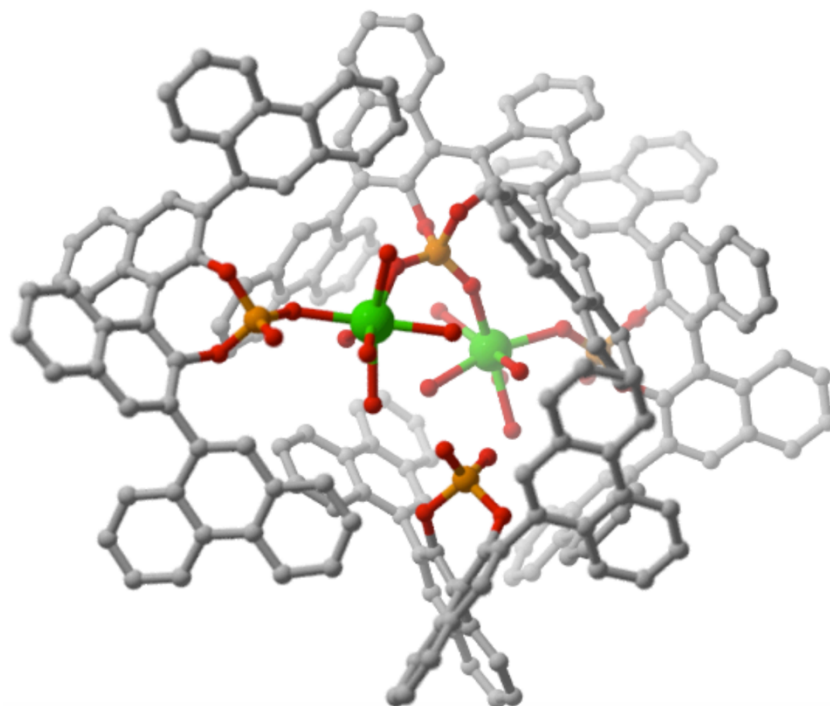
ORTEP: C = gray, O = red, N = Blue, Br = maroon

Determination of the Structure of Ca[B]₂: The absolute stereochemistry and structure of Ca[B]₂ was determined by X-ray diffraction. Ca[B]₂ was recrystallized from toluene. X-ray diffraction was performed at 99.99 K and raw frame data were processed using SAINT. Molecular structure was solved using the algorithm implemented in SHELXT and refined on F^2 by full-matrix least-squares techniques. The GOF = 0.928 for 2078 variables refined to $R^1 = 0.0630$ for 20787 reflections with $I > 2\sigma(I)$. A multi-scan absorption correction was performed and the Flack parameter was 0.026(10). Further information can be found in the CIF file. This crystal was deposited in the Cambridge Crystallographic Data Centre and assigned as CCDC 1531265.

X-ray crystal structure of Ca[B]₂:



ORTEP: C = gray, O = red, P = orange, Ca = pink



CYL View: C = gray, O = red, P = orange, Ca = green

Chapter 3

La[N(SiMe₃)₂]₃-Catalyzed Deoxygenative Reduction of Amides
with Pinacolborane. Scope and Mechanism.

Portions of this chapter appear in the following publications:

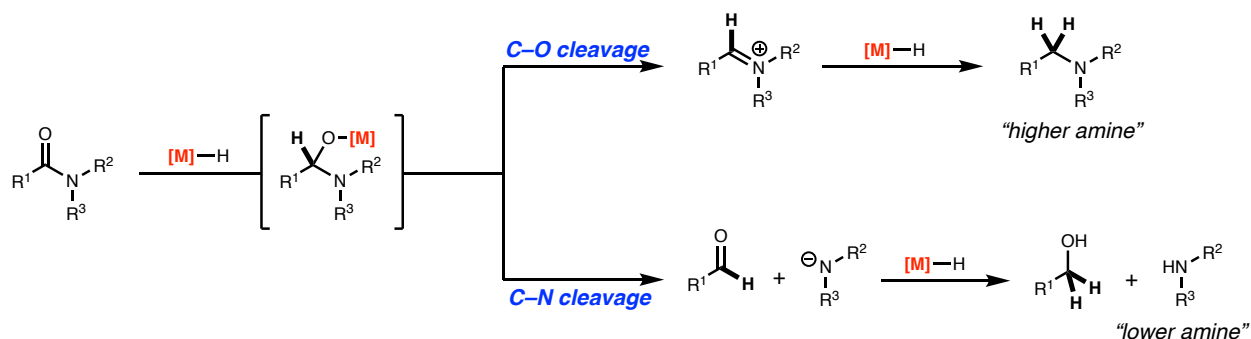
Christopher J. Barger, Rachel D. Dicken, Victoria L. Weidner, Alessandro Motta, Tracy L. Lohr,
and Tobin J. Marks, La[N(SiMe₃)₂]₃-Catalyzed Deoxygenative Reduction of Amides with
Pinacolborane. Scope and Mechanism. *J. Am. Chem. Soc.* **2020**, *142* (17), 8019-8028;
Rachel D. Dicken, Alessandro Motta, and Tobin J. Marks, Homoleptic Lanthanide Amide
Catalysts for Organic Synthesis: Experiment and Theory. *ACS Catal.* **2021**, *11* (5), 2715-2734.

3. Chapter 3

3.1 Introduction

Carbonyl reduction is among the most important and valuable transformations in organic synthesis.¹⁶⁸⁻¹⁷⁰ Among the various carbonyl-based functional groups, the reduction of amides to the corresponding amines has proven to be the most challenging due to the significant resonance stabilization provided by the delocalization of the nitrogen lone pair. This increased stabilization yields a significant reduction in the electrophilicity of the amide C=O bond compared to that of ketones, aldehydes, and esters.¹⁷¹⁻¹⁷³ Therefore, amides are far less susceptible to nucleophilic attack and do not readily undergo reduction in the presence of mild hydride sources, instead requiring more highly reactive reducing agents.

In addition to the relatively low reactivity towards nucleophilic addition, a second fundamental challenge regarding amide reduction lies in the selectivity of C–N vs C–O bond cleavage. In general, amide reduction can proceed via two main pathways depending upon the stability of the tetrahedral intermediate formed during the course of the reaction (Scheme 3.1). While C–O bond cleavage to yield the more valuable “higher amine” is often the more desirable reduction pathway, C–N bond cleavage to afford the “lower amine” can also be synthetically advantageous. Though traditional hydride reducing agents such as lithium aluminum hydride (LAH) and diisobutylaluminum hydride (DIBAL) have proven to be reliable reagents for various carbonyl reductions, when employed in amide reductions, undesirable side reactions and a lack of selectivity between C–O and C–N bond cleavage are not uncommon.¹⁷⁴⁻¹⁷⁷ Due to these limitations, the development of more selective and convenient methods for amide reduction has gained increasing attention.

Scheme 3.1 General reaction pathways in the reduction of amides.

This chapter outlines the development of the $La[N(SiMe_3)_2]_3$ -catalyzed deoxygenative reduction of tertiary and secondary amides with pinacolborane (HBpin). The reaction, which yields amines and $O(Bpin)_2$, operates under mild conditions and tolerates nitro, halide, and amino functional groups. The amide reduction is also completely selective for C=O bond reduction, with the exclusion of both competing inter- and intramolecular alkene/alkyne hydroboration. Kinetic studies indicate that amide reduction obeys an unusual mixed-order rate law which is proposed to originate from saturation of the catalyst complex with HBpin. Kinetic and thermodynamic studies, isotopic labeling, and DFT calculations using energetic span analysis suggest the role of a $[(Me_3Si)_2N]_2La-OCHR(NR'_2)[HBpin]$ active catalyst, and hydride transfer is proposed to be ligand-centered. These results add to the growing list of transformations that commercially available La^{NTMS} is competent to catalyze, further underscoring the value and versatility of lanthanide complexes in homogeneous catalysis.

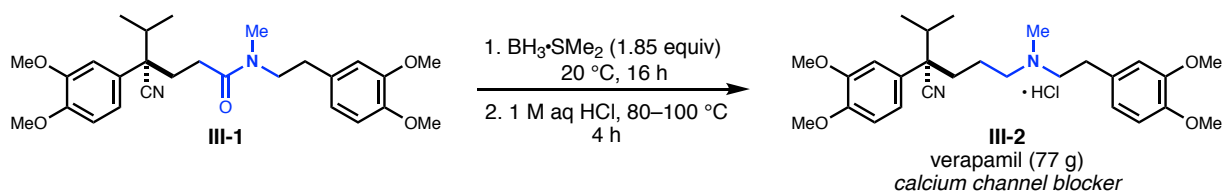
3.2 Background and Motivation

The deoxygenative reduction of amides to amines is an important transformation in academic, pharmaceutical, and industrial synthetic chemistry (Scheme 3.2).^{168, 178-181} The natural

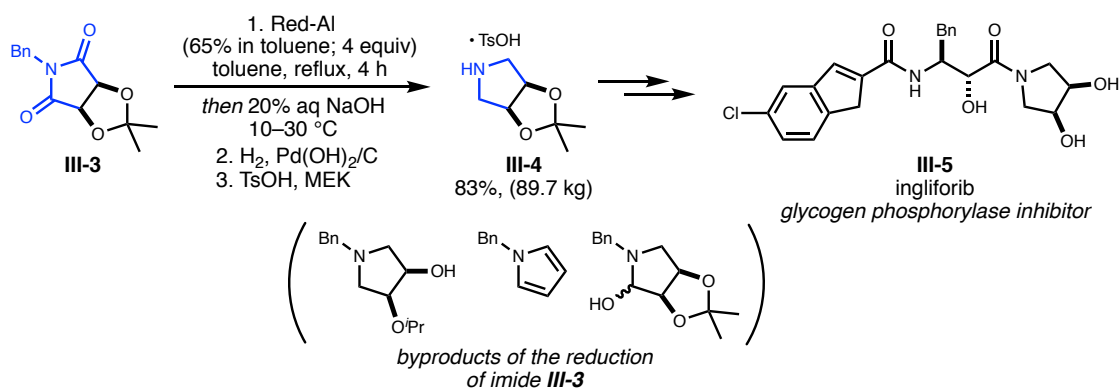
prevalence and synthetic accessibility of amides makes them valuable precursors to amines, but the inertness of the resonance-stabilized amide C=O bond generally necessitates the use of harsh reductants such as LiAlH_4 , BH_3 , and pressurized H_2 .^{170, 182-184} These reagents present significant safety concerns and often suffer from poor functional group tolerance, particularly with nitro gr-

Scheme 3.2 Examples of large-scale deoxygenative reductions of amides in the pharmaceutical industry.

A) Chemoselective reduction of amide III-1 en route to verapamil (III-2)



B) Red-Al reduction of imide III-3 to pyrrolidine III-4 en route to ingliforib (III-5)

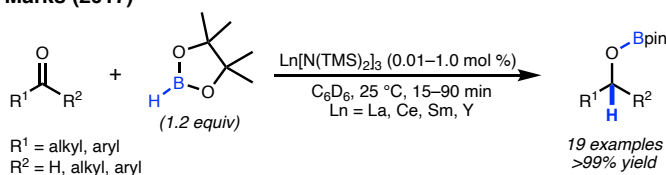


roups and alkenes/alkynes. As such, novel methods enabling the safe, selective, and efficient reduction of amides would be valuable additions to the synthetic chemist's toolkit.¹⁸⁵ Significant progress has been made in this area, with much of the focus directed toward catalytic hydrosilylation.¹⁸⁶⁻¹⁸⁸ Interestingly, amide reduction via catalytic hydroboration (with mild, easily handled boranes such as HBpin) is largely unexplored, especially with lanthanide catalysts,^{64, 189-191} despite extensive precedent for the use of boranes as reductants for ketones and aldehydes,¹⁹¹⁻²⁰⁰ as well as the intense recent interest in the more challenging reduction of esters via

hydroboration.^{60, 191, 201-204} Recently, we reported that the homoleptic lanthanide amide $\text{La}[\text{N}(\text{SiMe}_3)_2]_3$ (La^{NTMS}) displays extremely high catalytic activity for a variety of carbonyl reductions using HBpin, with 25–60 °C turnover frequencies as high as 40,000 h^{-1} for ketones and aldehydes and 400 h^{-1} for esters (Scheme 3.3).^{60, 62} With these results in mind, we sought to explore the La^{NTMS} -catalyzed hydroboration of more challenging amides.

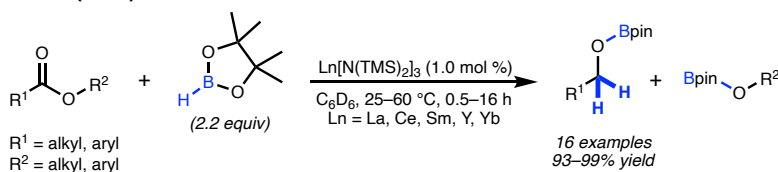
Scheme 3.3 (A) Ln^{NTMS} -Catalyzed Hydroboration of Ketones and Aldehydes with HBpin; (B) Ln^{NTMS} -Catalyzed Hydroboration of Esters with HBpin.

A) Marks (2017)



- low catalyst loadings
- earth abundant La
- wide substrate scope
- fast rxn times

B) Marks (2019)



- rapid reduction
- selective over alkenes and alkynes
- mechanistic investigation

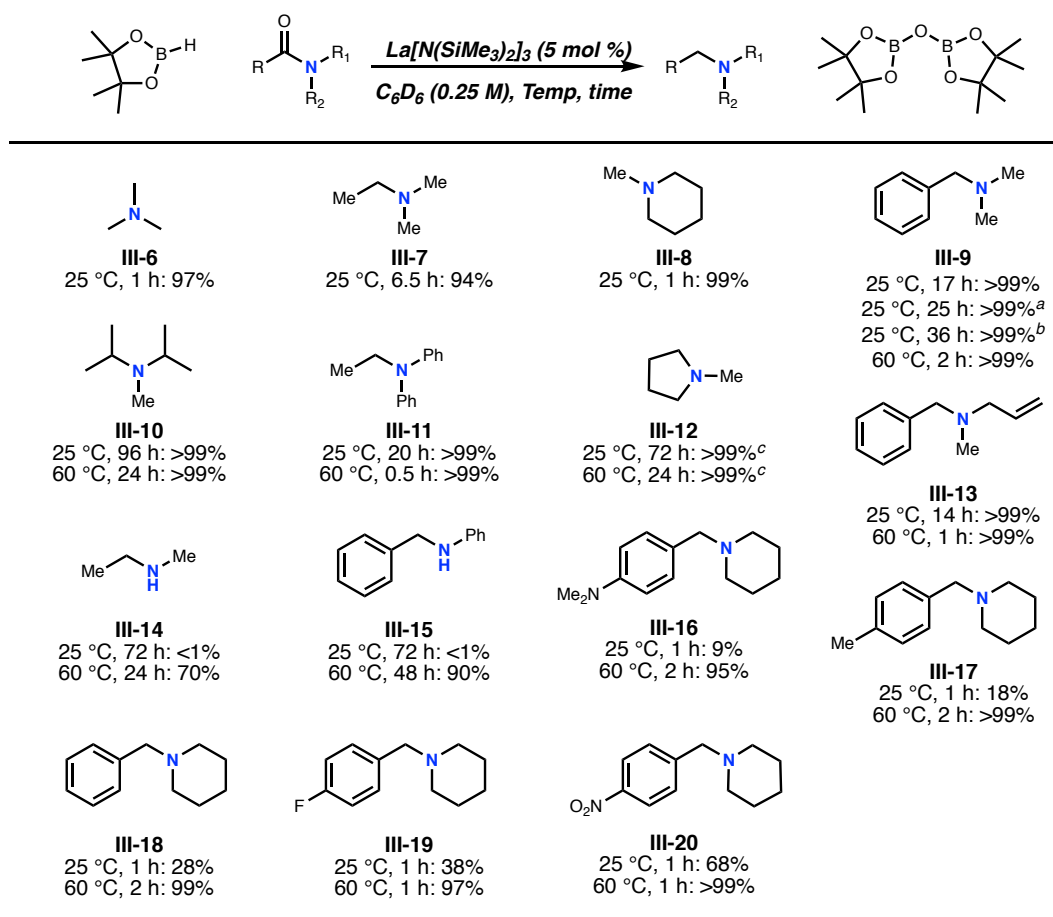
Tris[*N,N*-bis(trimethylsilyl)amido]lanthanide complexes ($\text{Ln}[\text{N}(\text{SiMe}_3)_2]_3$, abbreviated here as Ln^{NTMS}) are encountered frequently in the lanthanide catalysis literature, both as precursors to more complex lanthanide organometallics²⁰⁵⁻²¹⁵ and as homogeneous catalysts, particularly for hydrofunctionalization/reduction of alkenes and alkynes.^{22, 51-53, 56-58, 61, 216-220} These complexes are commercially available for many lanthanides, or can be readily synthesized and purified, rendering them highly accessible and of great interest to the synthetic methods community.^{38, 39, 221} A report from the Marks laboratory showed that it is possible to carry out the catalytic synthesis of amides with Ln^{NTMS} ,²²² but the La^{NTMS} -catalyzed reduction of amides had

not yet been investigated. Given this, and the proven ability of La^{NTMS} to catalyze carbonyl hydroboration, La^{NTMS} -catalyzed amide hydroboration was an intriguing target.

Here we report that La^{NTMS} effectively mediates the deoxygenative reduction of a variety of alkyl and aryl amides to the corresponding amines. This system, which utilizes a commercially available catalyst, mild reaction conditions, and easily handled HBpin, constitutes a significant advance over traditional amide reduction methods, and is the first report of a borane-based amide reduction catalyzed by a lanthanide complex. We discuss here the scope of this transformation, as well as a proposed mechanism informed by a combined experimental-theoretical investigation.

3.3 Hydroboration Scope Development of the Deoxygenative Reduction of Amides

Amide reduction is found to occur via deoxygenation to yield the corresponding amine and bis(pinacolboryl)oxide (pinB-O-Bpin, ^1H NMR: δ 1.00 ppm, ^{11}B NMR: δ 21.7 ppm in C_6D_6) as a co-product (Table 3.1), analogous to that reported for other borane- and silane-based reductions.^{64, 188, 223} Near quantitative conversion of amide to amine is observed for each of the substrates examined (Table 3.1) at a catalyst loading of 5 mol%, and acidic workup of preparative reactions (0.5 g scale) affords the amine hydrochloride product in good yields without the need for column chromatography (see Experimental Section 3.73). Although only 2 equiv of HBpin (relative to amide) is formally required by stoichiometry for complete amide reduction, 5 equiv was typically found necessary to achieve full conversion over the time and temperature range selected. This is likely attributable to reversible formation of transient amide-borane and amine-borane adducts which, once formed, would effectively reduce the amount of active HBpin available in solution. Considering the DFT-derived geometries in the proposed cat-

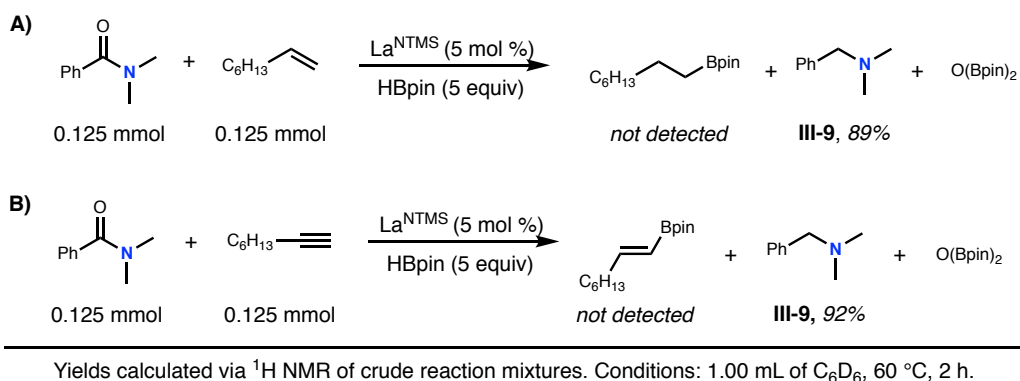
Table 3.1 Scope of the La^{NTMS}-Catalyzed Amide Reduction with Pinacolborane.

Reaction performed on a 0.25 mmol scale. % yield determined via ¹H NMR integrations vs hexamethylbenzene as an internal standard. ^a Reaction performed using Y[N(SiMe₃)₂]₃. ^b Reaction performed using Sm[N(SiMe₃)₂]₃. ^c Reaction performed using 10 equiv HBpin.

alytic cycle, bulky HBpin-amide or HBpin-amine adducts would be expected to approach the catalytic complex and participate in amide reduction with greater difficulty. Such effects were previously observed in similar reductions, and other catalytic systems require HBpin to be held in even greater excess.¹⁹⁰ Tertiary amides are reduced cleanly at 25 °C, although sterically encumbered amides and imides (Table 3.1, **III-12**) require elevated temperature (60 °C) for rapid reduction. Formamides (R = H) generally react more rapidly than amides (R ≠ H; e.g., Table 3.1, **III-6** vs **III-7**). Similarly, steric encumbrance at the R² and R³ positions depresses the turnover

rate (e.g., Table 3.1, **III-6** vs **III-10**). Even with HBpin in excess, the reduction of amides is completely chemoselective over the hydroboration of alkenes and alkynes in intermolecular competition experiments (Scheme 3.4).

Scheme 3.4 Selective Reduction of *N,N*-Dimethylbenzamide in the Presence of 1-Octene (A) and 1-Octyne (B).



Likewise, no intramolecular alkene hydroboration products are observed during the reduction of *N*-allyl-*N*-methylbenzamide (Table 3.1, **III-13**). In addition to La^{NTMS}, the catalytic activity of commercially available Sm^{NTMS} and Y^{NTMS} was also investigated for the reduction of *N,N*-dimethylbenzamide (Table 3.1, **III-9**). While the reaction proceeds similarly in all three cases, the observed rate of reduction diminishes (as expected) as the ionic radius of the central metal decreases (i.e., La > Sm > Y).

Secondary amides proved somewhat more challenging, requiring both elevated temperatures and longer reaction times to reach satisfactory yields (Table 3.1, **III-14** and **III-11**). This is likely attributable to the rapid conversion of La^{NTMS} to a lanthanide tris-amidate species *in situ*, possibly hindering formation of the active catalyst for amide reduction (Figure 3.1). Such a reactivity pattern has been reported previously²²⁴ and is supported by the presence of free HN(SiMe₃)₂ in the ¹H NMR spectrum of the secondary amide reaction mixture. In an attempt to

fully characterize these tris-amidate complexes, the stoichiometric reaction of La^{NTMS} and benzanilide (1:3) was conducted. Upon mixing, the ^1H NMR spectrum shows the complete conversion of the La^{NTMS} signal (δ 0.29 ppm, C_6D_6) to a new signal corresponding to $\text{HN}(\text{SiMe}_3)_2$ (δ 0.10 ppm, C_6D_6). Additionally, upon complexation, the aromatic proton signals belonging to benzanilide become quite broad when compared to the ^1H NMR spectrum of the secondary ami-

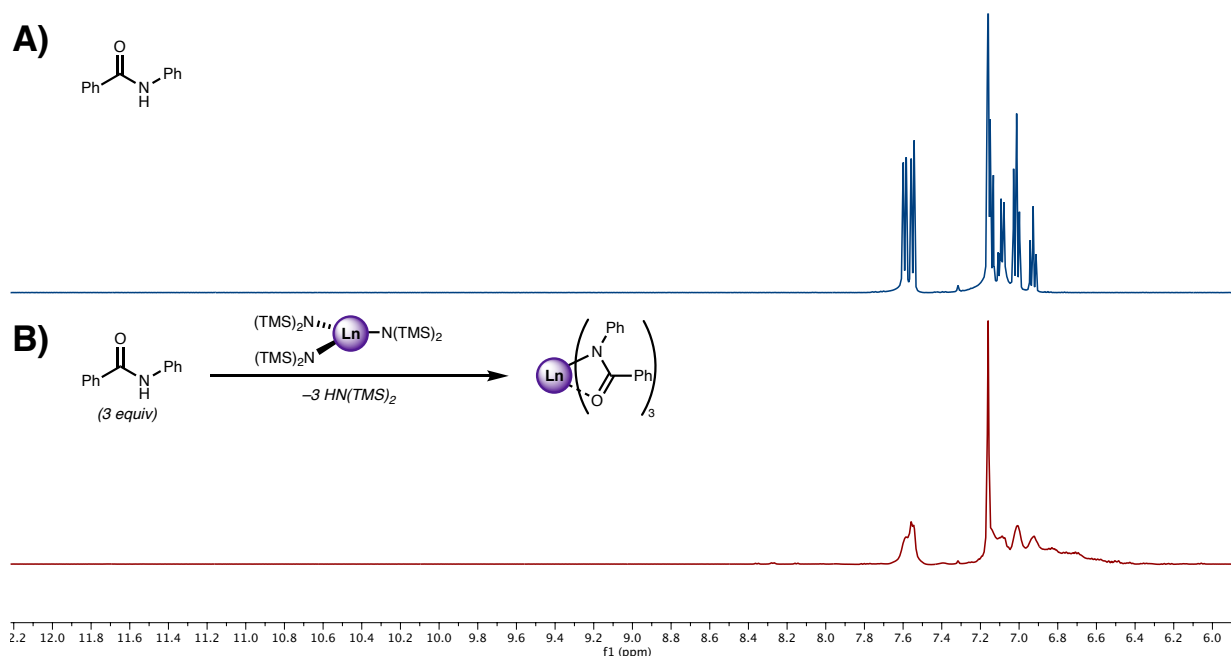


Figure 3.1 Observed Reaction of La^{NTMS} with Secondary Amides. (A) ^1H NMR (500 MHz) spectrum of benzanilide in C_6D_6 ; (B) ^1H NMR (500 MHz) spectrum of *in situ* formed lanthanum tris-amidate catalyst obtained from benzanilide and La^{NTMS} (3:1 molar ratio) in C_6D_6 .

de alone (Figure 3.1). Variable-temperature (VT) NMR studies were next performed in toluene- d_8 due to the superior temperature profile enabled by toluene vs benzene. However, the aromatic proton signals of the La -benzanilide tris-amidate species do not sharpen or coalesce with increasing temperature (up to 100 $^\circ\text{C}$ in toluene- d_8). Furthermore, integrations of these spectra provide minimal information. However, *in situ* studies conducted by adding amide and HBpin to

the aforementioned 1:3 mixture of La^{NTMS} and benzanilide (i.e., forming the lanthanide tris-amidate species *in situ*) suggest this species is a less active but nevertheless competent amide reduction catalyst. Our attempts to isolate these tris-amidate complexes were unsuccessful.

Reduction does not occur with the two primary amides tested (acetamide and benzamide), and instead an intractable, off-white precipitate is formed. While ligand insertion into carbon-heteroatom double bonds has been observed previously with similar rare earth silylamide complexes,²²⁵ DFT studies indicate that, in this system, a ligand insertion pathway is energetically unfavorable (see Experimental Section 3.7.9). Furthermore, spectroscopic studies reveal that upon addition of benzamide to La^{NTMS} , $\text{HN}(\text{SiMe}_3)_2$ is produced instantaneously with precipitation of a catalytically inactive La-amide species. Characterization of this marginally soluble species by ^1H and ^{29}Si NMR spectroscopy suggests that it is a La-hemiaminalate complex, e.g., $[(\text{Me}_3\text{Si})_2\text{N}]_2\text{La}\{\eta^2\text{-OC}(\text{NH})\text{Ph}\}$ (monomeric or oligomeric; see Experimental Section 3.7.5).²²⁶ Formation of this marginally soluble complex likely precludes the HBpin coordination necessary for efficient reduction to take place.

3.4 Kinetics and Mechanism

To probe the mechanism of this reaction, the rate law for catalytic *N,N*-dimethylbenzamide reduction was determined by a combination of initial rates analysis at various catalyst concentrations (for the order in La^{NTMS} concentration) and by monitoring substrate consumption under pseudo-first-order conditions (see Experimental Section 3.7.5 for details). Amide reduction is found to proceed with a first-order dependence on the La^{NTMS} concentration and zero-order dependence on the amide concentration (Figure 3.2). The order in HBpin was not amenable to determination under pseudo-zero-order conditions (10 equiv of

amide), as evidenced by a non-linear correlation for zeroth-, first-, and second-order plots, indicating that HBpin consumption is likely mixed-order for amide reduction (Figure 3.3). Initial rates analysis reveals that at low HBpin concentrations ($[\text{HBpin}] < 1.67 \text{ M}$, 5–7 equiv vs amide), the rate has a first-order dependence on HBpin concentration;

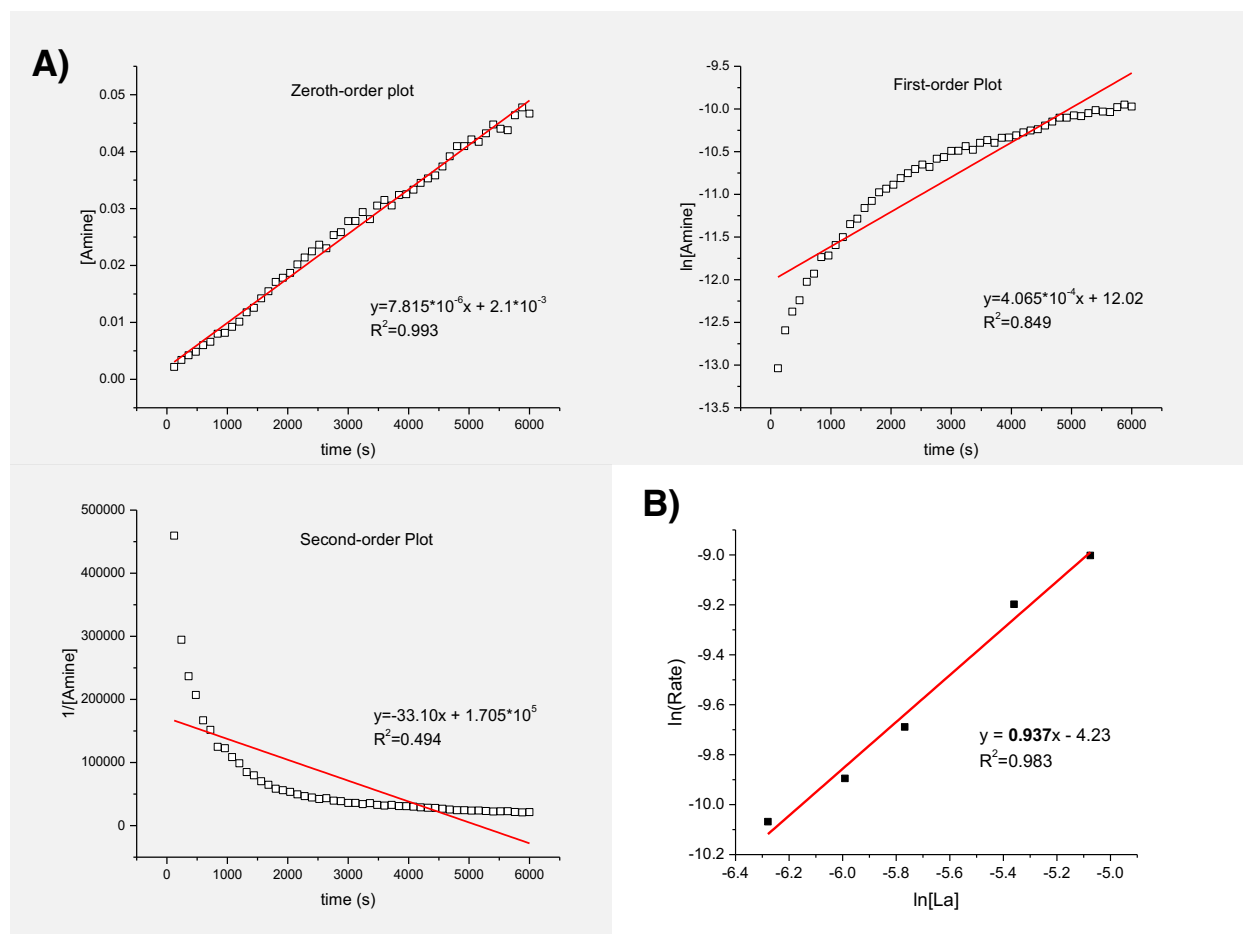


Figure 3.2 (A) Pseudo-first-order plots for reaction order in *N,N*-dimethylbenzamide (HBpin in 10-fold excess).^a The zeroth-order plot ($[\text{Amine}]$ vs. time) is linear, while the other two plots are not. (B) Ln vs. ln plot for the determination of the reaction order of La^{NTMS} for reduction of *N,N*-dimethylbenzamide (see Section 3.7.5 for details). ^aReaction conditions: La^{NTMS} (6.25 μmol), *N,N*-dimethylbenzamide (0.125 mmol), HBpin (1.25 mmol), C_6Me_6 (0.0330 mmol), C_6D_6 ($V_{\text{total}} = 1.00 \text{ mL}$).

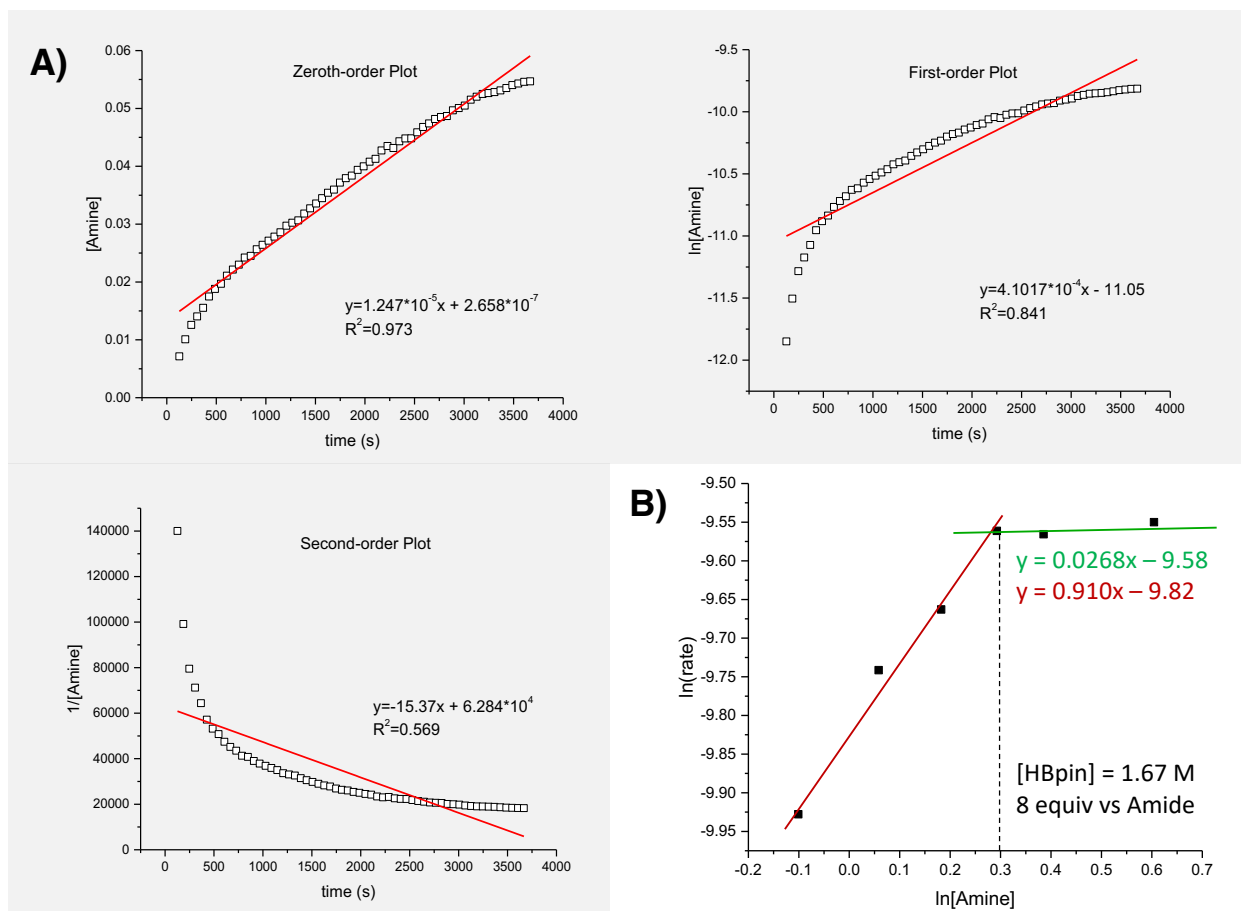


Figure 3.3 (A) Pseudo-first-order plots for reaction order in HBpin for amide reduction (10-fold excess of amide).^a None of the plots are linear, indicating HBpin consumption is likely mixed-order for amide reduction. (B) Ln vs. Ln plot for the determination of reaction order of HBpin in amide reduction. A mixed-order system is observed, wherein at $[\text{HBpin}] < 1.67 \text{ M}$, the order in HBpin = 1 (slope = $0.910 \approx 1$, vide infra for derivation and explanation). At $[\text{HBpin}] \geq 1.67 \text{ M}$, the order in HBpin = 0 (slope = $0.0268 \approx 0$). ^aReaction conditions: La^{NTMS} ($6.25 \mu\text{mol}$), *N,N*-dimethylbenzamide (1.25 mmol), HBpin (0.125 mmol), C_6Me_6 (0.0330 mmol), C_6D_6 ($V_{\text{total}} = 1.00 \text{ mL}$).

however, a transition occurs when $[\text{HBpin}] \geq 1.67 \text{ M}$ (≥ 8 equiv vs amide), and the order in HBpin becomes zero. This mixed-order system (eq 3.1) is reminiscent of Michaelis-Menten kinetics, wherein the turnover-limiting step in the catalytic cycle depends on an equilibrium

involving a substrate-catalyst complex.²²⁷ While this regime is not frequently encountered outside of enzyme catalysis,²²⁸ there are a few notable examples where saturation kinetics are ob-

$$\text{Rate} = k[\text{La}^{\text{NTMS}}]^1[\text{Amide}]^1[\text{HBpin}]^{1/0} \quad (3.1)$$

served in hydroelementation reactions.^{204, 229-231} The presence of an equilibrium between a La complex and HBpin in or immediately preceding the turnover-limiting step could explain the unusual rate behavior observed above. However, a non-equilibrium process, such as the availability of two different turnover-determining transition states, the relative energies of which depend on [HBpin], could also explain this rate law. As such, activation parameters for the reduction of *N,N*-dimethylbenzamide were determined at both low [HBpin] (5 equiv of HBpin vs amide) and high [HBpin] (10 equiv of HBpin vs amide) conditions over a temperature range of 30–70 °C (Figure 3.4). Both low and high [HBpin] conditions yield very similar activation parameters consisting of relatively small and positive enthalpies ($\Delta H^\ddagger = 10.3$ and 11.3 kcal/mol, respectively) and extremely large and negative entropies ($\Delta S^\ddagger = -49.7$ and -46.4 e.u., respectiv-

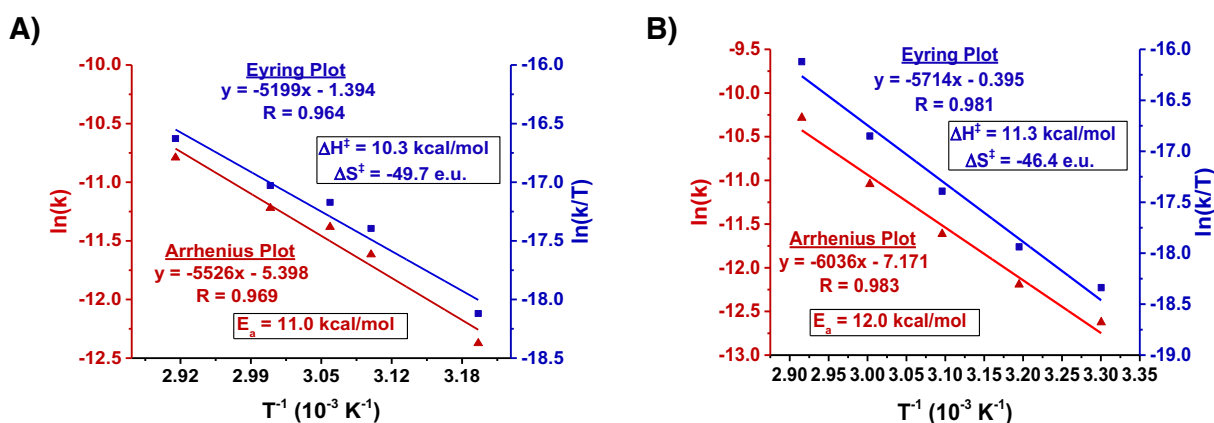


Figure 3.4 Eyring (blue) and Arrhenius (red) plots for the reduction of *N,N*-dimethylbenzamide. (A) low [HBpin] (5 equiv); (B) high [HBpin] (10 equiv).

ely). These data support assignment of a transition state that is highly organized, sterically congested, and associative, and they strongly suggest the same rate-determining step is operative in low and high [HBpin] reactions, indicating the mixed-order rate law is most likely due to saturation of the catalyst complex with HBpin at ~ 8 equiv of HBpin vs amide (i.e., the reaction becomes pseudo-first-order at this point; *vide infra* for a closer examination with DFT techniques).

To gauge the impact of electron density at the carbonyl carbon on the rate of amide reduction, a Hammett plot (Figure 3.5) was created using a series of *para*-substituted benzoyl piperidines. A slight increase in activity is observed for substrates with electron-withdrawing substituents at the R position, as indicated by a small, positive value for the Hammett parameter ρ of 0.56. Additional mechanistic details were obtained from isotopic labeling studies. Replacing HBpin with DBpin (see Experimental Section 3.7.5 for details) leads to complete disappearance

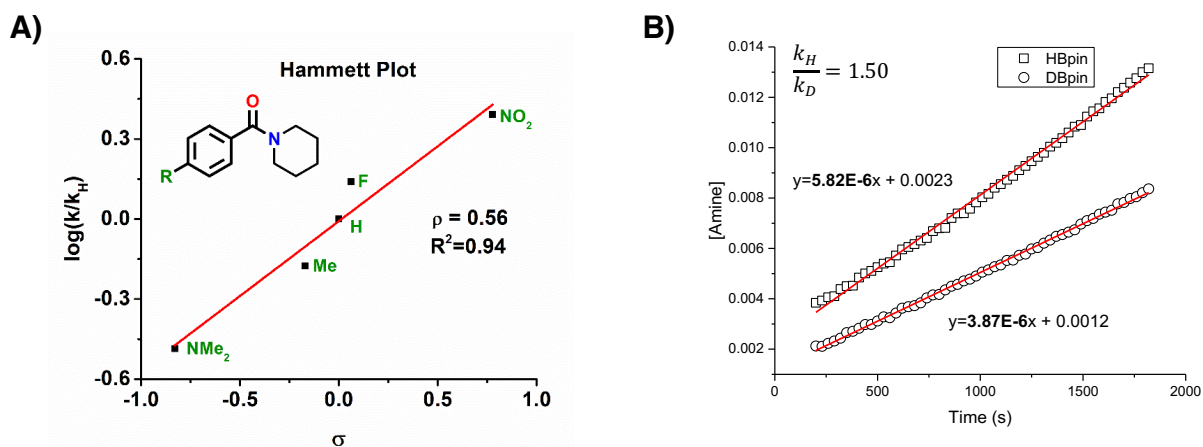


Figure 3.5 (A) Hammett plot generated from the reduction of *para*-substituted *N*-benzoylpiperidines with HBpin.^a (B) Plots for the determination of the kinetic isotope effect for reduction of *N,N*-dimethylbenzamide using HBpin and DBpin. ^aRates determined via integration of product ¹H NMR signals relative to a hexamethylbenzene internal standard.

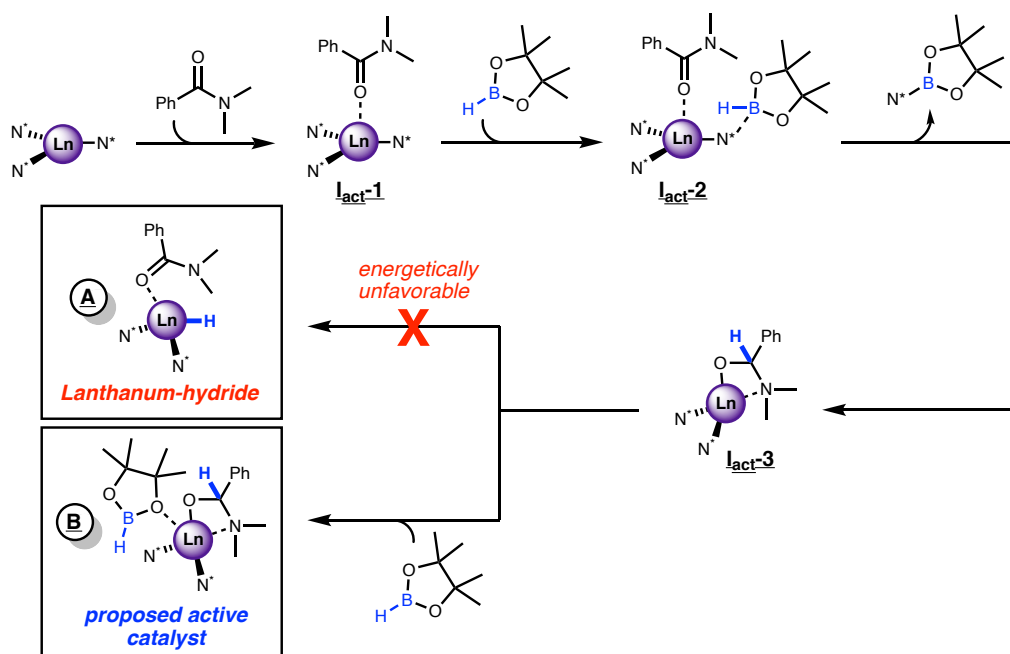
of the $R^1CH_2NR^2R^3$ 1H NMR resonance when DBpin is the reductant. Rate studies with DBpin and HBpin yield a kinetic isotope effect (KIE) of 1.50 for reduction of *N,N*-dimethylbenzamide (Figure 3.5).

3.5 Computational Mechanistic Analysis

Informed by the above kinetic and thermodynamic data, DFT modeling was next employed to better understand the mechanism of La^{NTMS} -catalyzed amide hydroboration. In order to accurately model the behavior of the central metal, various computational approaches were taken, using a number of different basis sets including LANL2DZ, LANL2DZ+pol,²³² and Def2-SVP.²³³ However, the addition of such polarization functions affords negligible changes in the stabilization energies of the key intermediates and transition states along the proposed reaction coordinate (see Experimental Section, Table 3.2). Therefore, as in our previous work detailing a similar reduction of esters,⁶⁰ the LANL2DZ basis set was ultimately used to model the lanthanum atom in this transformation. It will be seen that the active catalyst for this transformation is found to be the lanthanum hemiaminal species $[(Me_3Si)_2N]_2La-OCHR(NR'_2)-[HBpin]$ (Scheme 3.5, **B**), a species which bears a striking resemblance to the active catalyst this laboratory found recently for La^{NTMS} -catalyzed ester hydroboration.⁶⁰ While the transient nature of this complex (*vide infra*) precludes its NMR spectroscopic observation *in situ*, the formation of this species is supported by the appearance of 1.0 equiv (relative to La^{NTMS}) of pinB-N(SiMe₃)₂ in the 1H NMR spectra of catalytic reactions (at δ 1.03 and δ 0.37 ppm),²³⁴ indicating that the hydroboronolysis of a single -N(SiMe₃)₂ precatalyst ligand occurs. The formation of pinB-N(SiMe₃)₂ could also be indicative of a metal-hydride active catalyst (e.g., $[(Me_3Si)_2N]_2La-H$), (**A**, Scheme 3.5) however the energy required to form such a species (+20.5 kcal/mol vs -21.2 kcal/mol barrierless for structure **B**)

makes its presence in the catalytic cycle highly unlikely (Scheme 3.5). Moreover, no spectroscopic evidence indicating the presence of a La–H species is observed.

Scheme 3.5 Proposed catalyst activation process for the hydroboration/ reduction of amides catalyzed by La^{NTMS} .



Attempts to isolate complex **B** were unsuccessful due to the formation of an off-cycle product containing ring-opened pinacolborane (see Experimental Section 3.7.6 for characterization details) that predominates at the low substrate concentrations required for stoichiometric studies. This is identical to the deactivation product observed for La^{NTMS} -catalyzed ester hydroboration and is analogous to that found in lanthanocene-catalyzed pyridine dearomatization (Figure 3.6).^{60, 235} In an attempt to further investigate the proposed catalyst activation process shown in Scheme 3.5, NMR-monitored stoichiometric experiments were conducted. Species **I_{act-1}** was obtained from a 1:1 mixture of La^{NTMS} and *N,N*-dimethylbenzamide. Full conversion of the $\text{La}[\text{N}(\text{SiMe}_3)_2]_3$ proton signal at δ 0.29 ppm (C_6D_6) to

a new signal at δ 0.41 ppm (C_6D_6) indicates the formation of what is presumed to be **I_{act-1}** (see Experimental Section 3.7.6). Regarding species **I_{act-2}** and **I_{act-3}**, we attempted to isolate and characterize these intermediates by adding 1.0 equiv of HBpin to a 1:1 mixture of La^{NTMS} and *N,N*-dimethylbenzamide (**I_{act-1}**), however, the resulting spectra revealed a complex mixture of products and obvious decomposition. The ratios of La^{NTMS} , amide, and HBpin were also varied but these too yielded mixtures of products. Additionally, adding 1.0 equiv of amide to a solution of a pre-coordinated HBpin- La^{NTMS} complex was carried out, but attempts to isolate or unambiguously characterize **I_{act-2}** or **I_{act-3}** were ultimately unsuccessful.

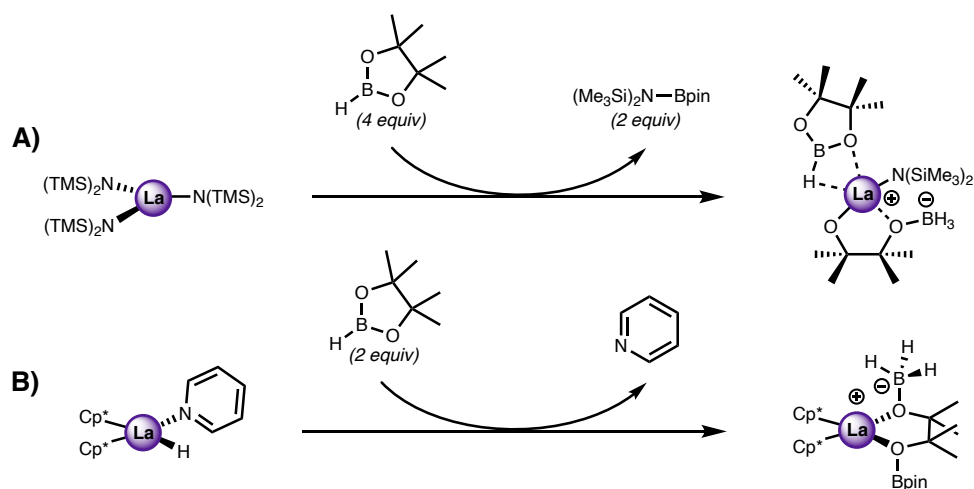


Figure 3.6 (A) Off-cycle product observed in stoichiometric studies of both amide and ester hydroboration catalyzed by La^{NTMS} .⁶⁰ (B) Comparable deactivation product reported for $[Cp^*_2LaH]_2$ -catalyzed pyridine dearomatization characterized by single-crystal X-ray diffraction; $Cp^* = \eta^5$ -pentamethylcyclopentadienyl.²²⁹

The proposed mechanistic pathway consists of four major steps (Figure 3.7). First, coordination of an additional amide molecule and approach of the Lewis acidic boron center of the coordinated HBpin molecule toward the hemiaminal oxygen of active catalyst **B**, leads to the formation of a new B–O bond and dissociation of the La–O bond. This step, which yields a La-

coordinated pinacolborate species, proceeds spontaneously, providing an overall stabilization energy of 19.4 kcal/mol and producing **C** as a relative minimum in the energetic profile (Figure 3.8). Next, a HBpin molecule approaches the catalyst complex. Hydride transfer from the La-coordinated hemiaminal-hydroborate species to the coordinated HBpin forms La-coordinated $[\text{H}_2\text{Bpin}]^-$, a species often proposed to facilitate hydride transfer in HBpin-mediated reductions.^{201, 204, 236-239} With reorganization, and the approach and subsequent coordination of an additional amide substrate after **TS1**, the complex then forms species **D** with a stabilization energy of 18.4 kcal/mol. A significant portion of this stabilization energy coming from amide co-

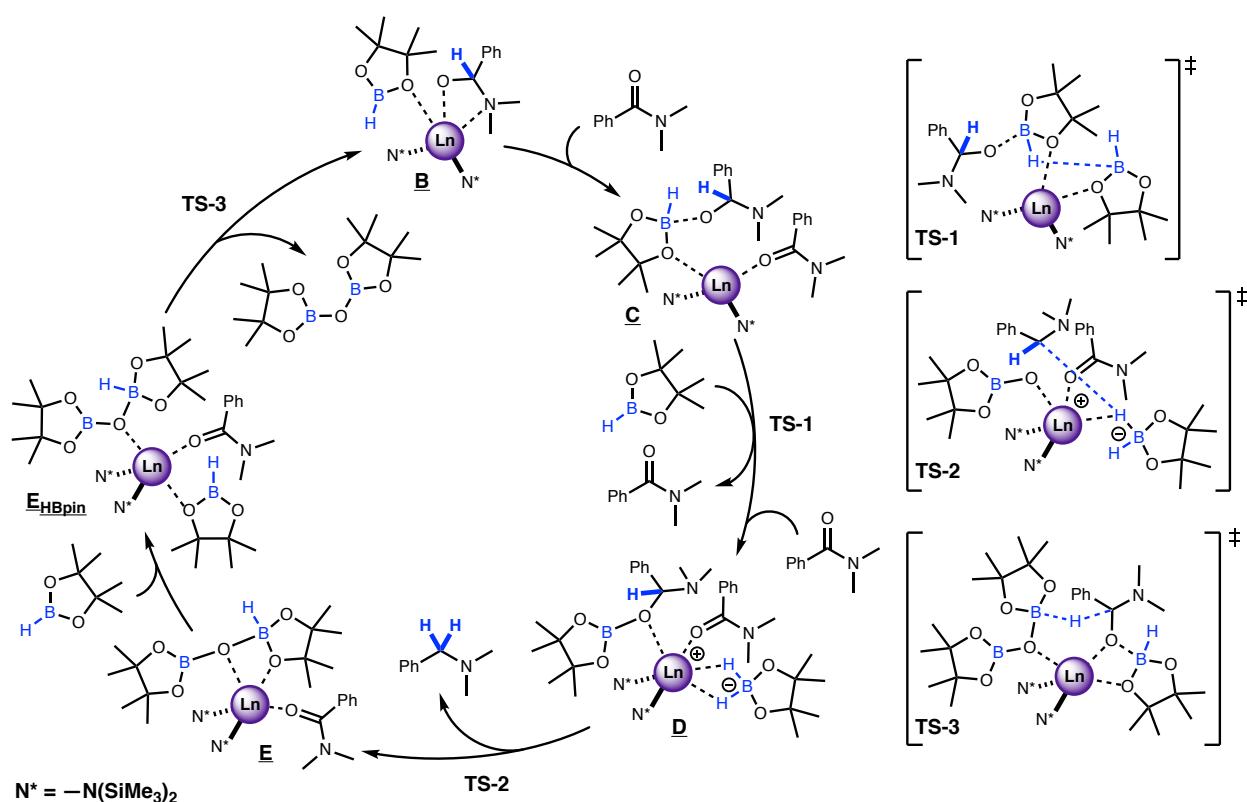


Figure 3.7 Proposed DFT-computed catalytic cycle and transition states for the catalytic hydroboration/reduction of *N,N*-dimethylbenzamide catalyzed by La^{NTMS} .

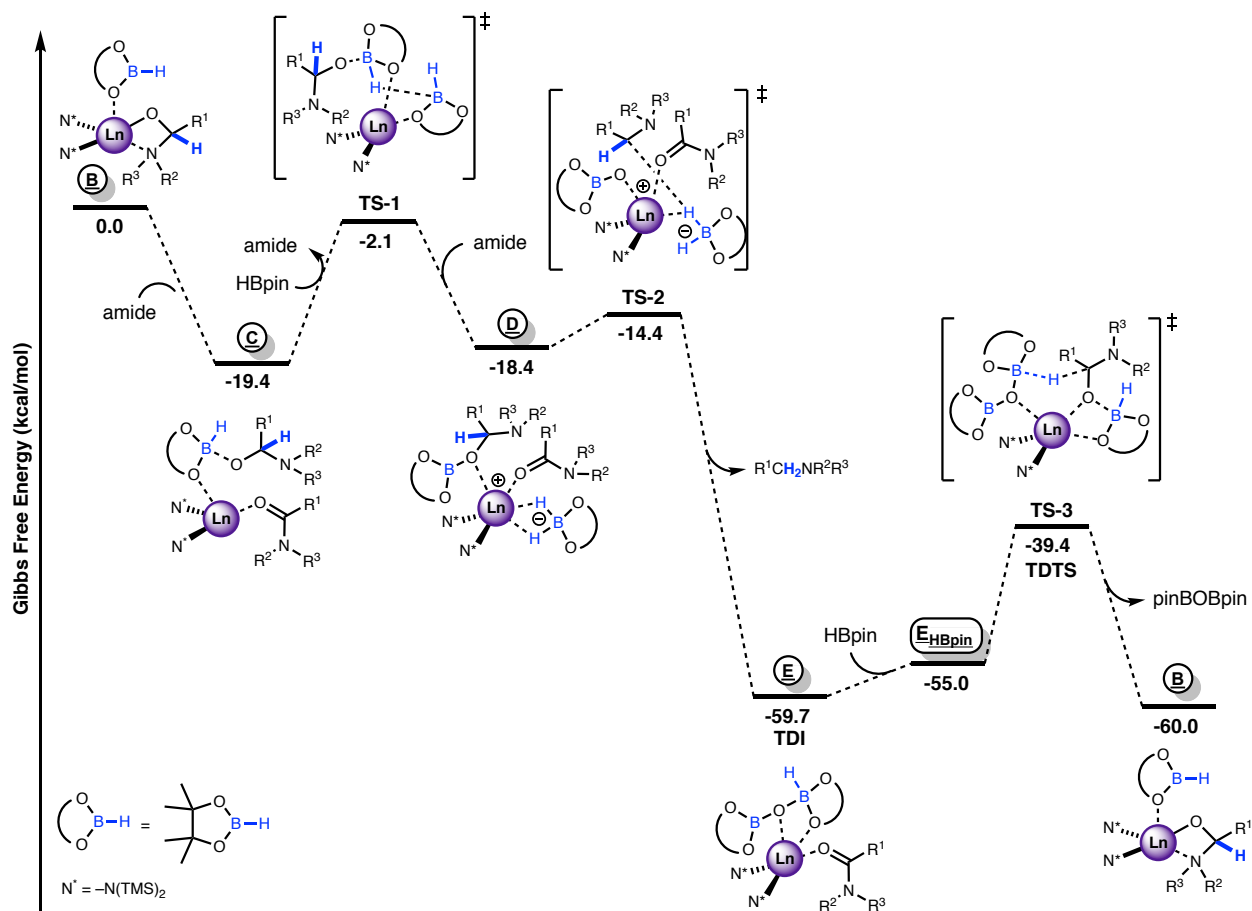


Figure 3.8 DFT-computed Gibbs free energy profile/catalytic cycle for the hydroboration/reduction of *N,N*-dimethylbenzamide catalyzed by La^{NTMS} .

ordination alone (Figure 3.8). Third, C–O bond scission of the hemiaminal-borane species **D** results in a transient carbocationic species and La-bound –OBpin (**TS2**). The carbocationic species is subsequently reduced by $[\text{H}_2\text{Bpin}]^-$ to yield free amine. This step proceeds with a 4.0 kcal/mol barrier and is highly exergonic (–41.3 kcal/mol) forming species **E**. Next, a second HBpin molecule approaches the catalyst complex forming complex E_{HBpin} . Even though this step is slightly exoenthalpic ($\Delta H = -3.2$ kcal/mol), the entropy gain related to the association process shifts up the energy value along the Gibbs free energy profile ($\Delta G = 4.7$ kcal/mol). Finally, hydride transfer from the activated HBpin of E_{HBpin} to the coordinated amide substrate acquired

in the second step allows for the formation of the pinB-O-Bpin co-product and restoration of the active catalyst **B**. It is worth noting that because the reaction described requires an excess of HBpin, it is plausible that an equilibrium exists between catalyst-amide and catalyst-HBpin coordination. For this reason, it is likely that other intermediates which are not shown in Figure 3.8 do exist within the proposed catalytic cycle. DFT calculation also supports this notion (see Experimental Section 3.7.7). However, the proposed catalytic cycle includes only the most stable intermediates and transition states, as these species are the largest contributors to the thermodynamic and kinetic behavior experimentally observed. In the transition state structure (**TS3**), HBpin interacts weakly with the carbonyl oxygen of the coordinated amide. This step is isoergonic and proceeds with an energy barrier of 20.3 kcal/mol. The above energetic profile shows that species **E** can be assigned as the turnover-determining intermediate (TDI) and **TS3** can be assigned as the turnover determining transition state (TDTS). The computed parameters, $\Delta H^\ddagger = 10.9$ kcal/mol and $\Delta S^\ddagger \approx -35$ e.u., agree well with the experimental findings. Moreover, the formation of the **E_{HBpin}** complex convincingly explains the shift from first to zero-order [HBpin] experimentally observed by increasing the HBpin concentration (Figure 3.3B).

A first-order dependence on [HBpin] is expected, as HBpin enters the catalytic cycle between the TDI and TDTS, in agreement with the low [HBpin] rate law determined experimentally, $\text{Rate} = k[\text{La}^{\text{NTMS}}]^1[\text{Amide}]^0[\text{HBpin}]^1$ (*vide supra*). However, the observation that a high HBpin concentration can induce saturation of the catalyst complex with HBpin (effectively eliminating **E_{HBpin}** from the energetic profile) likely underlies the first-to-zero-order transition observed for [HBpin] in the rate law.

In addition to the activation parameters discussed above, other experimental observations point to **E** and **TS3** as the TDI and TDTS, respectively. Steric encumbrance on the amide

substrate strongly depresses the reaction rates at 25 °C, which is to be expected for an associative, crowded transition state such as **TS3**. A small, positive Hammett ρ value ($\rho = 0.56$, Figure 3.4) indicates that the transition state is stabilized by withdrawal of electron density from the carbonyl carbon, but to a much lesser extent than is observed for typical base-catalyzed ester cleavages ($\rho = 1.9\text{--}2.5$).¹⁹³ This supports the present assignment that the turnover-limiting step involves nucleophilic hydride attack on a carbonyl bond that has been activated, in this case by simultaneous C=O coordination to both HBpin and La, priming the acyl carbon for nucleophilic attack and diminishing ρ . Similar results were recently found for the analogous ester hydroboration process.⁶⁰ Finally, the observed HBpin/DBpin KIE of 1.50 indicates that a bond to an HBpin-derived hydride is broken or formed during the rate-determining step.²⁴⁰ No other KIEs have been reported for amide hydroboration, making direct comparison impossible, but this value is significantly smaller than KIEs found for several comparable reactions.²⁴¹⁻²⁴⁴ However, this laboratory recently reported a nearly identical KIE (1.49) for ester hydroboration.⁶⁰ Notably, in the TDTS of both systems, the B–H bond of a coordinated hemiaminal-/hemiacetal-hydroborate is broken, and a new C–H bond is formed.

3.6 Conclusion

The scope and mechanism of La^{NTMS}-catalyzed, pinacolborane-based deoxygenative reduction of a diverse group of variously substituted amides are reported. The catalyst shows complete selectivity for amide reduction over nitro groups, alkenes, and alkynes, even at temperatures as high as 60 °C and catalyst loadings of 5 mol%. A combined experimental/theoretical analysis of the mechanism of this reaction reveals an unusual catalytic cycle involving ligand-centered hydride transfer. This gives rise to a rate law that is mixed-order

with respect to HBpin: Rate = $k[\text{La}^{\text{NTMS}}]^1[\text{Amide}]^0[\text{HBpin}]^1$ at low [HBpin] and Rate = $k[\text{La}^{\text{NTMS}}]^1[\text{Amide}]^0[\text{HBpin}]^0$ at high [HBpin]. This represents the first time a lanthanide catalyst has been employed for the pinacolborane-based reduction of amides, and it is the first attempt at a computationally aided analysis of the mechanism of amide hydroboration. By combining a mild reductant such as HBpin with a highly active and readily accessible catalyst like La^{NTMS} , a safer, more selective, and convenient route to amide reduction has been realized, highlighting the important role lanthanide catalysis can play in experimental chemical synthesis.

3.7 Experimental

3.7.1 Materials and Methods

All manipulations of air-sensitive materials were carried out with rigorous exclusion of oxygen and moisture in flame- or oven-dried Schlenk-type glassware on a dual-manifold Schlenk line or in an argon-filled glovebox with a high capacity recirculator (<1 ppm O_2). Benzene- d_6 (Cambridge Isotope Laboratories; 99+ atom % D) was stored over Na/K alloy and vacuum transferred prior to use. $\text{La}[\text{N}(\text{SiMe}_3)_2]_3$ (La^{NTMS})* and hexamethylbenzene were purchased from Sigma-Aldrich Co. and sublimed under high-vacuum (10^{-6} Torr). Pinacolborane (“HBpin”) was purchased from Sigma-Aldrich Co. and distilled under high-vacuum (10^{-6} Torr) to remove trace boronic acid impurities. Amide substrates were purchased from Sigma-Aldrich Co. and used as received or prepared according to established procedures. The products of amide deoxygenation were isolated as the amine hydrochlorides and then characterized by ^1H NMR and ^{13}C NMR spectroscopy, unless otherwise noted.

*The La^{NTMS} precatalyst can also be used as received without further purification.

3.7.2 Physical and Analytical Measurements

NMR spectra were recorded on a Bruker Avance III (500 MHz, ^1H ; 125 MHz, ^{13}C ; 125 MHz, ^{29}Si), Varian Inova 500 (500 MHz, ^1H ; 125 MHz, ^{13}C), Agilent DD MR-400 (400 MHz, ^1H ; 100 MHz, ^{13}C ; 128 MHz, ^{11}B ;), or Agilent DD2 500 (500 MHz, ^1H ; 125 MHz, ^{13}C). Chemical shifts (δ) for ^1H are referenced to residual solvent resonances (δ 7.16 ppm for benzene- d_6 ; δ 7.26 ppm for CDCl_3 ; δ 4.79 ppm for D_2O). ^{13}C shifts are referenced to residual solvent resonances (δ 128.06 ppm for benzene- d_6 ; δ 77.16 ppm for CDCl_3) or external SiMe_4 standard. ^{11}B shifts are referenced to an external $\text{BF}_3\cdot\text{OEt}_2$ standard. ^{29}Si shifts are referenced to an external SiMe_4 standard. NMR scale reactions were carried out either in Teflon-sealed J. Young tubes or rubber septum-sealed tubes (*vide infra*).

3.7.3 Amide Hydroboration/Reduction Experimental Procedures

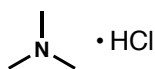
General Method A (NMR-scale reaction involving solid amides): In a glovebox, the amide (0.25 mmol), internal standard hexamethylbenzene (50 μmol), and HBpin (1.25 mmol) were dissolved in C_6D_6 (total volume 1.0 mL). This solution was injected into a vial containing La^{NTMS} (12.5 μmol), and shaken to dissolve the catalyst. The reaction mixture was transferred to a J. Young capped NMR tube, and the reaction was monitored by ^1H NMR spectroscopy.

General Method B (NMR-scale reaction involving liquid amides): In a glovebox, La^{NTMS} (12.5 μmol) was placed in a septum-sealed NMR tube, and the cap was wrapped in Parafilm®. Internal standard (50 μmol), HBpin (1.25 mmol), and C_6D_6 were added to a septum-sealed vial. Outside of the glovebox (to prevent amine poisoning of the glovebox circulation catalyst), the liquid amide (0.25 mmol) was injected into the vial with HBpin and internal standard, the vial was shaken, and the contents were injected into the NMR tube containing the catalyst, all under N_2 . The tube was shaken to dissolve the catalyst, and the reaction was monitored by ^1H NMR spectroscopy.

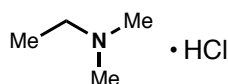
General Method C (Scale-Up/Isolation of Amine Hydrochlorides): In a glovebox, La^{NTMS} (0.125mmol) was weighed into a 25 mL round-bottom flask and dissolved in benzene (5 mL). HBpin (12.5 mmol) and amide (2.5 mmol) were dissolved in benzene (5 mL), and the solution was injected into the stirred catalyst solution at 25 °C or 60 °C. Low boiling amines (trimethylamine, *N,N*-dimethylethylamine, *N*-methylpyrrolidine, *N*-methylethylamine) were isolated by evaporation. Nitrogen gas was bubbled into a solution containing the reaction mixture and a cannula needle was used to bubble the volatile amine product into a 1 M HCl/methanol solution cooled to 0 °C. The methanol was then removed by rotary evaporation, and the remaining solid was washed with pentanes. Amines with boiling points similar to HBpin (*N*-methylpiperidine and *N,N*-diisopropylmethylamine) were first isolated by distillation under vacuum. To the distillate, 1 M HCl/methanol was added, precipitating a solid that was subsequently collected and washed with pentanes. The remaining high-boiling or solid amines were isolated by first removing HBpin under vacuum, re-dissolving the amine in benzene, and then filtering the solution through a basic alumina plug to remove trace HBpin, pinB-O-Bpin, and the catalyst. A 1 M HCl/methanol solution was then added, precipitating a solid that was collected and washed with ether or pentanes.

3.7.4 Amide Hydroboration/Reduction Characterization Data

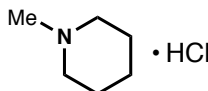
Characterization data for the products of amide reduction are given below. Products were converted to amine•HCl (unless otherwise noted) and characterized by ^1H and ^{13}C NMR spectroscopy. Previously unreported products were compared to amine•HCl synthesized from commercially available amines. For full ^1H NMR and ^{13}C NMR spectra of amine products, see Appendix B.



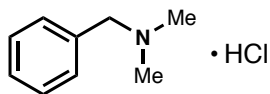
Trimethylamine hydrochloride (Compound III-6). Compound III-6 was prepared by General Method C. The product was isolated as a white solid (0.119 g, 1.25 mmols, 50%). ^1H NMR (500 MHz, D_2O) δ 2.93 (s, 9 H) ppm; ^{13}C NMR (125 MHz, D_2O) δ 44.76 ppm. NMR spectra are identical to those reported in the literature.¹⁹⁰



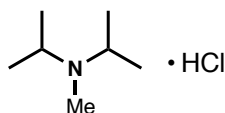
***N,N*-dimethylethylamine hydrochloride (Compound III-7).** Compound III-7 was prepared by General Method C. The product was isolated as a white solid (0.153 g, 1.40 mmols, 56%). ^1H NMR (500 MHz, D_2O) δ 3.20 (q, $J = 7.2$ Hz, 2H, N- CH_2CH_3), 2.87 (s, 6H, N- CH_3), 1.32 (t, $J = 7.3$ Hz, 3H, N- CH_2CH_3) ppm; ^{13}C NMR (125 MHz, D_2O) δ 53.01 (N- CH_2CH_3), 42.01 (N- CH_3), 9.02 (N- CH_2CH_3) ppm. NMR spectra are identical to those reported in the literature.¹⁹⁰



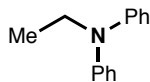
***N*-methylpiperidine hydrochloride (Compound III-8).** Compound III-8 was prepared by General Method C. The product was isolated as a white solid (0.298 g, 2.20 mmols, 88%). ^1H NMR (500 MHz, D_2O) δ 3.48 (d, $J = 12.7$ Hz, 2H N- C_5H_{10}), 2.95 (t, $J = 12.5$ Hz, 2H, N- C_5H_{10}), 2.84 (s, 3H, Me), 2.02 – 1.89 (m, 2H, N- C_5H_{10}), 1.88 – 1.65 (m, 3H, N- C_5H_{10}), 1.54 – 1.40 (m, 1H, N- C_5H_{10}) ppm; ^{13}C NMR (125 MHz, D_2O) δ 54.92 (N- C_5H_{10}), 43.19 (N-Me), 22.98 (N- C_5H_{10}), 20.61 (N- C_5H_{10}) ppm. NMR spectra are identical to samples prepared from commercially available amine.



***N,N*-dimethylbenzylamine hydrochloride (Compound III-9).** Compound III-9 was prepared by General Method C. The product was isolated as a white solid (0.339 g, 1.97 mmols, 79%). ¹H NMR (500 MHz, D₂O) δ 7.58 – 7.49 (m, 5H, N-CH₂Ph), 4.33 (s, 2H, N-CH₂Ph), 2.87 (s, 6H, N-CH₃) ppm; ¹³C NMR (125 MHz, D₂O) δ 130.77 (N-CH₂Ph), 130.15 (N-CH₂Ph), 129.30 (N-CH₂Ph), 61.12 (N-CH₂Ph), 42.07 (N-CH₃) ppm. NMR spectra are identical to those reported in the literature.¹⁹⁰

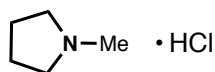


***N,N*-diisopropylmethylamine hydrochloride (Compound III-10).** Compound III-10 was prepared by General Method C. The product was isolated as a white solid (0.349 g, 2.30 mmols, 92%). ¹H NMR (500 MHz, D₂O) δ 3.70 (septet, *J* = 6.7 Hz, 2H, N-[CH(CH₃)₂]₂), 2.70 (s, 3H, N-CH₃), 1.33 (dd, *J* = 6.7 Hz, 19.2 Hz, 12 H, N-[CH(CH₃)₂]₂) ppm; ¹³C NMR (125 MHz, D₂O) δ 54.92 (N-CH(CH₃)₂), 30.68 (N-Me), 18.06 (N-CH(CH₃)₂), 15.57 (N-CH(CH₃)₂) ppm. NMR spectra are identical to samples prepared from commercially available amine.

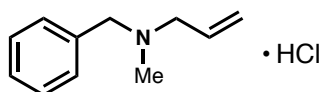


***N,N*-diphenylethylamine (Compound III-11).** Compound III-11 was prepared by General Method A (>99%, determined via ¹H NMR integration using Hexamethylbenzene as an internal standard). ¹H NMR (500 MHz, C₆D₆) δ 7.13 – 7.08 (m, 4H, N-Ph), 6.93 – 6.89 (m, 4H, N-Ph),

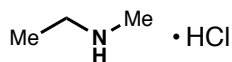
6.86 – 6.81 (m, 2H, *N-Ph*), 3.47 (q, $J = 7.0$ Hz, 2H, NCH_2CH_3), 0.97 (t, $J = 7.0$ Hz, 3H, NCH_2CH_3) ppm; ^{13}C NMR (125 MHz, C_6D_6) δ 148.28 (*N-Ph*), 129.58 (*N-Ph*), 121.46 (*N-Ph*), 121.38 (*N-Ph*), 46.51 ($N-CH_2CH_3$), 12.77 ($N-CH_2CH_3$) ppm. NMR spectra are identical to those reported in the literature.²⁴⁵



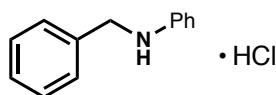
***N*-methylpyrrolidine hydrochloride (Compound III-12).** Compound III-12 was prepared by General Method C. The product was isolated as an oily solid (0.277 g, 2.28 mmols, 91%). 1H NMR (500 MHz, D_2O) δ 3.69 – 3.62 (m, 2H, $N-C_4H_8$), 3.11 – 3.03 (m, 2H, $N-C_4H_8$), 2.93 (s, 3H, *N-Me*), 2.22 – 2.13 (m, 2H, $N-C_4H_8$); 2.08 – 1.98 (m, 2H, $N-C_4H_8$) ppm; ^{13}C NMR (125 MHz, D_2O) δ 55.76 ($N-C_4H_8$), 40.56 ($N-C_4H_8$), 22.83 (*N-Me*) ppm. NMR spectra are identical to samples prepared from commercially available amine.



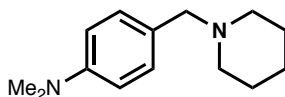
***N*-allyl-*N*-methylbenzylamine hydrochloride (Compound III-13).** Compound III-13 was prepared by General Method C. The product was isolated as a white solid (0.461 g, 2.33 mmols, 93%). 1H NMR (500 MHz, Chloroform-*d*) δ 7.65 – 7.59 (m, 2H, *Ph*), 7.48 – 7.42 (m, 3H, *Ph*), 6.29 – 6.17 (m, 1H, $NCH_2CH=CH_2$), 5.59 (d, $J = 10.1$ Hz, 1H, $NCH_2CH=CH_2$), 5.49 (d, $J = 17.2$ Hz, 1H, $NCH_2CH=CH_2$), 4.20 – 4.00 (m, 2H, $N-CH_2$), 3.77 – 3.40 (m, 2H, $PhCH_2$), 2.63 (d, 3H, $N-CH_3$ coupling to *N-H*) ppm; ^{13}C NMR (125 MHz, $CDCl_3$) δ 131.30, 130.34, 129.60, 128.50, 126.65, 126.09, 59.01, 57.77, 38.89 ppm. NMR spectra are identical to those reported in the literature.²⁴⁶



***N*-methylethanamine hydrochloride (Compound III-14).** Compound III-14 was prepared by General Method C. The product was isolated as a white solid (0.158 g, 1.65 mmols, 66%). ¹H NMR (500 MHz, D₂O) δ 3.09 (q, *J* = 7.5 Hz, 2H, N-CH₂CH₃), 2.70 (s, 3H, N-CH₃), 1.28 (t, *J* = 7.5 Hz, 3H, N-CH₂CH₃) ppm; ¹³C NMR (125 MHz, D₂O) δ 44.23 (N-CH₂CH₃), 32.12 (N-CH₃), 10.33 (N-CH₂CH₃) ppm. NMR spectra are identical to samples prepared from commercially available amine.

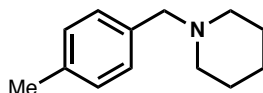


***N*-benzylaniline hydrochloride (Compound III-15).** Compound III-15 was prepared by General Method C. The product was isolated as a gray solid (0.412 g, 0.188 mmols, 75%). ¹H NMR (500 MHz, Chloroform-*d*) δ 7.40 – 7.29 (m, 7H, *Ph*), 7.28 – 7.20 (m, 3H, *Ph*), 4.36 (s, 2H, PhCH₂-N) ppm; ¹³C NMR (125 MHz, CDCl₃) δ 134.45 (*Ph*), 133.93 (*Ph*), 131.17 (*Ph*), 129.82 (*Ph*), 129.55 (*Ph*), 129.29 (*Ph*), 128.84 (*Ph*), 124.00 (*Ph*), 56.09 (PhCH₂-N) ppm. NMR spectra are identical to samples prepared from commercially available amine.

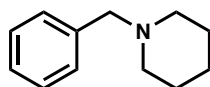


***N,N*-dimethyl-4-(piperidin-1-ylmethyl)benzamine (Compound III-16).** Compound III-16 was prepared by General Method B (95%, determined via ¹H NMR integration using Hexamethylbenzene as an internal standard). ¹H NMR (500 MHz, C₆D₆) δ 7.54 (d, *J* = 8.1 Hz, 2H, *Ph*), 6.46 (d, *J* = 8.1 Hz, 2H, *Ph*), 3.45 (br s, 2H, PhCH₂Npip), 2.48 (s, 6H, PhNMe₂), 2.31

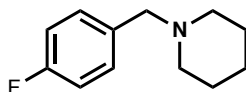
(br s, 4H, *pip*), 1.56 (p, $J = 5.9$ Hz, 4H, *pip*), 1.39 – 1.29 (m, 2H, *pip*) ppm; ^{13}C NMR (125 MHz, C_6D_6) δ 136.24 (*Ph*), 134.86 (*Ph*), 131.86 (*Ph*), 121.25 (*Ph*), 62.96 ($\text{PhCH}_2\text{-Npip}$), 55.58 (*N-pip*), 48.72 (PhNMe_2), 23.25 (*N-pip*), 17.02 (*N-pip*) ppm. NMR spectra are identical to those reported in the literature.²⁴⁷



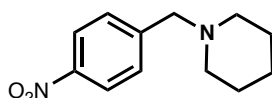
4-methylbenzylpiperidine (Compound III-17). Compound III-17 was prepared by General Method B (>99%, determined via ^1H NMR integration using Hexamethylbenzene as an internal standard). ^1H NMR (500 MHz, C_6D_6) δ 7.28 (d, $J = 8.1$ Hz, 2H, *Ph*), 7.02 (d, $J = 8.1$ Hz, 2H, *Ph*), 3.35 (br s, 2H, PhCH_2Npip), 2.29 (br s, 4H, *pip*), 2.15 (s, 3H, PhCH_3), 1.54 (p, $J = 5.9$ Hz, 4H, *pip*), 1.39 – 1.28 (m, 2H, *pip*) ppm; ^{13}C NMR (125 MHz, C_6D_6) δ 136.81 (*Ph*), 136.32 (*Ph*), 131.76 (*Ph*), 129.26 (*Ph*), 63.97 ($\text{PhCH}_2\text{-Npip}$), 54.85 (*N-pip*), 26.55 (*N-pip*), 21.15 (*MePh*), 16.94 (*N-pip*) ppm. NMR spectra are identical to those reported in the literature.²⁴⁸



N-benzylpiperidine (Compound III-18). Compound III-18 was prepared by General Method B (99%, determined via ^1H NMR integration using Hexamethylbenzene as an internal standard). ^1H NMR (500 MHz, C_6D_6) δ 7.38 – 7.33 (m, 2H, *Ph*), 7.22 – 7.15 (m, 2H, *Ph*), 7.12 – 7.07 (m, 1H, *Ph*), 3.33 (s, 2H, PhCH_2Npip), 2.26 (br s, 4H, *pip*), 1.47 (p, $J = 5.6$ Hz, 4H, *pip*), 1.35 – 1.25 (m, 2H, *pip*) ppm; ^{13}C NMR (125 MHz, C_6D_6) δ 139.86 (*Ph*), 131.76 (*Ph*), 129.21 (*Ph*), 127.10 (*Ph*), 64.17 ($\text{PhCH}_2\text{-Npip}$), 54.86 (*N-pip*), 26.52 (*N-pip*), 16.94 (*N-pip*) ppm. NMR spectra are identical to those reported in the literature.²⁴⁹



4-fluorobenzylpiperidine (Compound III-19). Compound III-19 was prepared by General Method A (97%, determined via ^1H NMR integration using Hexamethylbenzene as an internal standard). ^1H NMR (500 MHz, C_6D_6) δ 7.20 – 7.08 (m, 2H, *Ph*), 6.87 – 6.80 (m, 2H, *Ph*), 3.19 (s, 2H, PhCH_2Npip), 2.20 (br s, 4H, *pip*), 1.45 (p, $J = 5.4$ Hz, 4H, *pip*), 1.32 – 1.24 (m, 2H, *pip*) ppm; ^{13}C NMR (125 MHz, C_6D_6) δ 131.76 (*Ph*), 130.62 (*Ph*), 115.24 (*Ph*), 115.07 (*Ph*), 63.17 ($\text{PhCH}_2\text{-Npip}$), 54.71 (*N-pip*), 26.48 (*N-pip*), 16.94 (*N-pip*) ppm. NMR spectra are identical to those reported in the literature.²⁵⁰



4-nitrobenzylpiperidine (Compound III-20). Compound III-20 was prepared by General Method A (>99%, determined via ^1H NMR integration using Hexamethylbenzene as an internal standard). ^1H NMR (500 MHz, C_6D_6) δ 7.88 (d, $J = 7.9$ Hz, 2H, *Ph*), 7.01 (d, $J = 7.9$ Hz, 2H, *Ph*), 3.05 (s, 2H, PhCH_2Npip), 2.10 (br s, 4H, *pip*), 1.43 (p, $J = 5.4$ Hz, 4H, *pip*), 1.23 – 1.19 (m, 2H, *pip*) ppm; ^{13}C NMR (125 MHz, C_6D_6) δ 145.02 (*Ph*), 144.58 (*Ph*), 126.75 (*Ph*), 121.04 (*Ph*), 60.45 ($\text{PhCH}_2\text{-Npip}$), 52.28 (*N-pip*), 23.92 (*N-pip*), 22.22 (*N-pip*) ppm. NMR spectra are identical to those reported in the literature.²⁴⁷

3.7.5 Amide Hydroboration/Reduction Kinetic Analysis

General NMR-Scale Reaction for Kinetic Monitoring by ^1H NMR Arrays: In a glovebox, amide and HBpin were mixed in a vial and dissolved in C_6D_6 ($V_{\text{total}} = 1.0$ mL). Hexamethylbenzene was used as an internal standard. The solution was then added to a rubber

septum-sealed NMR tube, wrapped with Parafilm®, and removed from the glovebox. At the NMR instrument, the magnet was locked, tuned, and shimmed to the sample, then a stock solution containing an appropriate loading of the $\text{La}[\text{N}(\text{SiMe}_3)_2]_3$ catalyst was injected into the NMR tube. The tube was shaken, reinserted into the instrument, and the experiment was started. Single (^1H NMR) scans were collected at regular intervals. Substrate and/or product concentrations were determined relative to the intensity of the internal standard resonance and plotted versus time.

Kinetic Analysis: Kinetic analysis of the NMR-scale reactions described above was carried out by collecting multiple (>15) data points early in the reaction (<20% conversion). Under these conditions, the reaction can be approximated as pseudo-zero-order with respect to the substrate concentrations. The product concentration was measured from the area of the $\text{R}^1\text{CH}_2\text{NR}^2\text{R}^3$ product peaks relative to the C_6Me_6 internal standard. Data were fit by least-squares analysis ($R^2 > 0.98$) according to eq 3.2, where “ t ” is time, “[product]” is the concentration of product at time t , and “ m ” is the rate of reaction.

$$[\text{product}] = mt \quad (3.2)$$

Reaction orders for HBpin and *N,N*-dimethylbenzamide were determined by running reactions under pseudo-first-order conditions (10-fold excess of non-measured reactant). The order of the reactant not held in excess was determined from the linearity of plots of $[\text{A}]$ vs. time (zeroth-order), $\ln[\text{A}]$ vs. time (first-order), and $[\text{A}]^{-1}$ vs. time (second-order).²⁵¹ As discussed in Section 3.4, the order in HBpin for amide reduction was not amenable to determination under pseudo-first-order conditions (Figure 3.3A) and instead had to be determined by initial rates analysis (Figure 3.3B).

The order for La^{NTMS} was determined from the rates of reduction of *N,N*-dimethylbenzamide at 5 different catalyst loadings (0.5–2.5%). The rates were measured as the slope of the line for the plot of [Product] vs. time (conversion <20%). These rates were then plotted as $\ln(\text{rate})$ vs. $\ln[\text{La}^{\text{NTMS}}]$. The negative rate of disappearance of La^{NTMS} is proportional to the concentration of La^{NTMS} to the order (α) (eq 3.3). Therefore, the order is the slope of a plot of $\ln(\text{rate})$ vs. $\ln[\text{La}^{\text{NTMS}}]$ (eq 3.4).²³⁵

$$\frac{-d[\text{La}^{\text{NTMS}}]}{dt} = k_{\text{obs}}[\text{La}^{\text{NTMS}}]^\alpha \quad (3.3)$$

$$\ln(\text{rate}) = \ln(k_{\text{obs}}) + \alpha \ln[\text{La}^{\text{NTMS}}] \quad (3.4)$$

Isotopic Labeling Studies: DBpin was synthesized according to literature procedures.²⁵² Under a strong flow of nitrogen, $\text{BD}_3 \cdot \text{SMe}_2$ (Cambridge Isotope Laboratories, 8.5 mmol, 10 M) was diluted in dichloromethane (10 mL) in an addition funnel. The resulting solution was added dropwise over 30 min to a solution of pinacol (8.5 mmol, 1.0 g) in 20 mL of dichloromethane held at 0 °C. After addition was complete, the solution was brought to rt and stirred until bubbling was no longer observed (approx. 1 h). DBpin was isolated via distillation (0 °C at 10 mmHg) and characterized by ^1H and ^{11}B NMR spectroscopy. ^1H NMR (400 MHz, C_6D_6): δ 1.00 (s, 12H, DBpin); $^{11}\text{B}\{^1\text{H}\}$ NMR (128 MHz, C_6D_6): δ 28.37 (t, $^2J_{\text{DB}} = 22.8$ Hz, DBpin). Rate studies were carried out with HBpin and DBpin under the same ^1H NMR kinetic monitoring conditions outlined above using *N,N*-dimethylbenzamide.

Variable-Temperature Kinetic Analysis: Temperature-dependent rate data were obtained via arrayed NMR scans as described above. Temperatures were set on the NMR instrument using an external temperature controller and calibrated using ethylene glycol (> 25 °C) or methanol (< 25 °C) standards. Rates at each temperature were determined from the average of three trials. These

data were then plotted as $1000/T$ vs. $\ln(k/T)$. From the resulting plot, the enthalpy and entropy of the transition state was obtained using the Eyring equation (eq 3.5). The linear form of the Eyring equation (shown here) yields a straight line with negative slope, $\frac{-\Delta H^\ddagger}{R}$, and y-intercept,

$$\ln \frac{k_B}{h} + \frac{\Delta S^\ddagger}{R}.$$

$$\ln \frac{k}{T} = \frac{-\Delta H^\ddagger}{RT} + \ln \frac{k_B}{h} + \frac{\Delta S^\ddagger}{R} \quad (3.5)$$

From a plot of $1000/T$ vs. $\ln(k)$, the activation energy (E_a) was obtained using the Arrhenius equation (eq 3.6), where E_a is the negative slope multiplied by R .

$$\ln k = -\frac{E_a}{RT} + \ln A \quad (3.6)$$

Hammett Analysis: A series of *para*-substituted *N*-benzoyl piperidines was synthesized from the corresponding benzaldehydes according to literature procedures (^1H and ^{13}C NMR spectra were identical to those previously reported).²⁵³ Reduction rates were determined by ^1H NMR spectroscopy (*vide supra*). The rates of reduction for each substrate were plotted according to the Hammett equation (eq 3.7), so that the slope of the line gives rho (ρ), which indicates the sensitivity of the reaction to the electron density at the carbonyl carbon of the substrate.²⁵⁴

$$\log \frac{k}{k_H} = \sigma \rho \quad (3.7)$$

Competition Studies: To gauge the selectivity of La^{NTMS} for amide hydroboration over olefin/alkyne hydroboration, intermolecular competition experiments were performed using 1-octene and 1-octyne. *N,N*-dimethylbenzamide (0.125 mmol), 1-octene/1-octyne (0.125 mmol), and HBpin (0.625 mmol) were dissolved in C_6D_6 in a J. Young capped NMR tube. La^{NTMS} (6.25

μmol) was added and the tube was shaken. After 2 h at 60 °C, complete conversion of the *N,N*-dimethylbenzamide was observed, with no concomitant reduction of olefin.

Primary Amide Reduction: Reduction does not occur with the two primary amides tested (acetamide and benzamide), and instead an intractable, off-white precipitate is observed. To determine the identity of the precipitate formed during primary amide reduction, first La^{NTMS} (50 μmol , 1 equiv) and benzamide (50 μmol , 1 equiv) were dissolved in C_6D_6 in a J. Young capped NMR tube at 25 °C in an inert atmosphere glovebox. A white precipitate was immediately formed and allowed to settle to the bottom of the NMR tube. The solvent was decanted and the J. Young capped NMR tube containing the white precipitate was sealed, removed from the glovebox, and dried on a high vacuum line. After drying, the NMR tube was again sealed and taken into the glovebox where the precipitate was dissolved in THF to give a pale yellow solution. A sealed capillary containing $\text{DMSO-}d_6$ was added to the NMR tube to provide a solvent lock. NMR spectroscopic experiments were then performed (Figures 3.10, *top* and Figure 3.11, *top*). After all data were collected, the NMR tube containing the precipitate dissolved in THF was opened under strong flow of argon and 1 drop of D_2O was added in order to confirm ligand identities via hydrolysis of the metal complex. The tube was gently inverted to obtain a homogeneous solution before additional NMR experiments were performed, again using a $\text{DMSO-}d_6$ solvent lock (Figure 3.10, *bottom* and Figure 3.11, *bottom*). The spectroscopic experiments support the identity of the precipitate to be the unsymmetrical La-hemiaminalate complex $[(\text{Me}_3\text{Si})_2\text{N}]_2\text{La}\{\eta^2\text{-OC(NH)Ph}\}$ which is not catalytically active under the reaction conditions described here. Based on the low solubility of this complex, it is plausible that it may exist as an oligomeric species, having bridging hemiaminalate ligands. There is no spectroscopic

evidence of a ligand insertion reaction between the La^{NTMS} precatalyst and the primary amide (i.e., $-\text{N}(\text{SiMe}_3)_2$ insertion into the amide $\text{C}=\text{O}$ bond).

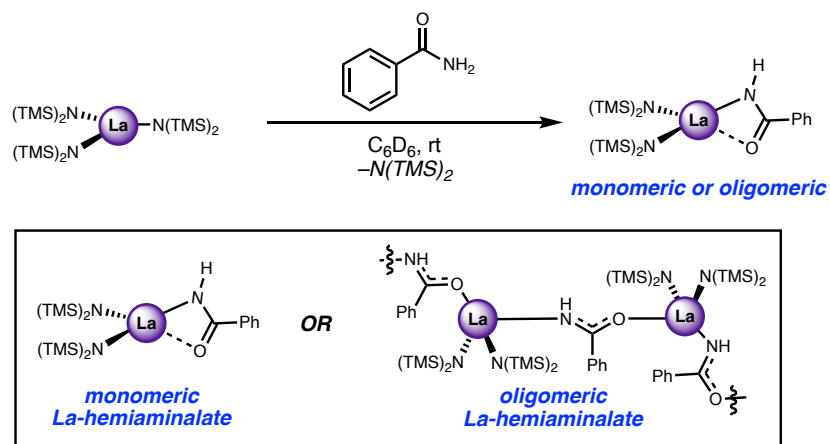


Figure 3.9 Proposed monomeric or oligomeric La -hemiaminalate complex $[(\text{Me}_3\text{Si})_2\text{N}]_2\text{La}\{\eta^2\text{-OC}(\text{NH})\text{Ph}\}$ obtained from the reaction of La^{NTMS} with the primary amide benzamide.

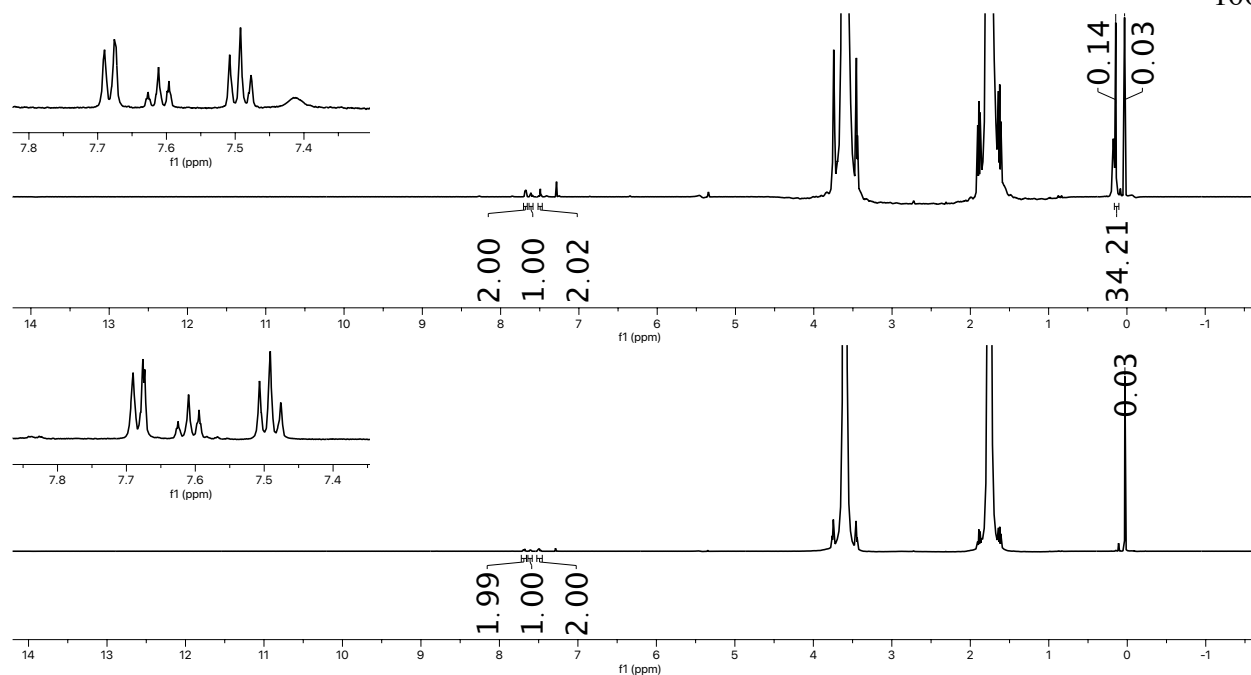


Figure 3.10 Top: ¹H NMR (500 MHz) spectrum of a proposed La-hemiaminalate complex [(Me₃Si)₂N]₂La{η²-OC(NH)Ph} obtained as a precipitate from the reaction of benzamide and La^{NTMS} (1:1 molar ratio) in C₆D₆. Spectrum obtained from a solution of precipitate in THF with a sealed capillary containing DMSO-*d*₆. (HN(SiMe₃)₂: δ 0.03 ppm); Bottom: ¹H NMR (500 MHz) spectrum of the D₂O-quenched proposed La-hemiaminalate complex [(Me₃Si)₂N]₂La{η²-OC(NH)Ph} obtained as a precipitate from the reaction of benzamide and La^{NTMS} (1:1 molar ratio) in C₆D₆. Spectrum obtained from a solution of precipitate in THF with a sealed capillary containing DMSO-*d*₆. (HN(SiMe₃)₂: δ 0.03 ppm).

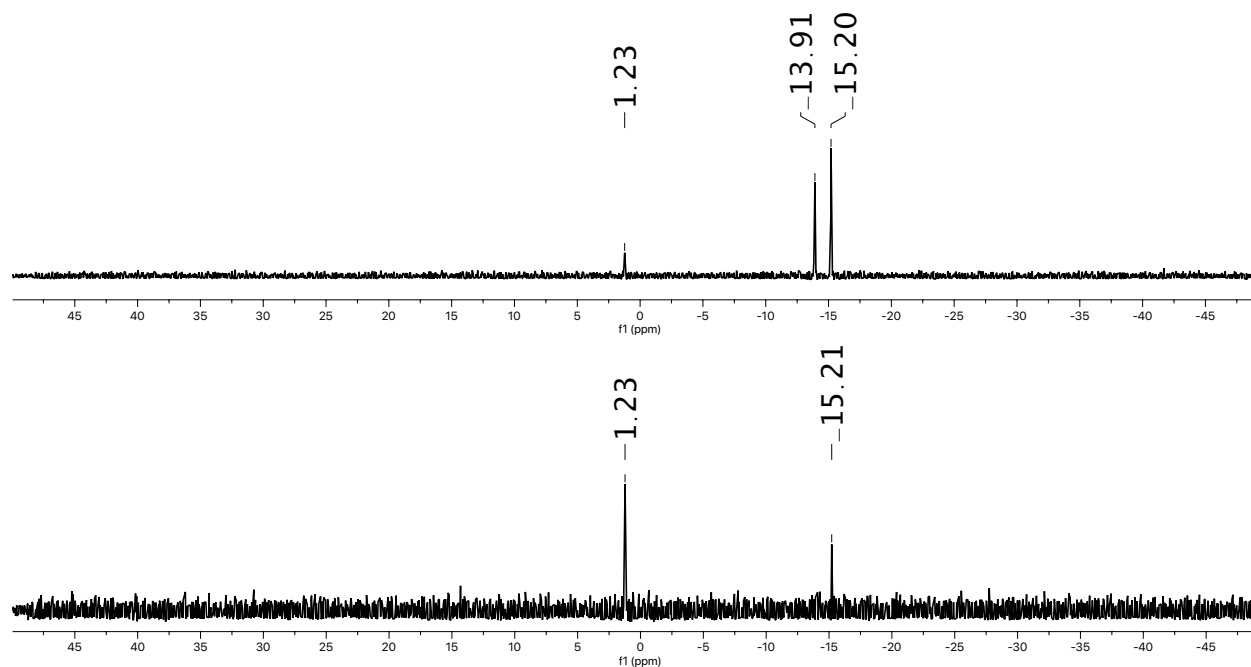


Figure 3.11 Top: ^{29}Si NMR (125 MHz) spectrum of a proposed La-hemiaminalate complex $[(\text{Me}_3\text{Si})_2\text{N}]_2\text{La}\{\eta^2\text{-OC}(\text{NH})\text{Ph}\}$ obtained as a precipitate from the reaction of benzamide and La^{NTMS} (1:1 molar ratio) in C_6D_6 . Spectrum obtained from a solution of precipitate in THF with a sealed capillary containing $\text{DMSO-}d_6$. ($\text{HN}(\text{SiMe}_3)_2$: δ 1.23 ppm); Bottom: ^{29}Si NMR (125 MHz) spectrum of the D_2O -quenched proposed La-hemiaminalate complex $[(\text{Me}_3\text{Si})_2\text{N}]_2\text{La}\{\eta^2\text{-OC}(\text{NH})\text{Ph}\}$ obtained as a precipitate from the reaction of benzamide and La^{NTMS} (1:1 molar ratio) in C_6D_6 . Spectrum obtained from a solution of precipitate in THF with a sealed capillary containing $\text{DMSO-}d_6$. ($\text{HN}(\text{SiMe}_3)_2$: δ 1.23 ppm).

Secondary Amide Reduction: To determine the active catalyst for secondary amide reduction, La^{NTMS} (2.08 μmol , 1 equiv) and benzanilide (6.25 μmol , 3 equiv) were dissolved in C_6D_6 in a J. Young capped NMR tube. After 15 min at 25 $^\circ\text{C}$, no La^{NTMS} was observed in the ^1H NMR spectrum (δ 0.30 ppm), and only free $\text{HN}(\text{SiMe}_3)_2$ (δ 0.10 ppm) was present, indicating complete conversion of the precatalyst to a lanthanide tris-amidate species had occurred. Introducing additional benzanilide (0.125 mmol) and HBpin (0.625 mmol) to this *in situ* generated catalyst resulted in $\sim 90\%$ conversion of the amide to the desired amine product.

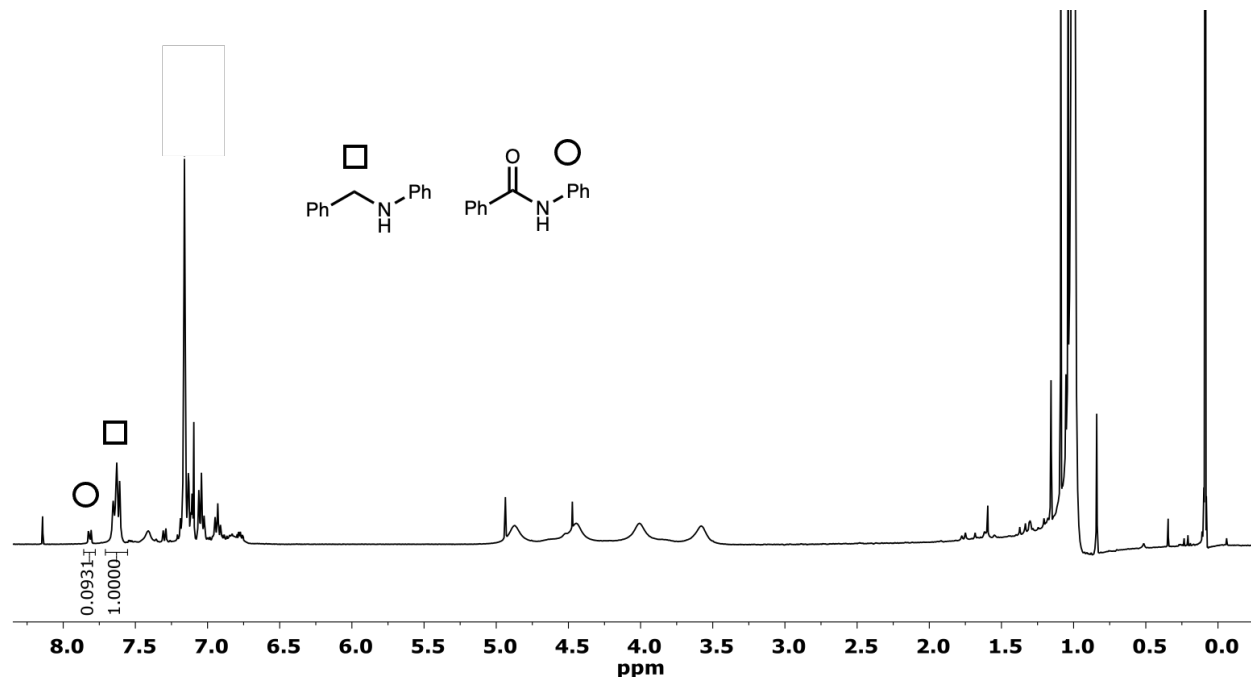


Figure 3.12 ^1H NMR (500 MHz) spectrum of the reduction of benzanilide with HBpin using an *in situ* formed lanthanum tris-amidate catalyst.

3.7.6 Stoichiometric Reactivity Studies

Catalyst activation intermediate **I_{act-1}** was obtained from a 1:1 mixture of the La^{NTMS} precatalyst and N,N -dimethylbenzamide. This intermediate was characterized using ^1H and ^{13}C

NMR spectroscopy (Figure 3.15 and 3.16). Attempts to experimentally characterize additional catalyst activation intermediates were carried out by monitoring stoichiometric mixtures of La^{NTMS} , HBpin, and *N,N*-dimethylbenzamide via ^1H and ^{11}B NMR spectroscopy. However, only the proposed off-cycle/deactivation product described in Section 3.5 is observed. When various mixtures of La^{NTMS} and HBpin are examined (0.5–6.0 equiv HBpin), the spectrum below is obtained with varying degrees of conversion of La^{NTMS} . Full conversion is observed upon reaction with 4 equiv of HBpin, which aligns well with the proposed deactivation pathway. However, additional, uncharacterized decomposition products are observed at such high HBpin concentrations, and therefore 1:3 La^{NTMS} :HBpin mixtures were studied further (Figure 3.17–3.19). A solution of La^{NTMS} , HBpin and *N,N*-dimethylbenzamide (1:3:1) yields incomplete reduction of the amide, as evidenced by the appearance of $\text{O}(\text{Bpin})_2$ and amine, but primarily the off-cycle product described below.

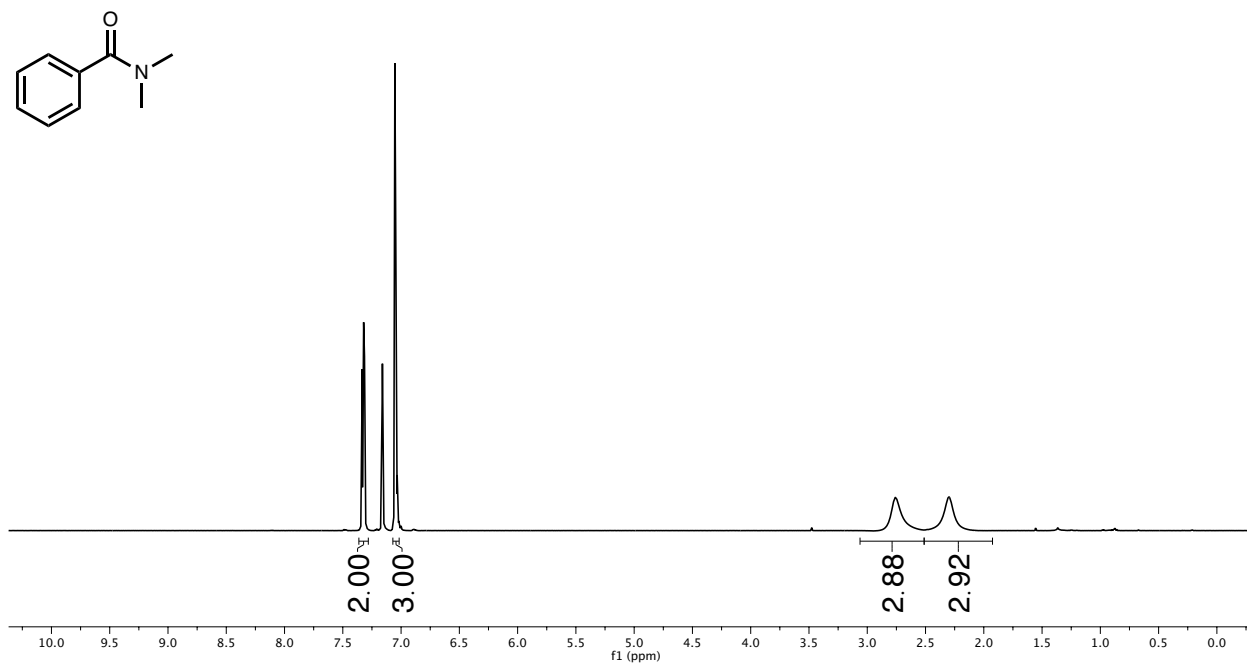


Figure 3.13 ^1H NMR (500 MHz) spectrum of *N,N*-dimethylbenzamide in C_6D_6 included for reference.

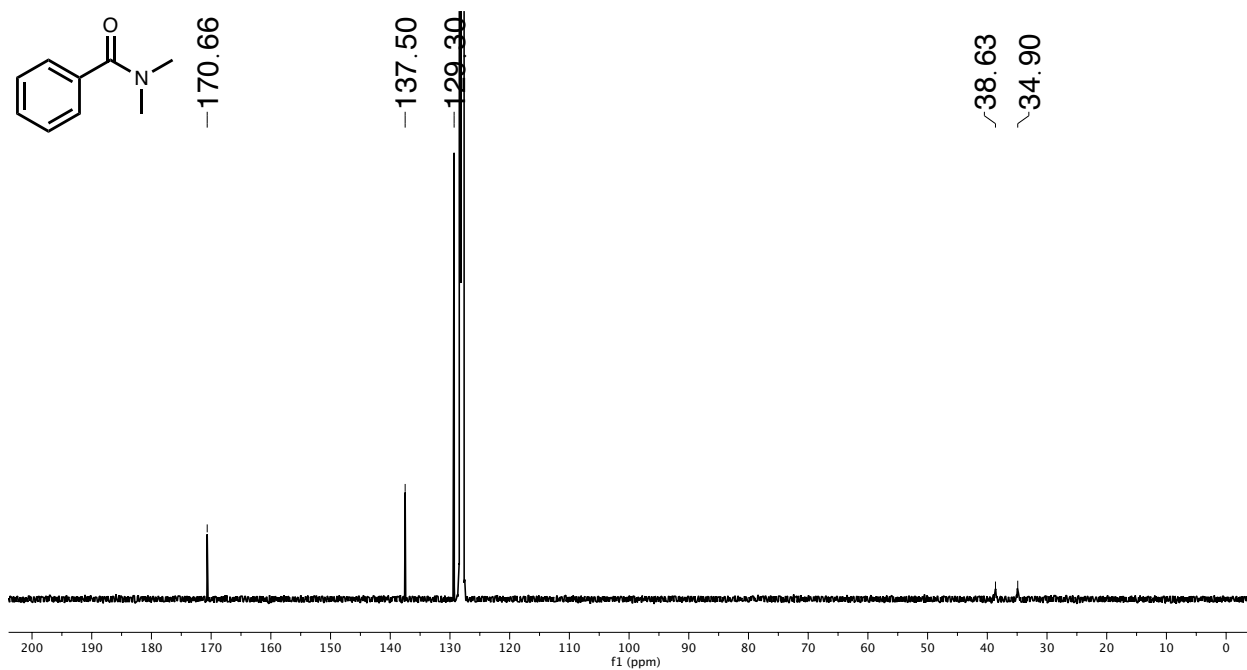


Figure 3.14 ^{13}C NMR (125 MHz) spectrum of *N,N*-dimethylbenzamide in C_6D_6 included for reference.

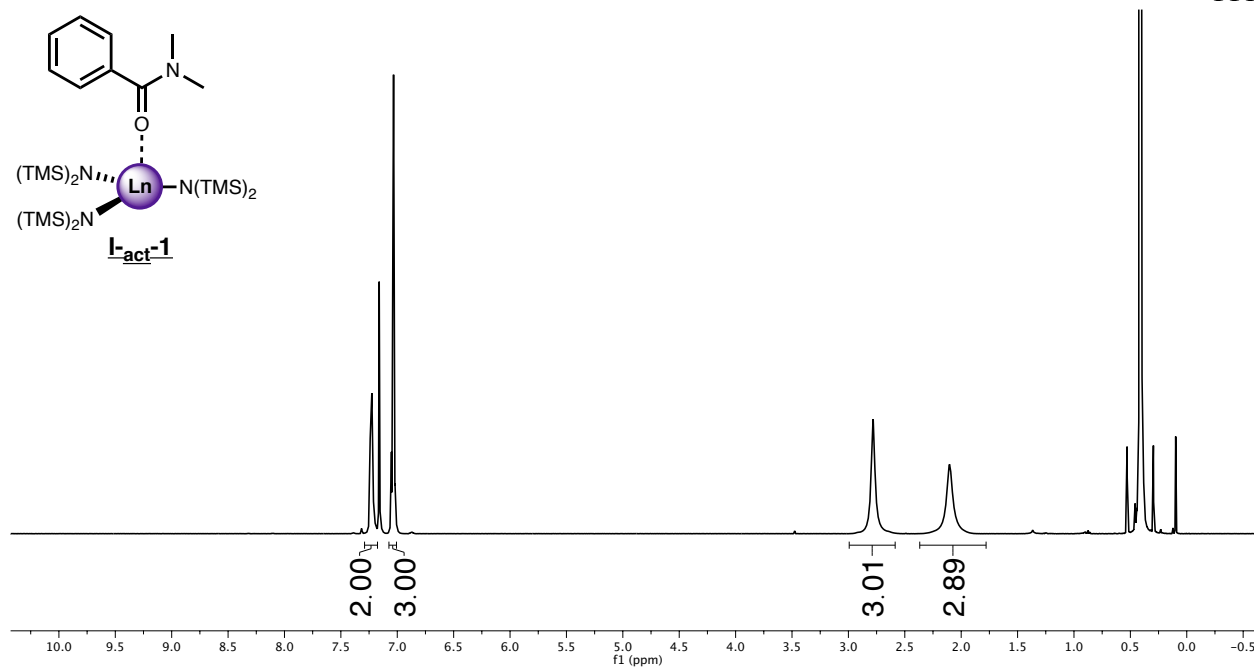


Figure 3.15 ^1H NMR (500 MHz) spectrum of the proposed catalyst activation intermediate **L_{act}-1** in C_6D_6 .

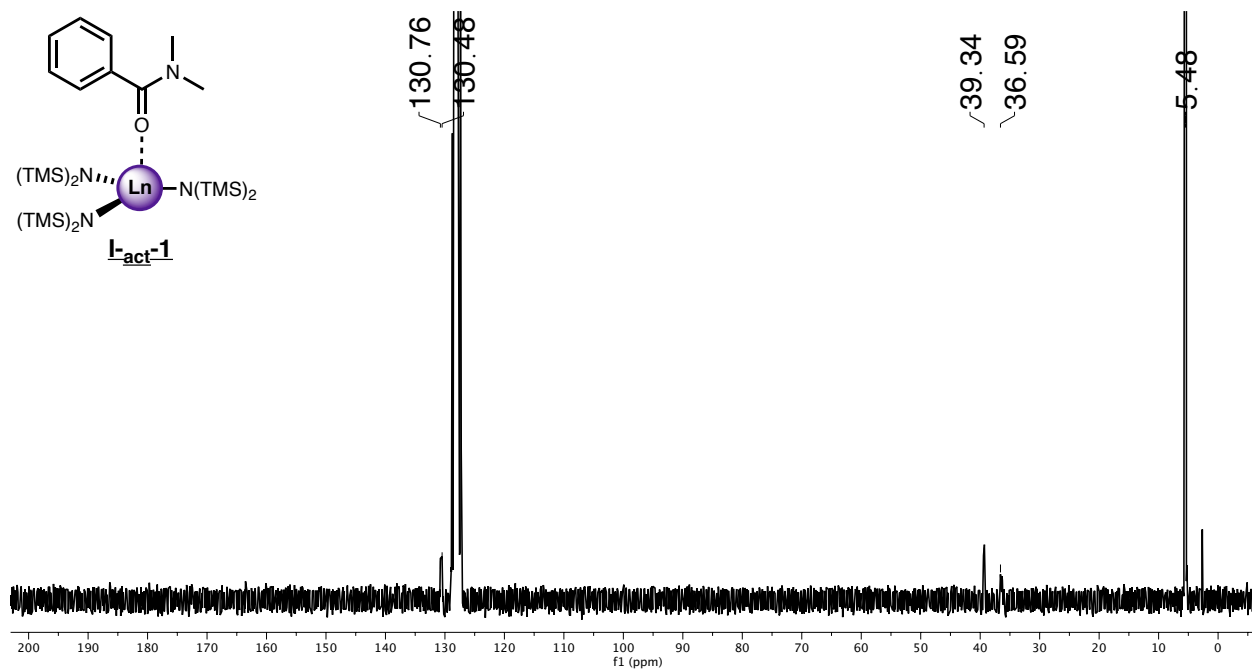


Figure 3.16 ^{13}C NMR (125 MHz) spectrum of the proposed catalyst activation intermediate **L_{act}-1** in C_6D_6 .

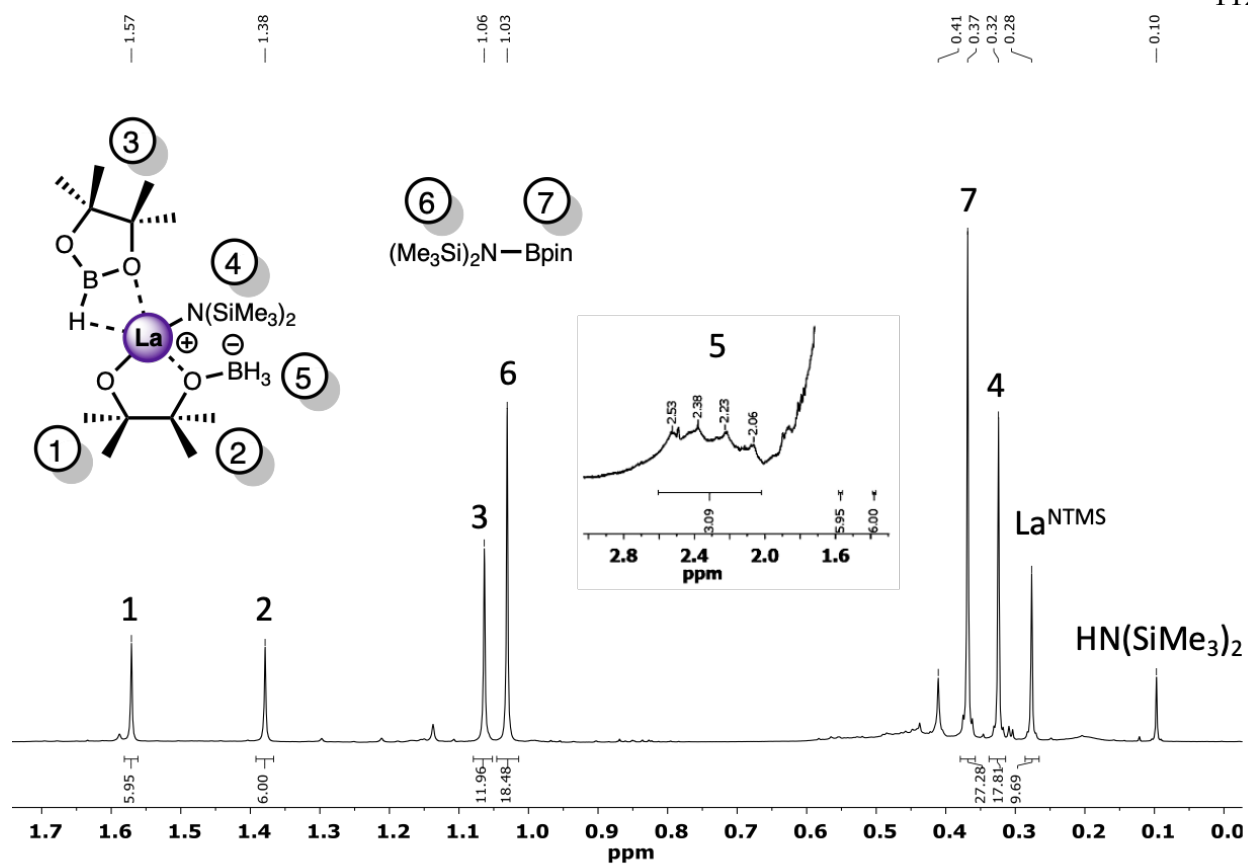


Figure 3.17 ^1H NMR (500 MHz) spectrum of the catalyst deactivation product (Figure 3.6) obtained from 1:3 mixture of La^{NTMS} and HBpin in C_6D_6 .

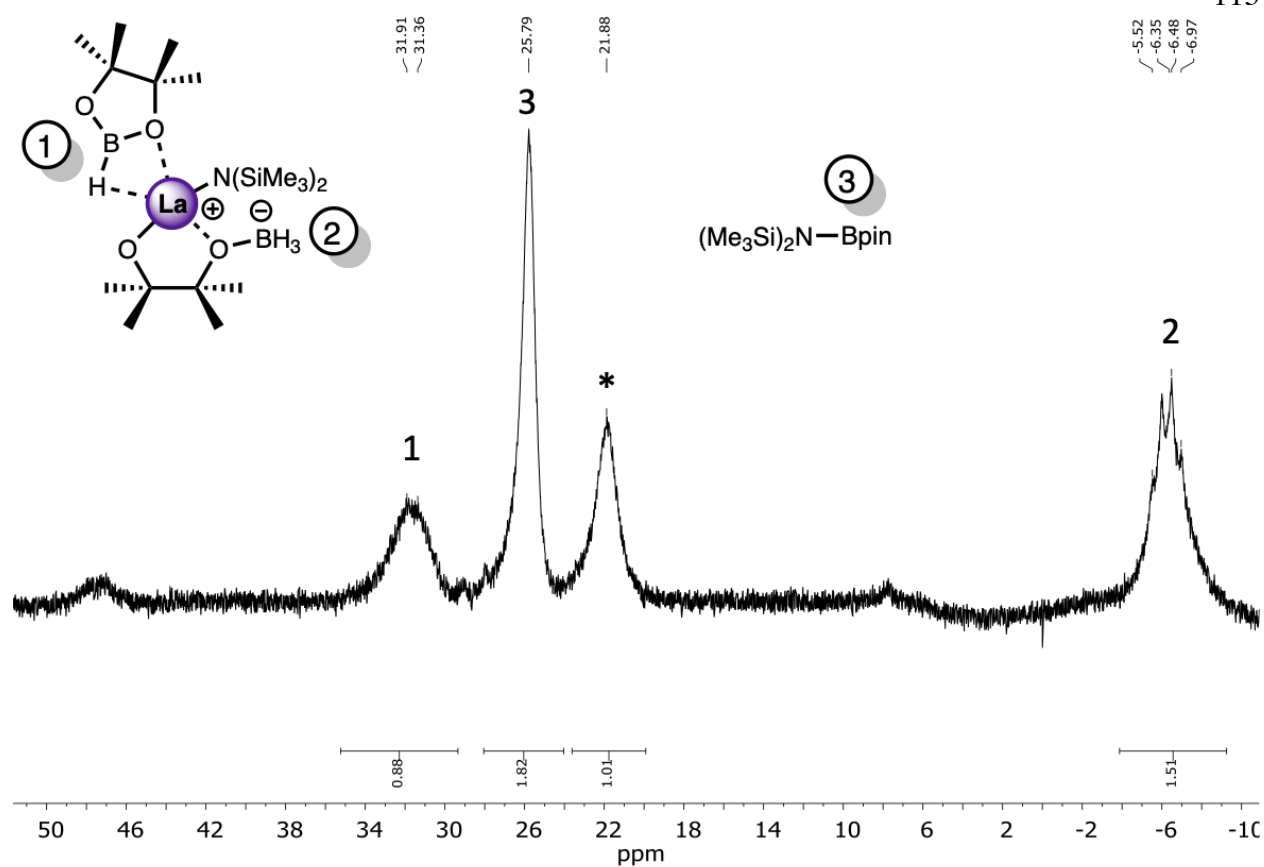


Figure 3.18 ^{11}B NMR (128 MHz) spectrum of the catalyst deactivation product (Figure 3.6) obtained from 1:3 mixture of La^{NTMS} and HBpin in C_6D_6 . * = Unidentified side product, possibly weakly and reversibly coordinated pinB-N(SiMe₃)₂ or B₂pin₃. The peak at δ 31.6 ppm is a broad doublet, likely due to coordination of the B-H to the metal center or exchange with RBH_3^- . The downfield shift is similar to previously reported coordinated boranes.²⁵⁵

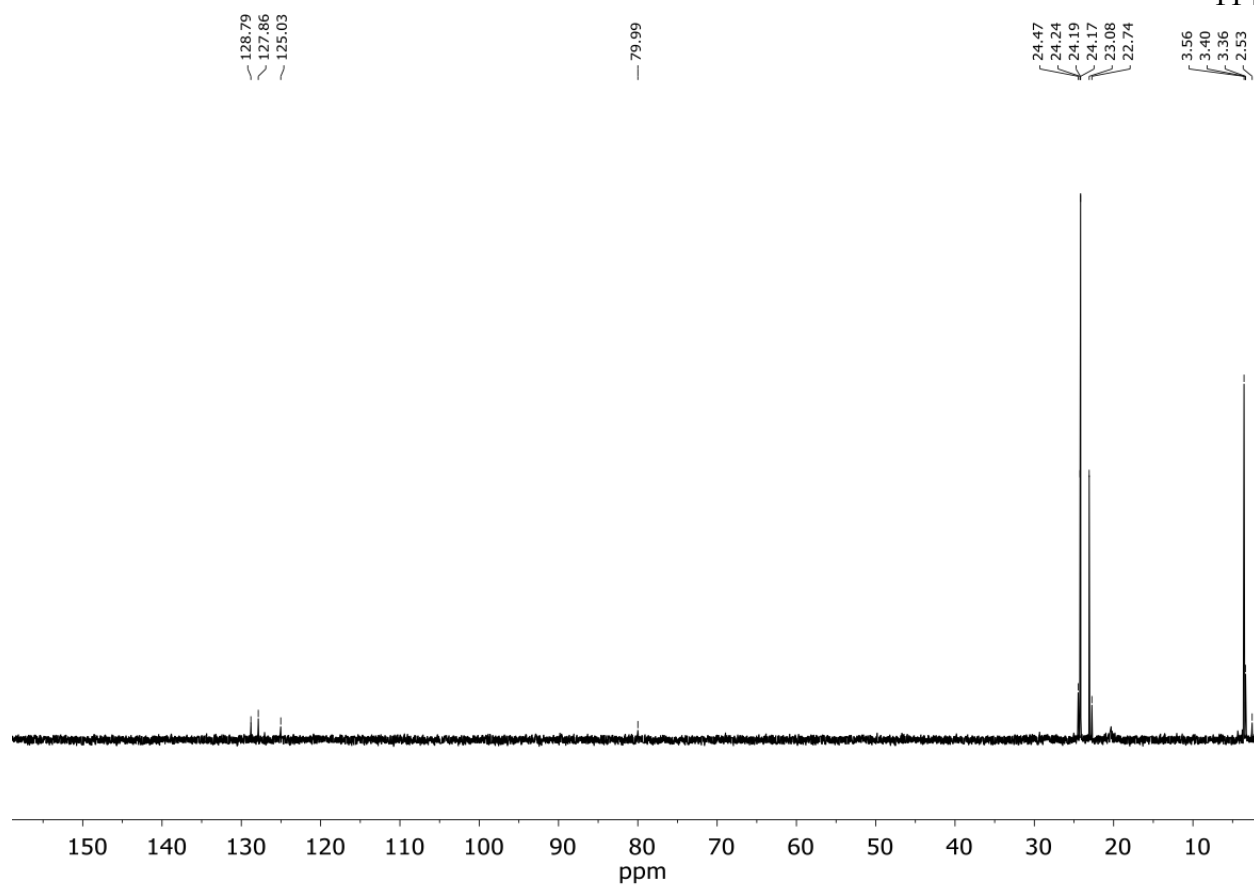


Figure 3.19 ^{13}C NMR (125 MHz) spectrum of the catalyst deactivation product (Figure 3.6) obtained from 1:3 mixture of La^{NTMS} and HBpin in C_6D_6 .

3.7.7 Computational Details

Geometry optimizations of all reactants, products, intermediates, and transition states were carried out along the entire catalytic cycle. Calculations were performed adopting the M06 hybrid meta-GGA functional. The effective core potential of Hay and Wadt,^{256, 257} (LANL2DZ) and the relative basis set were used for the La and Si atoms. The standard all-electron 6-31G** basis²⁵⁸ was used for all the remaining atoms. Molecular geometry optimization of stationary points was carried out without symmetry constraints and used analytical gradient techniques. The transition states were searched with the “distinguished reaction coordinate procedure” along the emerging bonds. *N,N*-dimethylbenzamide was adopted as substrate model. Frequency analysis was performed to obtain thermochemical information about the reaction pathways at 298 K using the harmonic approximation. The difference in translational and rotational entropy when moving from gas to solvent are accounted for by adding an energy contribution of $8RT$ to the Gibbs free energy of each species as detailed in the literature.²⁵⁹ Moreover, the effect of concentration on moving from 1 atm to 1 *M* is accounted for by adding an energy contribution of 1.89 kcal/mol ($RT\ln(P_{1M}/P_{1atm})$) to each species. All calculations were performed using the G16 code²⁶⁰ on a Linux cluster system.

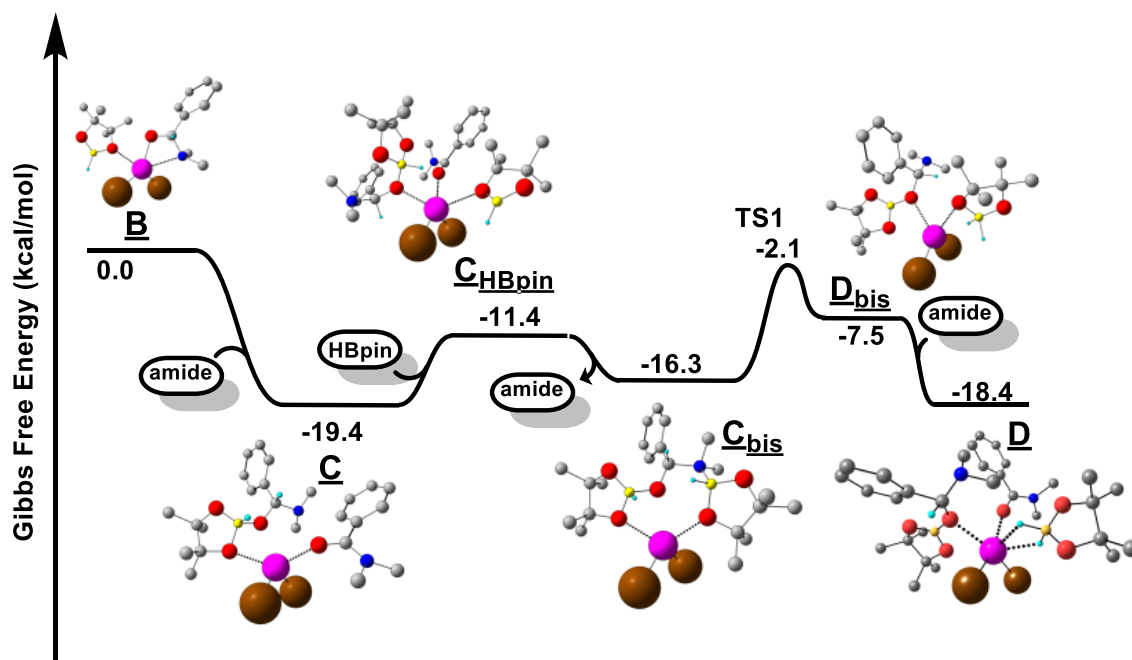


Figure 3.20 Gibbs free energy profile/catalytic cycle for the hydroboration/reduction of amides catalyzed by La^{NTMS} , and conversion of active catalyst **B** to species **D**.

3.7.8 Evaluation of the Effect of Different Basis Sets on the Accuracy of the Theoretical Model

It is well known that while 4f electrons must be considered when spectroscopic properties are being studied, it has been shown that the atomic 4f shells of the lanthanides are strongly stabilized and do not contribute significantly to the chemical bonding or reactivity.²⁶¹ For this reason, it is expected that adding a polarization function (*f* function) to the basis set used on the lanthanum atom should not have a significant effect on the calculated energetic profile corresponding to the catalytic cycle discussed in this work. Nevertheless, in order to investigate the effects of different basis sets a series of calculations on the key steps of the catalytic cycle were performed. In particular, to evaluate the first hydrogen exchange step we have applied alternative basis sets to the formation of complex **C** and **TS1**. Similarly, to evaluate the second hydrogen exchange step we have applied alternative basis sets to the formation of complex **E** and **TS2**. The data reported in Table 3.2 show the stabilization energy for the formation of complex **C**, **TS1**, complex **E** and **TS2** computed at the SCF level of theory (at zero Kelvin, without considering temperature and pressure) using different basis sets.

Table 3.2. Stabilization energy (kcal/mol) obtained using different basis sets computed at the SCF level of theory.

	LANL2DZ ^a	LAN2DZ + pol ^b	Def2-SVP ^c
C	-32.2	-32.0	-32.7
TS1	-11.0	-11.0	-13.6
E	-72.4	-72.4	-73.9
TS2	-61.1	-62.2	-62.6

^aECP and basis set applied to the lanthanum atom in the present work. ^bGeometry optimization using a polarization function (*f* function) added only to the basis set of the lanthanum atom.²³² ^cGeometry optimization using the Def2-SVP basis set reported by Ahlrich and coworkers on all atoms.²³³

It is evident that adding the polarization function to the LANL2DZ basis set (see Table 3.2, LANL2DZ + pol) produces negligible changes in the stabilization energies of complex **C**, **TS1** as well as complex **E**. Only **TS2** becomes slightly more stabilized, experiencing a decrease in energy by approximately 1 kcal/mol. Additionally, upon using a full electron basis set plus polarization for all atoms (see Table 3.2, Def2-SVP) we obtain a slightly greater stabilization for all intermediates and transition states shown above. Ultimately, these additional calculations suggest that adding the polarization function to the lanthanum atom does not significantly modify the stabilization energies along the catalytic cycle and it does not produce any significant improvement in the accuracy of the calculations.

3.7.9 DFT Examination of Primary Amide Hydroboration/Reduction

DFT calculations were performed to assess the feasibility of a ligand insertion reaction between the La^{NTMS} precatalyst and the primary amide benzamide (i.e., $\text{La-N}(\text{SiMe}_3)_2$ insertion into the amide $\text{C}=\text{O}$ bond) (Figure 3.21). The insertion of the La-silylamide group ($-\text{N}(\text{SiMe}_3)_2$) into the primary amide $\text{C}=\text{O}$ bond and subsequent silyl migration to yield a La-siloxide complex was modeled. First, the approach of the primary amide produces a stabilization of 17.4 kcal/mol due to an interaction between the carbonyl group of the amide and the La metal center. However, the insertion of the La-silylamide ($\text{La-N}(\text{SiMe}_3)_2$) into the primary amide $\text{C}=\text{O}$ bond is very endoergonic (+22.8 kcal/mol) with an energy barrier of +32.6 kcal/mol. Finally, the silyl migration and formation of a La-siloxide complex is exoergonic (-0.6 kcal/mol with an energy barrier of +21.2 kcal/mol). Thus, the overall reaction is slightly endoergonic (+4.8 kcal/mol) with an energy barrier of +44.0 kcal/mol.

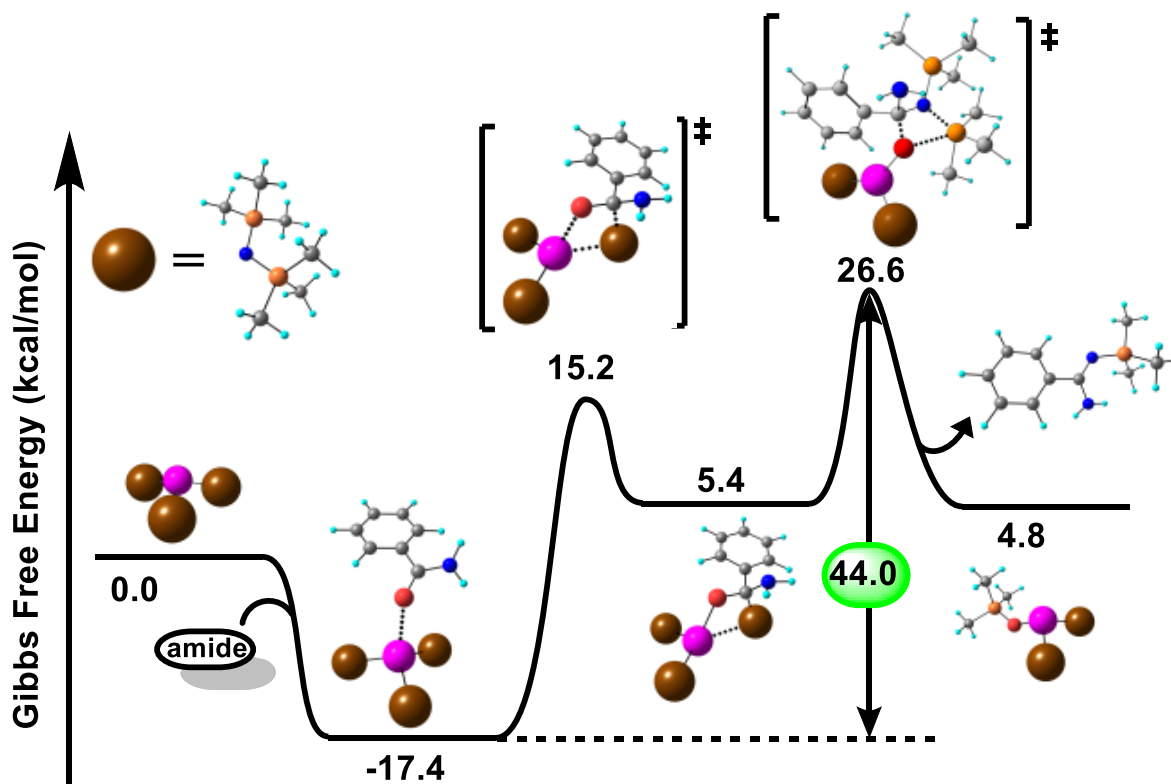


Figure 3.21 Gibbs free energy profile for a La-silylamide group (La-N(SiMe₃)₂) insertion of the La^{NTMS} precatalyst into the benzamide C=O bond and subsequent silyl migration to yield a La-siloxide complex.

3.7.10 DFT Examination of Catalyst Decomposition Pathway

DFT calculations were performed to better understand the decomposition path of the La^{NTMS} precatalyst induced by HBpin (Figure 3.22). The decomposition path involves four main steps. The coordination of the first HBpin leads to the formation of the pinBH-N(SiMe₃)₂⁻ borate species (**I_{deact-1}**, -7.0 kcal/mol). The second step is promoted by the approach of a second HBpin leading to hydride transfer from the pinBH-N(SiMe₃)₂⁻ species to the coordinated HBpin, producing a new H₂Bpin⁻ species and releasing pinB-N(SiMe₃)₂. This intermediate is stabilized by the coordination of a third HBpin (**I_{deact-2}**, -28.5 kcal/mol). The third step is analogous to the first one involving the formation of a new pinBH-N(SiMe₃)₂⁻ borate species (**I_{deact-3}**, -29.4

kcal/mol). The last step involves the ring-opening of the H_2Bpin^- species and the subsequent hydride transfer from $\text{pinBH-N}(\text{SiMe}_3)_2^-$ to the opened H_2Bpin^- , leading to the final product. A second $\text{pinB-N}(\text{SiMe}_3)_2$ molecule is released and a new HBpin coordinates and stabilizes the final product (-34.5 kcal/mol). This last step is the rate determining step with a Gibbs free energy barrier of 14.9 kcal/mol.

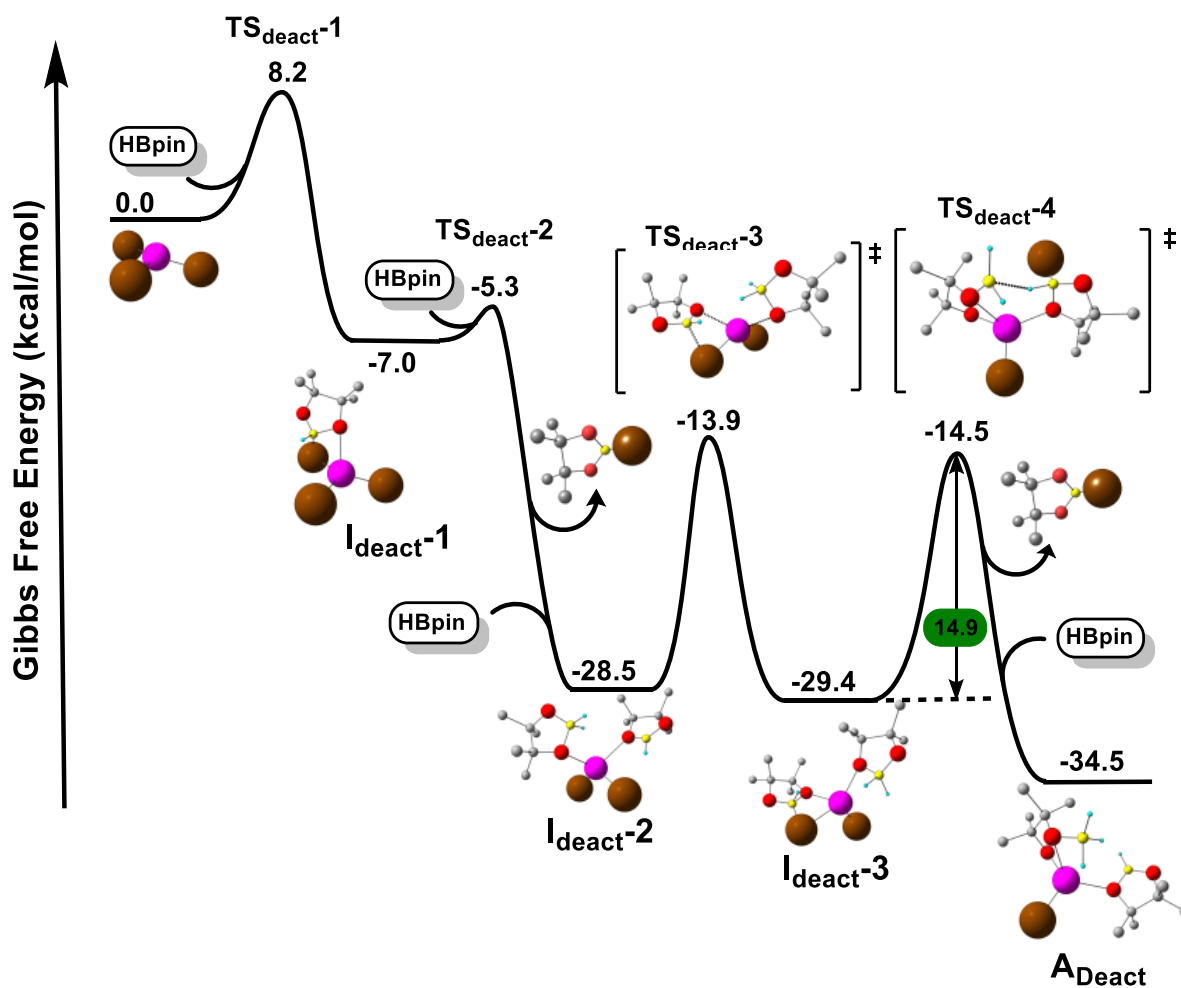


Figure 3.22 DFT-computed Gibbs free energy profile associated with the decomposition pathway of La^{NTMS} pre-catalyst induced by HBpin .

Chapter 4

Thesis Overview.

Portions of this chapter appear in the following publications:

Rachel D. Dicken, Alessandro Motta, and Tobin J. Marks, Homoleptic Lanthanide Amide Catalysts for Organic Synthesis: Experiment and Theory. *ACS Catal.* **2021**, *11* (5), 2715-2734.

4. Chapter 4

4.1 Overview and Outlook

As discussed in Chapter 1, though precious metal catalysis has allowed for tremendous advances in modern organic synthesis, there are also a number of disadvantages associated with their continued use in catalytic processes, including high cost and environmental impact, and uncertainty regarding their future availability. While the use of more abundant metals is clearly advantageous in many respects, the overall reactivity and selectivity of non-precious metals is often markedly different and therefore, they cannot act as direct substitutes for many of the catalytic processes currently dominated by the precious metals. However, considering the limitations associated with the use of precious metals, the development of more sustainable catalysts based on earth-abundant metals has gained increasing attention.

In Chapter 2, we outlined the development of an efficient and scalable catalytic asymmetric conjugate addition of primary and secondary amines to maleimides using a calcium(II)-phosphate catalyst. To our surprise, x-ray crystallographic studies of the pre-formed calcium phosphate complex indicate the formation of a $\text{Ca}_2[\mathbf{B}]_4 \cdot (\text{H}_2\text{O})_{10}$ species as opposed to the $\text{Ca}[\mathbf{B}]_2$ complex expected from the reaction of chiral phosphoric acid and calcium methoxide. Based on further spectroscopic studies, we hypothesize that the initial $\text{Ca}_2[\mathbf{B}]_4 \cdot (\text{H}_2\text{O})_{10}$ complex acts as a precatalyst which is activated via dehydration in the presence of 4 Å MS. Reorganization of this initial complex to form a more active $\text{Ca}[\mathbf{B}]_2$ complex then allows for coordination of the amine nucleophile to the Lewis acidic calcium center and subsequent nucleophilic attack on the maleimide, yielding medicinally relevant chiral aminosuccinimide products in high yields and enantioselectivities. Investigation into the exact mechanism of substrate activation via this system represents an interesting opportunity for further study.

In Chapter 3, we disclosed the $\text{La}[\text{N}(\text{TMS})_2]_3$ -catalyzed deoxygenative reduction of tertiary and secondary amides with pinacolborane (HBpin). It was found that this system is completely selective for amide reduction over a number of reducible functional groups (i.e., $\text{C}=\text{C}$, $\text{C}\equiv\text{C}$, NO_2 , etc.), yielding exclusively “higher amine” products in excellent yields. Kinetic studies indicate that amide reduction operates according to an unusual mixed-order rate law which is proposed to originate from HBpin induced saturation of the catalyst complex. Additionally, a combined experimental/theoretical analysis of the mechanism of this reaction reveals an unusual catalytic cycle involving ligand-centered hydride transfer. This represents the first time a lanthanide catalyst has been employed for the pinacolborane-based reduction of amides, and it is the first attempt at a computationally aided analysis of the mechanism of amide hydroboration. Further studies towards the application of this work to other $\text{C}=\text{X}$ bonds (X = heteroatom) are ongoing.

REFERENCES

1. Berzelius, J. J., *Jahresbericht über die Fortschritte der physischen Wissenschaften* **1836**, *15*, 237-245.
2. *Technology Vision 2020: The U.S. Chemical Industry*; American Chemical Society Department of Government Relations and Science Policy: Washington, DC, 1996.
3. Grand View Research, *Catalyst Market Size & Share, Industry Report, 2020-2027*; 2020. <https://www.grandviewresearch.com/industry-analysis/catalyst-market> (accessed 2021-06-23)
4. Busacca, C. A.; Fandrick, D. R.; Song, J. J.; Senanayake, C. H., The Growing Impact of Catalysis in the Pharmaceutical Industry. *Adv. Synth. Catal.* **2011**, *353* (11-12), 1825-1864.
5. *CRC Handbook of Chemistry and Physics*. 97 ed.; CRC Press: Boca Raton, FL, 2016.
6. Nuss, P.; Eckelman, M. J., Life Cycle Assessment of Metals: A Scientific Synthesis. *PLoS One* **2014**, *9* (7), e101298.
7. Palladium Price. <https://markets.businessinsider.com/commodities/palladium-price> (accessed 2021-06-23).
8. United States Geological Survey, *Mineral Commodity Summaries, Platinum-Group Metals*. 2021.
9. Rare earth elements - prices. <https://en.institut-seltene-erden.de/our-service-2/Metal-prices/rare-earth-prices/> (accessed 2021-06-23).
10. Hunt, A. J.; Farmer, T. J.; Clark, J. H., CHAPTER 1 Elemental Sustainability and the Importance of Scarce Element Recovery. In *Element Recovery and Sustainability*, The Royal Society of Chemistry: 2013; pp 1-28.
11. Amin, S. B.; Marks, T. J., Versatile Pathways for In Situ Polyolefin Functionalization with Heteroatoms: Catalytic Chain Transfer. *Angew. Chem. Int. Ed.* **2008**, *47* (11), 2006-2025.
12. Amin, S. B.; Seo, S.; Marks, T. J., Organo- Ir^{III} , d^0 -Mediated Synthesis of Amine-Capped Polyethylenes. Scope and Mechanism. *Organometallics* **2008**, *27* (11), 2411-2420.

13. Edelman, F. T., Lanthanide amidinates and guanidates in catalysis and materials science: a continuing success story. *Chem. Soc. Rev.* **2012**, *41* (23), 7657-7672.
14. Haxel, G. B.; Hedrick, J. B.; Orris, G. J.; Stauffer, P. H.; Hendley, J. W. *Rare earth elements: critical resources for high technology*; 087-02; 2002.
15. Tse, P.-K. *China's rare-earth industry*; 2011-1042; 2011.
16. Kostelnik, T. I.; Orvig, C., Radioactive Main Group and Rare Earth Metals for Imaging and Therapy. *Chem. Rev.* **2019**, *119* (2), 902-956.
17. Yi, Z.; Luo, Z.; Qin, X.; Chen, Q.; Liu, X., Lanthanide-Activated Nanoparticles: A Toolbox for Bioimaging, Therapeutics, and Neuromodulation. *Acc. Chem. Res.* **2020**.
18. Zhou, J.; Leño Jr., J. L.; Liu, Z.; Jin, D.; Wong, K.-L.; Liu, R.-S.; Bünzli, J.-C. G., Impact of Lanthanide Nanomaterials on Photonic Devices and Smart Applications. *Small* **2018**, *14* (40), 1801882.
19. Edelman, F. T.; Farnaby, J. H.; Jaroschik, F.; Wilson, B., Lanthanides and actinides: Annual survey of their organometallic chemistry covering the year 2018. *Coord. Chem. Rev.* **2019**, *398*, 113005.
20. Liu, H.; Eisen, M. S., Organo-f-Complexes for Efficient and Selective Hydroborations. *Synthesis* **2020**, *52* (5), 629-644.
21. Trifonov, A. A.; Basalov, I. V.; Kissel, A. A., Use of organolanthanides in the catalytic intermolecular hydrophosphination and hydroamination of multiple C–C bonds. *Dalton Trans.* **2016**, *45* (48), 19172-19193.
22. Weiss, C. J.; Marks, T. J., Organo-f-element catalysts for efficient and highly selective hydroalkoxylation and hydrothiolation. *Dalton Trans.* **2010**, *39* (29), 6576-6588.
23. Cotton, S., *Lanthanide and Actinide Chemistry*. John Wiley & Sons, Ltd: Uppingham, Rutland, UK, 2006.
24. Aspinall, H. C., *Chemistry of the f-Block Elements*. Taylor & Francis: Washington, 2001.
25. Friedman, H. G.; Choppin, G. R.; Feuerbacher, D. G., The shapes of the f orbitals. *J. Chem. Educ.* **1964**, *41* (7), 354.
26. Waterman, R., σ -Bond Metathesis: A 30-Year Retrospective. *Organometallics* **2013**, *32* (24), 7249-7263.

27. Yan, D.; Dai, P.; Chen, S.; Xue, M.; Yao, Y.; Shen, Q.; Bao, X., Highly efficient hydroboration of carbonyl compounds catalyzed by tris(methylcyclopentadienyl)lanthanide complexes. *Org. Biomol. Chem.* **2018**, *16* (15), 2787-2791.
28. Zhu, Z.; Dai, P.; Wu, Z.; Xue, M.; Yao, Y.; Shen, Q.; Bao, X., Lanthanide aryloxides catalyzed hydroboration of aldehydes and ketones. *Catal. Commun.* **2018**, *112*, 26-30.
29. Altenbuchner, P. T.; Kronast, A.; Kissling, S.; Vagin, S. I.; Herdtweck, E.; Pöthig, A.; Deglmann, P.; Loos, R.; Rieger, B., Mechanistic Investigations of the Stereoselective Rare Earth Metal-Mediated Ring-Opening Polymerization of β -Butyrolactone. *Chem. Eur. J.* **2015**, *21* (39), 13609-13617.
30. Jenter, J.; Roesky, P. W.; Ajellal, N.; Guillaume, S. M.; Susperregui, N.; Maron, L., Bis(phosphinimino)methanide borohydride complexes of the rare-earth elements as initiators for the ring-opening polymerization of ϵ -caprolactone: combined experimental and computational investigations. *Chem. Eur. J.* **2010**, *16* (15), 4629-4638.
31. Assary, R. S.; Atesin, A. C.; Li, Z.; Curtiss, L. A.; Marks, T. J., Reaction pathways and energetics of etheric C-O bond cleavage catalyzed by lanthanide triflates. *ACS Catal.* **2013**, *3* (9), 1908-1914.
32. Del Rosal, I.; Yahia, A.; Maron, L., Effects of the Grafting of Lanthanum Complexes on a Silica Surface on the Reactivity: Influence on Ethylene, Propylene, and 1,3-Butadiene Homopolymerization. *Inorg. Chem.* **2016**, *55* (20), 10024-10033.
33. Barros, N.; Eisenstein, O.; Maron, L., Catalytic hydrosilylation of olefins with organolanthanides: A DFT study. Part I: Hydrosilylation of propene by SiH₄. *Dalton Trans.* **2010**, *39* (44), 10749-10756.
34. Motta, A.; Lanza, G.; Fragalà, I. L.; Marks, T. J., Energetics and Mechanism of Organolanthanide-Mediated Aminoalkene Hydroamination/Cyclization. A Density Functional Theory Analysis. *Organometallics* **2004**, *23* (17), 4097-4104.
35. Tobisch, S., Organolanthanide-mediated intramolecular hydroamination/cyclization of conjugated aminodienes: A computational exploration of diverse mechanistic pathways for the regioselective generation of functionalized azacycles supported by a lanthanocene-based catalyst complex. *J. Am. Chem. Soc.* **2005**, *127* (34), 11979-11988.
36. Tobisch, S., Mechanistic Exploration of the Intramolecular Hydroalkoxylation of Allenyl Alcohols Mediated by Organolanthanide Complexes: A DFT Study. *Chem. Eur. J.* **2010**, *16* (17), 4995-4998.

37. Shannon, R. D., Revised effective ionic radii and systematic studies of interatomic distances in halides and chalcogenides. *Acta Cryst. A* **1976**, *32* (5), 751-767.
38. Alyea, E. C.; Bradley, D. C.; Copperthwaite, R. G., Three-co-ordinated transition metal compounds. Part I. The preparation and characterization of tris(bis(trimethylsilylamido)-derivatives of scandium, titanium, vanadium, chromium, and iron. *Journal of the Chemical Society, Dalton Trans.* **1972**, (14), 1580-1584.
39. Bradley, D. C.; Ghotra, J. S.; Hart, F. A., Three-co-ordination in lanthanide chemistry: tris[bis(trimethylsilyl)amido]lanthanide(III) compounds. *J. Chem. Soc., Chem. Commun.* **1972**, (6), 349-350.
40. Bradley, D. C.; Ghotra, J. S.; Hart, F. A., Low co-ordination numbers in lanthanide and actinide compounds. Part I. The preparation and characterization of tris{bis(trimethylsilyl)-amido}lanthanides. *J. Chem. Soc., Dalton Trans.* **1973**, (10), 1021-1023.
41. Bradley, D. C.; Ghotra, J. S.; Hart, F. A.; Hursthouse, M. B.; Raithby, P. R., Low co-ordination numbers in lanthanoid and actinoid compounds. Part 2. Syntheses, properties, and crystal and molecular structures of triphenylphosphine oxide and peroxy-derivatives of [bis(trimethylsilyl)-amido]lanthanoids. *J. Chem. Soc., Dalton Trans.* **1977**, (12), 1166-1172.
42. Anwander, R., Lanthanide amides. In *Organolanthanoid Chemistry: Synthesis, Structure, Catalysis*, Springer: Berlin, Heidelberg, 1996; Vol. 179, pp 33-112.
43. Lappert, M.; Protchenko, A.; Power, P.; Seeber, A., Amides of the Group 3 and Lanthanide Metals. In *Metal Amide Chemistry*, John Wiley & Sons, Ltd.: 2009; pp 79-120.
44. Nagae, H.; Shibata, Y.; Tsurugi, H.; Mashima, K., Aminomethylation Reaction of ortho-Pyridyl C-H Bonds Catalyzed by Group 3 Metal Triamido Complexes. *J. Am. Chem. Soc.* **2015**, *137* (2), 640-643.
45. Ye, P.; Shao, Y.; Zhang, F.; Zou, J.; Ye, X.; Chen, J., Rare-Earth-Metal-Catalyzed Synthesis of Azaindoles and Naphthyridines via C-H Cyclization of Functionalized Pyridines. *Adv. Synth. Catal.* **2020**, *362* (4), 851-857.
46. Komeyama, K.; Sasayama, D.; Kawabata, T.; Takehira, K.; Takaki, K., Rare-Earth Silylamide-Catalyzed Monocoupling Reaction of Isocyanides with Terminal Alkynes. *J. Org. Chem.* **2005**, *70* (26), 10679-10687.

47. Komeyama, K.; Sasayama, D.; Kawabata, T.; Takehira, K.; Takaki, K., Direct mono-insertion of isocyanides into terminal alkynes catalyzed by rare-earth silylamides. *Chem. Commun.* **2005**, (5), 634-636.
48. Shao, Y.; Zhang, F.; Zhang, J.; Zhou, X., Lanthanide-Catalyzed Reversible Alkynyl Exchange by Carbon–Carbon Single-Bond Cleavage Assisted by a Secondary Amino Group. *Angew. Chem. Int. Ed.* **2016**, 55 (38), 11485-11489.
49. Shen, Q.; Huang, W.; Wang, J.; Zhou, X., Ln[N(SiMe₃)₂]₃/RNH₂ Catalyzed Monoaddition of Terminal Alkynes to Nitriles: A Novel and Concise Access to the Synthesis of Ynones. *Organometallics* **2008**, 27 (2), 301-303.
50. Ye, P.; Shao, Y.; Xie, L.; Shen, K.; Cheng, T.; Chen, J., Lanthanide-Catalyzed Tandem Insertion of Secondary Amines with 2-Alkynylbenzonnitriles: Synthesis of Aminoisoindoles. *Asian J. Chem.* **2018**, 13 (23), 3681-3690.
51. Bürgstein, M. R.; Berberich, H.; Roesky, P. W., Homoleptic Lanthanide Amides as Homogeneous Catalysts for Alkyne Hydroamination and the Tishchenko Reaction. *Chem. Eur. J.* **2001**, 7 (14), 3078-3085.
52. Horino, Y.; Livinghouse, T., Alkene and Diene Hydrosilylations Catalyzed by Lanthanum Tris[bis(trimethylsilyl)amide]. *Organometallics* **2004**, 23 (1), 12-14.
53. Kawaoka, A. M.; Douglass, M. R.; Marks, T. J., Homoleptic Lanthanide Alkyl and Amide Precatalysts Efficiently Mediate Intramolecular Hydrophosphination/Cyclization. Observations on Scope and Mechanism. *Organometallics* **2003**, 22 (23), 4630-4632.
54. Kim, Y. K.; Livinghouse, T.; Bercaw, J. E., Intramolecular alkene hydroaminations catalyzed by simple amido derivatives of the Group 3 metals. *Tetrahedron Lett.* **2001**, 42 (16), 2933-2935.
55. Komeyama, K.; Kawabata, T.; Takehira, K.; Takaki, K., Rare-Earth Silylamide-Catalyzed Selective Dimerization of Terminal Alkynes and Subsequent Hydrophosphination in One Pot. *J. Org. Chem.* **2005**, 70 (18), 7260-7266.
56. Seo, S.; Marks, T. J., Lanthanide-Catalyst-Mediated Tandem Double Intramolecular Hydroalkoxylation/Cyclization of Dialkynyl Dialcohols: Scope and Mechanism. *Chem. Eur. J.* **2010**, 16 (17), 5148-5162.
57. Seo, S.; Yu, X.; Marks, T. J., Intramolecular Hydroalkoxylation/Cyclization of Alkynyl Alcohols Mediated by Lanthanide Catalysts. Scope and Reaction Mechanism. *J. Am. Chem. Soc.* **2009**, 131 (1), 263-276.

58. Yu, X.; Seo, S.; Marks, T. J., Effective, Selective Hydroalkoxylation/Cyclization of Alkynyl and Allenyl Alcohols Mediated by Lanthanide Catalysts. *J. Am. Chem. Soc.* **2007**, *129* (23), 7244-7245.
59. Barger, C. J.; Dicken, R. D.; Weidner, V. L.; Motta, A.; Lohr, T. L.; Marks, T. J., La[N(SiMe₃)₂]₃-Catalyzed Deoxygenative Reduction of Amides with Pinacolborane. Scope and Mechanism. *J. Am. Chem. Soc.* **2020**.
60. Barger, C. J.; Motta, A.; Weidner, V. L.; Lohr, T. L.; Marks, T. J., La[N(SiMe₃)₂]₃-Catalyzed Ester Reductions with Pinacolborane: Scope and Mechanism of Ester Cleavage. *ACS Catal.* **2019**, *9* (10), 9015-9024.
61. Horino, Y.; Livinghouse, T.; Stan, M., Alkene-Pinacolborane Hydroborations Catalyzed by Lanthanum Tris[bis(trimethylsilyl)amide]. *Synlett* **2004**, *2004* (14), 2639-2641.
62. Weidner, V. L.; Barger, C. J.; Delferro, M.; Lohr, T. L.; Marks, T. J., Rapid, Mild, and Selective Ketone and Aldehyde Hydroboration/Reduction Mediated by a Simple Lanthanide Catalyst. *ACS Catal.* **2017**, *7* (2), 1244-1247.
63. Xu, X.; Kang, Z.; Yan, D.; Xue, M., La[N(SiMe₃)₂]₃-Catalyzed Hydroboration of Esters and Other Challenging Unsaturated Groups. *Chin. J. Chem.* **2019**, *37* (11), 1142-1146.
64. Ye, P.; Shao, Y.; Ye, X.; Zhang, F.; Li, R.; Sun, J.; Xu, B.; Chen, J., Homoleptic Bis(trimethylsilyl)amides of Yttrium Complexes Catalyzed Hydroboration Reduction of Amides to Amines. *Org. Lett.* **2020**, *22* (4), 1306-1310.
65. Allred, A. L., Electronegativity values from thermochemical data. *J. Inorg. Nuc. Chem.* **1961**, *17* (3), 215-221.
66. Lambert, C.; von Ragué Schleyer, P., Are Polar Organometallic Compounds "Carbanions"? The Gegenion Effect on Structure and Energies of Alkali-Metal Compounds. *Angew. Chem. Int. Ed.* **1994**, *33* (11), 1129-1140.
67. Harder, S., From Limestone to Catalysis: Application of Calcium Compounds as Homogeneous Catalysts. *Chem. Rev.* **2010**, *110* (7), 3852-3876.
68. Hill, M. S.; Liptrot, D. J.; Weetman, C., Alkaline earths as main group reagents in molecular catalysis. *Chem. Soc. Rev.* **2016**, *45* (4), 972-988.
69. Harder, S., *Alkaline-Earth Metal Compounds*. 1 ed.; Springer: Berlin, Heidelberg, 2013.

70. Westerhausen, M.; Koch, A.; Görls, H.; Krieck, S., Heavy Grignard Reagents: Synthesis, Physical and Structural Properties, Chemical Behavior, and Reactivity. *Chem. Eur. J.* **2017**, *23* (7), 1456-1483.
71. Ajellal, N.; Carpentier, J.-F.; Guillaume, C.; Guillaume, S. M.; Helou, M.; Poirier, V.; Sarazin, Y.; Trifonov, A., Metal-catalyzed immortal ring-opening polymerization of lactones, lactides and cyclic carbonates. *Dalton Trans.* **2010**, *39* (36), 8363-8376.
72. Chisholm, M. H.; Gallucci, J. C.; Phomphrai, K., Well-Defined Calcium Initiators for Lactide Polymerization. *Inorg. Chem.* **2004**, *43* (21), 6717-6725.
73. Harder, S.; Feil, F.; Knoll, K., Novel Calcium Half-Sandwich Complexes for the Living and Stereoselective Polymerization of Styrene. *Angew. Chem. Int. Ed.* **2001**, *40* (22), 4261-4264.
74. Koby, R. F.; Doerr, A. M.; Rightmire, N. R.; Schley, N. D.; Brennessel, W. W.; Long, B. K.; Hanusa, T. P., Mechanochemical Formation, Solution Rearrangements, and Catalytic Behavior of a Polymorphic Ca/K Allyl Complex. *Chem. Eur. J.* **2021**, *27* (31), 8195-8202.
75. Liu, N.; Liu, D.; Liu, B.; Zhang, H.; Cui, D., Stereoselective polymerization of rac-lactide catalyzed by zwitterionic calcium complexes. *Polym. Chem.* **2021**, *12* (10), 1518-1525.
76. Barrett, A. G. M.; Crimmin, M. R.; Hill, M. S.; Procopiou, P. A., Heterofunctionalization catalysis with organometallic complexes of calcium, strontium and barium. *Proc. Math. Phys. Eng. Sci.* **2010**, *466* (2116), 927-963.
77. Nixon, T. D.; Ward, B. D., Calcium amido-bisoxazoline complexes in asymmetric hydroamination/cyclisation catalysis. *Chem. Commun.* **2012**, *48* (96), 11790-11792.
78. Qi, C.; Hasenmaile, F.; Gandon, V.; Lebœuf, D., Calcium(II)-Catalyzed Intra- and Intermolecular Hydroamidation of Unactivated Alkenes in Hexafluoroisopropanol. *ACS Catal.* **2018**, *8* (3), 1734-1739.
79. Stegner, P. C.; Eyselein, J.; Ballmann, G. M.; Langer, J.; Schmidt, J.; Harder, S., Calcium catalyzed enantioselective intramolecular alkene hydroamination with chiral C2-symmetric bis-amide ligands. *Dalton Trans.* **2021**, *50* (9), 3178-3185.
80. Brand, S.; Elsen, H.; Langer, J.; Grams, S.; Harder, S., Calcium-Catalyzed Arene C-H Bond Activation by Low-Valent AlI. *Angew. Chem. Int. Ed.* **2019**, *58* (43), 15496-15503.

81. Yang, Y.; Wang, H.; Ma, H., Unprecedented Reaction Pathway of Sterically Crowded Calcium Complexes: Sequential C–N Bond Cleavage Reactions Induced by C–H Bond Activations. *Asian J. Chem.* **2017**, *12* (2), 239-247.
82. Zheng, X.; del Rosal, I.; Xu, X.; Yao, Y.; Maron, L.; Xu, X., Calcium-mediated C(sp³)–H Activation and Alkylation of Alkylpyridines. *Inorg. Chem.* **2021**, *60* (7), 5114-5121.
83. Cao, R.; Antilla, J. C., Imine Amidation Catalyzed by a Chiral VAPOL Calcium Phosphate. *Org. Lett.* **2020**, *22* (15), 5958-5962.
84. Liu, R.; Krishnamurthy, S.; Wu, Z.; Tummalapalli, K. S. S.; Antilla, J. C., Chiral Calcium Phosphate Catalyzed Enantioselective Amination of 3-Aryl-2-benzofuranones. *Org. Lett.* **2020**, *22* (20), 8101-8105.
85. Rueping, M.; Bootwicha, T.; Kambutong, S.; Sugiono, E., Asymmetric Calcium Catalysis: Highly Enantioselective Carbonyl-Ene and Friedel–Crafts Reactions for the Synthesis of Quaternary α -Hydroxy Esters Bearing a Trifluoromethyl Group. *Asian J. Chem.* **2012**, *7* (6), 1195-1198.
86. Simón, L.; Paton, R. S., The True Catalyst Revealed: The Intervention of Chiral Ca and Mg Phosphates in Brønsted Acid Promoted Asymmetric Mannich Reactions. *J. Am. Chem. Soc.* **2018**, *140* (16), 5412-5420.
87. Zhang, Z.; Zheng, W.; Antilla, J. C., Highly Enantioselective Catalytic Benzoyloxylation of 3-Aryloxindoles Using Chiral VAPOL Calcium Phosphate. *Angew. Chem. Int. Ed.* **2011**, *50* (5), 1135-1138.
88. Zheng, W.; Zhang, Z.; Kaplan, M. J.; Antilla, J. C., Chiral Calcium VAPOL Phosphate Mediated Asymmetric Chlorination and Michael Reactions of 3-Substituted Oxindoles. *J. Am. Chem. Soc.* **2011**, *133* (10), 3339-3341.
89. *Chiral Amine Synthesis: Methods, Developments and Applications*. Wiley-VHC Verlag GmbH & Co. KGaA: Weinheim, Germany, 2010.
90. Price, C. C.; Roberts, R. M., The Synthesis of 4-Hydroxyquinolines.1 I. Through Ethoxymethylenemalonic Ester. *J. Am. Chem. Soc.* **1946**, *68* (7), 1204-1208.
91. Johnson, W. S.; Woroch, E. L.; Buell, B. G., Cyclization Studies in the Quinoline Series. A New Synthesis of 4-Aminoquinolines. *J. Am. Chem. Soc.* **1949**, *71* (6), 1901-1905.

92. MacPhillamy, H. B.; Dziemian, R. L.; Lucas, R. A.; Kuehne, M. E., The Alkaloids of *Tabernanthe iboga*. Part VI.1 The Synthesis of the Selenium Dehydrogenation Products from Ibogamine. *J. Am. Chem. Soc.* **1958**, *80* (9), 2172-2178.
93. Kano, S.; Ebata, T.; Shibuya, S., Formation of 2,3-dihydro-4(1H)-quinolones and related compounds via Fries-type acid-catalysed rearrangement of 1-arylazetid-2-ones. *J. Chem. Soc., Perkin Trans.* **1980**, (0), 2105-2111.
94. Kinas, R.; Pankiewicz, K.; Stec, W. J.; Farmer, P. B.; Foster, A. B.; Jarman, M., Synthesis and absolute configuration of the optically active forms of 2-[bis(2-chloroethyl)amino]-4-methyltetrahydro-2H-1,3,2-oxazaphosphorine 2-oxide (4-methylcyclophosphamide). *J. Org. Chem.* **1977**, *42* (9), 1650-1652.
95. D'Angelo, J.; Maddaluno, J., Enantioselective synthesis of β -amino esters through high pressure-induced addition of amines to α,β -ethylenic esters. *J. Am. Chem. Soc.* **1986**, *108* (25), 8112-8114.
96. Jenner, G., Catalytic high pressure synthesis of hindered β -aminoesters. *Tetrahedron Lett.* **1995**, *36* (2), 233-236.
97. Furukawa, M.; Okawara, T.; Terawaki, Y., Asymmetric Syntheses of β -Amino Acids by the Addition of Chiral Amines to C=C Double Bonds. *Chem. Pharm. Bull.* **1977**, *25* (6), 1319-1325.
98. Hawkins, J. M.; Fu, G. C., Asymmetric Michael reactions of 3,5-dihydro-4H-dinaphth[2,1-c:1',2'-e]azepine with methyl crotonate. *J. Org. Chem.* **1986**, *51* (14), 2820-2822.
99. Estermann, H.; Seebach, D., Diastereoselektive Alkylierung von 3-Aminobutansäure in der 2-Stellung. *Helv. Chim. Acta* **1988**, *71* (7), 1824-1839.
100. Juaristi, E.; Escalante, J.; Lamatsch, B.; Seebach, D., Enantioselective synthesis of β -amino acids. 2. Preparation of the like stereoisomers of 2-methyl- and 2-benzyl-3-aminobutanoic acid. *J. Org. Chem.* **1992**, *57* (8), 2396-2398.
101. Davies, S. G.; Smith, A. D.; Price, P. D., The conjugate addition of enantiomerically pure lithium amides as homochiral ammonia equivalents: scope, limitations and synthetic applications. *Tetrahedron: Asymmetry* **2005**, *16* (17), 2833-2891.
102. Davies, S. G.; Fletcher, A. M.; Roberts, P. M.; Thomson, J. E., The conjugate addition of enantiomerically pure lithium amides as chiral ammonia equivalents part II: 2005–2011. *Tetrahedron: Asymmetry* **2012**, *23* (15), 1111-1153.

103. Liu, M.; Sibi, M. P., Recent advances in the stereoselective synthesis of β -amino acids. *Tetrahedron* **2002**, *40* (58), 7991-8035.
104. Xu, L.-W.; Xia, C.-G., A Catalytic Enantioselective Aza-Michael Reaction: Novel Protocols for Asymmetric Synthesis of β -Amino Carbonyl Compounds. *Eur. J. Org. Chem.* **2005**, *2005* (4), 633-639.
105. Enders, D.; Wang, C.; Liebich, J. X., Organocatalytic Asymmetric Aza-Michael Additions. *Chem. Eur. J.* **2009**, *15* (42), 11058-11076.
106. Kawatsura, M.; Hartwig, J. F., Transition Metal-Catalyzed Addition of Amines to Acrylic Acid Derivatives. A High-Throughput Method for Evaluating Hydroamination of Primary and Secondary Alkylamines. *Organometallics* **2001**, *20* (10), 1960-1964.
107. Liu, J.; Li, H.; Spannenberg, A.; Franke, R.; Jackstell, R.; Beller, M., Selective Palladium-Catalyzed Aminocarbonylation of Olefins to Branched Amides. *Angew. Chem. Int. Ed.* **2016**, *55* (43), 13544-13548.
108. Bellavista, T.; Meninno, S.; Lattanzi, A.; Della Sala, G., Asymmetric Hydroazidation of Nitroalkenes Promoted by a Secondary Amine-Thiourea Catalyst. *Adv. Synth. Catal.* **2015**, *357* (14-15), 3365-3373.
109. Guerin, D. J.; Horstmann, T. E.; Miller, S. J., Amine-Catalyzed Addition of Azide Ion to α,β -Unsaturated Carbonyl Compounds. *Org. Lett.* **1999**, *1* (7), 1107-1109.
110. Guerin, D. J.; Miller, S. J., Asymmetric Azidation-Cycloaddition with Open-Chain Peptide-Based Catalysts. A Sequential Enantioselective Route to Triazoles. *J. Am. Chem. Soc.* **2002**, *124* (10), 2134-2136.
111. Horstmann, T. E.; Guerin, D. J.; Miller, S. J., Asymmetric Conjugate Addition of Azide to α,β -Unsaturated Carbonyl Compounds Catalyzed by Simple Peptides. *Angew. Chem. Int. Ed.* **2000**, *39* (20), 3635-3638.
112. Myers, J. K.; Jacobsen, E. N., Asymmetric Synthesis of β -Amino Acid Derivatives via Catalytic Conjugate Addition of Hydrazoic Acid to Unsaturated Imides. *J. Am. Chem. Soc.* **1999**, *121* (38), 8959-8960.
113. Taylor, M. S.; Zalatan, D. N.; Lerchner, A. M.; Jacobsen, E. N., Highly Enantioselective Conjugate Additions to α,β -Unsaturated Ketones Catalyzed by a (Salen)Al Complex. *J. Am. Chem. Soc.* **2005**, *127* (4), 1313-1317.

114. Didier, D.; Meddour, A.; Bezenine-Lafollée, S.; Collin, J., Samarium Iodobinaphtholate: An Efficient Catalyst for Enantioselective Aza-Michael Additions of *O*-Benzylhydroxylamine to *N*-Alkenoyloxazolidinones. *Eur. J. Org. Chem.* **2011**, *2011* (14), 2678-2684.
115. Li, W.; Yu, X.; Yue, Z.; Zhang, J., Asymmetric Construction of 2,3-Dihydroisoxazoles via an Organocatalytic Formal [3 + 2] Cycloaddition of Enynes with *N*-Hydroxylamines. *Org. Lett.* **2016**, *18* (16), 3972-3975.
116. Sibi, M. P.; Shay, J. J.; Liu, M.; Jasperse, C. P., Chiral Lewis Acid Catalysis in Conjugate Additions of *O*-Benzylhydroxylamine to Unsaturated Amides. Enantioselective Synthesis of β -Amino Acid Precursors. *J. Am. Chem. Soc.* **1998**, *120* (26), 6615-6616.
117. Yamagiwa, N.; Matsunaga, S.; Shibasaki, M., Heterobimetallic Catalysis in Asymmetric 1,4-Addition of *O*-Alkylhydroxylamine to Enones. *J. Am. Chem. Soc.* **2003**, *125* (52), 16178-16179.
118. Chen, Y. K.; Yoshida, M.; MacMillan, D. W. C., Enantioselective Organocatalytic Amine Conjugate Addition. *J. Am. Chem. Soc.* **2006**, *128* (29), 9328-9329.
119. Wang, L.; Shirakawa, S.; Maruoka, K., Asymmetric Neutral Amination of Nitroolefins Catalyzed by Chiral Bifunctional Ammonium Salts in Water-Rich Biphasic Solvent. *Angew. Chem. Int. Ed.* **2011**, *50* (23), 5327-5330.
120. Weiß, M.; Borchert, S.; Rémond, E.; Jugé, S.; Gröger, H., Asymmetric addition of a nitrogen nucleophile to an enoate in the presence of a chiral phase-transfer catalyst: A novel approach toward enantiomerically enriched protected β -amino acids. *Heteroat. Chem.* **2012**, *23* (2), 202-209.
121. Dinér, P.; Nielsen, M.; Marigo, M.; Jørgensen, K. A., Enantioselective Organocatalytic Conjugate Addition of *N*-Heterocycles to α,β -Unsaturated Aldehydes. *Angew. Chem. Int. Ed.* **2007**, *46* (12), 1983-1987.
122. Lv, J.; Wu, H.; Wang, Y., Organocatalytic Enantioselective aza-Michael Additions of *N*-Heterocycles to α,β -Unsaturated Enones. *Eur. J. Org. Chem.* **2010**, *2010* (11), 2073-2083.
123. Wang, J.; Li, H.; Zu, L.; Wang, W., Enantioselective Organocatalytic Michael Addition Reactions between *N*-Heterocycles and Nitroolefins. *Org. Lett.* **2006**, *8* (7), 1391-1394.

124. Enders, D.; Wang, C.; Raabe, G., Enantioselective Synthesis of 3H-Pyrrolo[1,2-a]indole-2-carbaldehydes via an Organocatalytic Domino Aza-Michael/Aldol Condensation Reaction. *Synthesis* **2009**, *2009* (24), 4119-4124.
125. Uraguchi, D.; Nakashima, D.; Ooi, T., Chiral Arylamino-phosphonium Barfates as a New Class of Charged Brønsted Acid for the Enantioselective Activation of Nonionic Lewis Bases. *J. Am. Chem. Soc.* **2009**, *131* (21), 7242-7243.
126. Yang, H.-M.; Li, L.; Li, F.; Jiang, K.-Z.; Shang, J.-Y.; Lai, G.-Q.; Xu, L.-W., Silicon-Based Lewis Acid Assisted Cinchona Alkaloid Catalysis: Highly Enantioselective Aza-Michael Reaction under Solvent-Free Conditions. *Org. Lett.* **2011**, *13* (24), 6508-6511.
127. Hamashima, Y.; Somei, H.; Shimura, Y.; Tamura, T.; Sodeoka, M., Amine-Salt-Controlled, Catalytic Asymmetric Conjugate Addition of Various Amines and Asymmetric Protonation. *Org. Lett.* **2004**, *6* (11), 1861-1864.
128. Phua, P. H.; White, A. J. P.; de Vries, J. G.; Hii, K. K., Enabling Ligand Screening for Palladium-Catalysed Enantioselective Aza-Michael Addition Reactions. *Adv. Synth. Catal.* **2006**, *348* (4-5), 587-592.
129. Fadini, L.; Togni, A., Ni(II) Complexes containing chiral tridentate phosphines as new catalysts for the hydroamination of activated olefins. *Chem. Commun.* **2003**, (1), 30-31.
130. Sundararajan, G.; Prabakaran, N., A New Polymer-Anchored Chiral Catalyst for Asymmetric Michael Addition Reactions. *Org. Lett.* **2001**, *3* (3), 389-392.
131. Wang, L.; Chen, J.; Huang, Y., Highly Enantioselective Aza-Michael Reaction between Alkyl Amines and β -Trifluoromethyl β -Aryl Nitroolefins. *Angew. Chem. Int. Ed.* **2015**, *54* (51), 15414-15418.
132. Phillips, E. M.; Riedrich, M.; Scheidt, K. A., *N*-Heterocyclic Carbene-Catalyzed Conjugate Additions of Alcohols. *J. Am. Chem. Soc.* **2010**, *132* (38), 13179-13181.
133. Bouzard, D.; Di Cesare, P.; Essiz, M.; Jacquet, J. P.; Ledoussal, B.; Remuzon, P.; Kessler, R. E.; Fung-Tomc, J., Fluoronaphthyridines as antibacterial agents. 4. Synthesis and structure-activity relationships of 5-substituted 6-fluoro-7-(cycloalkylamino)-1,4-dihydro-4-oxo-1,8-naphthyridine-3-carboxylic acids. *J. Med. Chem.* **1992**, *35* (3), 518-525.
134. Hoang, C. T.; Nguyen, V. H.; Alezra, V.; Kouklovsky, C., 3-Aminopyrrolidines from α -Aminoacids: Total Synthesis of (+)-Nemonapride from d-Alanine. *J. Org. Chem.* **2008**, *73* (3), 1162-1164.

135. Thompson, S. K.; Washburn, D. G.; Frazee, J. S.; Madauss, K. P.; Hoang, T. H.; Lapinski, L.; Grygielko, E. T.; Glace, L. E.; Trizna, W.; Williams, S. P.; Duraiswami, C.; Bray, J. D.; Laping, N. J., Rational design of orally-active, pyrrolidine-based progesterone receptor partial agonists. *Bioorg. Med. Chem. Lett.* **2009**, *19* (16), 4777-4780.
136. Washburn, D. G.; Hoang, T. H.; Frazee, J. S.; Johnson, L.; Hammond, M.; Manns, S.; Madauss, K. P.; Williams, S. P.; Duraiswami, C.; Tran, T. B.; Stewart, E. L.; Grygielko, E. T.; Glace, L. E.; Trizna, W.; Nagilla, R.; Bray, J. D.; Thompson, S. K., Discovery of orally active, pyrrolidinone-based progesterone receptor partial agonists. *Bioorg. Med. Chem. Lett.* **2009**, *19* (16), 4664-4668.
137. Andersson, C.-M.; Croston, G.; Hansen, E. L.; Uldam, A. K. US 2002/0004513 A1, 2002.
138. Chiyoda, K.; Shimokawa, J.; Fukuyama, T., Total Syntheses of All the Amathaspiramides. *Angew. Chem. Int. Ed.* **2012**, *51* (10), 2505-2508.
139. King, D.; Thompson, L. A.; Shi, J.; Thangathirupathy, S.; Warriar, J. S.; Islam, I.; Macor, J. R. US 2015/0191452 A1, 2015.
140. Thomas, A.; Bhavar, P. K.; Lingam, V. S. P. R.; Joshi, N. K. WO 2004/022536 A1, 2004.
141. Wagner, T. T.; Howard, H. R. US 2006/0019998 A1, 2006.
142. Zhang, Y. J.; Wang, Z.; Sprous, D.; Nabioullin, R., In silico design and synthesis of piperazine-1-pyrrolidine-2,5-dione scaffold-based novel malic enzyme inhibitors. *Bioorg. Med. Chem. Lett.* **2006**, *16* (3), 525-528.
143. Kobayashi, S.; Yamashita, Y., Alkaline Earth Metal Catalysts for Asymmetric Reactions. *Acc. Chem. Res.* **2011**, *44* (1), 58-71.
144. Begouin, J.-M.; Niggemann, M., Calcium-Based Lewis Acid Catalysts. *Chem. Eur. J.* **2013**, *19* (25), 8030-8041.
145. Davies, J.; Leonori, D., The first calcium-catalysed Nazarov cyclisation. *Chem. Commun.* **2014**, *50* (96), 15171-15174.
146. Domzalska, A.; Ulikowski, A.; Furman, B., *Chiral Lewis Acids in Organic Synthesis*. Wiley-VCH Verlag GmbH & Co. KGaA: 2017.

147. Dulin, C. C.; Murphy, K. L.; Nolin, K. A., Calcium-catalyzed Friedel–Crafts addition of 1-methylindole to activated cyclopropanes. *Tetrahedron Lett.* **2014**, *55* (38), 5280-5282.
148. Lebœuf, D.; Schulz, E.; Gandon, V., Calcium(II)-Catalyzed Aza-Piancatelli Reaction. *Org. Lett.* **2014**, *16* (24), 6464-6467.
149. Meyer, V. J.; Fu, L.; Marquardt, F.; Niggemann, M., Calcium-Catalyzed Cycloisomerization of Enynes. *Adv. Synth. Catal.* **2013**, *355* (10), 1943-1947.
150. Shimizu, S.; Tsubogo, T.; Xu, P.; Kobayashi, S., Calcium-Catalyzed Asymmetric Synthesis of 3-Tetrasubstituted Oxindoles: Efficient Construction of Adjacent Quaternary and Tertiary Chiral Centers. *Org. Lett.* **2015**, *17* (8), 2006-2009.
151. Wilkins, L. C.; Melen, R. L., Enantioselective Main Group Catalysis: Modern Catalysts for Organic Transformations. *Coord. Chem. Rev.* **2016**, *324*, 123-139.
152. Hatano, M.; Ikeno, T.; Matsumura, T.; Torii, S.; Ishihara, K., Chiral Lithium Salts of Phosphoric Acids as Lewis Acid–Base Conjugate Catalysts for the Enantioselective Cyanosilylation of Ketones. *Adv. Synth. Catal.* **2008**, *350* (11-12), 1776-1780.
153. Hatano, M.; Moriyama, K.; Maki, T.; Ishihara, K., Which Is the Actual Catalyst: Chiral Phosphoric Acid or Chiral Calcium Phosphate? *Angew. Chem. Int. Ed.* **2010**, *49* (22), 3823-3826.
154. Ingle, G. K.; Liang, Y.; Mormino, M. G.; Li, G.; Fronczek, F. R.; Antilla, J. C., Chiral Magnesium BINOL Phosphate-Catalyzed Phosphination of Imines: Access to Enantioenriched α -Amino Phosphine Oxides. *Org. Lett.* **2011**, *13* (8), 2054-2057.
155. Lalli, C.; Dumoulin, A.; Lebée, C.; Drouet, F.; Guérineau, V.; Touboul, D.; Gandon, V.; Zhu, J.; Masson, G., Chiral Calcium–BINOL Phosphate Catalyzed Diastereo- and Enantioselective Synthesis of syn-1,2-Disubstituted 1,2-Diamines: Scope and Mechanistic Studies. *Chem. Eur. J.* **2015**, *21* (4), 1704-1712.
156. Lee, A.; Scheidt, K. A., A Cooperative *N*-Heterocyclic Carbene/Chiral Phosphate Catalysis System for Allenolate Annulations. *Angew. Chem. Int. Ed.* **2014**, *53* (29), 7594-7598.
157. Li, G.; Liang, T.; Wojtas, L.; Antilla, J. C., An Asymmetric Diels–Alder Reaction Catalyzed by Chiral Phosphate Magnesium Complexes: Highly Enantioselective Synthesis of Chiral Spirooxindoles. *Angew. Chem. Int. Ed.* **2013**, *52* (17), 4628-4632.

158. Liang, T.; Li, G.; Wojtas, L.; Antilla, J. C., Chiral metal phosphate catalysis: highly asymmetric hetero-Diels–Alder reactions. *Chem. Commun.* **2014**, 50 (91), 14187-14190.
159. Parmar, D.; Sugiono, E.; Raja, S.; Rueping, M., Complete Field Guide to Asymmetric BINOL-Phosphate Derived Brønsted Acid and Metal Catalysis: History and Classification by Mode of Activation; Brønsted Acidity, Hydrogen Bonding, Ion Pairing, and Metal Phosphates. *Chem. Rev.* **2014**, 114 (18), 9047-9153.
160. Rueping, M.; Bootwicha, T.; Kambutong, S.; Sugiono, E., Asymmetric calcium catalysis: highly enantioselective carbonyl-ene and Friedel-Crafts reactions for the synthesis of quaternary α -hydroxy esters bearing a trifluoromethyl group. *Asian J. Chem.* **2012**, 7 (6), 1195-1198.
161. Rueping, M.; Bootwicha, T.; Sugiono, E., Chiral Brønsted Acids and Their Calcium Salts in Catalytic Asymmetric Mannich Reactions of Cyclic 1,3-Diketones. *Synlett* **2011**, 3, 323-326.
162. Rueping, M.; Nachtsheim, B. J.; Ieawsuwan, W.; Atodiresei, I., Modulating the Acidity: Highly Acidic Brønsted Acids in Asymmetric Catalysis. *Angew. Chem. Int. Ed.* **2011**, 50 (30), 6706-6720.
163. Maddaluno, J.; Corruble, A.; Leroux, V.; Plé, G.; Duhamel, P., Handy access to chiral *N,N'*-disubstituted 3-aminopyrrolidines. *Tetrahedron: Asymmetry* **1992**, 3 (10), 1239-1242.
164. Ashton, P. R.; Calcagno, P.; Spencer, N.; Harris, K. D. M.; Philp, D., Using Polarization Effects to Alter Chemical Reactivity: A Simple Host Which Enhances Amine Nucleophilicity. *Org. Lett.* **2000**, 2 (10), 1365-1368.
165. Bi, Y.; Bailly, L.; Marsais, F.; Levacher, V.; Papamicaël, C.; Dupas, G., Chemoselective, accelerated and stereoselective aza-Michael addition of amines to *N*-phenylmaleimide by using TMEDA based receptors. *Tetrahedron: Asymmetry* **2004**, 15 (23), 3703-3706.
166. Pangborn, A. B.; Giardello, M. A.; Grubbs, R. H.; Rosen, R. K.; Timmers, F. J., Safe and Convenient Procedure for Solvent Purification. *Organometallics* **1996**, 15 (5), 1518-1520.
167. Perrin, D. D.; Armarego, W. L. F., *Purification of Laboratory Chemicals*. 3rd ed.; Pergamon Press: Oxford, 1988.
168. Andersson, P. G.; Munslo, I. J., *Modern Reduction Methods*. Wiley: New York, 2008.

169. Hudlicky, M., *Reductions in Organic Chemistry*. Ellis Horwood Ltd.: Chichester, U.K., 1984.
170. Seyden-Penne, J., *Reductions by the Alumino- and Borohydrides in Organic Synthesis*. 2 ed.; Wiley-VCH: Weinheim, Germany, 1997.
171. Bennet, A. J.; Wang, Q. P.; Slebocka-Tilk, H.; Somayaji, V.; Brown, R. S.; Santarsiero, B. D., Relationship between amidic distortion and ease of hydrolysis in base. If amidic resonance does not exist, then what accounts for the accelerated hydrolysis of distorted amides? *J. Am. Chem. Soc.* **1990**, *112* (17), 6383-6385.
172. Greenberg, A.; Breneman, C. M.; Liebman, J. F., *The Amide Linkage: Structural Significance in Chemistry, Biochemistry, and Materials Science*. Wiley: New York, 2003.
173. Slebocka-Tilk, H.; Brown, R. S., Effect of distortion on the hydrolytic reactivity of amides. 2. *N*-Pyramidalization: decomposition of *N*-benzoylaziridines in aqueous media. *J. Org. Chem.* **1987**, *52* (5), 805-808.
174. Becker, C. W.; Dembofsky, B. T.; Hall, J. E.; Jacobs, R. T.; Pivonka, D. E.; Ohnmacht, C. J., Synthesis of Single-Enantiomer 6-Hydroxy-7-phenyl-1,4-oxazepan-5-ones. *Synthesis* **2005**, (15), 2549-2561.
175. Brown, H. C.; Kim, S. C., An Unusual Reduction of Tertiary Amides with Carbon-Nitrogen Fission. *Synthesis* **1977**, (9), 635-636.
176. Jackson, M.; Mander, L.; Spotswood, T., Reduction of *N*-substituted azetidines to azetidines. *Aust. J. Chem.* **1983**, *36* (4), 779-788.
177. Trauner, D.; Schwarz, J. B.; Danishefsky, S. J., Total Synthesis of (+)-Halichlorine: An Inhibitor of VCAM-1 Expression. *Angew. Chem. Int. Ed.* **1999**, *38* (23), 3542-3545.
178. Cornils, B.; Hermann, W. A.; Beller, M.; Paciella, R., *Applied Homogeneous Catalysis with Organometallic Compounds: A Comprehensive Handbook in Four Volumes*. Wiley-VCH Verlag GmbH & Co.: Weinheim, Germany, 2017; Vol. 4.
179. Magano, J.; Dunetz, J. R., Large-Scale Carbonyl Reductions in the Pharmaceutical Industry. *Org. Process Res. Dev.* **2012**, *16* (6), 1156-1184.
180. Otera, J., *Modern Carbonyl Chemistry*. Wiley-VCH: Weinheim, Germany, 2000.
181. Roberts, S. M.; Whittall, J., *Regio- and Stereo-Controlled Oxidations and Reductions*. John Wiley & Sons: West Sussex, England, 2007; Vol. 5.

182. Smith, A. M.; Whyman, R., Review of Methods for the Catalytic Hydrogenation of Carboxamides. *Chem. Rev.* **2014**, *114* (10), 5477-5510.
183. Smith, M., *Advanced Organic Chemistry: Reactions, Mechanisms, and Structure*. Wiley: Hoboken, NJ, 2013.
184. Werkmeister, S.; Junge, K.; Beller, M., Catalytic Hydrogenation of Carboxylic Acid Esters, Amides, and Nitriles with Homogeneous Catalysts. *Org. Process Res. Dev.* **2014**, *18* (2), 289-302.
185. Constable, D. J. C.; Dunn, P. J.; Hayler, J. D.; Humphrey, G. R.; Leazer, J. J. L.; Linderman, R. J.; Lorenz, K.; Manley, J.; Pearlman, B. A.; Wells, A.; Zaks, A.; Zhang, T. Y., Key green chemistry research areas—a perspective from pharmaceutical manufacturers. *Green Chem.* **2007**, *9* (5), 411-420.
186. Marciniec, B., *Hydrosilylation: A Comprehensive Review on Recent Advances*. Springer: The Netherlands, 2009.
187. Roy, A. K., A Review of Recent Progress in Catalyzed Homogeneous Hydrosilation (Hydrosilylation). In *Advances in Organometallic Chemistry*, West, R.; Hill, A. F.; Fink, M. J., Eds. Academic Press: 2007; Vol. 55, pp 1-59.
188. Volkov, A.; Tinnis, F.; Slagbrand, T.; Trillo, P.; Adolfsson, H., Chemoselective reduction of carboxamides. *Chem. Soc. Rev.* **2016**, *45* (24), 6685-6697.
189. Das, S.; Karmakar, H.; Bhattacharjee, J.; Panda, T. K., Aluminium complex as an efficient catalyst for the chemo-selective reduction of amides to amines. *Dalton Trans.* **2019**, *48* (31), 11978-11984.
190. Lampland, N. L.; Hovey, M.; Mukherjee, D.; Sadow, A. D., Magnesium-Catalyzed Mild Reduction of Tertiary and Secondary Amides to Amines. *ACS Catal.* **2015**, *5* (7), 4219-4226.
191. Mukherjee, D.; Shirase, S.; Spaniol, T. P.; Mashima, K.; Okuda, J., Magnesium hydridotriphenylborate [Mg(thf)₆][HBPh₃]₂: a versatile hydroboration catalyst. *Chem. Commun.* **2016**, *52* (89), 13155-13158.
192. Chong, C. C.; Kinjo, R., Catalytic Hydroboration of Carbonyl Derivatives, Imines, and Carbon Dioxide. *ACS Catal.* **2015**, *5* (6), 3238-3259.

193. Das, U. K.; Higman, C. S.; Gabidullin, B.; Hein, J. E.; Baker, R. T., Efficient and Selective Iron-Complex-Catalyzed Hydroboration of Aldehydes. *ACS Catal.* **2018**, *8* (2), 1076-1081.
194. Huang, Z.; Liu, D.; Camacho-Bunquin, J.; Zhang, G.; Yang, D.; López-Encarnación, J. M.; Xu, Y.; Ferrandon, M. S.; Niklas, J.; Poluektov, O. G.; Jellinek, J.; Lei, A.; Bunel, E. E.; Delferro, M., Supported Single-Site Ti(IV) on a Metal–Organic Framework for the Hydroboration of Carbonyl Compounds. *Organometallics* **2017**, *36* (20), 3921-3930.
195. Kuciński, K.; Hreczycho, G., Potassium Fluoride-Catalyzed Hydroboration of Aldehydes and Ketones: Facile Reduction to Primary and Secondary Alcohols. *Eur. J. Org. Chem.* **2020**, *2020* (5), 552-555.
196. Manna, K.; Ji, P.; Greene, F. X.; Lin, W., Metal–Organic Framework Nodes Support Single-Site Magnesium–Alkyl Catalysts for Hydroboration and Hydroamination Reactions. *J. Am. Chem. Soc.* **2016**, *138* (24), 7488-7491.
197. Schneider, J.; Sindlinger, C. P.; Freitag, S. M.; Schubert, H.; Wesemann, L., Diverse Activation Modes in the Hydroboration of Aldehydes and Ketones with Germanium, Tin, and Lead Lewis Pairs. *Angew. Chem. Int. Ed.* **2017**, *56* (1), 333-337.
198. Vasilenko, V.; Blasius, C. K.; Wadepohl, H.; Gade, L. H., Mechanism-Based Enantiodivergence in Manganese Reduction Catalysis: A Chiral Pincer Complex for the Highly Enantioselective Hydroboration of Ketones. *Angew. Chem. Int. Ed.* **2017**, *56* (29), 8393-8397.
199. Wu, D.; Wang, R.; Li, Y.; Ganguly, R.; Hirao, H.; Kinjo, R., Electrostatic Catalyst Generated from Diazadiborinine for Carbonyl Reduction. *Chem.* **2017**, *3* (1), 134-151.
200. Zhang, G.; Cheng, J.; Davis, K.; Bonifacio, M. G.; Zajackowski, C., Practical and selective hydroboration of aldehydes and ketones in air catalysed by an iron(II) coordination polymer. *Green Chem.* **2019**, *21* (5), 1114-1121.
201. Arrowsmith, M.; Hill, M. S.; Hadlington, T.; Kociok-Köhn, G.; Weetman, C., Magnesium-Catalyzed Hydroboration of Pyridines. *Organometallics* **2011**, *30* (21), 5556-5559.
202. Barman, M. K.; Baishya, A.; Nembenna, S., Magnesium amide catalyzed selective hydroboration of esters. *Dalton Trans.* **2017**, *46* (13), 4152-4156.

203. Mukherjee, D.; Ellern, A.; Sadow, A. D., Magnesium-catalyzed hydroboration of esters: evidence for a new zwitterionic mechanism. *Chem. Sci.* **2014**, *5* (3), 959-964.
204. Patnaik, S.; Sadow, A. D., Interconverting Lanthanum Hydride and Borohydride Catalysts for C=O Reduction and C–O Bond Cleavage. *Angew. Chem. Int. Ed.* **2019**, *58* (8), 2505-2509.
205. Belot, J. A.; Wang, A.; McNeely, R. J.; Liable-Sands, L.; Rheingold, A. L.; Marks, T. J., Highly Volatile, Low Melting, Fluorine-Free Precursors for Metal-Organic Chemical Vapor Deposition of Lanthanide Oxide-Containing Thin Films. *Chem. Vap. Depos.* **1999**, *5* (2), 65-69.
206. Cotton, S. A., Lanthanide Amides. In *Encyclopedia of Inorganic and Bioinorganic Chemistry*, pp 1-11.
207. Dash, A. K.; Razavi, A.; Mortreux, A.; Lehmann, C. W.; Carpentier, J.-F., Amine Elimination Reactions between Homoleptic Silylamide Lanthanide Complexes and an Isopropylidene-Bridged Cyclopentadiene–Fluorene System. *Organometallics* **2002**, *21* (15), 3238-3249.
208. Döring, C.; Kempe, R., Synthesis and Structure of Aminopyridinato-Stabilized Yttrium and Lanthanum Amides and Their Reactivity towards Alkylaluminium Compounds. *Eur. J. Inorg. Chem.* **2009**, *2009* (3), 412-418.
209. Edelmann, F. T., Lanthanides and actinides: Annual survey of their organometallic chemistry covering the year 2017. *Coord. Chem. Rev.* **2018**, *370*, 129-223.
210. Hong, S.; Tian, S.; Metz, M. V.; Marks, T. J., C₂-Symmetric Bis(oxazolinato)lanthanide Catalysts for Enantioselective Intramolecular Hydroamination/Cyclization. *J. Am. Chem. Soc.* **2003**, *125* (48), 14768-14783.
211. Korobkov, I.; Gambarotta, S., Aluminate Samarium(II) and Samarium(III) Aryloxides. Isolation of a Single-Component Ethylene Polymerization Catalyst. *Organometallics* **2009**, *28* (14), 4009-4019.
212. Qian, Q.; Zhu, W.; Lu, C.; Zhao, B.; Yao, Y., Asymmetric Michael addition of malonates to unsaturated ketones catalyzed by rare earth metal complexes bearing phenoxy functionalized chiral diphenylprolinolate ligands. *Tetrahedron: Asymmetry* **2016**, *27* (19), 911-917.
213. Tian, S.; Arredondo, V. M.; Stern, C. L.; Marks, T. J., Constrained Geometry Organolanthanide Catalysts. Synthesis, Structural Characterization, and Enhanced

- Aminoalkene Hydroamination/Cyclization Activity. *Organometallics* **1999**, *18* (14), 2568-2570.
214. Vitanova, D. V.; Hampel, F.; Hultsch, K. C., Linked bis(β -diketiminato) yttrium and lanthanum complexes as catalysts in asymmetric hydroamination/cyclization of aminoalkenes (AHA). *J. Organomet. Chem.* **2011**, *696* (1), 321-330.
215. Wang, C.; Huang, L.; Lu, M.; Zhao, B.; Wang, Y.; Zhang, Y.; Shen, Q.; Yao, Y., Anionic phenoxy-amido rare-earth complexes as efficient catalysts for amidation of aldehydes with amines. *RSC Adv.* **2015**, *5* (115), 94768-94775.
216. Anwander, R., Lanthanide amides. In *Organolanthanoid Chemistry: Synthesis, Structure, Catalysis*, Berlin, Heidelberg, 1996; pp 33-112.
217. Hong, S.; Kawaoka, A. M.; Marks, T. J., Intramolecular Hydroamination/Cyclization of Conjugated Aminodienes Catalyzed by Organolanthanide Complexes. Scope, Diastereo- and Enantioselectivity, and Reaction Mechanism. *J. Am. Chem. Soc.* **2003**, *125* (51), 15878-15892.
218. Hong, S.; Marks, T. J., Organolanthanide-Catalyzed Hydroamination. *Acc. Chem. Res.* **2004**, *37* (9), 673-686.
219. Müller, T. E.; Hultsch, K. C.; Yus, M.; Foubelo, F.; Tada, M., Hydroamination: Direct Addition of Amines to Alkenes and Alkynes. *Chem. Rev.* **2008**, *108* (9), 3795-3892.
220. Roesky, P., *Molecular Catalysis of Rare-Earth Elements*. Springer-Verlag: Berlin, Heidelberg, 2010; Vol. 137.
221. Schuetz, S. A.; Day, V. W.; Sommer, R. D.; Rheingold, A. L.; Belot, J. A., Anhydrous Lanthanide Schiff Base Complexes and Their Preparation Using Lanthanide Triflate Derived Amides. *Inorg. Chem.* **2001**, *40* (20), 5292-5295.
222. Seo, S.; Marks, T. J., Mild Amidation of Aldehydes with Amines Mediated by Lanthanide Catalysts. *Org. Lett.* **2008**, *10* (2), 317-319.
223. Hawkeswood, S.; Stephan, D. W., Syntheses and reactions of the bis-boryloxide O(Bpin)₂ (pin = O₂C₂Me₄). *Dalton Trans.* **2005**, (12), 2182-2187.
224. Stanlake, L. J. E.; Beard, J. D.; Schafer, L. L., Rare-Earth Amidate Complexes. Easily Accessed Initiators For ϵ -Caprolactone Ring-Opening Polymerization. *Inorg. Chem.* **2008**, *47* (18), 8062-8068.

225. Yin, H.; Carroll, P. J.; Schelter, E. J., Reactions of a cerium(III) amide with heteroallenes: insertion, silyl-migration and de-insertion. *Chem. Commun.* **2016**, 52 (63), 9813-9816.
226. Yang, Y.; Anker, M. D.; Fang, J.; Mahon, M. F.; Maron, L.; Weetman, C.; Hill, M. S., Hydrodeoxygenation of isocyanates: snapshots of a magnesium-mediated C–O bond cleavage. *Chem. Sci.* **2017**, 8 (5), 3529-3537.
227. Punekar, N. S., *ENZYMES: Catalysis, Kinetics and Mechanisms*. Springer Nature: Singapore, 2018.
228. Swiegers, G. F., *Mechanical Catalysis: Methods of Enzymatic, Homogeneous, and Heterogeneous Catalysis*. John Wiley & Sons, Inc.: 2008.
229. Dunne, J. F.; Fulton, D. B.; Ellern, A.; Sadow, A. D., Concerted C–N and C–H Bond Formation in a Magnesium-Catalyzed Hydroamination. *J. Am. Chem. Soc.* **2010**, 132 (50), 17680-17683.
230. Harris, R. J.; Carden, R. G.; Duncan, A. N.; Widenhoefer, R. A., Kinetics and Mechanism of the Gold-Catalyzed Intermolecular Hydroalkoxylation of Allenes with Alcohols. *ACS Catal.* **2018**, 8 (9), 8941-8952.
231. Kalow, J. A.; Doyle, A. G., Mechanistic Investigations of Cooperative Catalysis in the Enantioselective Fluorination of Epoxides. *J. Am. Chem. Soc.* **2011**, 133 (40), 16001-16012.
232. Di Bella, S.; Lanza, G.; Fragalà, I. L., Equilibrium geometries and harmonic vibrational frequencies of lanthanum trihalides LaX₃ (X = F, Cl). A relativistic effective core potential ab initio MO study. *Chem. Phys. Lett.* **1993**, 214 (6), 598-602.
233. Weigend, F.; Ahlrichs, R., Balanced basis sets of split valence, triple zeta valence and quadruple zeta valence quality for H to Rn: Design and assessment of accuracy. *Phys. Chem. Chem. Phys.* **2005**, 7 (18), 3297-3305.
234. Ohki, Y.; Takikawa, Y.; Hatanaka, T.; Tatsumi, K., Reductive N–N Bond Cleavage of Diphenylhydrazine and Azobenzene Induced by Coordinatively Unsaturated Cp*Fe{N(SiMe₃)₂}₂. *Organometallics* **2006**, 25 (13), 3111-3113.
235. Dudnik, A. S.; Weidner, V. L.; Motta, A.; Delferro, M.; Marks, T. J., Atom-efficient regioselective 1,2-dearomatization of functionalized pyridines by an earth-abundant organolanthanide catalyst. *Nature Chem.* **2014**, 6 (12), 1100-1107.

236. Harder, S.; Spielmann, J., Calcium-mediated hydroboration of alkenes: “Trojan horse” or “true” catalysis? *J. Organomet. Chem.* **2012**, *698*, 7-14.
237. Hatanaka, T.; Ohki, Y.; Tatsumi, K., C–H Bond Activation/Borylation of Furans and Thiophenes Catalyzed by a Half-Sandwich Iron *N*-Heterocyclic Carbene Complex. *Asian J. Chem.* **2010**, *5* (7), 1657-1666.
238. Macaulay, C. M.; Gustafson, S. J.; Fuller, J. T.; Kwon, D.-H.; Ogawa, T.; Ferguson, M. J.; McDonald, R.; Lumsden, M. D.; Bischof, S. M.; Sydora, O. L.; Ess, D. H.; Stradiotto, M.; Turculet, L., Alkene Isomerization–Hydroboration Catalyzed by First-Row Transition-Metal (Mn, Fe, Co, and Ni) *N*-Phosphinoamidinate Complexes: Origin of Reactivity and Selectivity. *ACS Catal.* **2018**, *8* (11), 9907-9925.
239. Wei, C. S.; Jiménez-Hoyos, C. A.; Videa, M. F.; Hartwig, J. F.; Hall, M. B., Origins of the Selectivity for Borylation of Primary over Secondary C–H Bonds Catalyzed by Cp*-Rhodium Complexes. *J. Am. Chem. Soc.* **2010**, *132* (9), 3078-3091.
240. Laidler, K. J., *Chemical Kinetics*. Pearson Education: 1987.
241. Chong, C. C.; Hirao, H.; Kinjo, R., Metal-Free σ -Bond Metathesis in 1,3,2-Diazaphospholene-Catalyzed Hydroboration of Carbonyl Compounds. *Angew. Chem. Int. Ed.* **2015**, *54* (1), 190-194.
242. Liu, H.; Khononov, M.; Eisen, M. S., Catalytic 1,2-Regioselective Dearomatization of *N*-Heteroaromatics via a Hydroboration. *ACS Catal.* **2018**, *8* (4), 3673-3677.
243. Weetman, C.; Anker, M. D.; Arrowsmith, M.; Hill, M. S.; Kociok-Köhn, G.; Liptrot, D. J.; Mahon, M. F., Magnesium-catalysed nitrile hydroboration. *Chem. Sci.* **2016**, *7* (1), 628-641.
244. Zhang, F.; Song, H.; Zhuang, X.; Tung, C.-H.; Wang, W., Iron-Catalyzed 1,2-Selective Hydroboration of *N*-Heteroarenes. *J. Am. Chem. Soc.* **2017**, *139* (49), 17775-17778.
245. Bhojgude, S. S.; Kaicharla, T.; Biju, A. T., Employing Arynes in Transition-Metal-Free Monoarylation of Aromatic Tertiary Amines. *Org. Lett.* **2013**, *15* (21), 5452-5455.
246. Sitte, N. A.; Bursch, M.; Grimme, S.; Paradies, J., Frustrated Lewis Pair Catalyzed Hydrogenation of Amides: Halides as Active Lewis Base in the Metal-Free Hydrogen Activation. *J. Am. Chem. Soc.* **2019**, *141* (1), 159-162.
247. Molander, G. A.; Sandrock, D. L., Aminomethylations via Cross-Coupling of Potassium Organotrifluoroborates with Aryl Bromides. *Org. Lett.* **2007**, *9* (8), 1597-1600.

248. Drinkel, E. E.; Campedelli, R. R.; Manfredi, A. M.; Fiedler, H. D.; Nome, F., Zwitterionic-Surfactant-Stabilized Palladium Nanoparticles as Catalysts in the Hydrogen Transfer Reductive Amination of Benzaldehydes. *J. Org. Chem.* **2014**, *79* (6), 2574-2579.
249. Peruzzi, M. T.; Mei, Q. Q.; Lee, S. J.; Gagné, M. R., Chemoselective amide reductions by heteroleptic fluoroaryl boron Lewis acids. *Chem. Commun.* **2018**, *54* (46), 5855-5858.
250. Taylor, N. J.; Emer, E.; Preshlock, S.; Schedler, M.; Tredwell, M.; Verhoog, S.; Mercier, J.; Genicot, C.; Gouverneur, V., Derisking the Cu-Mediated ¹⁸F-Fluorination of Heterocyclic Positron Emission Tomography Radioligands. *J. Am. Chem. Soc.* **2017**, *139* (24), 8267-8276.
251. Pilling, M. J.; Seakins, P. W., *Reaction Kinetics*. Oxford University Press: New York, 1995.
252. Tucker, C. E.; Davidson, J.; Knochel, P., Mild and stereoselective hydroborations of functionalized alkynes and alkenes using pinacolborane. *J. Org. Chem.* **1992**, *57* (12), 3482-3485.
253. Tank, R.; Pathak, U.; Vimal, M.; Bhattacharyya, S.; Pandey, L. K., Hydrogen peroxide mediated efficient amidation and esterification of aldehydes: Scope and selectivity. *Green Chem.* **2011**, *13* (12), 3350-3354.
254. Hansch, C.; Leo, A.; Taft, R. W., A survey of Hammett substituent constants and resonance and field parameters. *Chem. Rev.* **1991**, *91* (2), 165-195.
255. Lachaize, S.; Essalah, K.; Montiel-Palma, V.; Vendier, L.; Chaudret, B.; Barthelat, J.-C.; Sabo-Etienne, S., Coordination Modes of Boranes in Polyhydride Ruthenium Complexes: σ -Borane versus Dihydridoborate. *Organometallics* **2005**, *24* (12), 2935-2943.
256. Yang, S. H.; Huh, J.; Jo, W. H., Density Functional Study on the Regioselectivity of Styrene Polymerization with an ansa-Metallocene Catalyst. *Organometallics* **2006**, *25* (5), 1144-1150.
257. Yang, S. H.; Huh, J.; Yang, J. S.; Jo, W. H., A Density Functional Study on the Stereoselectivity of Styrene Polymerization with ansa-Metallocene Catalyst. *Macromolecules* **2004**, *37* (15), 5741-5751.
258. Rassolov, V. A.; Pople, J. A.; Ratner, M. A.; Windus, T. L., 6-31G* basis set for atoms K through Zn. *J. Chem. Phys.* **1998**, *109* (4), 1223-1229.

259. Yu, Y. B.; Privalov, P. L.; Hodges, R. S., Contribution of translational and rotational motions to molecular association in aqueous solution. *Biophys. J.* **2001**, *81* (3), 1632-1642.
260. Frisch, M. J.; Trucks, G. W.; Schlegel, H. B.; Scuseria, G. E.; Robb, M. A.; Cheeseman, J. R.; Scalmani, G.; Barone, V.; Petersson, G. A.; Nakatsuji, H.; Li, X.; Caricato, M.; Marenich, A. V.; Bloino, J.; Janesko, B. G.; Gomperts, R.; Mennucci, B.; Hratchian, H. P.; Ortiz, J. V.; Izmaylov, A. F.; Sonnenberg, J. L.; Williams-Young, D.; Ding, F.; Lipparini, F.; Egidi, F.; Goings, J.; Peng, B.; Petrone, A.; Henderson, T.; Ranasinghe, D.; Zakrzewski, V. G.; Gao, J.; Rega, N.; Zheng, G.; Liang, W.; Hada, M.; Ehara, M.; Toyota, K.; Fukuda, R.; Hasegawa, J.; Ishida, M.; Nakajima, T.; Honda, Y.; Kitao, O.; Nakai, H.; Vreven, T.; Throssell, K.; Montgomery Jr., J. A.; Peralta, J. E.; Ogliaro, F.; Bearpark, M. J.; Heyd, J. J.; Brothers, E. N.; Kudin, K. N.; Staroverov, V. N.; Keith, T. A.; Kobayashi, R.; Normand, J.; Raghavachari, K.; Rendell, A. P.; Burant, J. C.; Iyengar, S. S.; Tomasi, J.; Cossi, M.; Millam, J. M.; Klene, M.; Adamo, C.; Cammi, R.; Ochterski, J. W.; Martin, R. L.; Morokuma, K.; Farkas, O.; Foresman, J. B.; Fox, D. J., *Gaussian 16, Revision B.01*. Gaussian, Inc., Wallingford CT: 2016.
261. Dolg, M.; Stoll, H., Chapter 152 Electronic structure calculations for molecules containing lanthanide atoms. In *Handbook on the Physics and Chemistry of Rare Earths*, Elsevier: 1996; Vol. 22, pp 607-729.

APPENDICES

Appendix A

Supplementary to Chapter 2

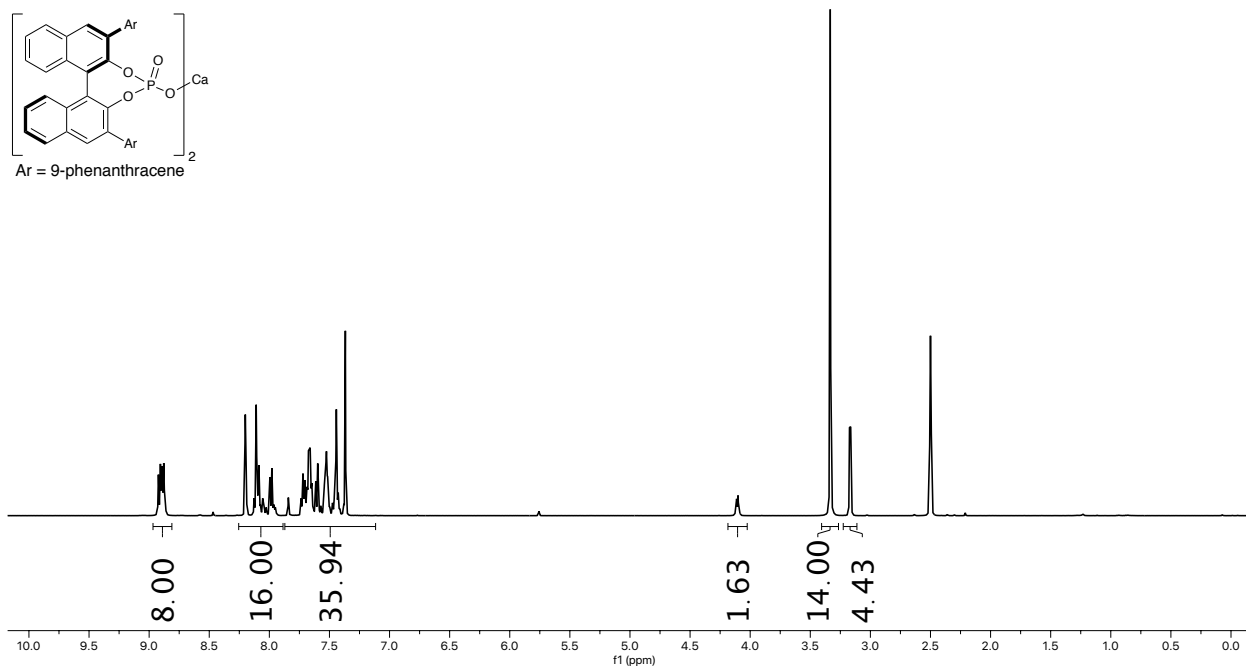
Data included in this appendix appear in the following publication:

Brice E. Uno, Rachel D. Dicken, Louis R. Redfern, Charlotte M. Stern, Greg G. Krzywicki, and Karl A. Scheidt, Calcium(II)-catalyzed enantioselective conjugate addition of amines. *Chem. Sci.*

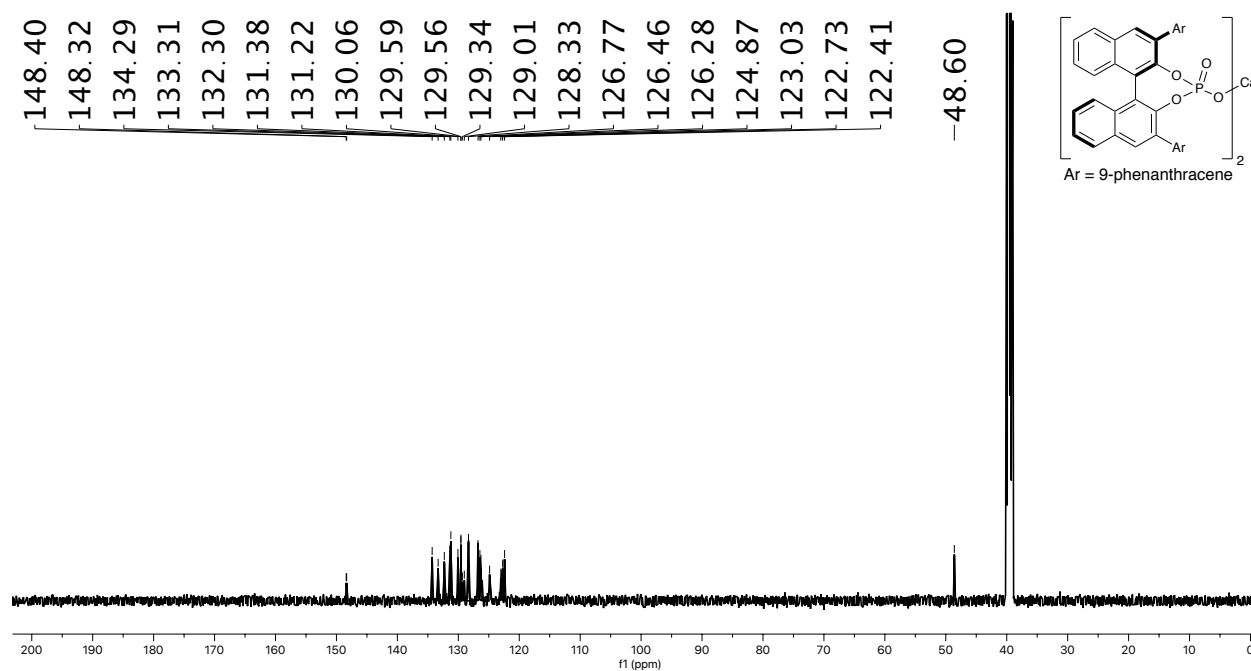
2018, 9, 1634-1639.

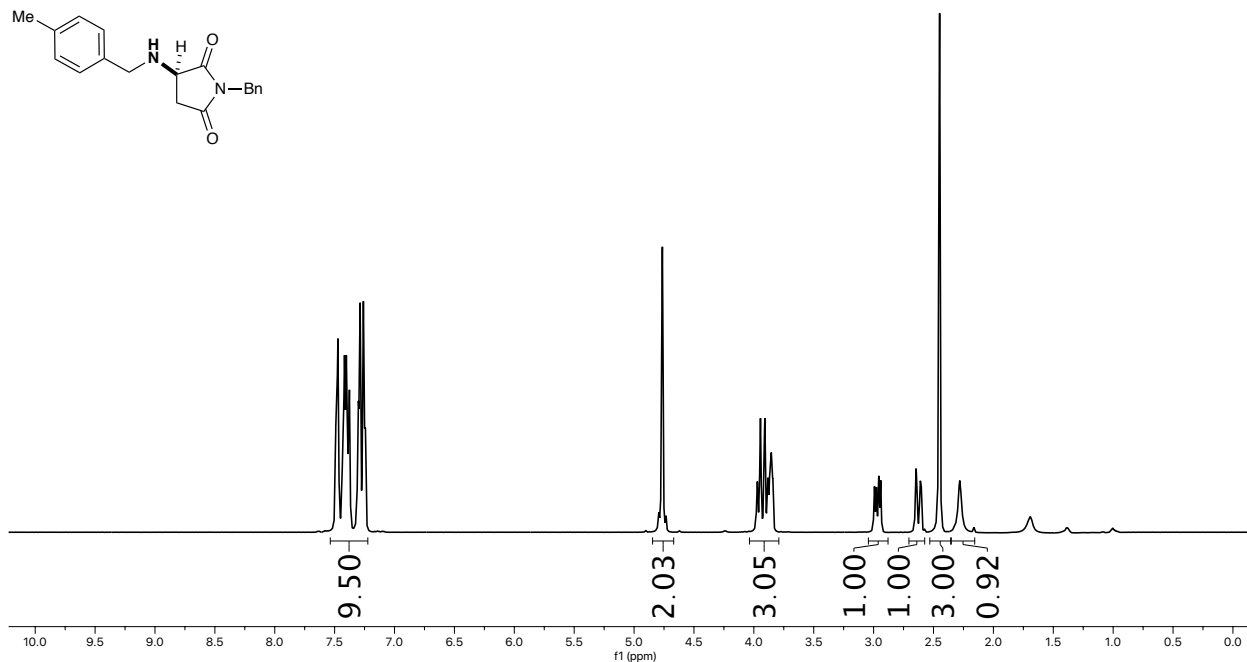
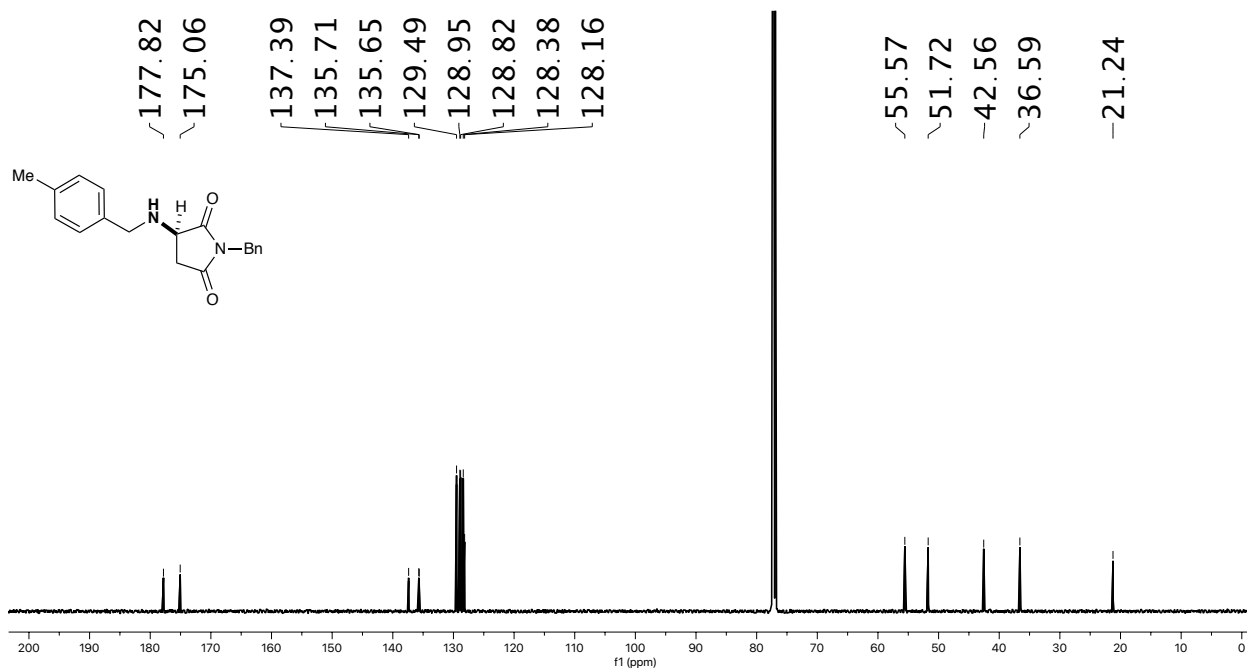
A1. NMR Spectra

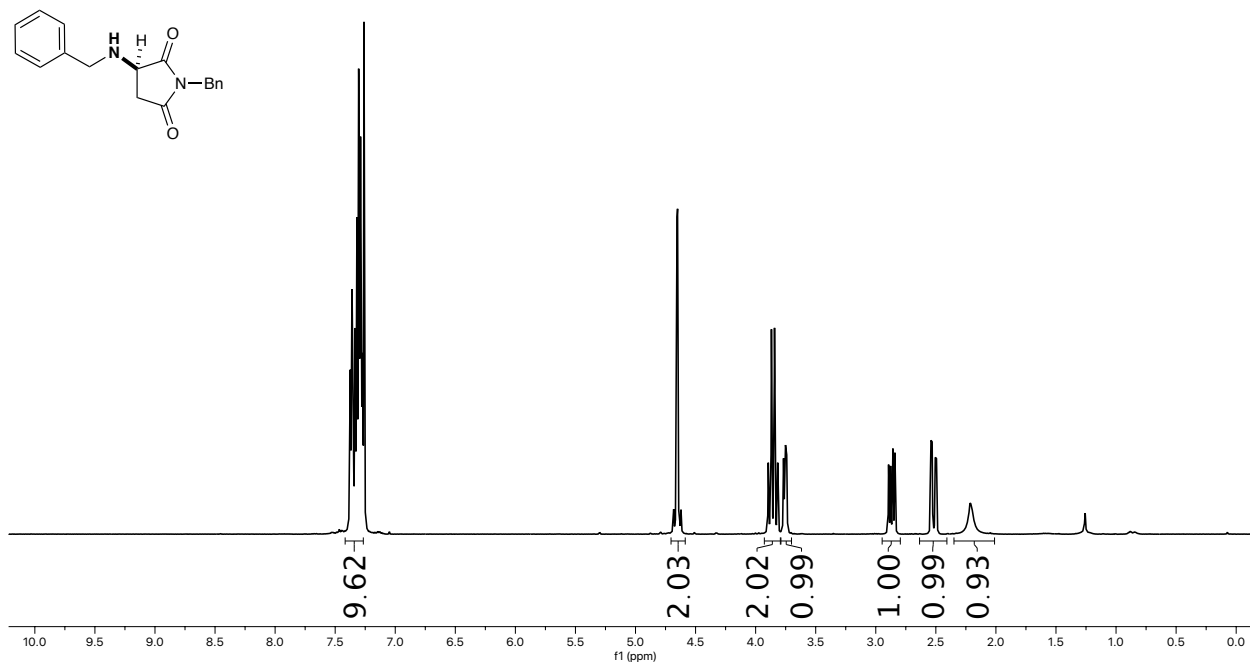
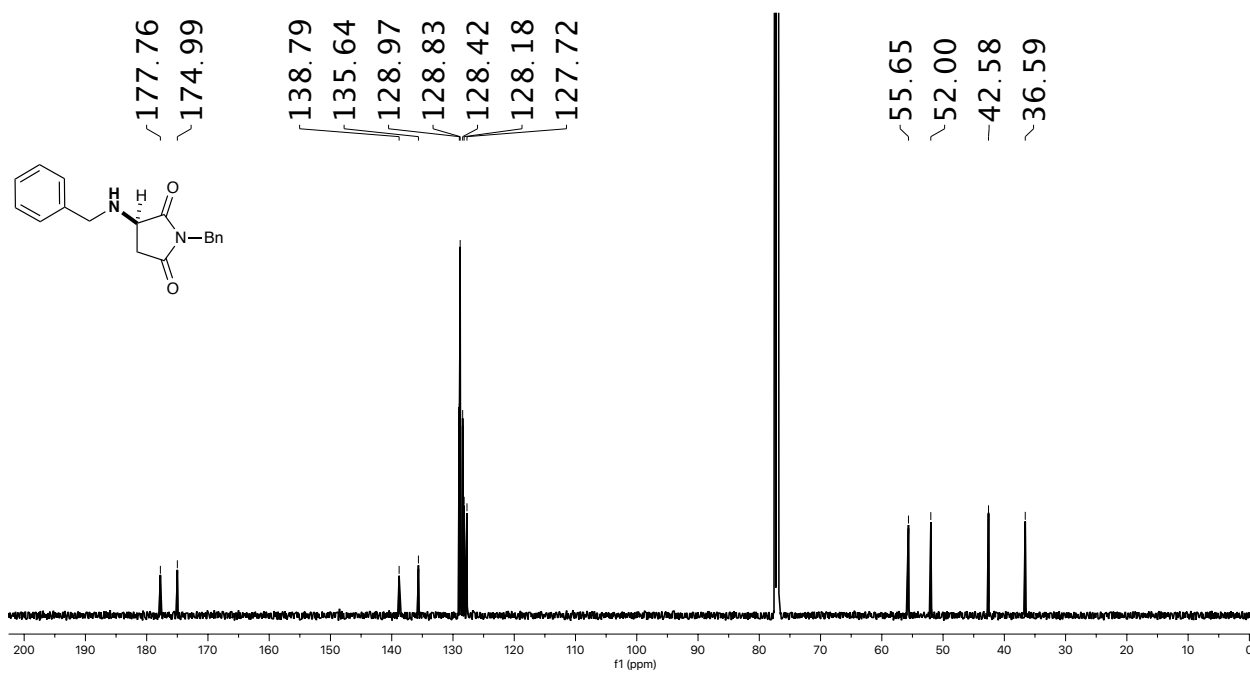
^1H NMR spectrum of $\text{Ca}[\text{B}]_2$ (500 MHz, $\text{DMSO-}d_6$).

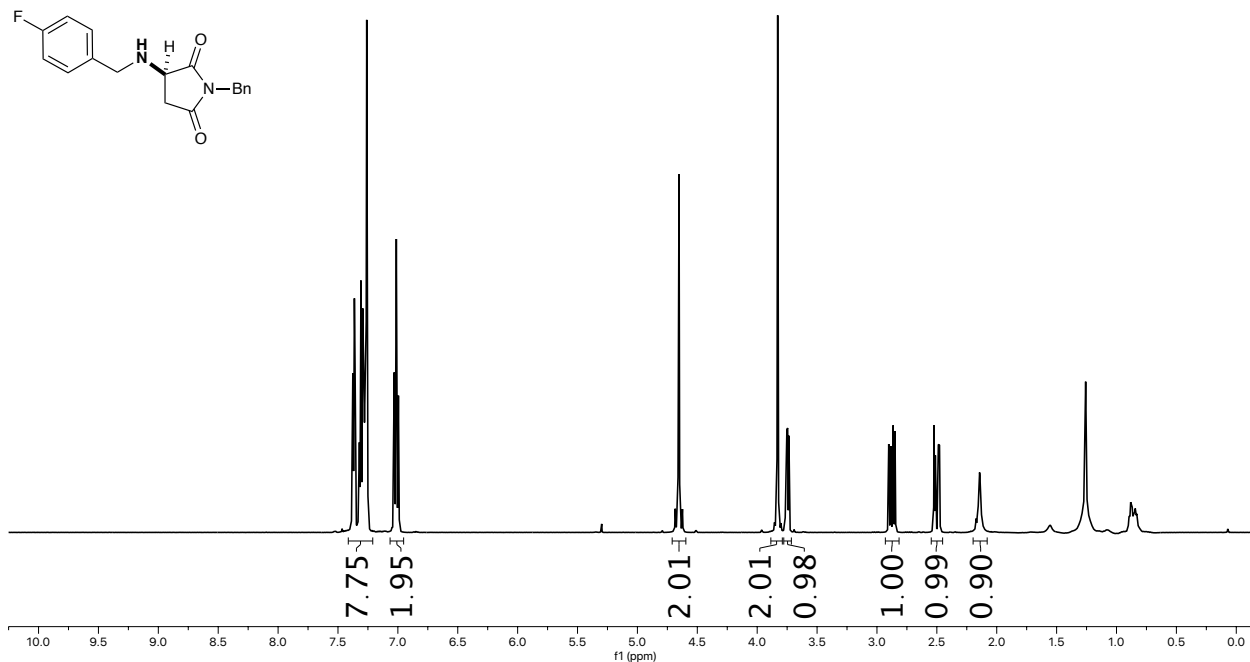
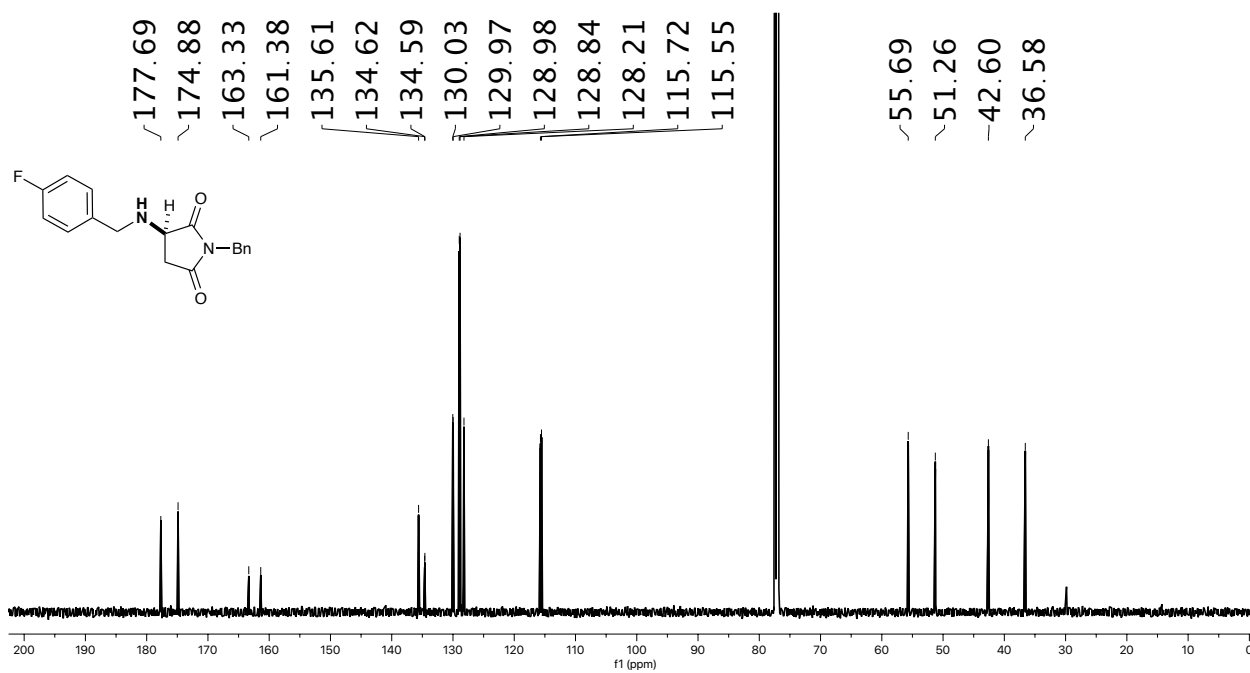


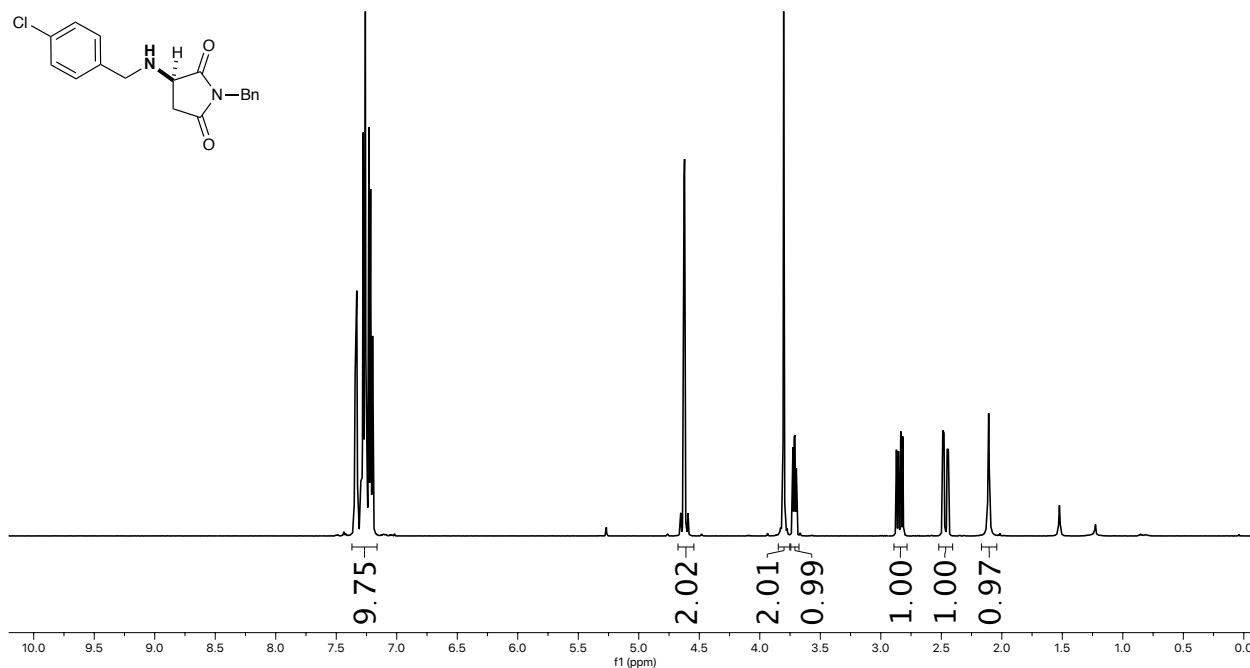
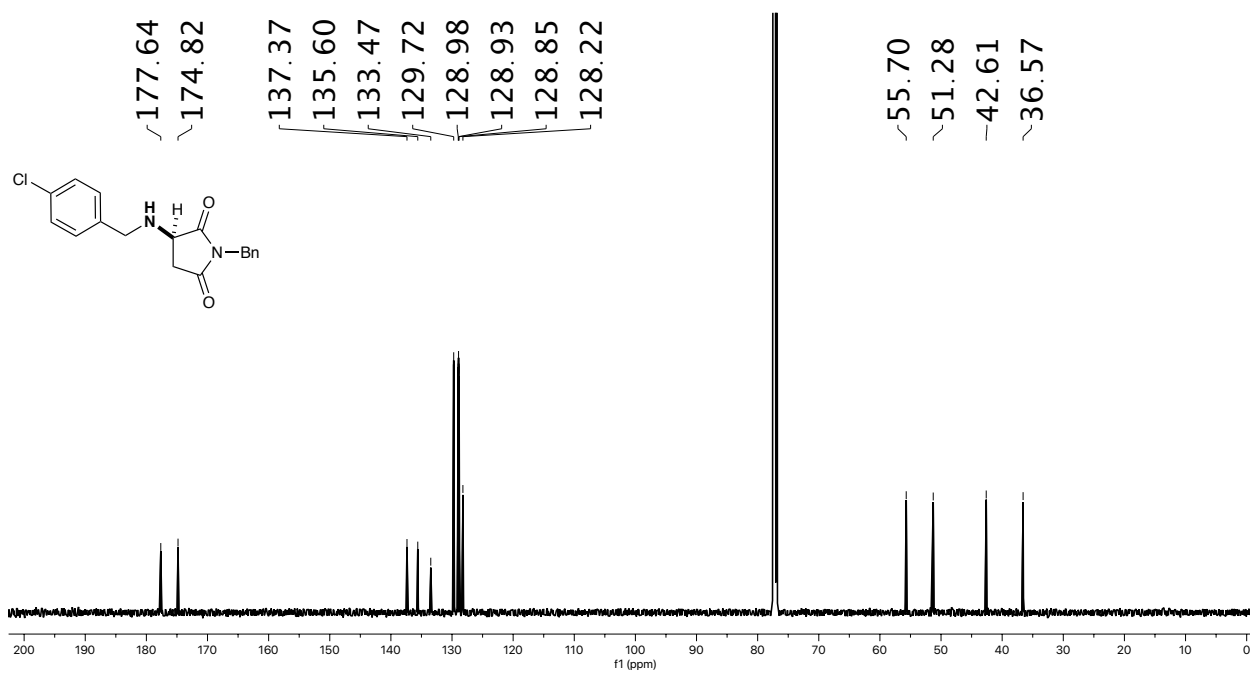
^{13}C NMR spectrum of $\text{Ca}[\text{B}]_2$ (126 MHz, $\text{DMSO-}d_6$).

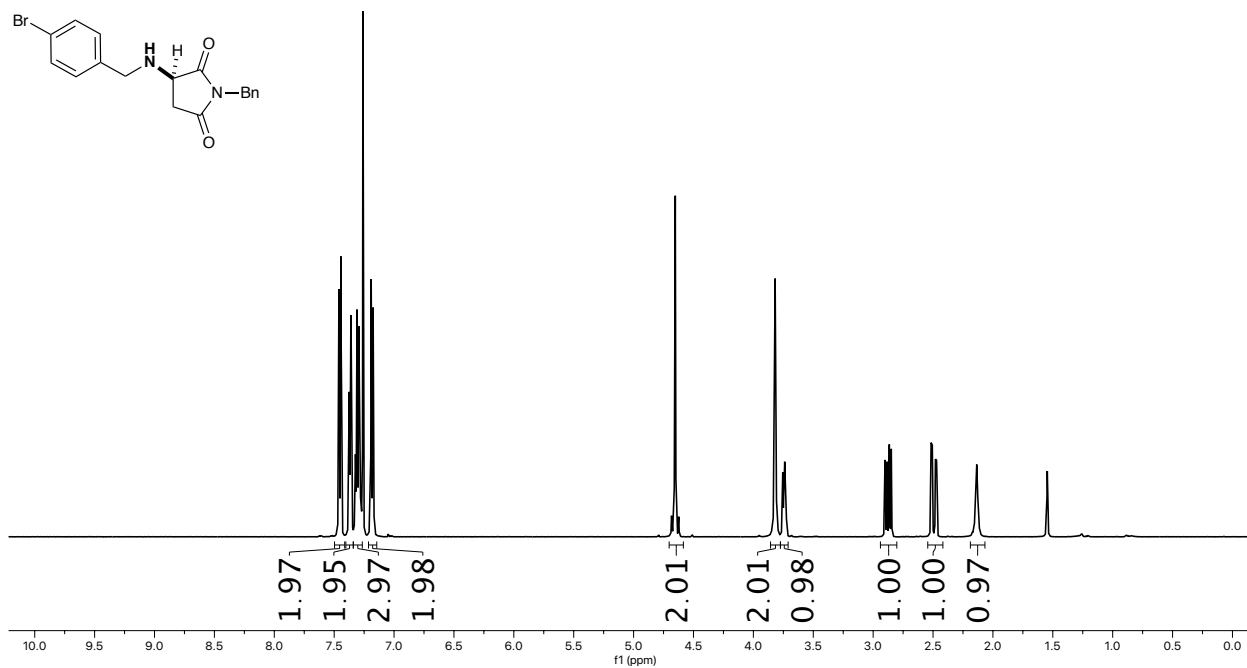
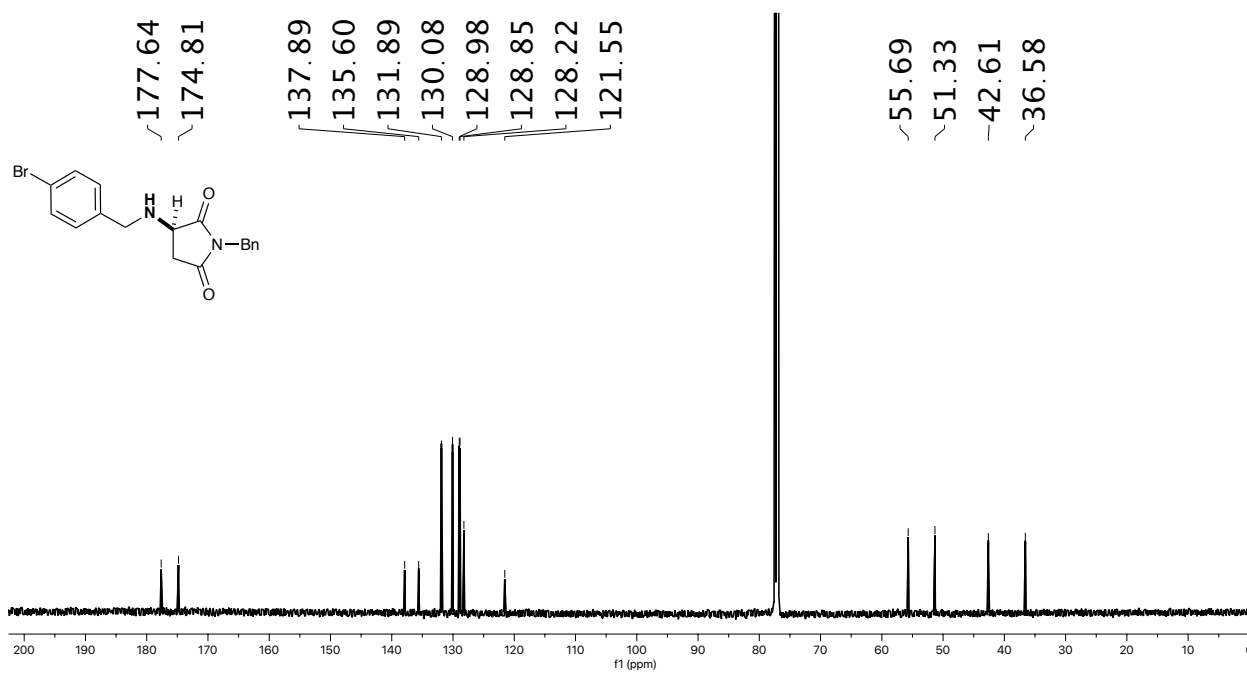


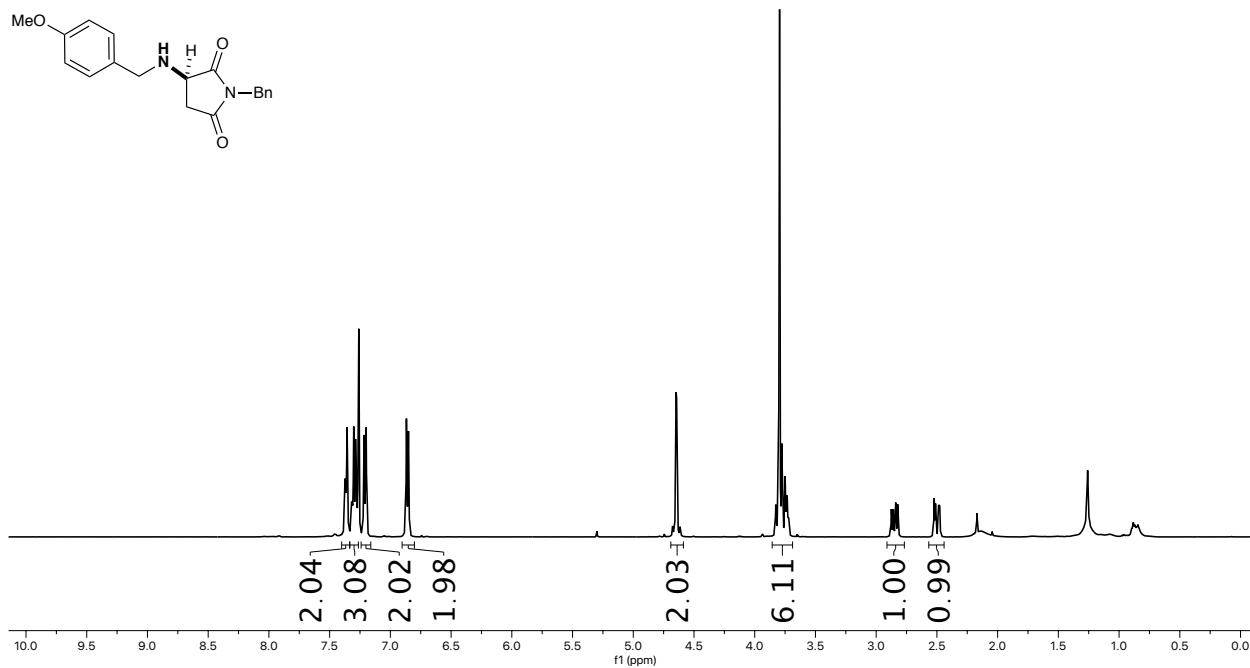
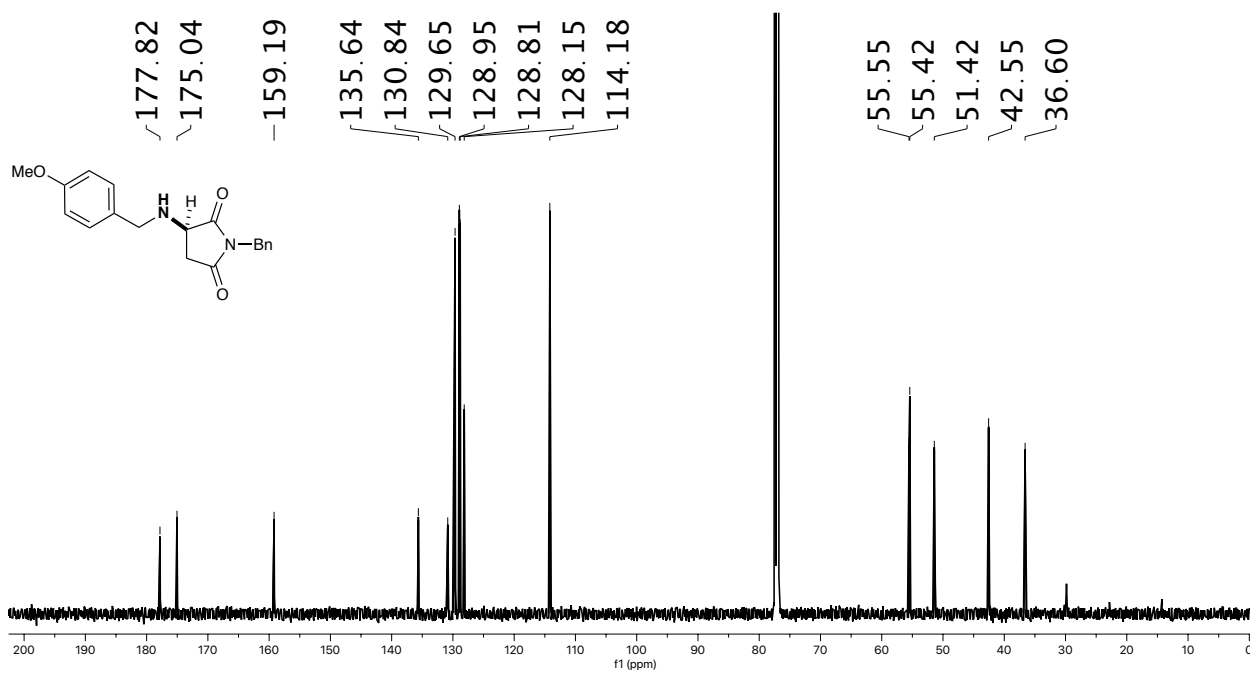
¹H NMR spectrum of II-6 (500 MHz, Chloroform-*d*).**¹³C NMR spectrum of II-6 (126 MHz, Chloroform-*d*).**

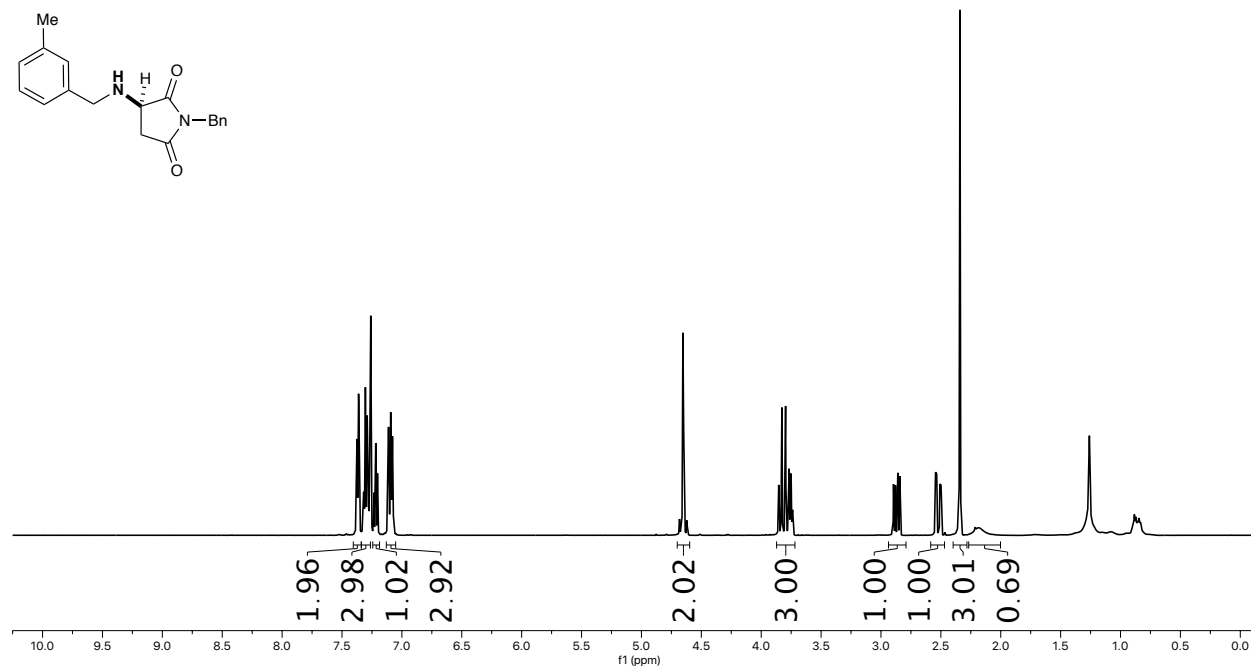
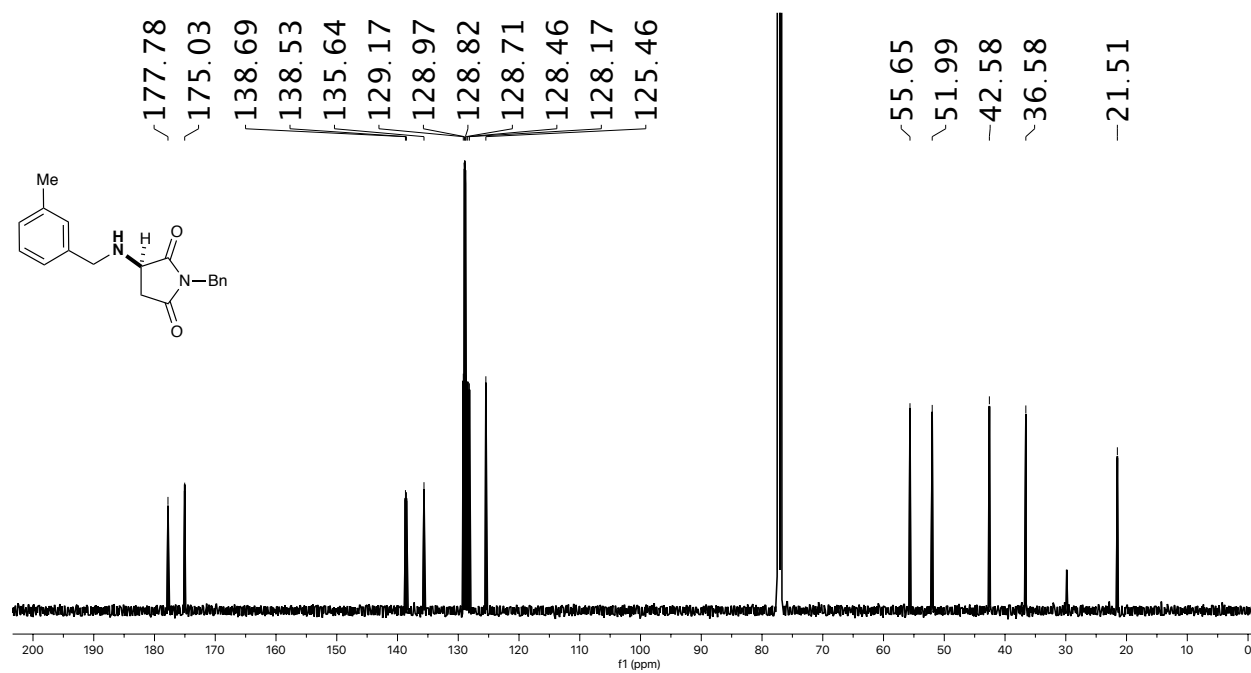
¹H NMR spectrum of II-7 (500 MHz, Chloroform-*d*).**¹³C NMR spectrum of II-7 (126 MHz, Chloroform-*d*).**

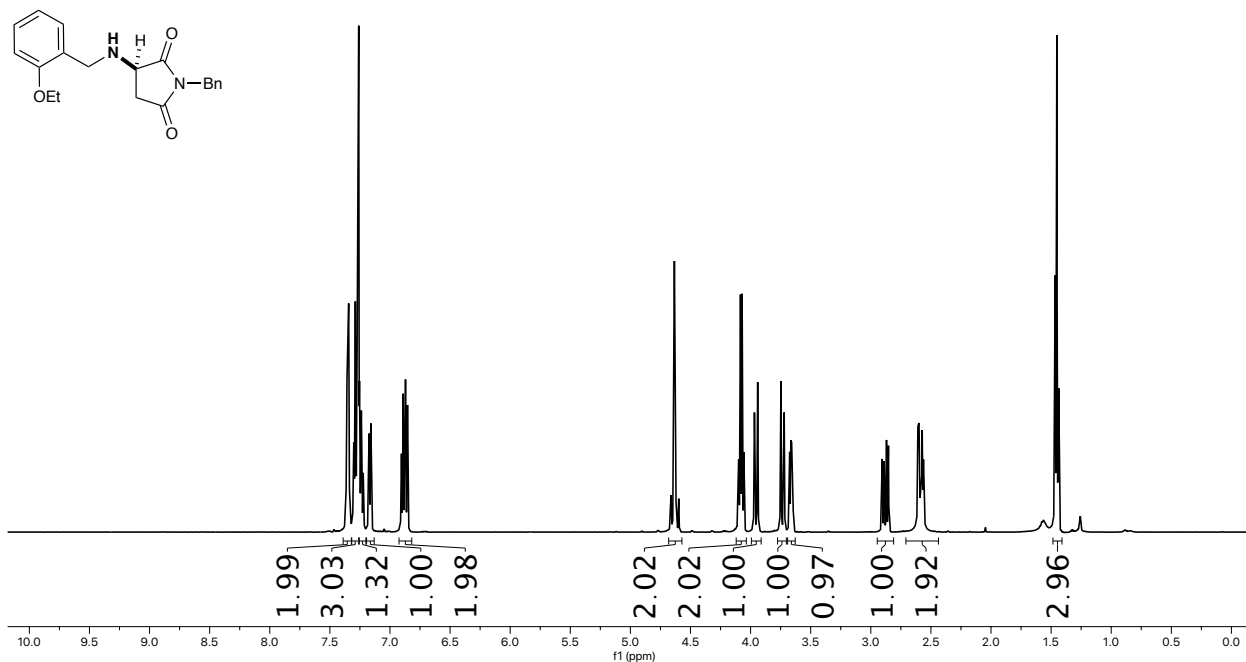
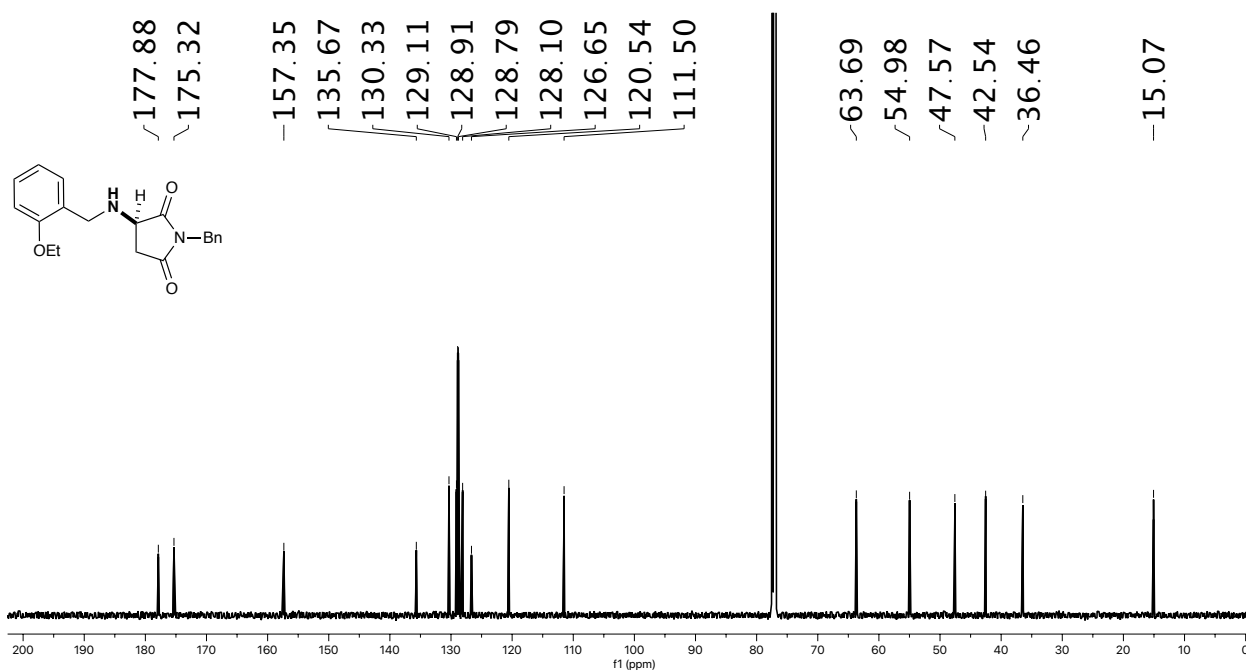
¹H NMR spectrum of II-8 (500 MHz, Chloroform-*d*).**¹³C NMR spectrum of II-8 (126 MHz, Chloroform-*d*).**

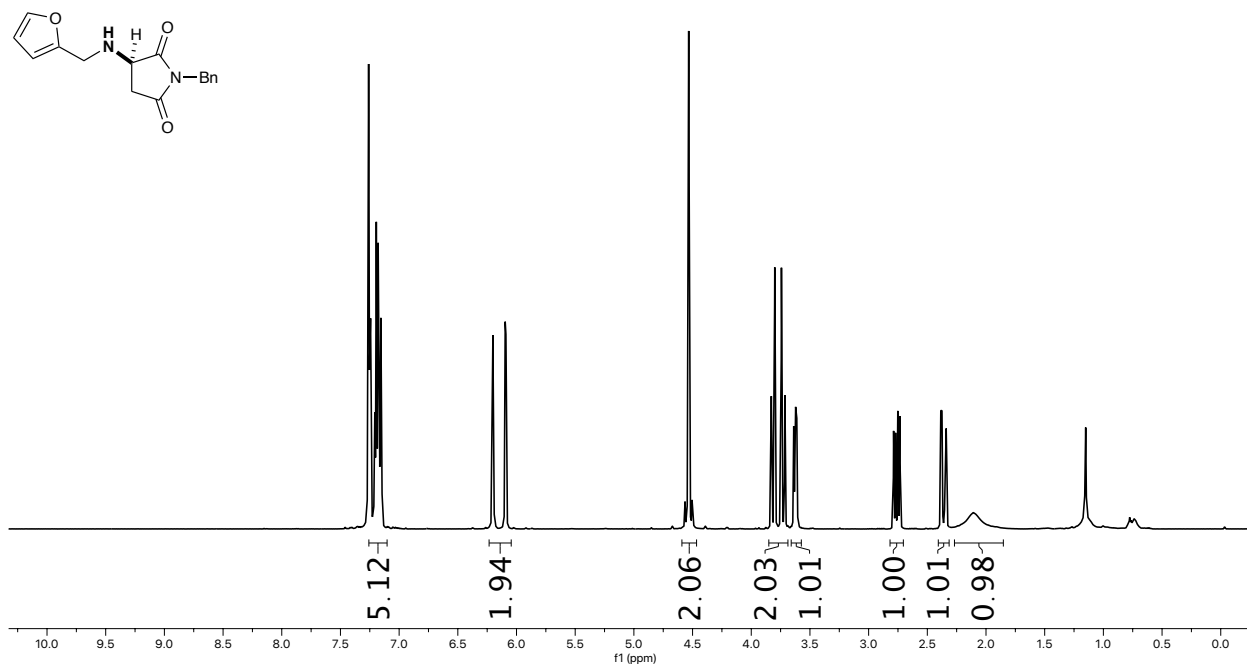
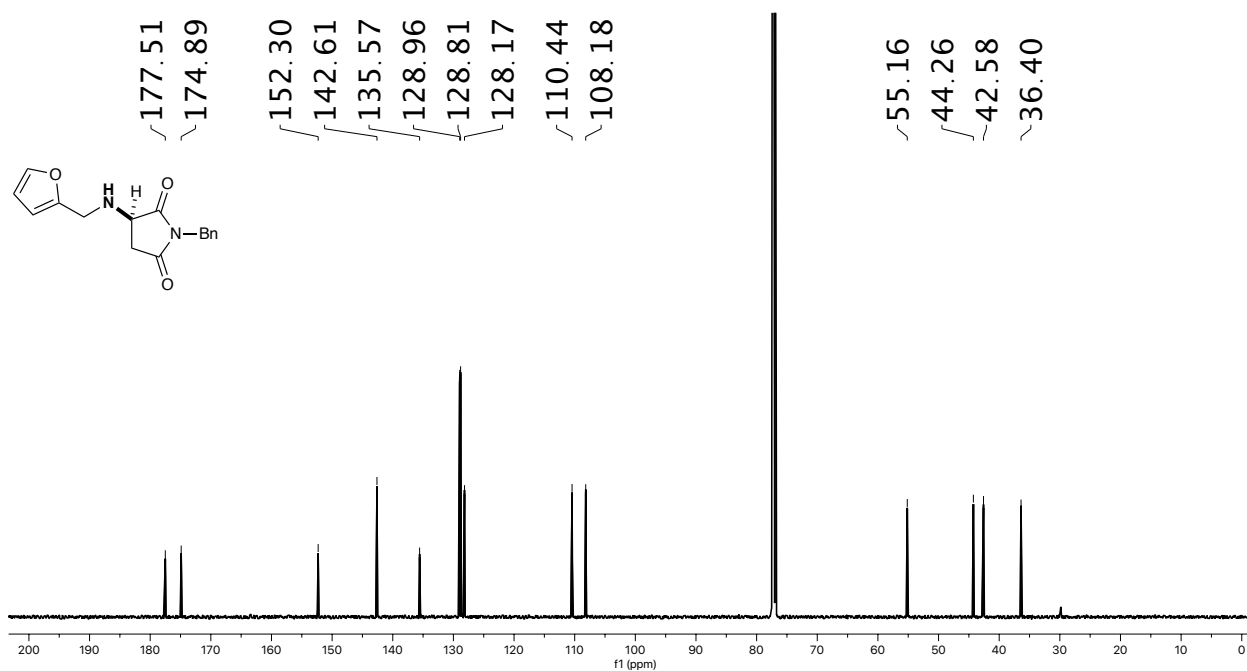
¹H NMR spectrum of II-9 (500 MHz, Chloroform-*d*).**¹³C NMR spectrum of II-9 (126 MHz, Chloroform-*d*).**

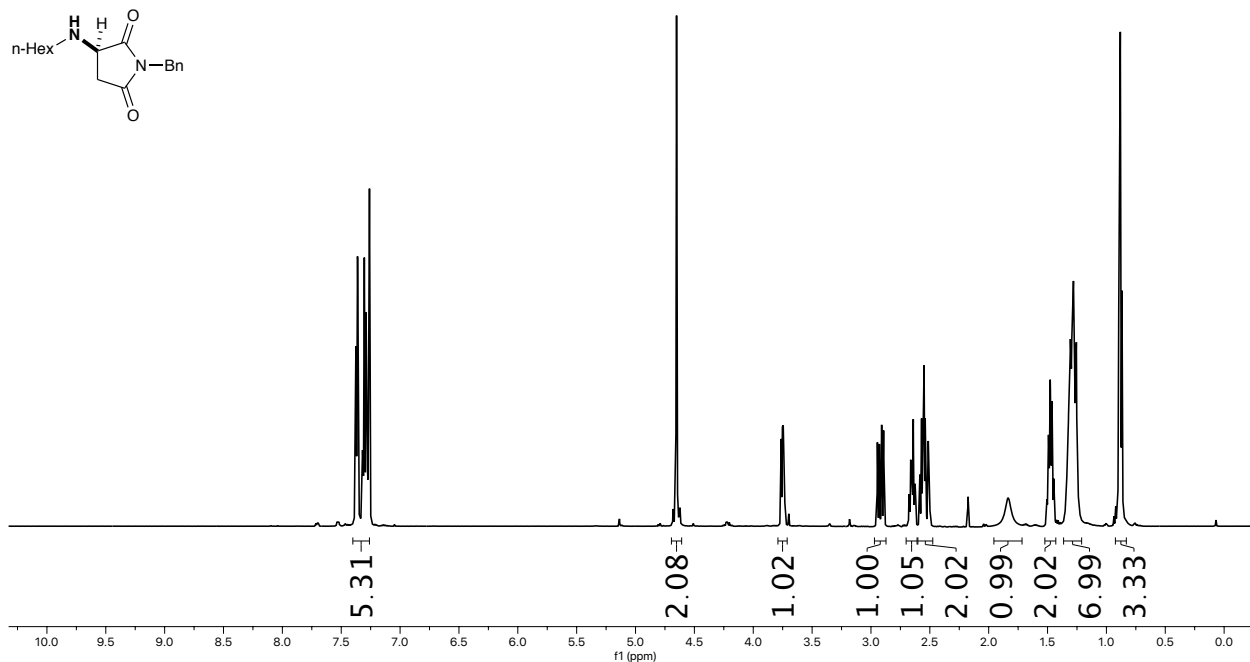
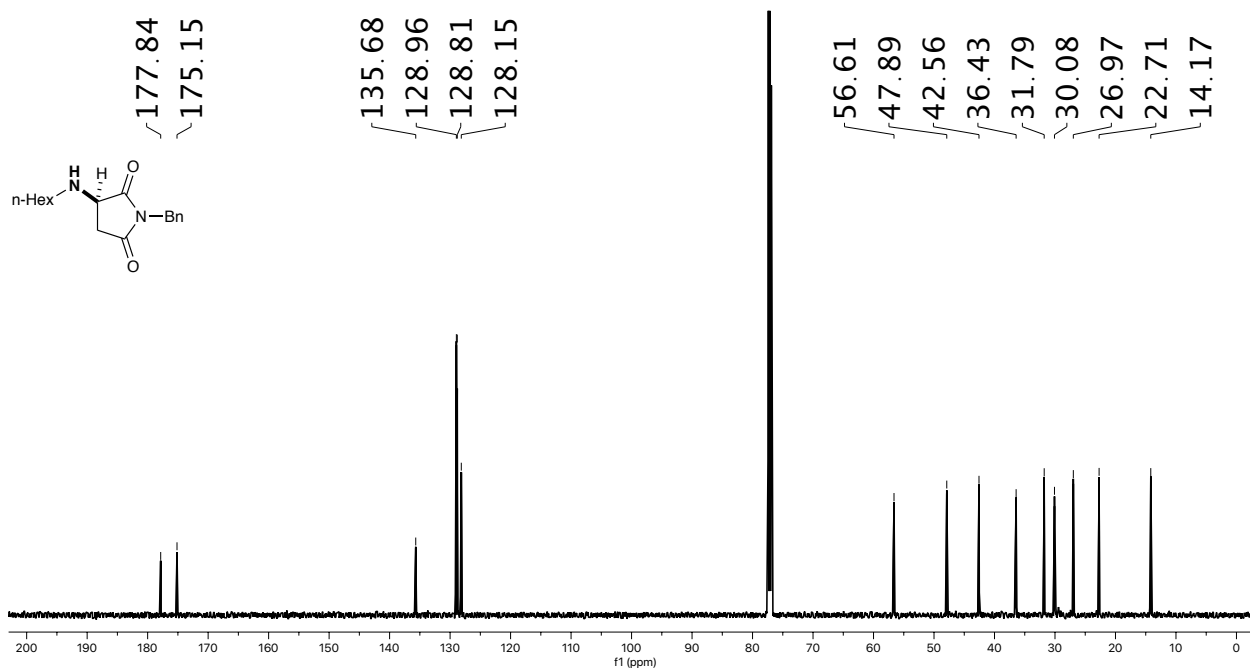
¹H NMR spectrum of II-10 (500 MHz, Chloroform-*d*).**¹³C NMR spectrum of II-10 (126 MHz, Chloroform-*d*).**

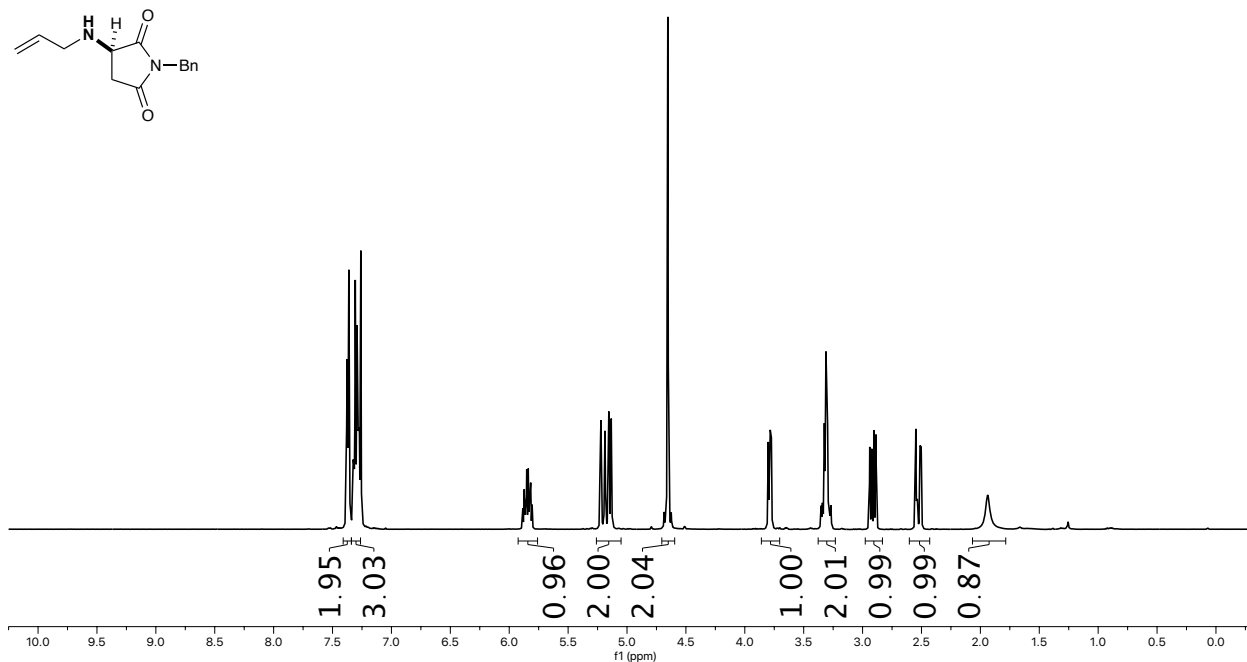
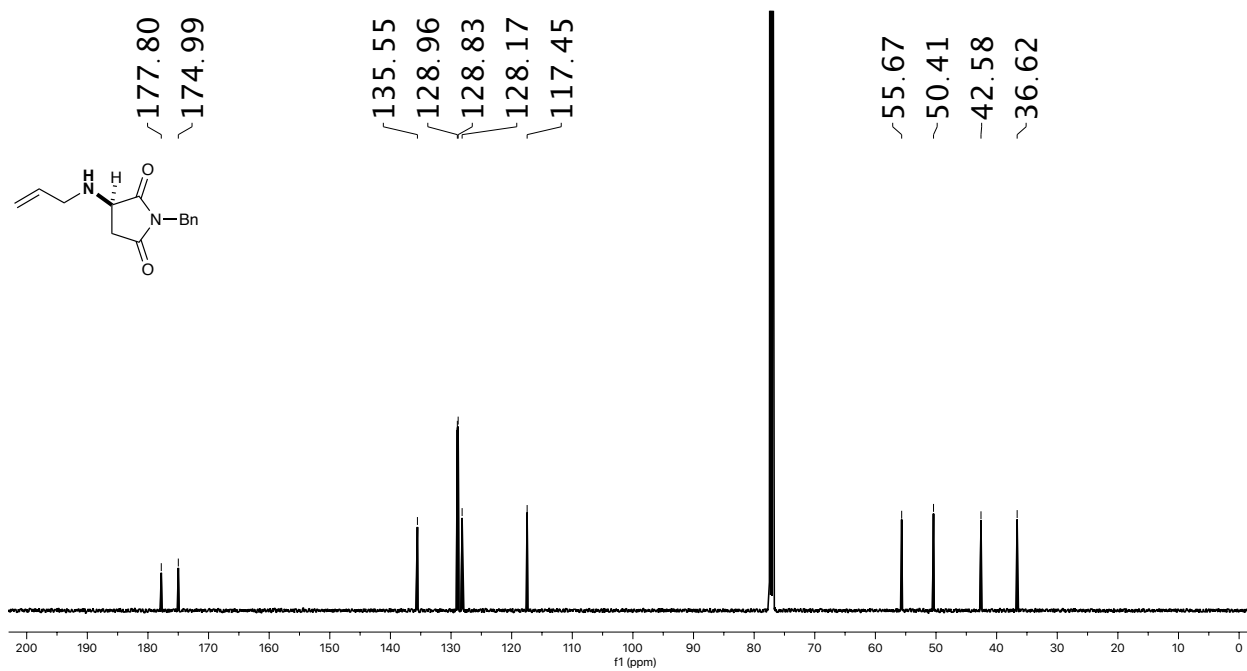
¹H NMR spectrum of II-11 (500 MHz, Chloroform-*d*).**¹³C NMR spectrum of II-11 (126 MHz, Chloroform-*d*).**

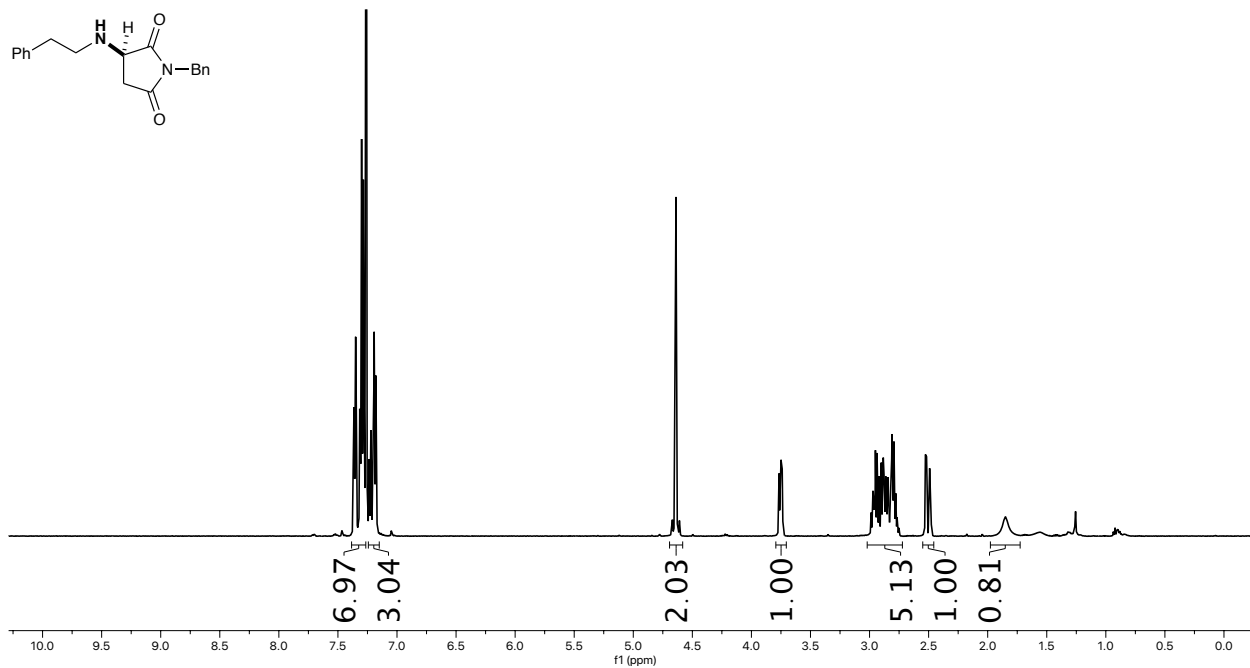
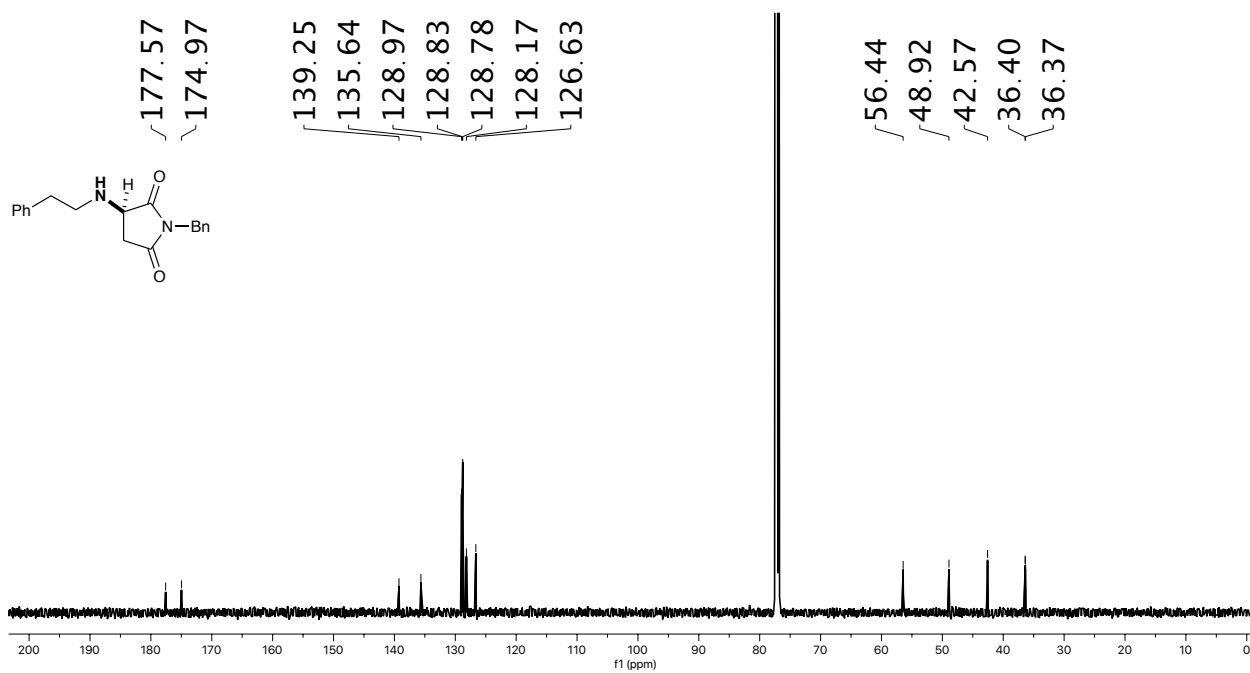
¹H NMR spectrum of II-12 (500 MHz, Chloroform-*d*).**¹³C NMR spectrum of II-12 (126 MHz, Chloroform-*d*).**

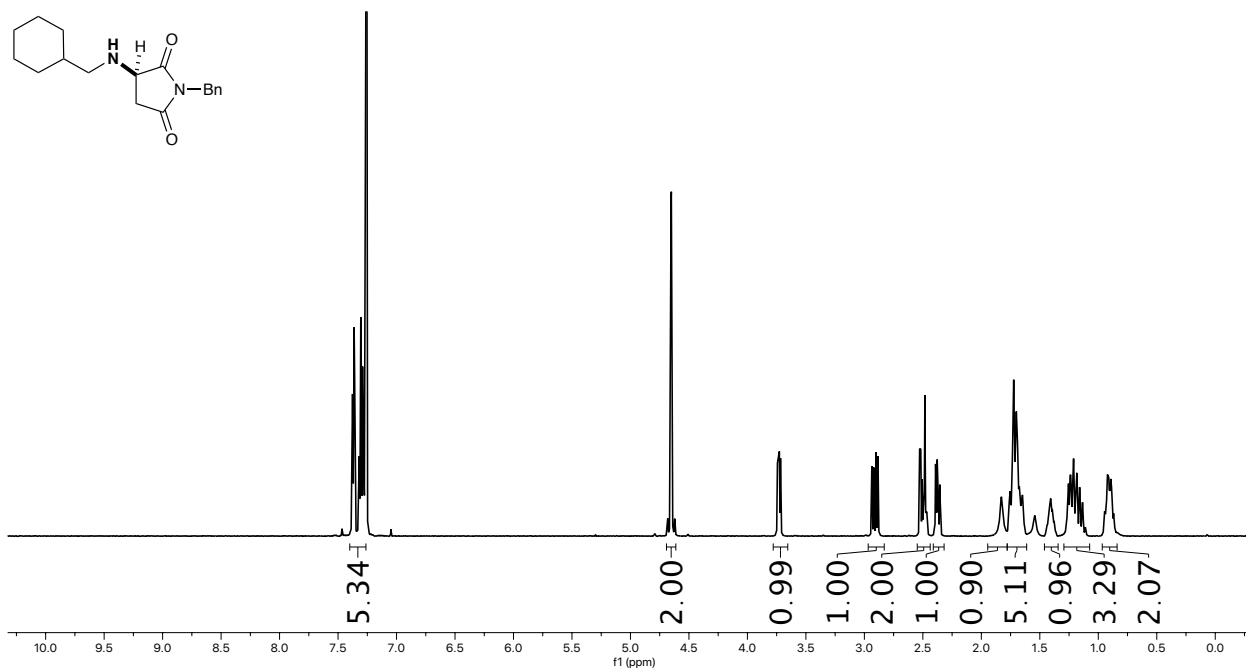
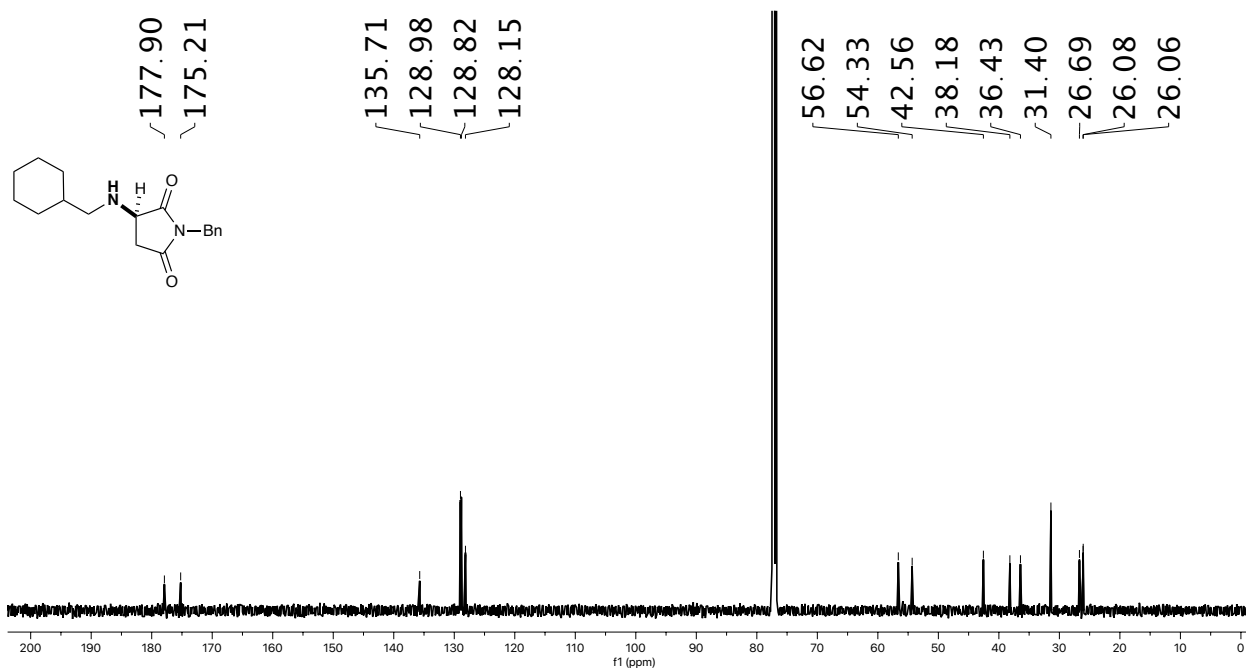
¹H NMR spectrum of II-13 (500 MHz, Chloroform-*d*).**¹³C NMR spectrum of II-13 (126 MHz, Chloroform-*d*).**

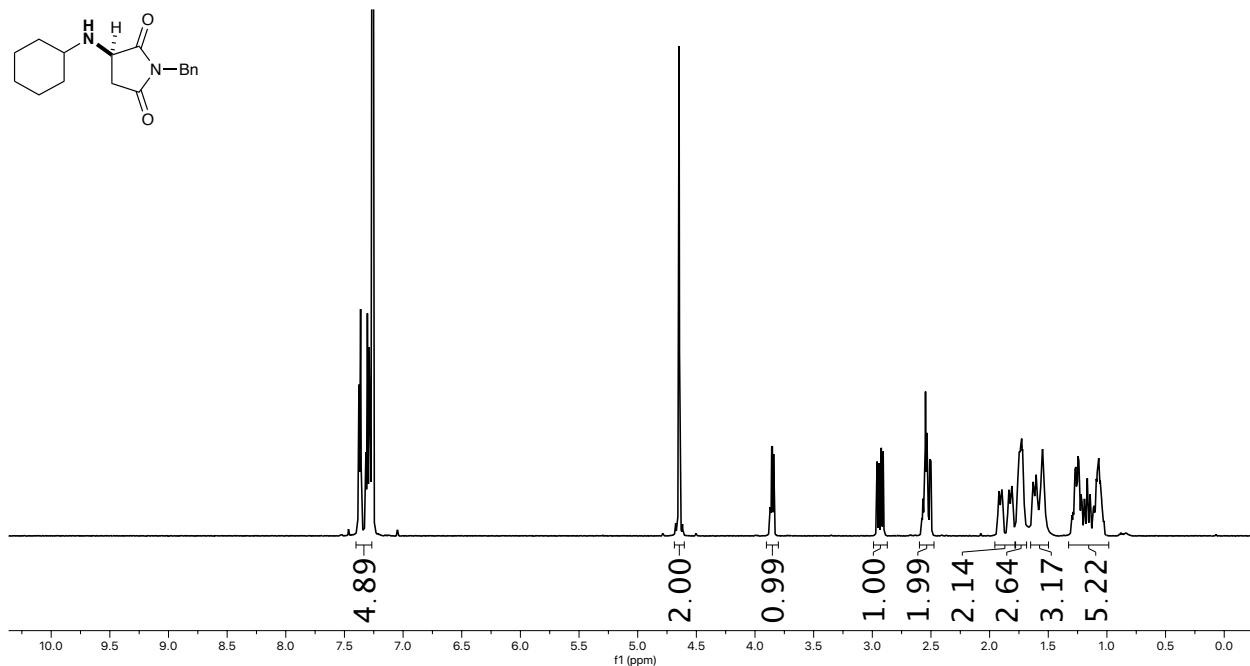
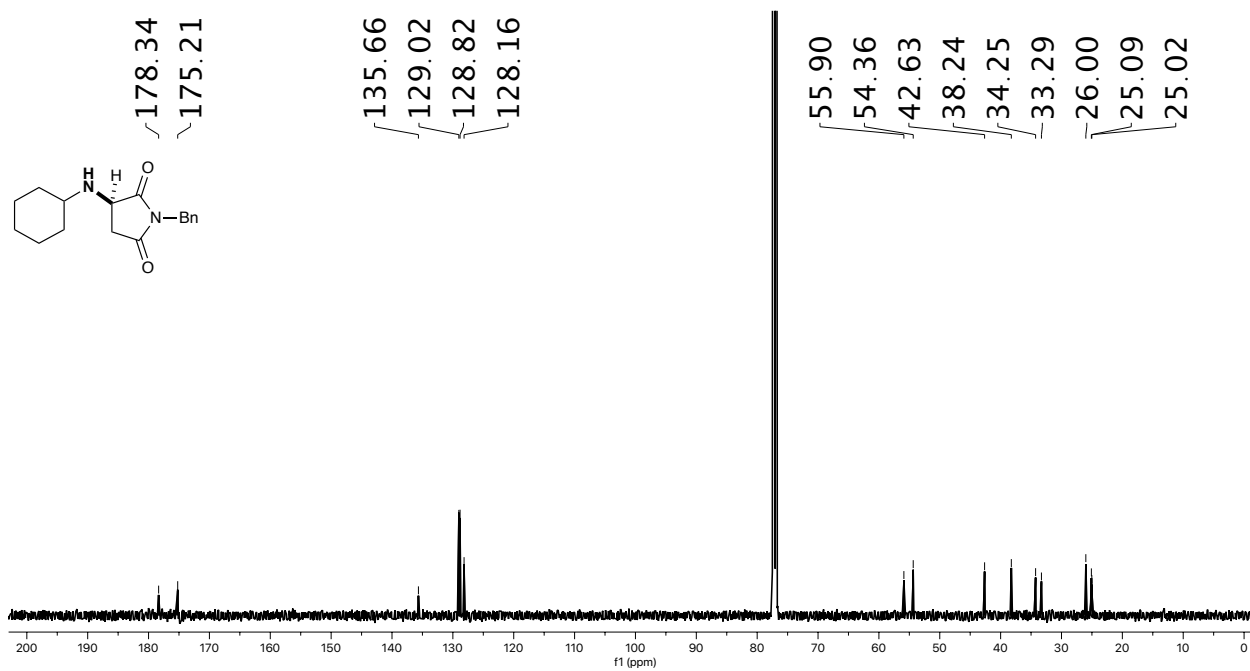
¹H NMR spectrum of II-14 (500 MHz, Chloroform-*d*).**¹³C NMR spectrum of II-14 (126 MHz, Chloroform-*d*).**

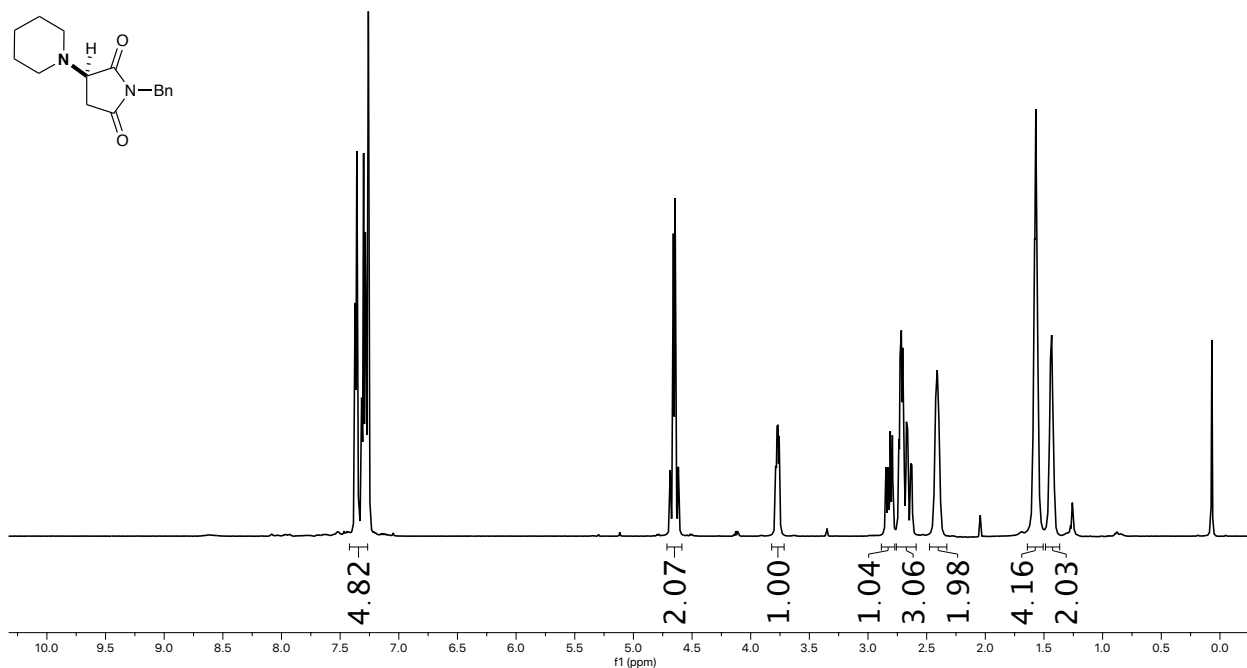
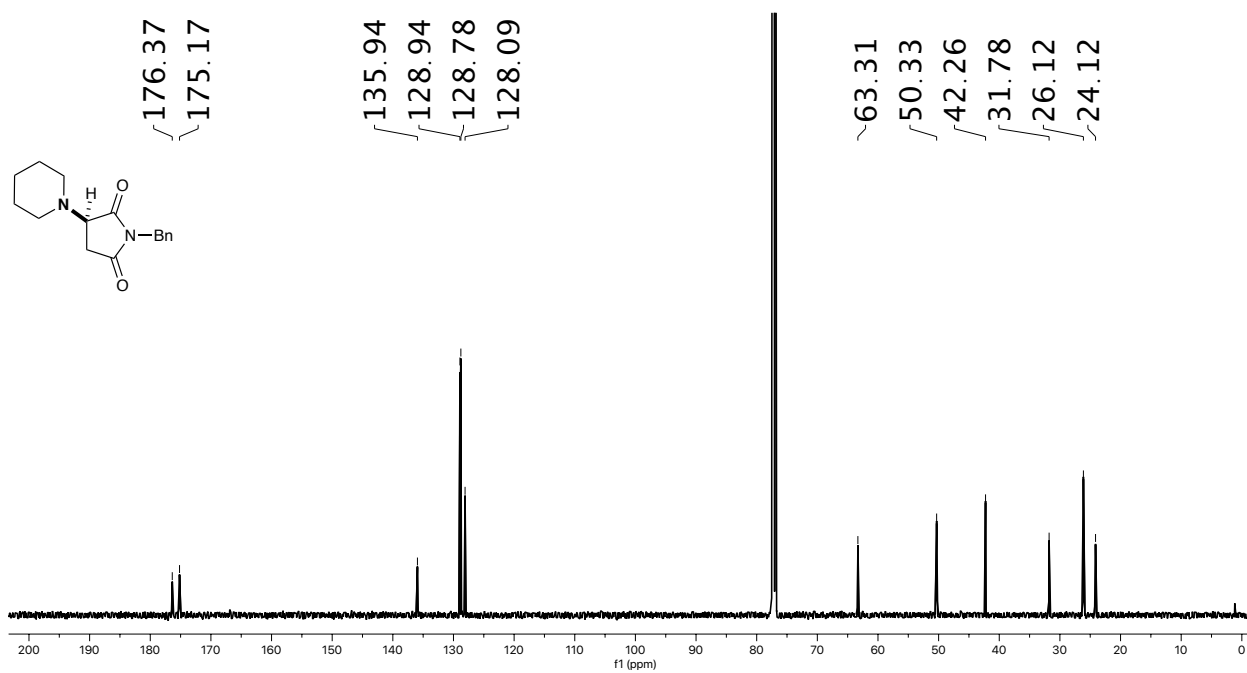
¹H NMR spectrum of II-15 (500 MHz, Chloroform-*d*).**¹³C NMR spectrum of II-15 (126 MHz, Chloroform-*d*).**

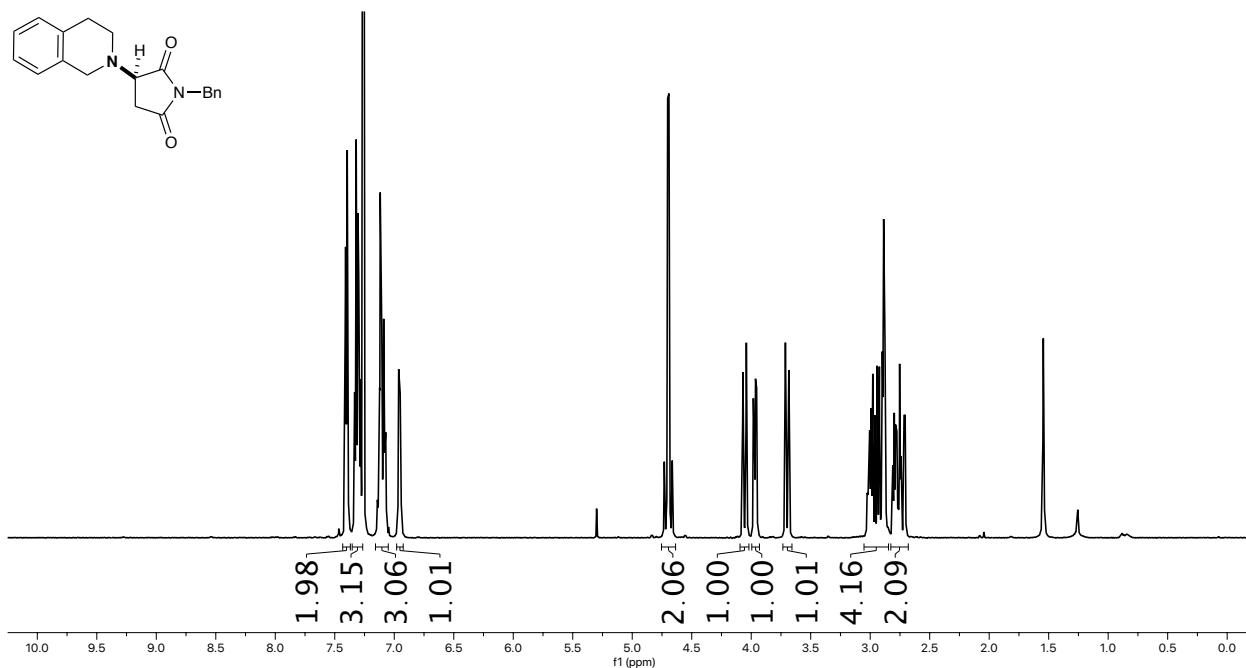
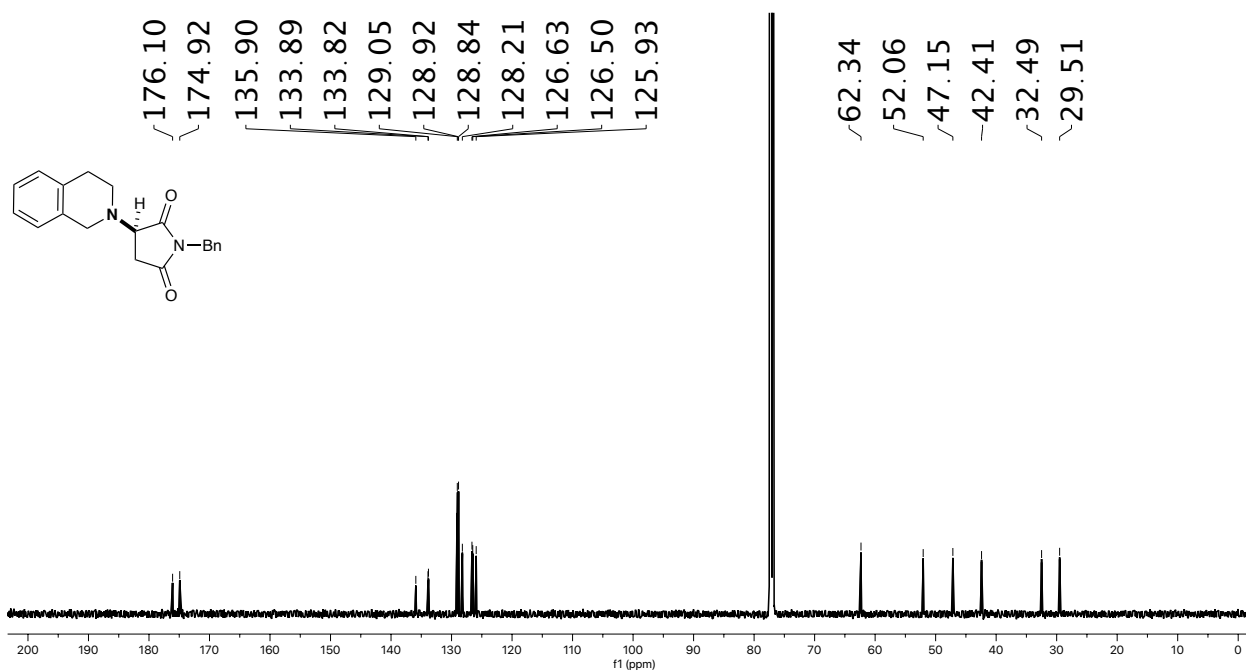
¹H NMR spectrum of II-16 (500 MHz, Chloroform-*d*).**¹³C NMR spectrum of II-16 (126 MHz, Chloroform-*d*).**

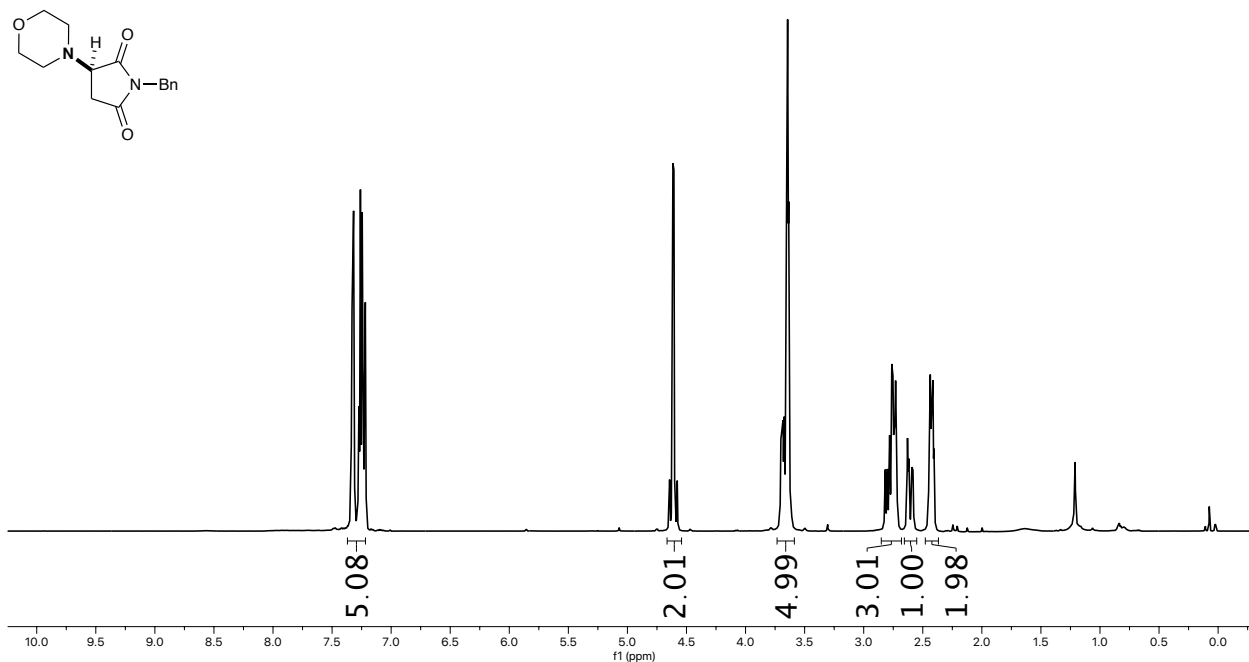
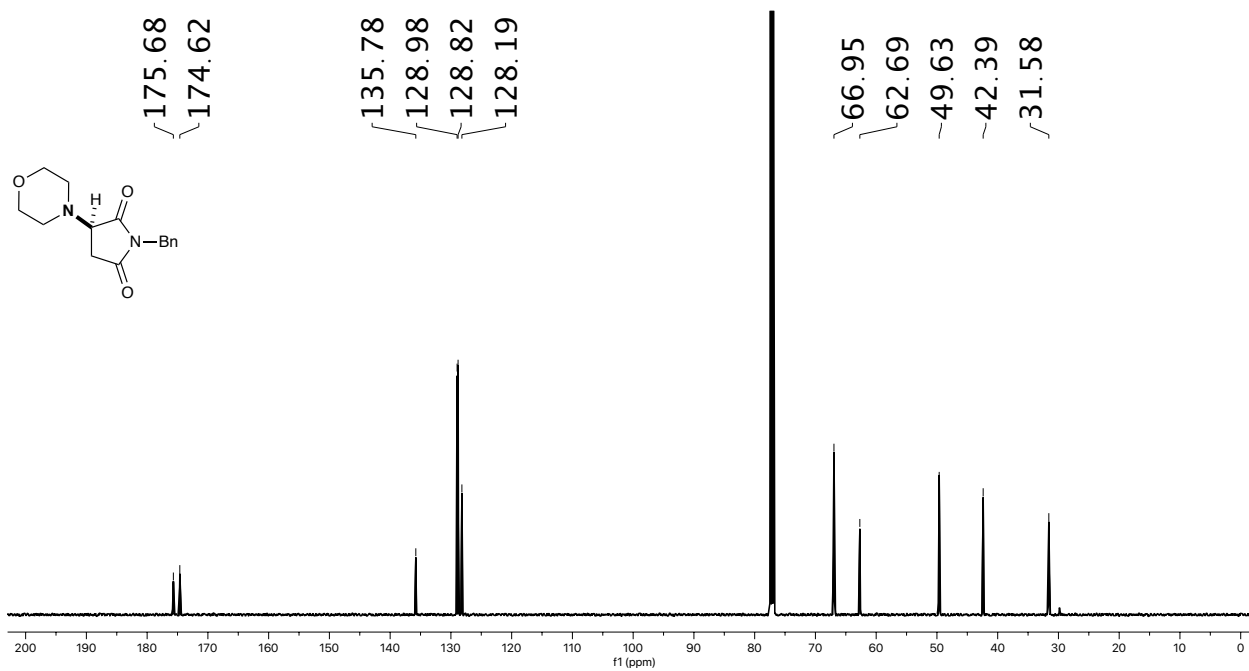
¹H NMR spectrum of II-17 (500 MHz, Chloroform-*d*).**¹³C NMR spectrum of II-17 (126 MHz, Chloroform-*d*).**

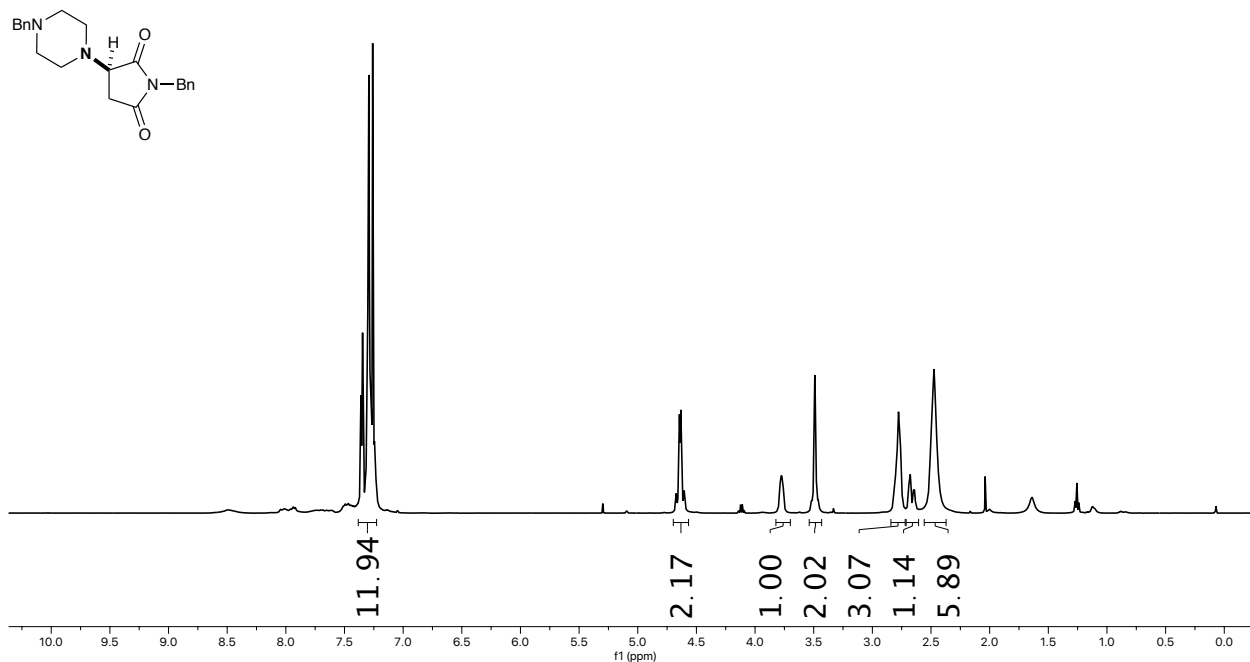
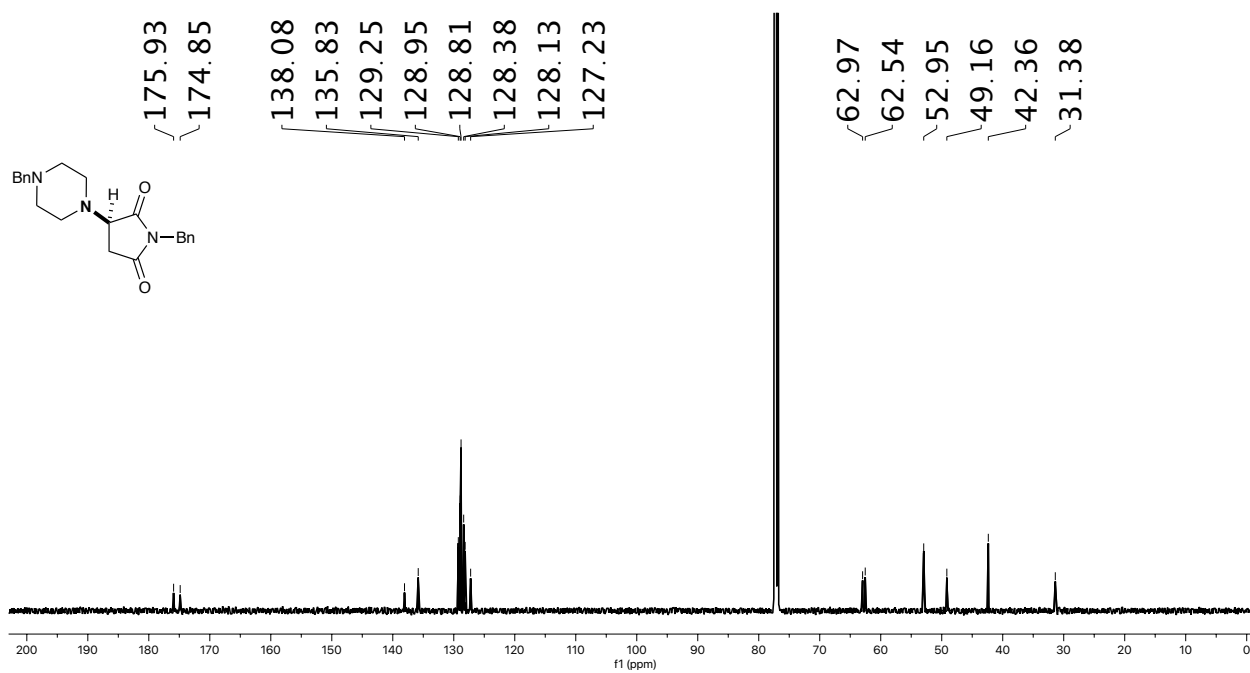
¹H NMR spectrum of II-18 (500 MHz, Chloroform-*d*).**¹³C NMR spectrum of II-18 (126 MHz, Chloroform-*d*).**

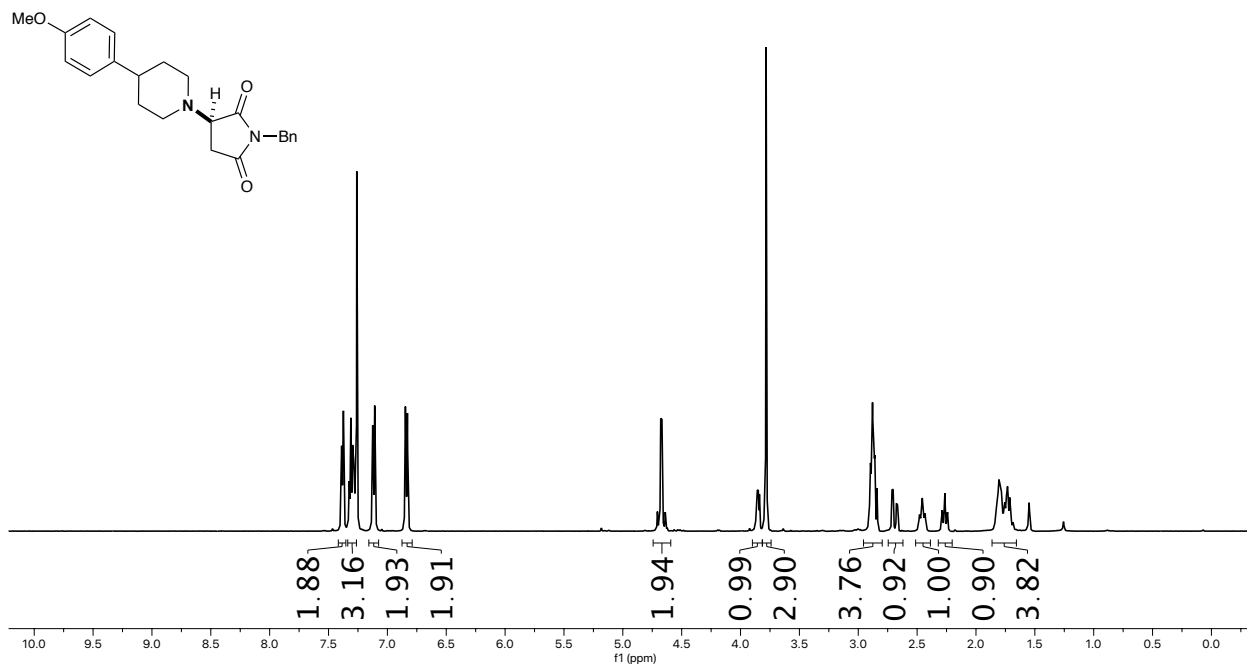
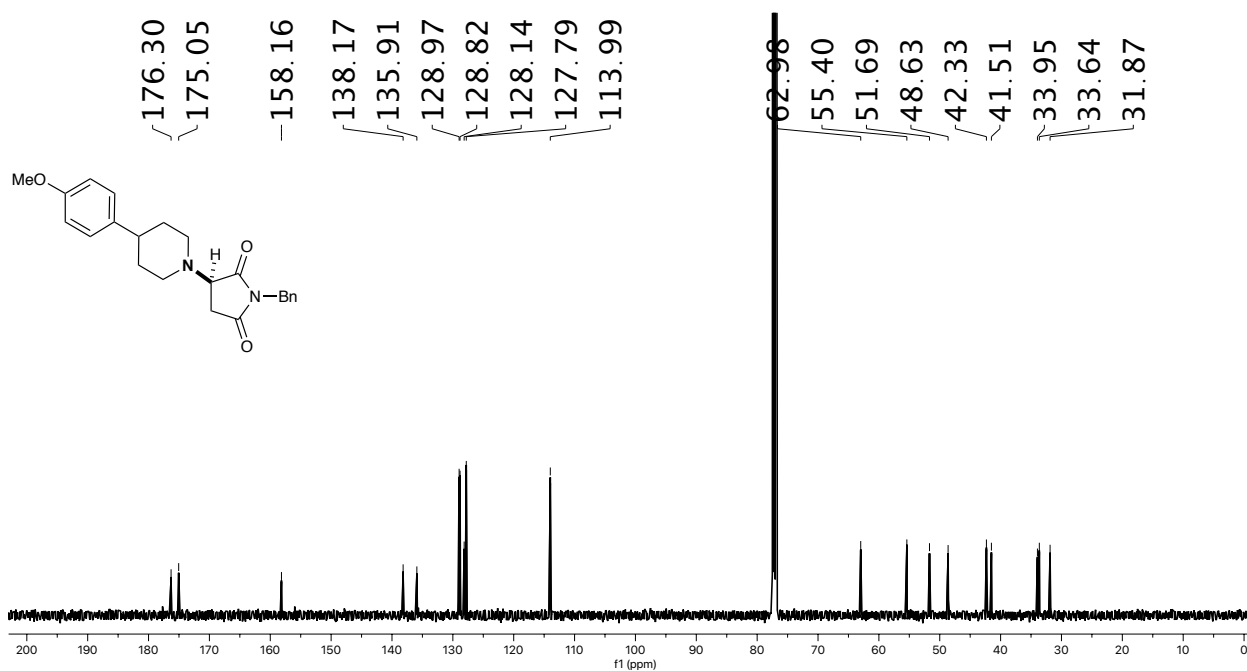
¹H NMR spectrum of II-19 (500 MHz, Chloroform-*d*).**¹³C NMR spectrum of II-19 (126 MHz, Chloroform-*d*).**

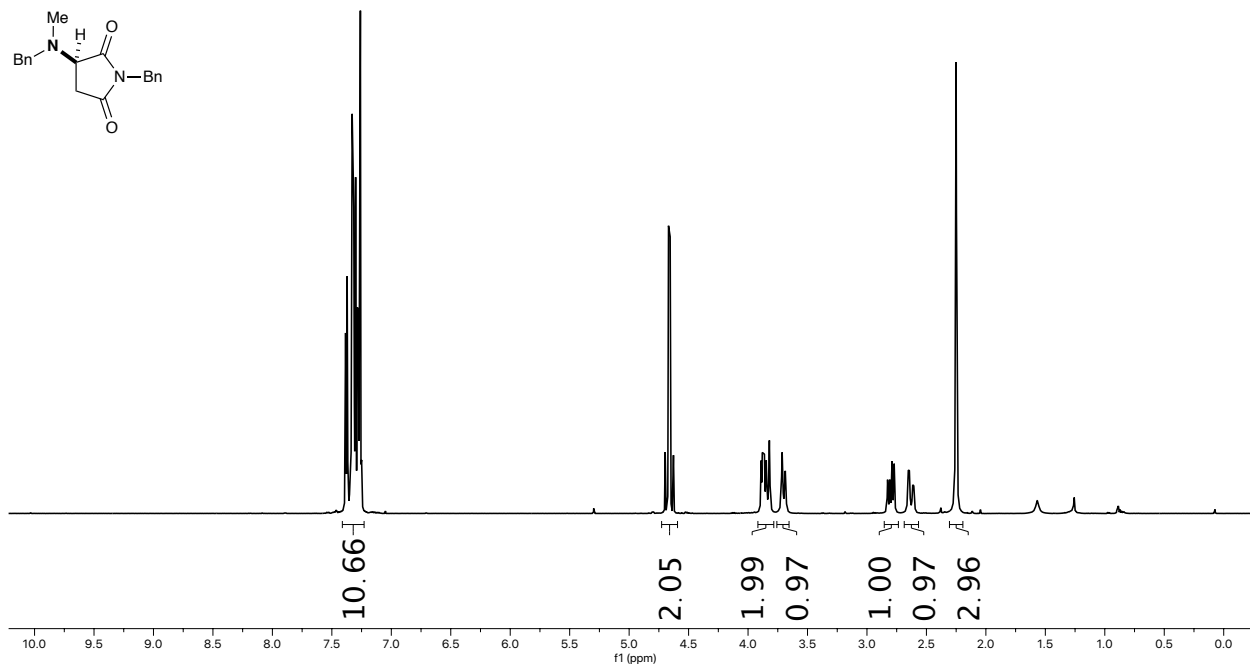
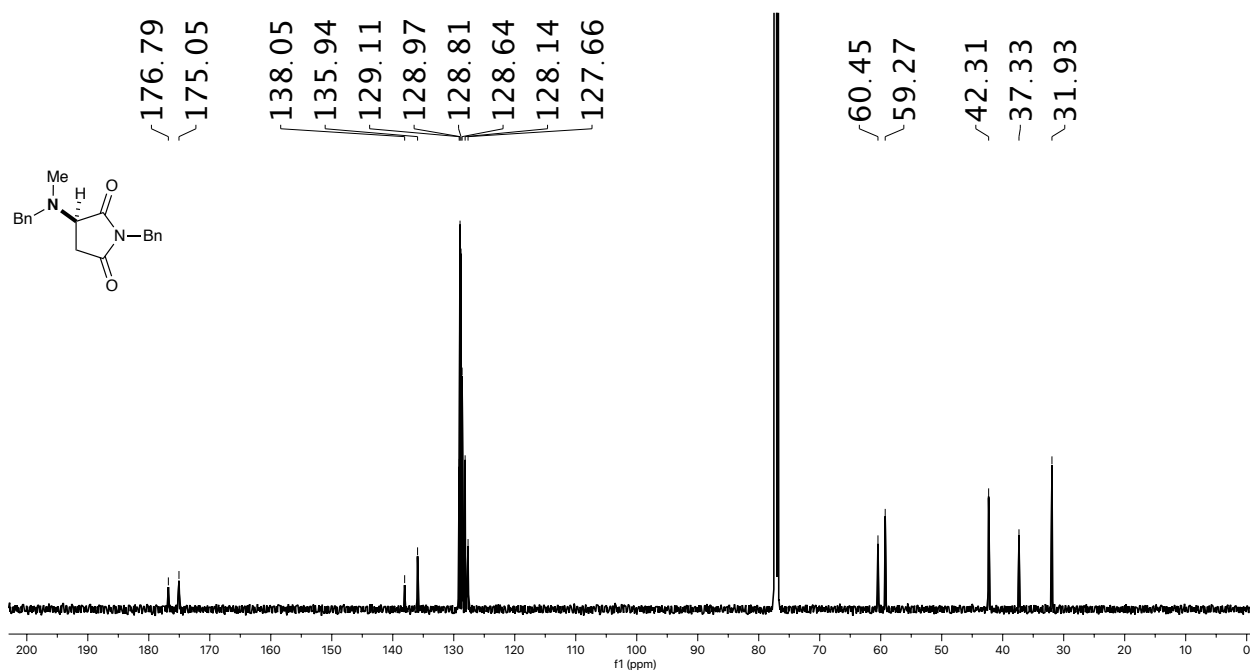
¹H NMR spectrum of II-20 (500 MHz, Chloroform-*d*).**¹³C NMR spectrum of II-20 (126 MHz, Chloroform-*d*).**

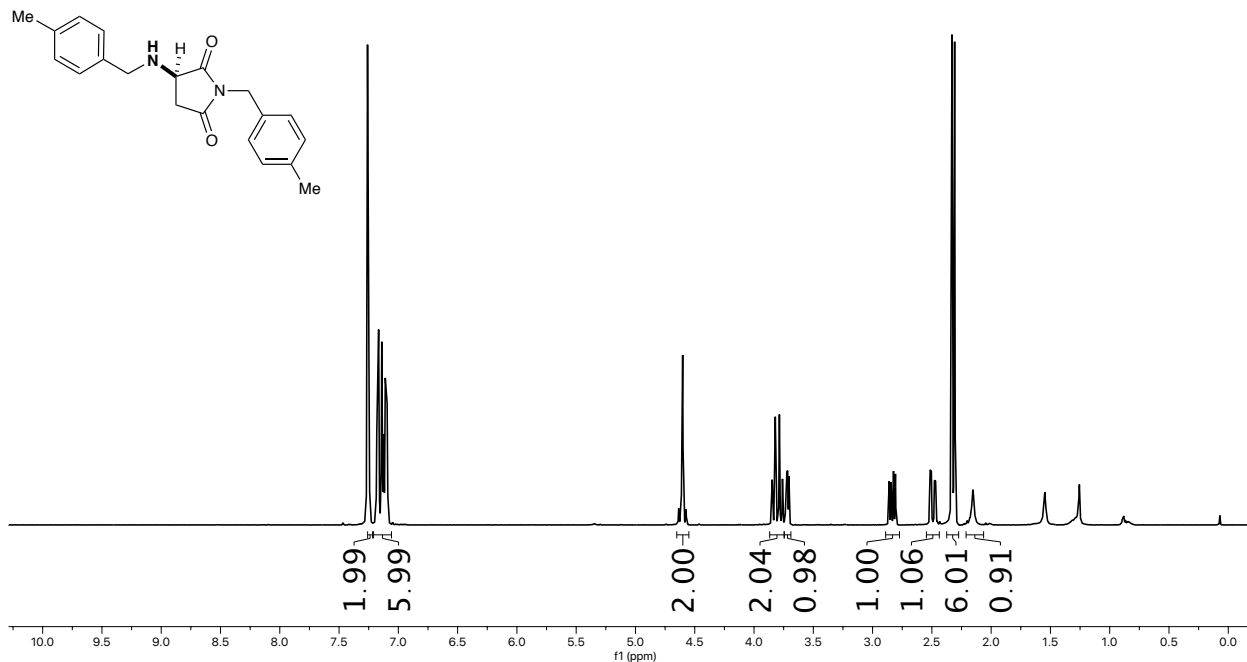
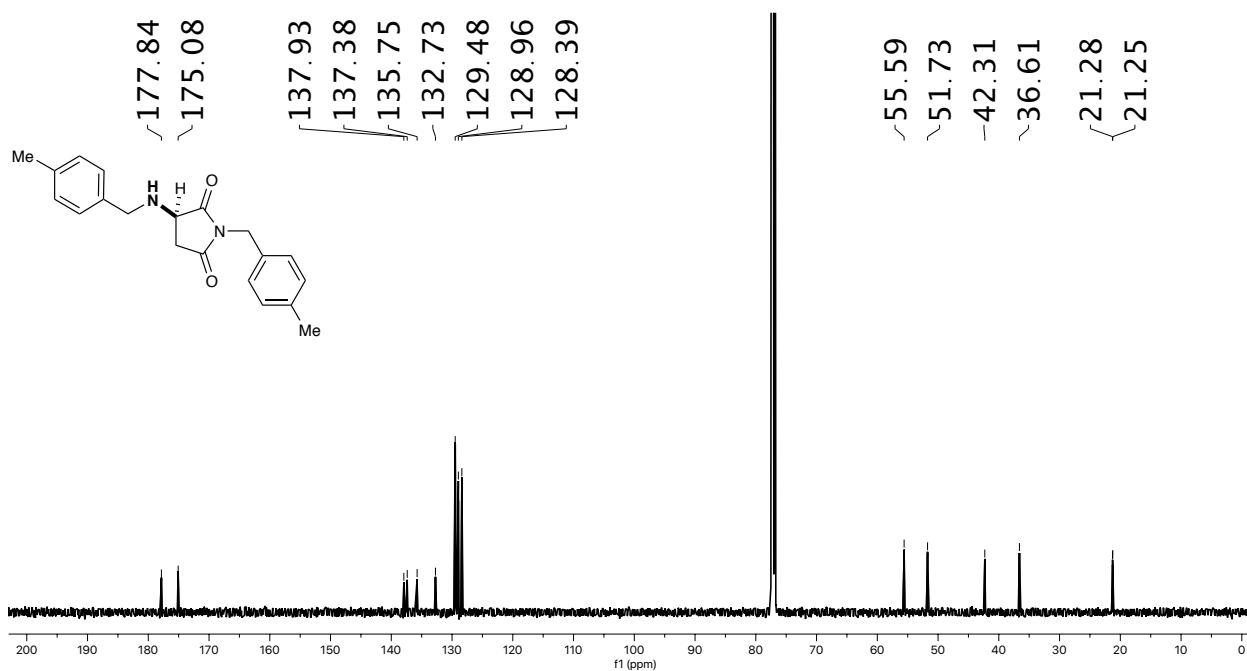
¹H NMR spectrum of II-21 (500 MHz, Chloroform-*d*).**¹³C NMR spectrum of II-21 (126 MHz, Chloroform-*d*).**

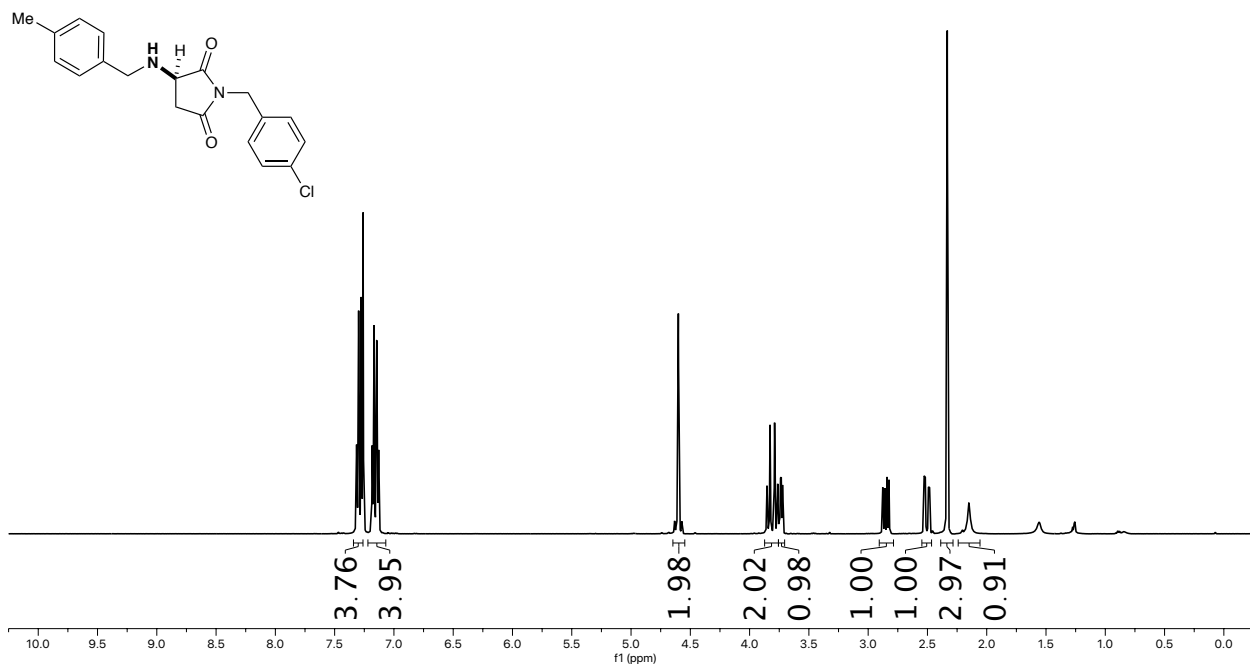
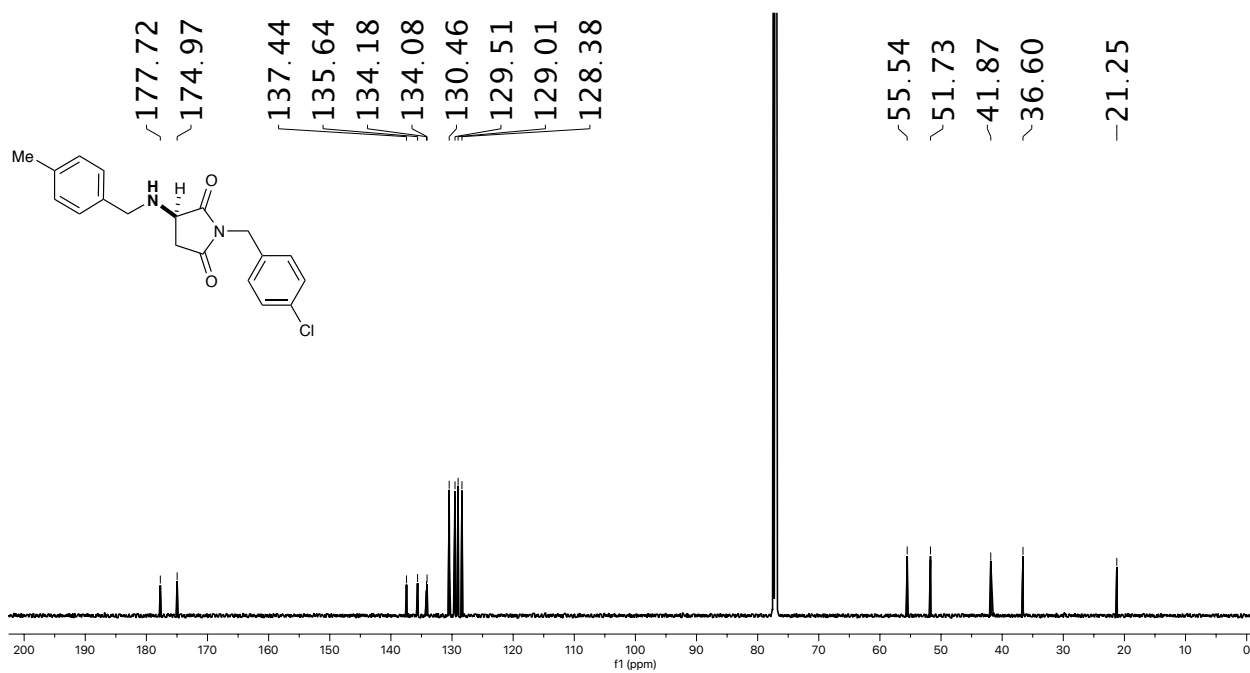
¹H NMR spectrum of II-22 (500 MHz, Chloroform-*d*).**¹³C NMR spectrum of II-22 (126 MHz, Chloroform-*d*).**

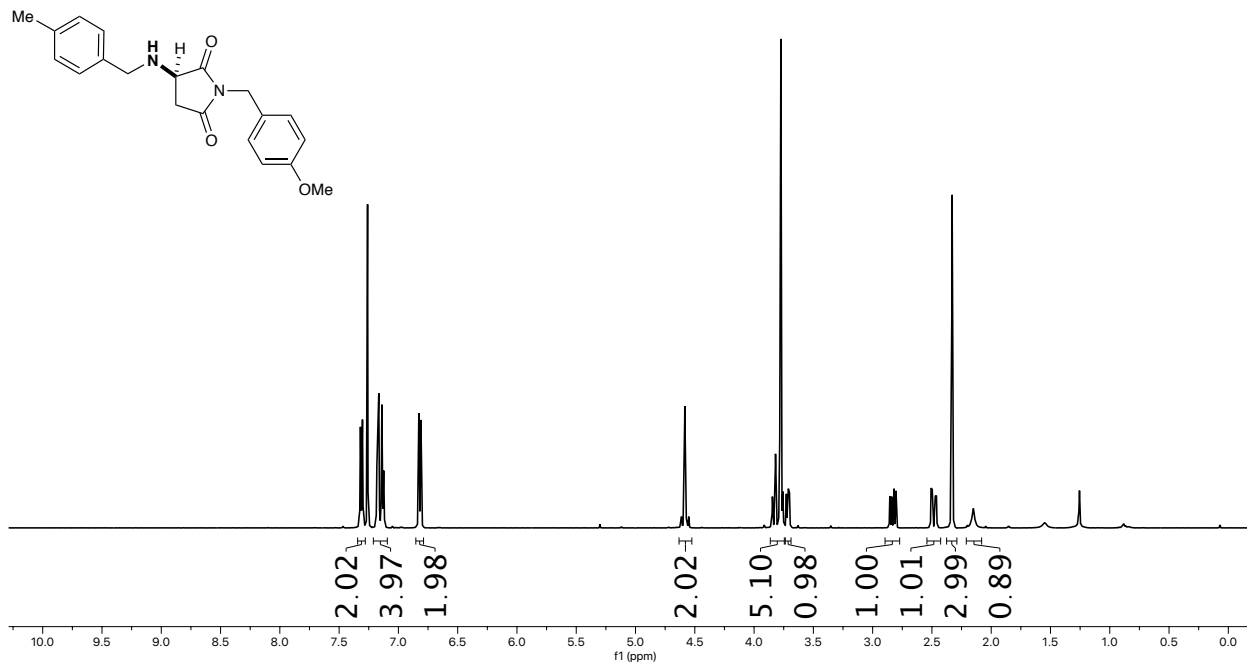
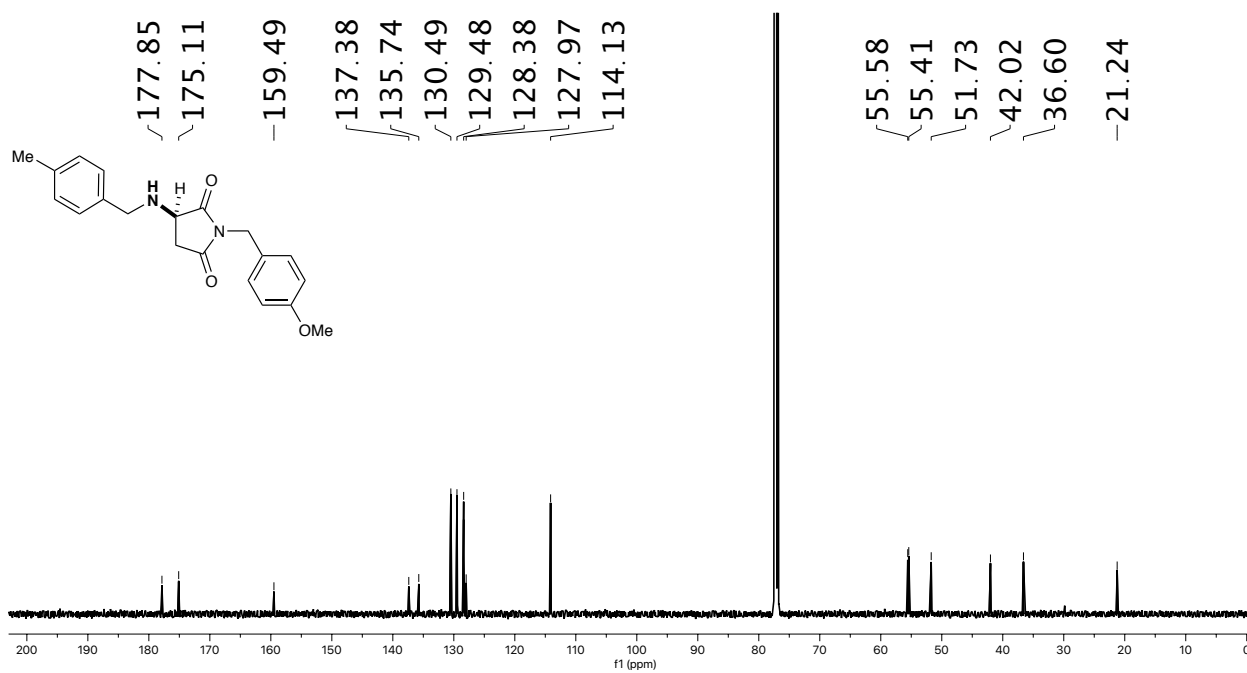
¹H NMR spectrum of II-23 (500 MHz, Chloroform-*d*).**¹³C NMR spectrum of II-23 (126 MHz, Chloroform-*d*).**

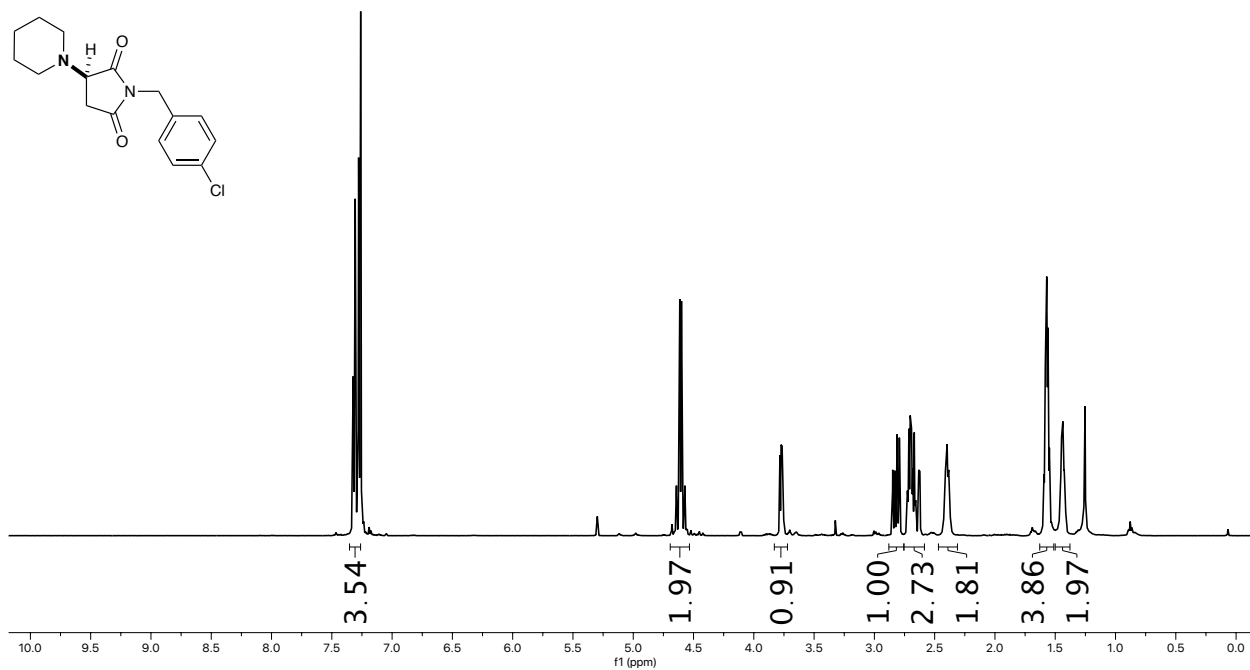
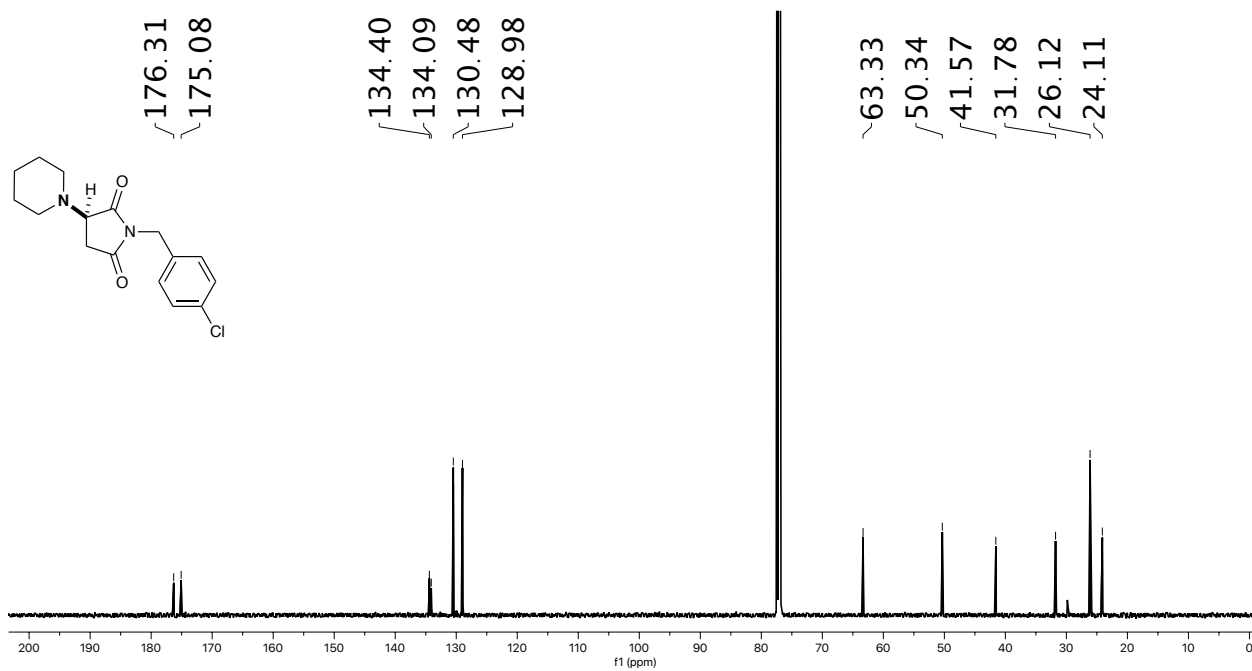
¹H NMR spectrum of II-24 (500 MHz, Chloroform-*d*).**¹³C NMR spectrum of II-24 (126 MHz, Chloroform-*d*).**

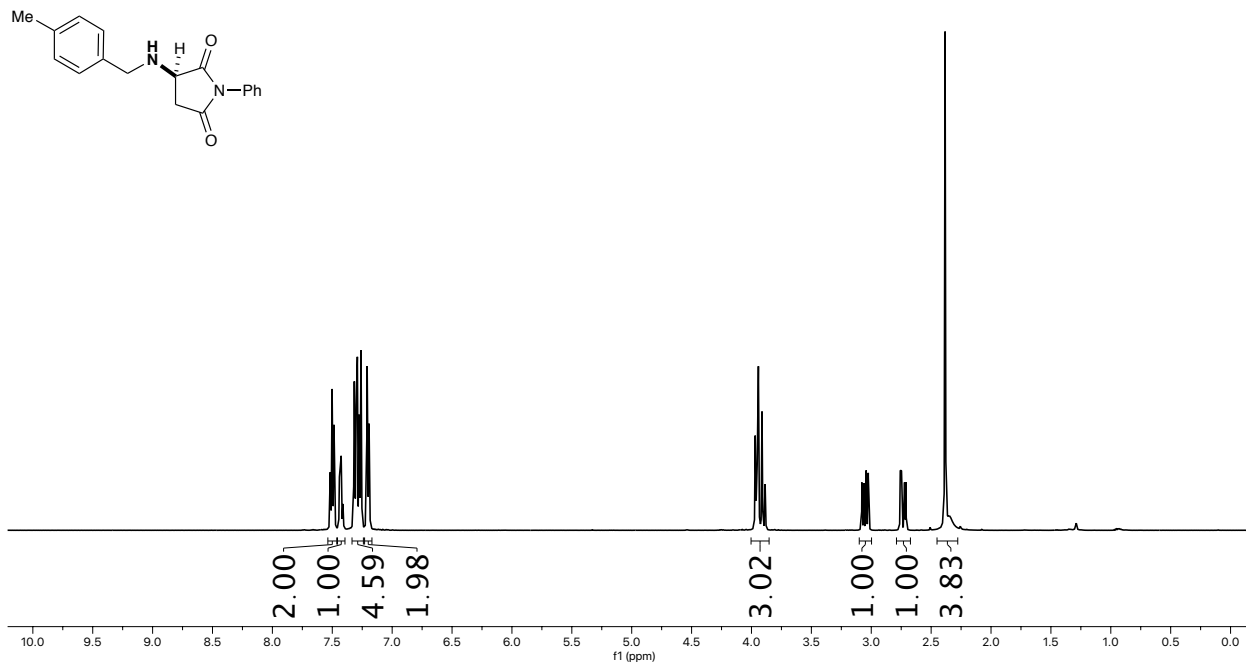
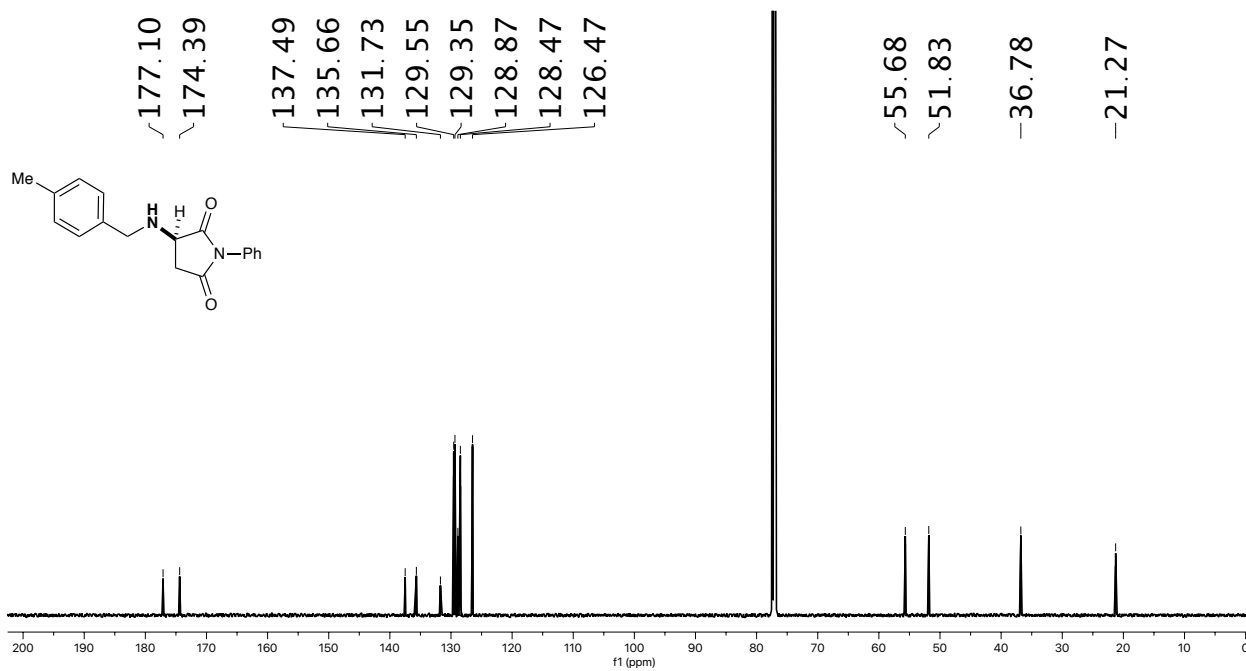
¹H NMR spectrum of II-25 (500 MHz, Chloroform-*d*).**¹³C NMR spectrum of II-25 (126 MHz, Chloroform-*d*).**

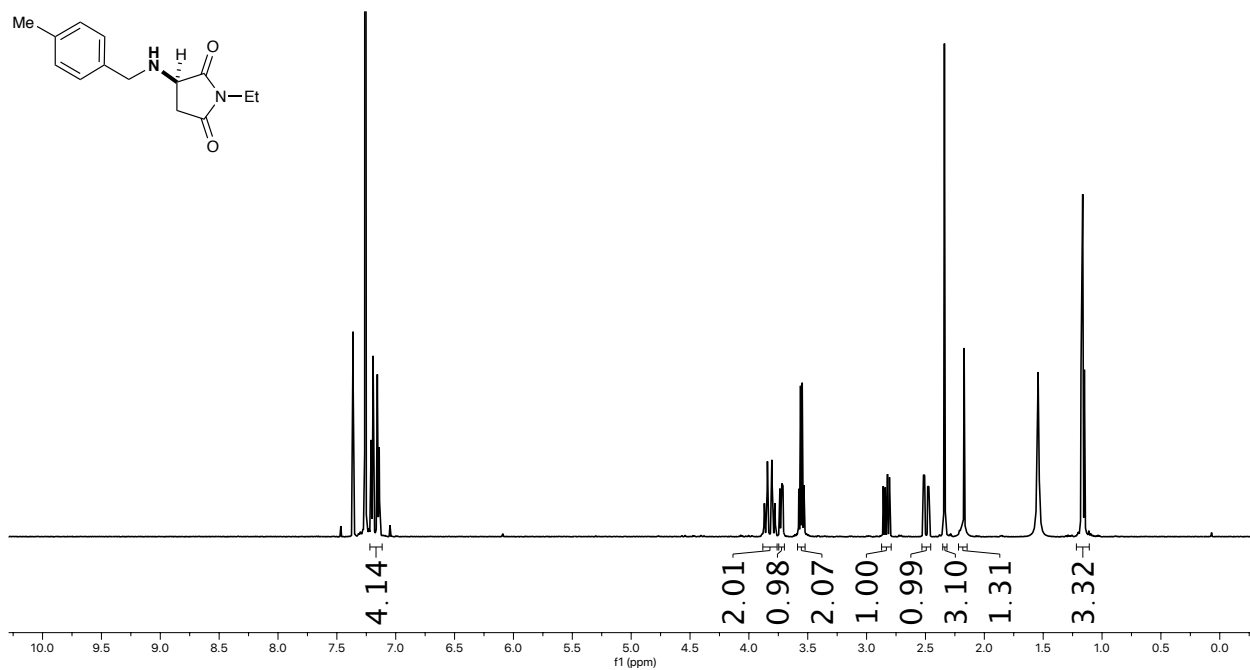
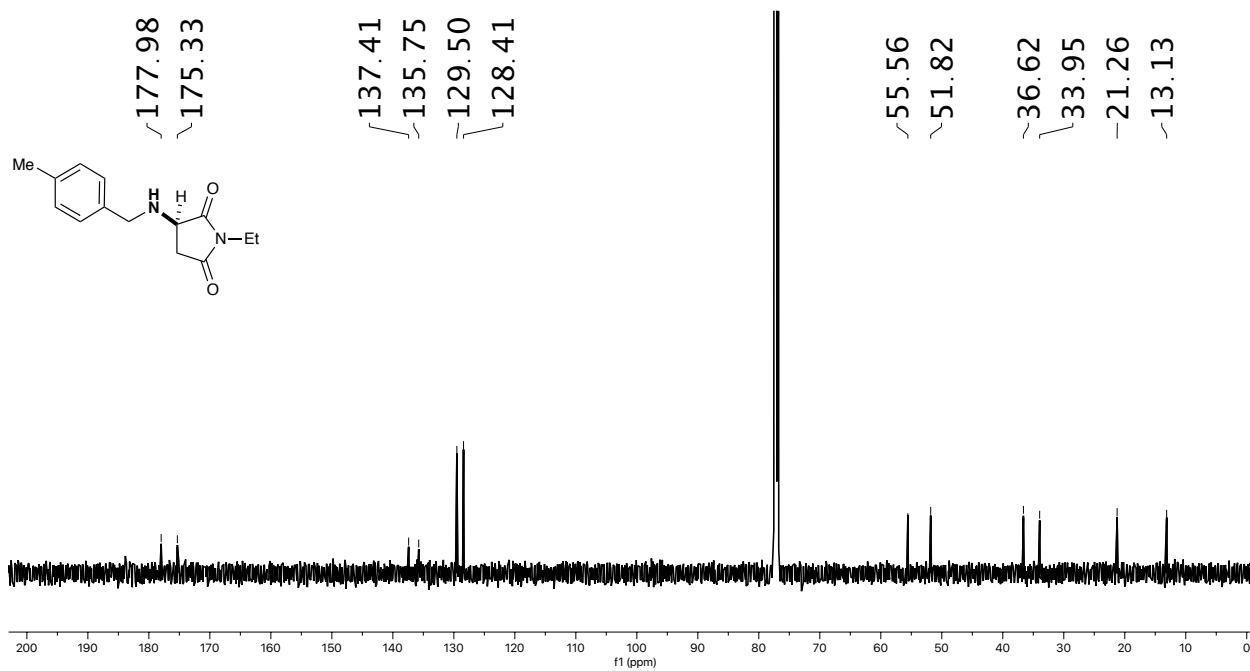
¹H NMR spectrum of II-26 (500 MHz, Chloroform-*d*).**¹³C NMR spectrum of II-26 (126 MHz, Chloroform-*d*).**

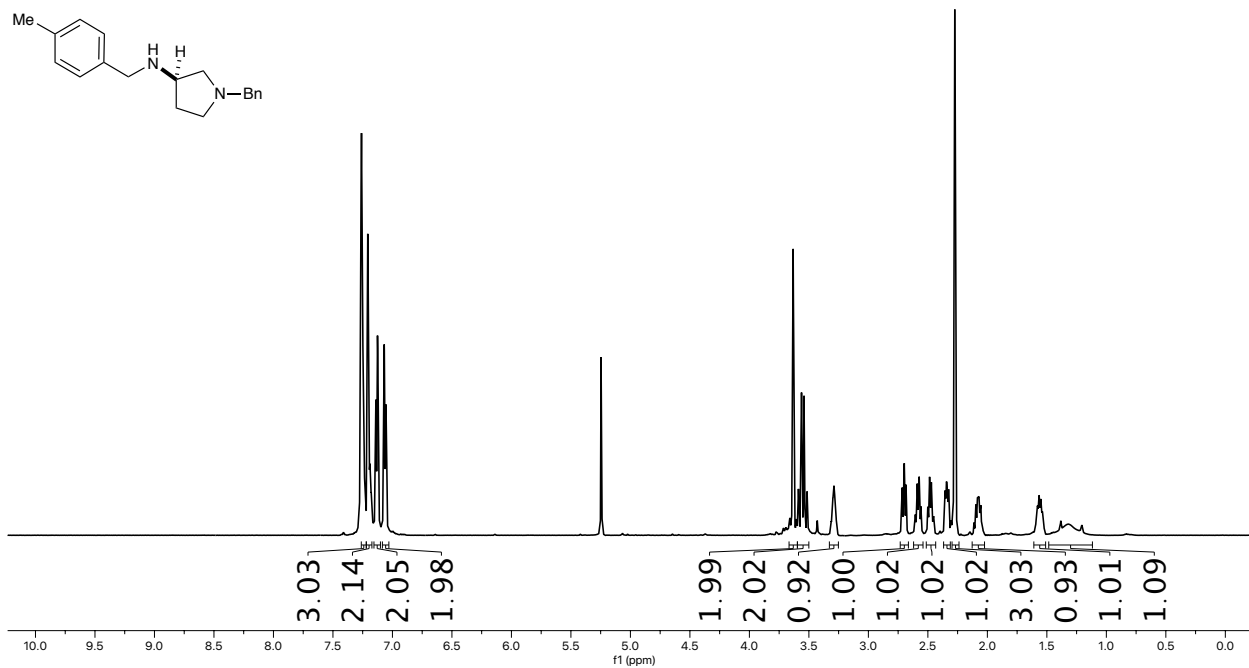
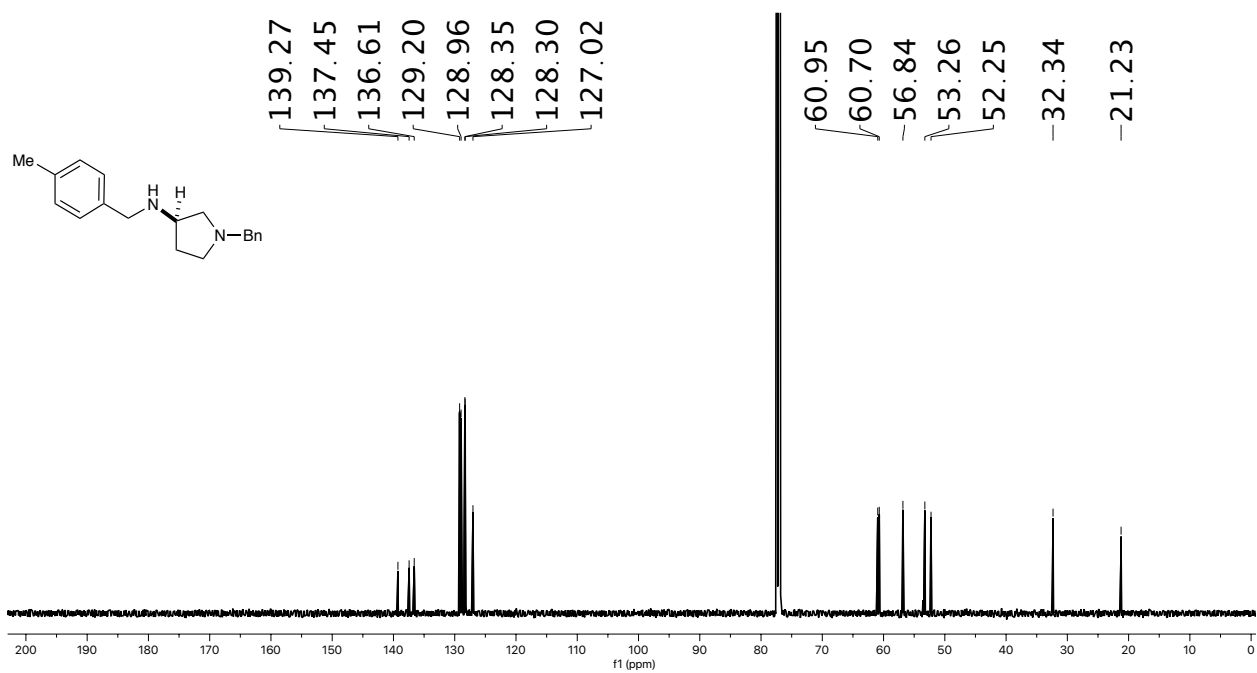
¹H NMR spectrum of II-27 (500 MHz, Chloroform-*d*).**¹³C NMR spectrum of II-27 (126 MHz, Chloroform-*d*).**

¹H NMR spectrum of II-28 (500 MHz, Chloroform-*d*).**¹³C NMR spectrum of II-28 (126 MHz, Chloroform-*d*).**

¹H NMR spectrum of II-29 (500 MHz, Chloroform-*d*).**¹³C NMR spectrum of II-29 (126 MHz, Chloroform-*d*).**

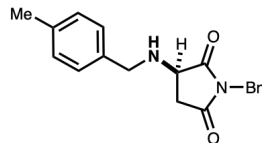
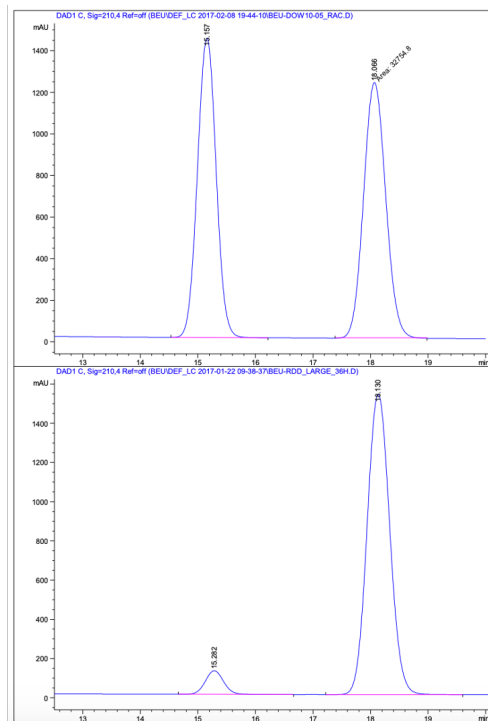
¹H NMR spectrum of II-30 (500 MHz, Chloroform-*d*).**¹³C NMR spectrum of II-30 (126 MHz, Chloroform-*d*).**

¹H NMR spectrum of II-31 (500 MHz, Chloroform-*d*).**¹³C NMR spectrum of II-31 (126 MHz, Chloroform-*d*).**

¹H NMR spectrum of II-34 (500 MHz, Chloroform-*d*).**¹³C NMR spectrum of II-34 (126 MHz, Chloroform-*d*).**

A2. HPLC Traces of Racemic and Enantioenriched Products

Chiral HPLC trace of racemic and enantioenriched II-6.



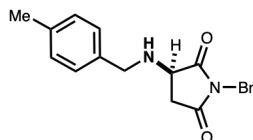
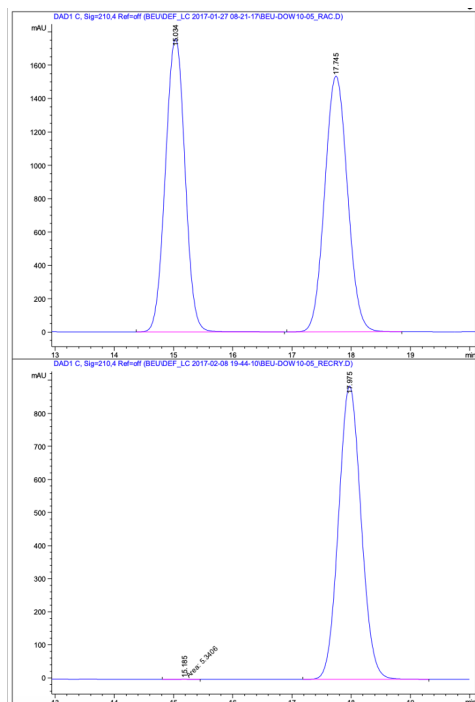
Signal 2: DAD1 C, Sig=210,4 Ref=off

Peak #	RetTime [min]	Type	Width [min]	Area [mAU*s]	Height [mAU]	Area %
1	15.157	BB	0.3562	3.25920e4	1438.98767	49.8755
2	18.066	MM	0.4447	3.27548e4	1227.72742	50.1245

Signal 2: DAD1 C, Sig=210,4 Ref=off

Peak #	RetTime [min]	Type	Width [min]	Area [mAU*s]	Height [mAU]	Area %
1	15.282	BB	0.3438	2668.22388	120.72897	6.0008
2	18.130	BB	0.4282	4.17964e4	1532.23572	93.9992

Chiral HPLC trace of racemic and enantioenriched II-6 after recrystallization.



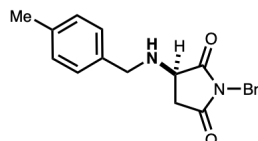
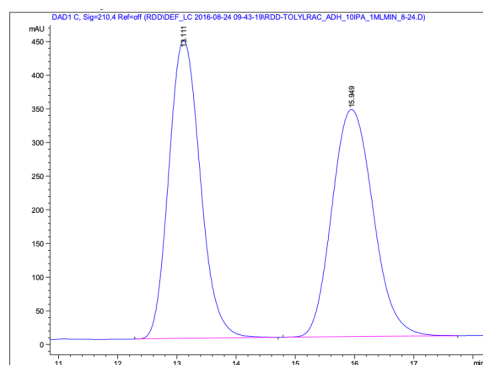
Signal 2: DAD1 C, Sig=210,4 Ref=off

Peak #	RetTime [min]	Type	Width [min]	Area [mAU*s]	Height [mAU]	Area %
1	15.034	BB	0.3636	4.03271e4	1758.21216	49.6235
2	17.745	BB	0.4216	4.09390e4	1532.84058	50.3765

Signal 2: DAD1 C, Sig=210,4 Ref=off

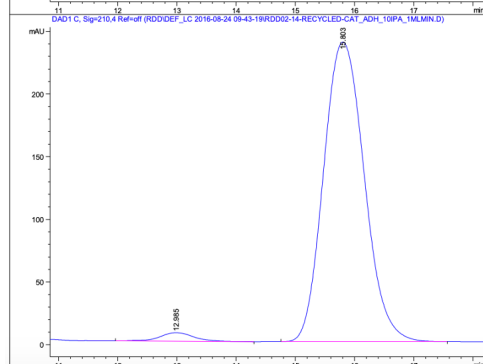
Peak #	RetTime [min]	Type	Width [min]	Area [mAU*s]	Height [mAU]	Area %
1	15.185	MM	0.3149	5.34060	2.82687e-1	0.0228
2	17.975	BB	0.4127	2.34513e4	886.38623	99.9772

Chiral HPLC trace of racemic and enantioenriched II-6 synthesized *via* reaction with recovered Ca[B]₂.



Signal 2: DAD1 C, Sig=210,4 Ref=off

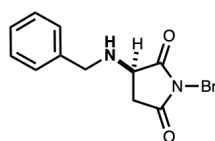
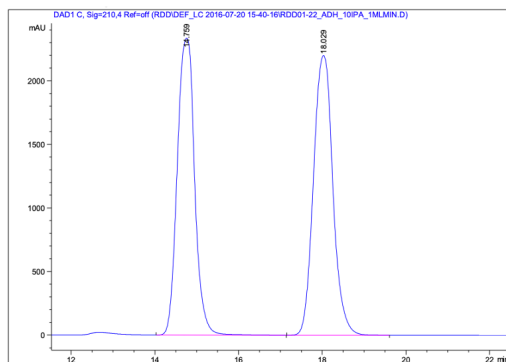
Peak #	RetTime [min]	Type	Width [min]	Area [mAU*s]	Height [mAU]	Area %
1	13.111	BB	0.5815	1.63209e4	443.31677	50.0216
2	15.949	BB	0.7681	1.63068e4	337.26083	49.9784



Signal 2: DAD1 C, Sig=210,4 Ref=off

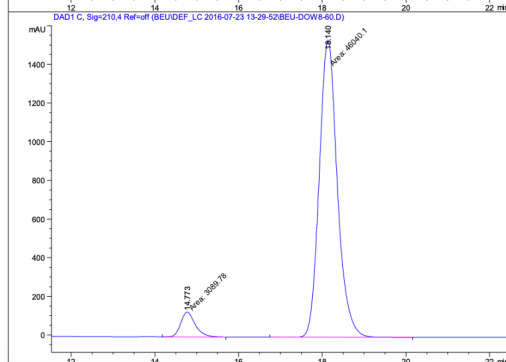
Peak #	RetTime [min]	Type	Width [min]	Area [mAU*s]	Height [mAU]	Area %
1	12.985	BB	0.6044	269.39487	6.73893	2.3068
2	15.803	BB	0.7572	1.14089e4	238.89505	97.6932

Chiral HPLC trace of racemic and enantioenriched II-7.



Signal 2: DAD1 C, Sig=210,4 Ref=off

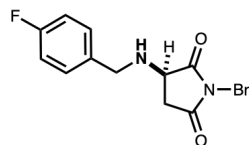
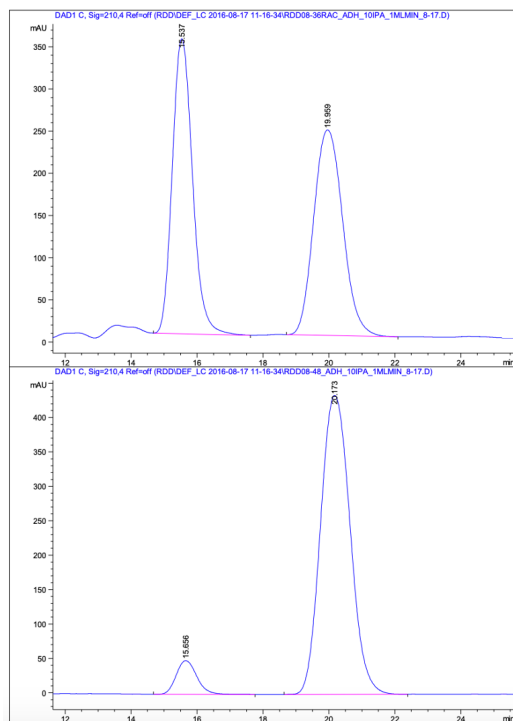
Peak #	RetTime [min]	Type	Width [min]	Area [mAU*s]	Height [mAU]	Area %
1	14.759	VB	0.4494	6.71655e4	2336.09424	48.6931
2	18.029	BB	0.5034	7.07709e4	2199.48340	51.3069



Signal 2: DAD1 C, Sig=210,4 Ref=off

Peak #	RetTime [min]	Type	Width [min]	Area [mAU*s]	Height [mAU]	Area %
1	14.773	MM	0.4003	3089.77832	128.65573	6.2890
2	18.140	MM	0.4997	4.60401e4	1535.71973	93.7110

Chiral HPLC trace of racemic and enantioenriched II-8.



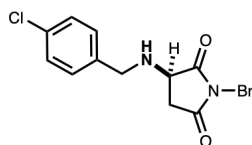
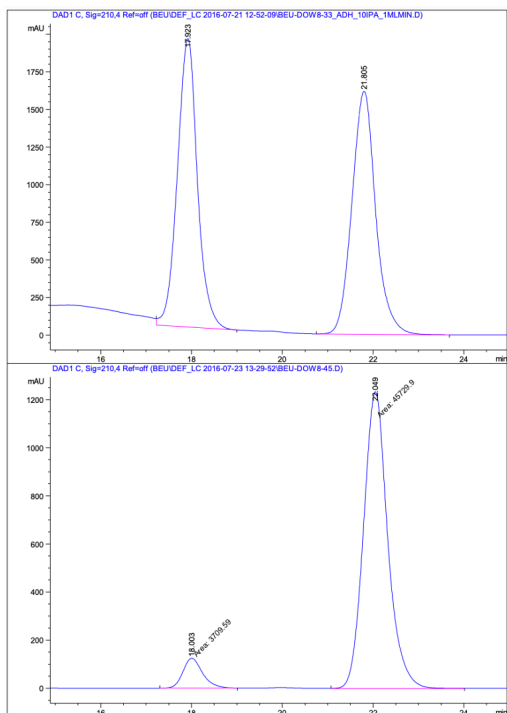
Signal 2: DAD1 C, Sig=210,4 Ref=off

Peak #	RetTime [min]	Type	Width [min]	Area [mAU*s]	Height [mAU]	Area %
1	15.537	BB	0.6708	1.48897e4	349.64786	49.9823
2	19.959	BB	0.9712	1.49003e4	243.72934	50.0177

Signal 2: DAD1 C, Sig=210,4 Ref=off

Peak #	RetTime [min]	Type	Width [min]	Area [mAU*s]	Height [mAU]	Area %
1	15.656	BB	0.6914	2142.71191	48.88052	7.3633
2	20.173	BB	0.9980	2.69571e4	434.41962	92.6367

Chiral HPLC trace of racemic and enantioenriched II-9.



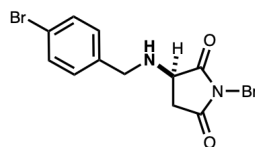
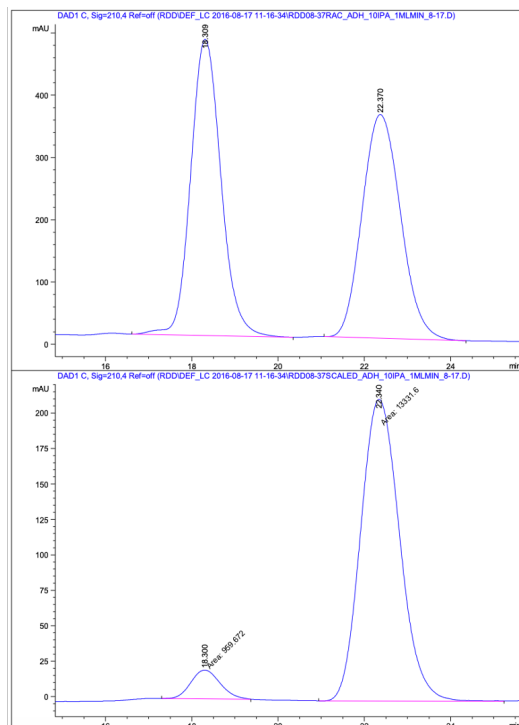
Signal 2: DAD1 C, Sig=210,4 Ref=off

Peak #	RetTime [min]	Type	Width [min]	Area [mAU*s]	Height [mAU]	Area %
1	17.923	VB	0.4680	5.88496e4	1917.96606	50.0455
2	21.805	BB	0.5564	5.87425e4	1614.99658	49.9545

Signal 2: DAD1 C, Sig=210,4 Ref=off

Peak #	RetTime [min]	Type	Width [min]	Area [mAU*s]	Height [mAU]	Area %
1	18.003	MM	0.4985	3709.58740	124.02554	7.5033
2	22.049	MM	0.6177	4.57299e4	1233.80652	92.4967

Chiral HPLC trace of racemic and enantioenriched II-10.



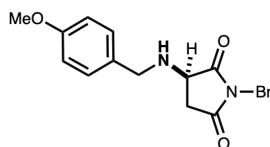
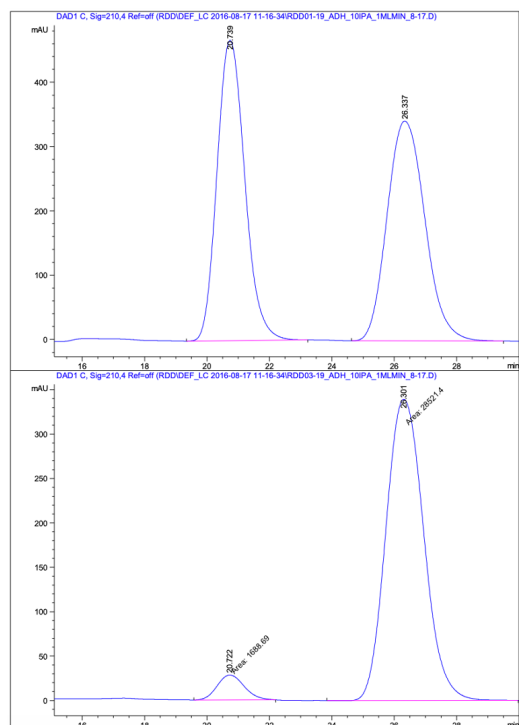
Signal 2: DAD1 C, Sig=210,4 Ref=off

Peak #	RetTime [min]	Type	Width [min]	Area [mAU*s]	Height [mAU]	Area %
1	18.309	BB	0.7636	2.32335e4	475.85065	51.0318
2	22.370	BB	0.9897	2.22940e4	359.37985	48.9682

Signal 2: DAD1 C, Sig=210,4 Ref=off

Peak #	RetTime [min]	Type	Width [min]	Area [mAU*s]	Height [mAU]	Area %
1	18.297	BB	0.7516	1010.53448	20.62597	7.0672
2	22.340	BB	0.9971	1.32884e4	212.62537	92.9328

Chiral HPLC trace of racemic and enantioenriched II-11.



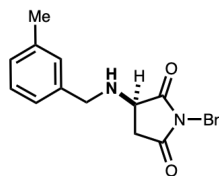
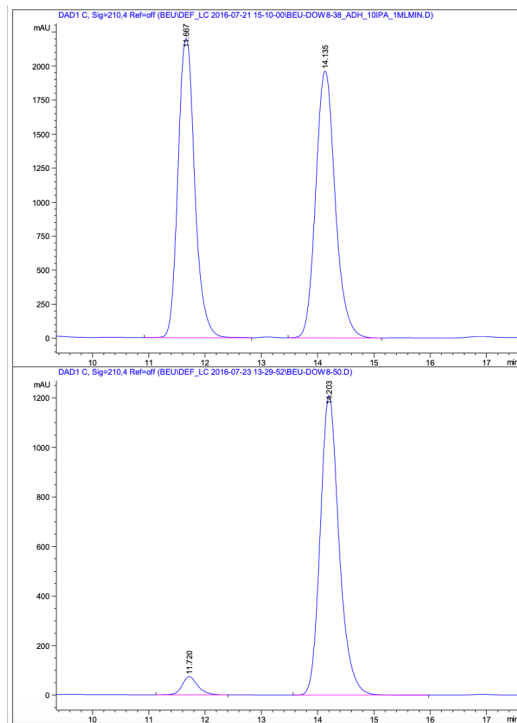
Signal 2: DAD1 C, Sig=210,4 Ref=off

Peak #	RetTime [min]	Type	Width [min]	Area [mAU*s]	Height [mAU]	Area %
1	20.739	BB	0.9739	2.89144e4	467.28027	50.0415
2	26.337	BB	1.3426	2.88665e4	342.02682	49.9585

Signal 2: DAD1 C, Sig=210,4 Ref=off

Peak #	RetTime [min]	Type	Width [min]	Area [mAU*s]	Height [mAU]	Area %
1	20.722	BB	0.9347	1730.00598	28.23901	5.7214
2	26.301	BB	1.3306	2.85073e4	339.16788	94.2786

Chiral HPLC trace of racemic and enantioenriched II-12.



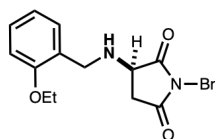
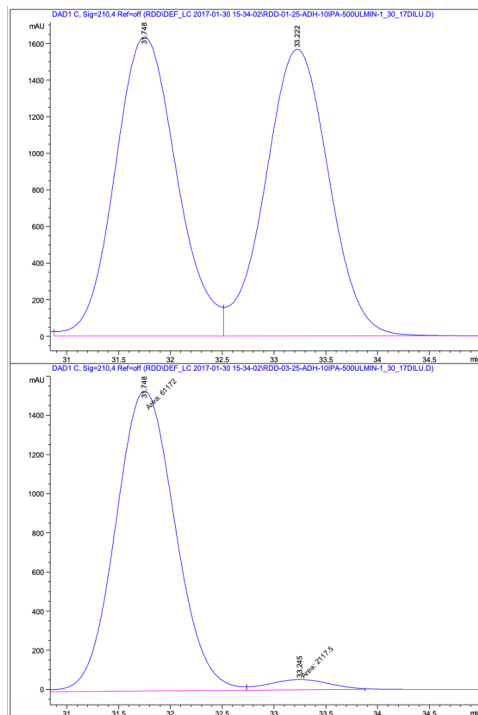
Signal 2: DAD1 C, Sig=210,4 Ref=off

Peak #	RetTime [min]	Type	Width [min]	Area [mAU*s]	Height [mAU]	Area %
1	11.667	BV	0.3187	4.53486e4	2198.07178	49.0752
2	14.135	BB	0.3701	4.70579e4	1960.18848	50.9248

Signal 2: DAD1 C, Sig=210,4 Ref=off

Peak #	RetTime [min]	Type	Width [min]	Area [mAU*s]	Height [mAU]	Area %
1	11.720	BB	0.2910	1419.42139	73.61469	4.8069
2	14.203	BB	0.3550	2.81096e4	1210.07690	95.1931

Chiral HPLC trace of racemic and enantioenriched II-13.



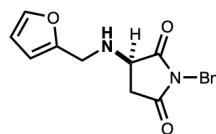
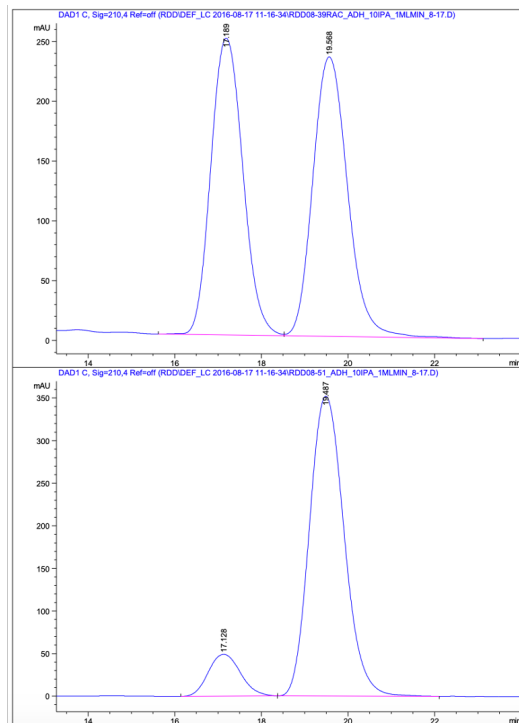
Signal 2: DAD1 C, Sig=210,4 Ref=off

Peak #	RetTime [min]	Type	Width [min]	Area [mAU*s]	Height [mAU]	Area %
1	31.748	VV	0.6436	6.77075e4	1633.26892	50.4118
2	33.222	VBA	0.6602	6.66012e4	1565.90356	49.5882

Signal 2: DAD1 C, Sig=210,4 Ref=off

Peak #	RetTime [min]	Type	Width [min]	Area [mAU*s]	Height [mAU]	Area %
1	31.748	MF	0.6652	6.11720e4	1532.58704	96.6543
2	33.245	FM	0.6720	2117.50317	52.51970	3.3457

Chiral HPLC trace of racemic and enantioenriched II-14.



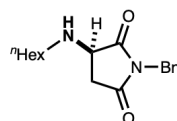
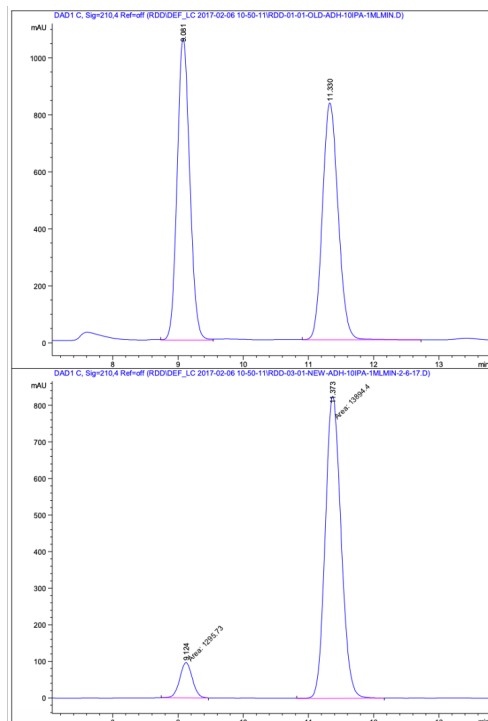
Signal 2: DAD1 C, Sig=210,4 Ref=off

Peak #	RetTime [min]	Type	Width [min]	Area [mAU*s]	Height [mAU]	Area %
1	17.189	BV	0.8192	1.27507e4	248.27483	49.4372
2	19.568	VB	0.8726	1.30410e4	233.86095	50.5628

Signal 2: DAD1 C, Sig=210,4 Ref=off

Peak #	RetTime [min]	Type	Width [min]	Area [mAU*s]	Height [mAU]	Area %
1	17.128	BB	0.8174	2530.27808	49.08475	11.4596
2	19.487	BB	0.8759	1.95498e4	352.04941	88.5404

Chiral HPLC trace of racemic and enantioenriched II-15.



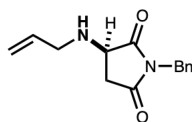
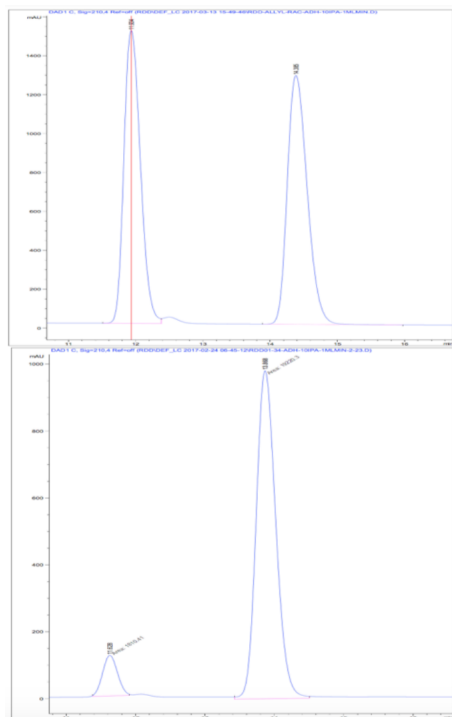
Signal 2: DAD1 C, Sig=210,4 Ref=off

Peak #	RetTime [min]	Type	Width [min]	Area [mAU*s]	Height [mAU]	Area %
1	9.081	VV	0.2081	1.41470e4	1057.62500	50.4317
2	11.330	VB	0.2612	1.39049e4	831.24164	49.5683

Signal 2: DAD1 C, Sig=210,4 Ref=off

Peak #	RetTime [min]	Type	Width [min]	Area [mAU*s]	Height [mAU]	Area %
1	9.124	MM	0.2241	1295.73181	96.35020	8.5301
2	11.373	MM	0.2804	1.38944e4	825.96472	91.4699

Chiral HPLC trace of racemic and enantioenriched II-16.



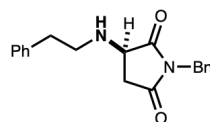
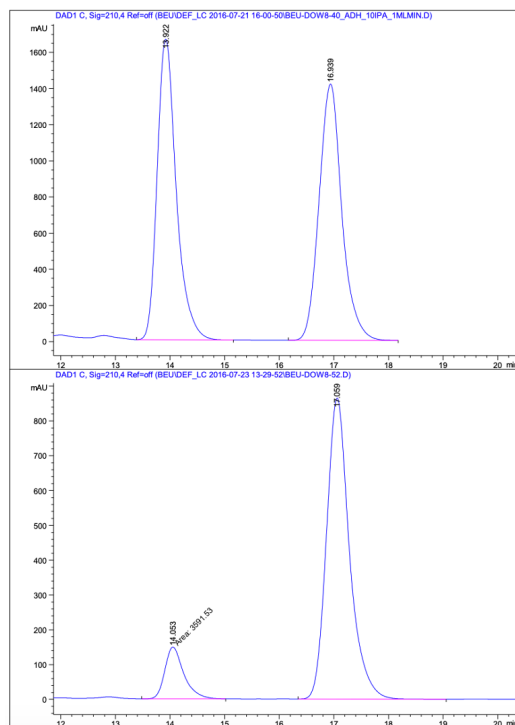
Signal 2: DAD1 C, Sig=210,4 Ref=off

Peak #	RetTime [min]	Type	Width [min]	Area [mAU*s]	Height [mAU]	Area %
1	11.934	BV	0.2689	2.56631e4	1505.54968	49.3905
2	14.385	BB	0.3217	2.62964e4	1279.97986	50.6095

Signal 2: DAD1 C, Sig=210,4 Ref=off

Peak #	RetTime [min]	Type	Width [min]	Area [mAU*s]	Height [mAU]	Area %
1	11.628	MM	0.2494	1810.41260	120.98617	8.6084
2	13.868	MM	0.3267	1.92203e4	980.60352	91.3916

Chiral HPLC trace of racemic and enantioenriched II-17.



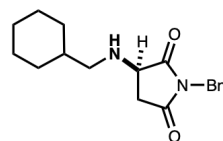
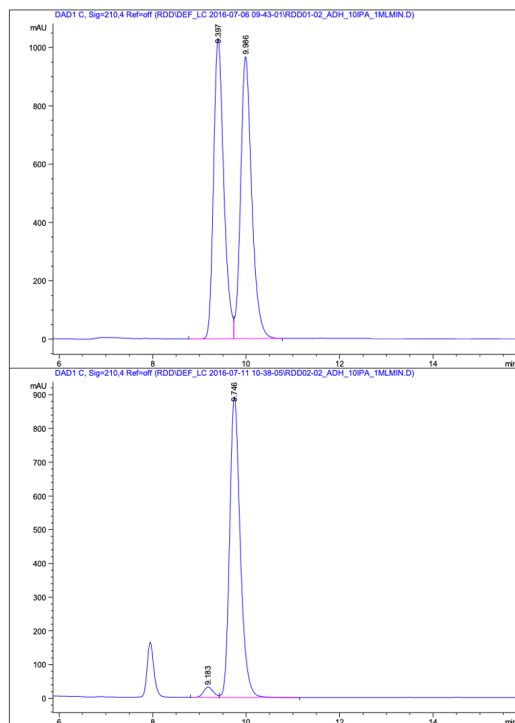
Signal 2: DAD1 C, Sig=210,4 Ref=off

Peak #	RetTime [min]	Type	Width [min]	Area [mAU*s]	Height [mAU]	Area %
1	13.922	BB	0.3703	4.05253e4	1662.80652	49.7130
2	16.939	BBA	0.4413	4.09932e4	1417.85779	50.2870

Signal 2: DAD1 C, Sig=210,4 Ref=off

Peak #	RetTime [min]	Type	Width [min]	Area [mAU*s]	Height [mAU]	Area %
1	14.053	MM	0.4021	3591.53125	148.85593	12.4573
2	17.059	BB	0.4405	2.52393e4	864.77283	87.5427

Chiral HPLC trace of racemic and enantioenriched II-18.



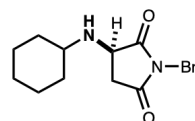
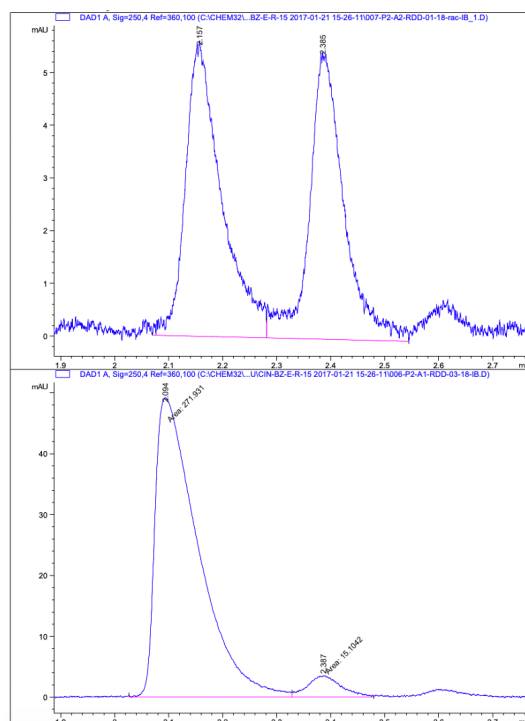
Signal 2: DAD1 C, Sig=210,4 Ref=off

Peak #	RetTime [min]	Type	Width [min]	Area [mAU*s]	Height [mAU]	Area %
1	9.397	BV	0.2308	1.56068e4	1030.02271	49.3709
2	9.986	VB	0.2511	1.60045e4	966.76324	50.6291

Signal 2: DAD1 C, Sig=210,4 Ref=off

Peak #	RetTime [min]	Type	Width [min]	Area [mAU*s]	Height [mAU]	Area %
1	9.183	BV	0.2190	440.46912	30.77402	3.0544
2	9.746	VB	0.2390	1.39802e4	891.28406	96.9456

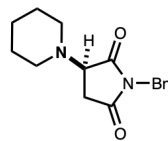
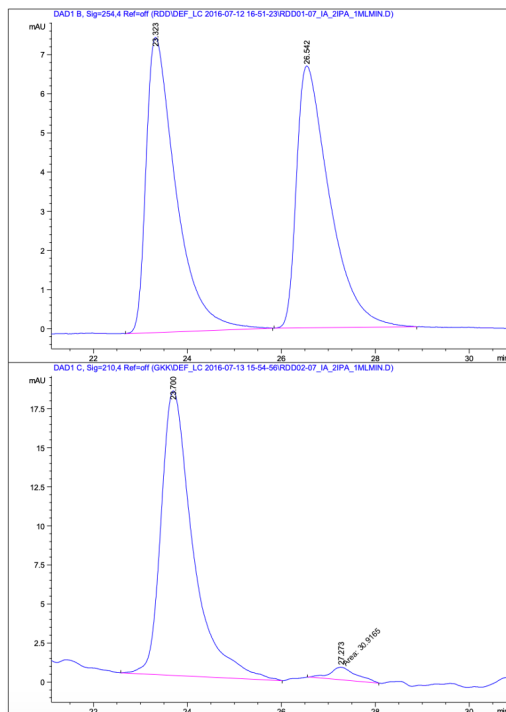
Chiral HPLC trace of racemic and enantioenriched II-19.



Peak #	RetTime [min]	Type	Width [min]	Area [mAU*s]	Height [mAU]	Area %
1	2.157	BV	0.0559	25.96450	5.56657	51.6035
2	2.385	VV R	0.0550	24.35085	5.36130	48.3965

Peak #	RetTime [min]	Type	Width [min]	Area [mAU*s]	Height [mAU]	Area %
1	2.094	MF	0.0921	271.93130	49.18518	94.7379
2	2.387	FM	0.0720	15.10422	3.49755	5.2621

Chiral HPLC trace of racemic and enantioenriched II-20.



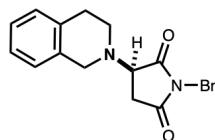
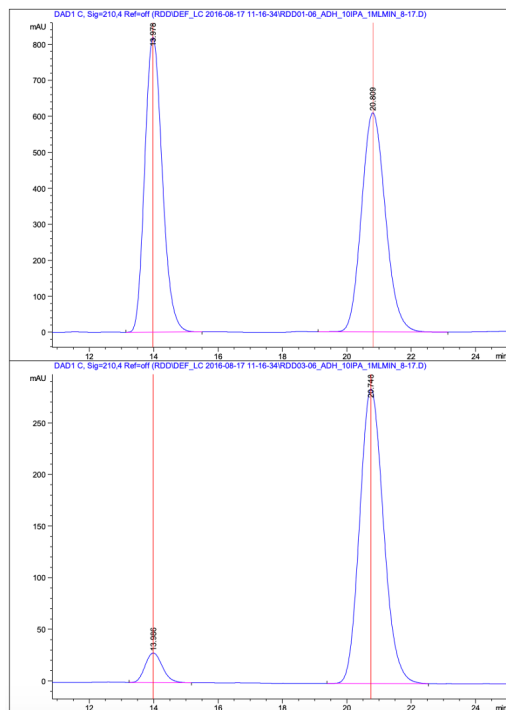
Signal 3: DAD1 C, Sig=210,4 Ref=off

Peak #	RetTime [min]	Type	Width [min]	Area [mAU*s]	Height [mAU]	Area %
1	23.323	BB	0.6516	1.26442e4	288.33511	50.1073
2	26.540	BB	0.7273	1.25901e4	256.22342	49.8927

Signal 3: DAD1 C, Sig=210,4 Ref=off

Peak #	RetTime [min]	Type	Width [min]	Area [mAU*s]	Height [mAU]	Area %
1	23.700	BB	0.6847	856.63623	18.21482	96.5167
2	27.273	MM	0.6432	30.91652	8.01082e-1	3.4833

Chiral HPLC trace of racemic and enantioenriched II-21.



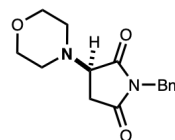
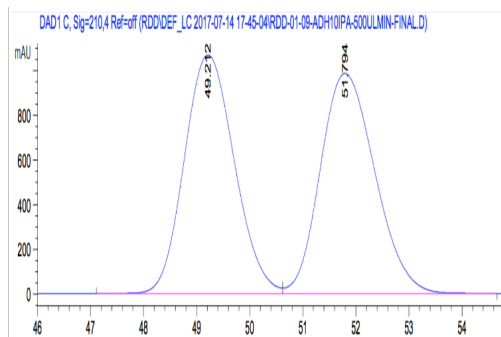
Signal 2: DAD1 C, Sig=210,4 Ref=off

Peak #	RetTime [min]	Type	Width [min]	Area [mAU*s]	Height [mAU]	Area %
1	13.978	BB	0.5953	3.09843e4	819.11908	49.6770
2	20.809	BB	0.8072	3.13872e4	609.10699	50.3230

Signal 2: DAD1 C, Sig=210,4 Ref=off

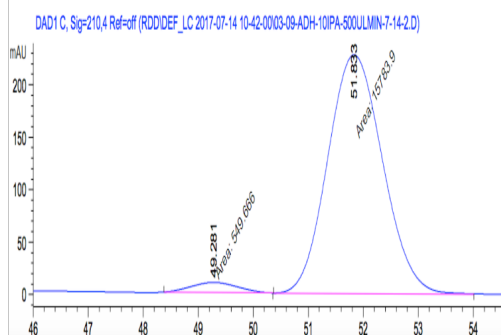
Peak #	RetTime [min]	Type	Width [min]	Area [mAU*s]	Height [mAU]	Area %
1	13.986	BB	0.5891	1076.27478	28.72956	6.8434
2	20.748	BB	0.8071	1.46510e4	285.32999	93.1566

Chiral HPLC trace of racemic and enantioenriched II-22.



Signal 2: DAD1 C, Sig=210,4 Ref=off

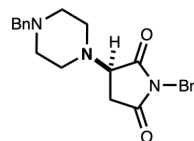
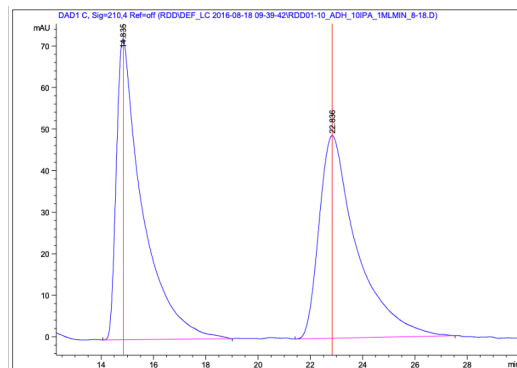
Peak #	RetTime [min]	Type	Width [min]	Area [mAU*s]	Height [mAU]	Area %
1	49.212	BV	1.0179	6.98475e4	1066.78760	49.8499
2	51.794	VB	1.1091	7.02682e4	984.04779	50.1501



Signal 2: DAD1 C, Sig=210,4 Ref=off

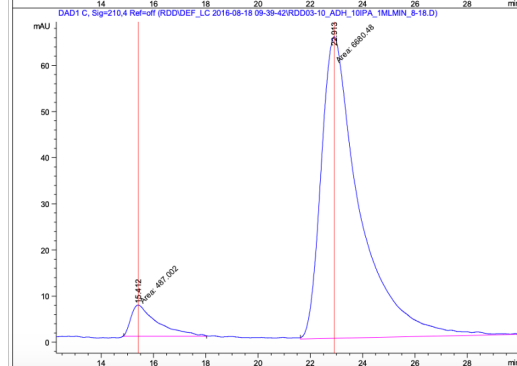
Peak #	RetTime [min]	Type	Width [min]	Area [mAU*s]	Height [mAU]	Area %
1	49.281	MM	0.9598	549.66602	9.54489	3.3652
2	51.833	MM	1.1567	1.57839e4	227.41969	96.6348

Chiral HPLC trace of racemic and enantioenriched II-23.



Signal 2: DAD1 C, Sig=210,4 Ref=off

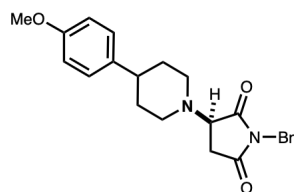
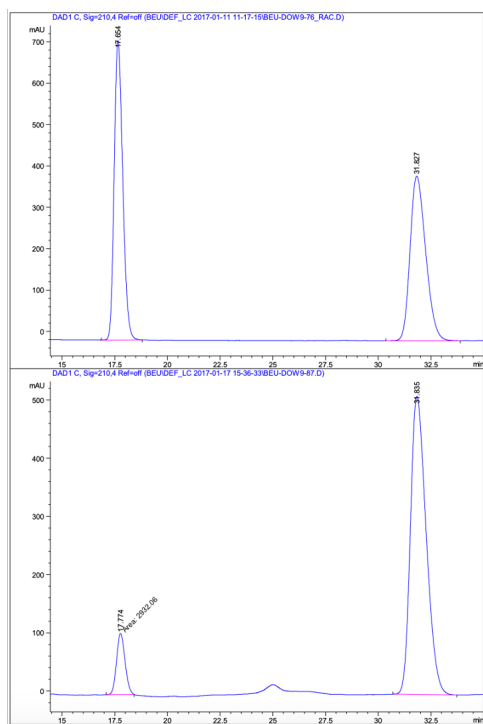
Peak #	RetTime [min]	Type	Width [min]	Area [mAU*s]	Height [mAU]	Area %
1	14.835	BB	0.9519	4990.94092	72.42825	50.5357
2	22.836	BB	1.4051	4885.12939	48.74817	49.4643



Signal 2: DAD1 C, Sig=210,4 Ref=off

Peak #	RetTime [min]	Type	Width [min]	Area [mAU*s]	Height [mAU]	Area %
1	15.412	MM	1.1937	487.00238	6.79948	6.7946
2	22.913	MM	1.7035	6680.48145	65.35913	93.2054

Chiral HPLC trace of racemic and enantioenriched II-24 synthesized *via* reaction at -20 °C.



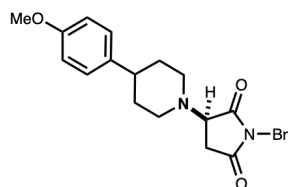
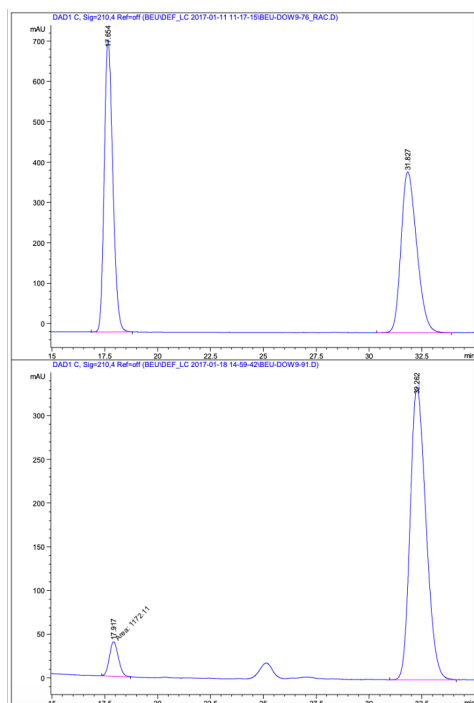
Signal 2: DAD1 C, Sig=210,4 Ref=off

Peak #	RetTime [min]	Type	Width [min]	Area [mAU*s]	Height [mAU]	Area %
1	17.654	BB	0.4382	2.03667e4	723.91608	49.8625
2	31.827	BB	0.7983	2.04790e4	397.99921	50.1375

Signal 2: DAD1 C, Sig=210,4 Ref=off

Peak #	RetTime [min]	Type	Width [min]	Area [mAU*s]	Height [mAU]	Area %
1	17.774	MM	0.4657	2932.06128	104.93056	9.9425
2	31.835	BB	0.8028	2.65582e4	512.30676	90.0575

Chiral HPLC trace of racemic and enantioenriched II-24 synthesized *via* reaction at -40 °C.



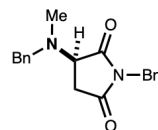
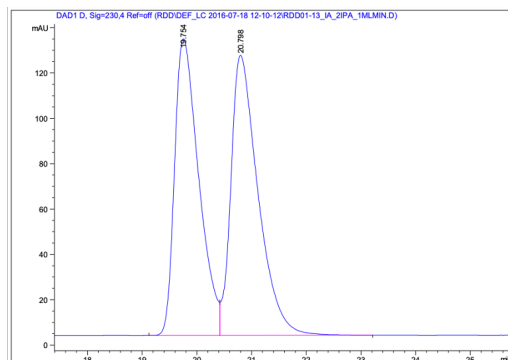
Signal 2: DAD1 C, Sig=210,4 Ref=off

Peak #	RetTime [min]	Type	Width [min]	Area [mAU*s]	Height [mAU]	Area %
1	17.654	BB	0.4382	2.03667e4	723.91608	49.8625
2	31.827	BB	0.7983	2.04790e4	397.99921	50.1375

Signal 2: DAD1 C, Sig=210,4 Ref=off

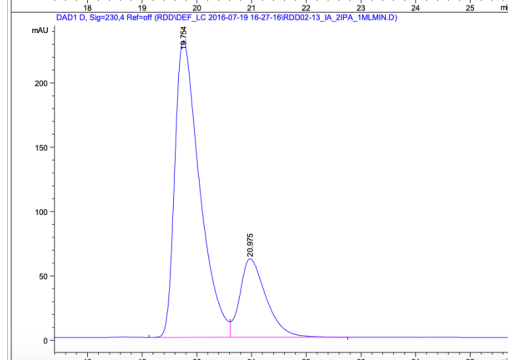
Peak #	RetTime [min]	Type	Width [min]	Area [mAU*s]	Height [mAU]	Area %
1	17.915	MM	0.4825	1140.01331	39.37619	6.1503
2	32.262	MM	0.8653	1.73959e4	335.07153	93.8497

Chiral HPLC trace of racemic and enantioenriched II-25.



Signal 4: DAD1 D, Sig=230,4 Ref=off

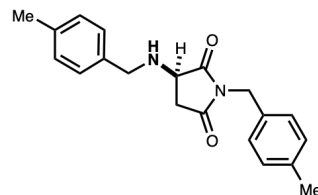
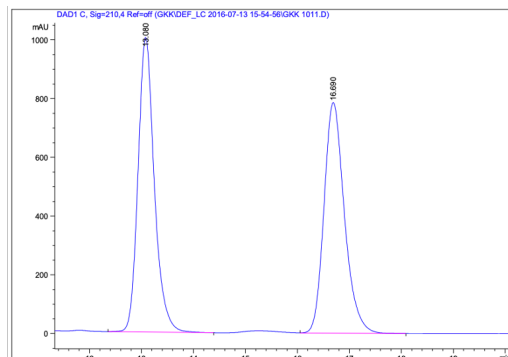
Peak #	RetTime [min]	Type	Width [min]	Area [mAU*s]	Height [mAU]	Area %
1	19.754	BV	0.4637	4011.88379	130.86577	48.4948
2	20.798	VB	0.5143	4260.92627	123.55144	51.5052



Signal 4: DAD1 D, Sig=230,4 Ref=off

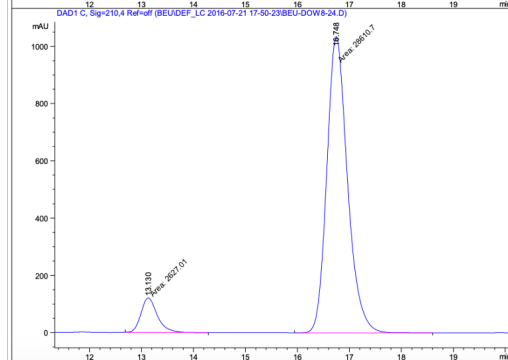
Peak #	RetTime [min]	Type	Width [min]	Area [mAU*s]	Height [mAU]	Area %
1	19.754	BV	0.4710	7256.53174	230.71039	78.1488
2	20.975	VB	0.4975	2029.00195	61.08556	21.8512

Chiral HPLC trace of racemic and enantioenriched II-26.



Signal 2: DAD1 C, Sig=210,4 Ref=off

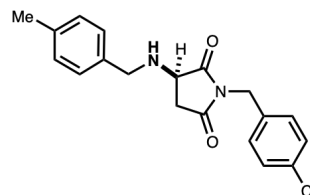
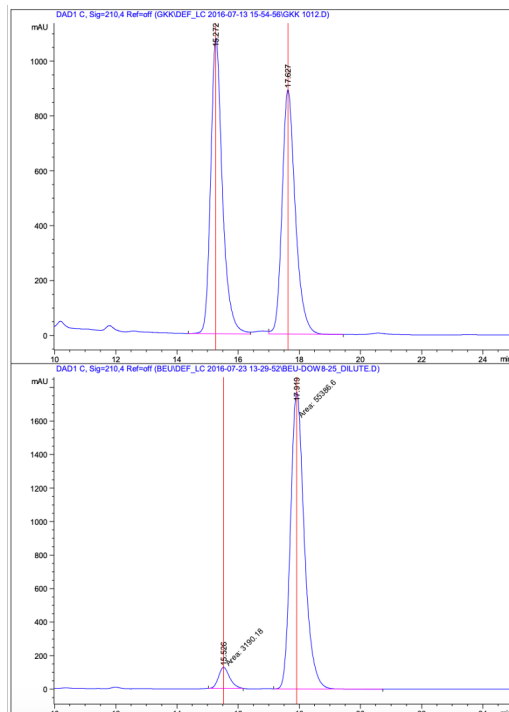
Peak #	RetTime [min]	Type	Width [min]	Area [mAU*s]	Height [mAU]	Area %
1	13.080	BB	0.3302	2.18455e4	1002.63434	50.4142
2	16.690	VB	0.4191	2.14866e4	785.52014	49.5858



Signal 2: DAD1 C, Sig=210,4 Ref=off

Peak #	RetTime [min]	Type	Width [min]	Area [mAU*s]	Height [mAU]	Area %
1	13.130	MM	0.3626	2627.00659	120.75199	8.4097
2	16.748	MM	0.4608	2.86107e4	1034.79272	91.5903

Chiral HPLC trace of racemic and enantioenriched II-27.



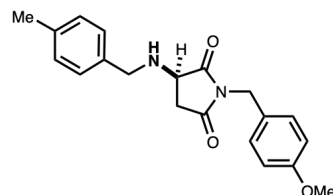
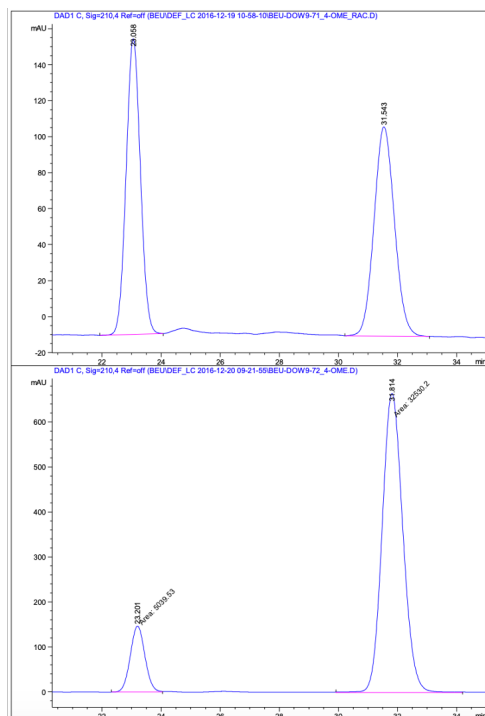
Signal 2: DAD1 C, Sig=210,4 Ref=off

Peak #	RetTime [min]	Type	Width [min]	Area [mAU*s]	Height [mAU]	Area %
1	15.272	BV	0.3997	2.86335e4	1078.62268	51.7079
2	17.627	VB	0.4561	2.67419e4	891.21863	48.2921

Signal 2: DAD1 C, Sig=210,4 Ref=off

Peak #	RetTime [min]	Type	Width [min]	Area [mAU*s]	Height [mAU]	Area %
1	15.526	MM	0.4228	3190.17920	125.76527	5.4461
2	17.919	MM	0.5209	5.53866e4	1772.05261	94.5539

Chiral HPLC trace of racemic and enantioenriched II-28.



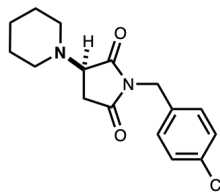
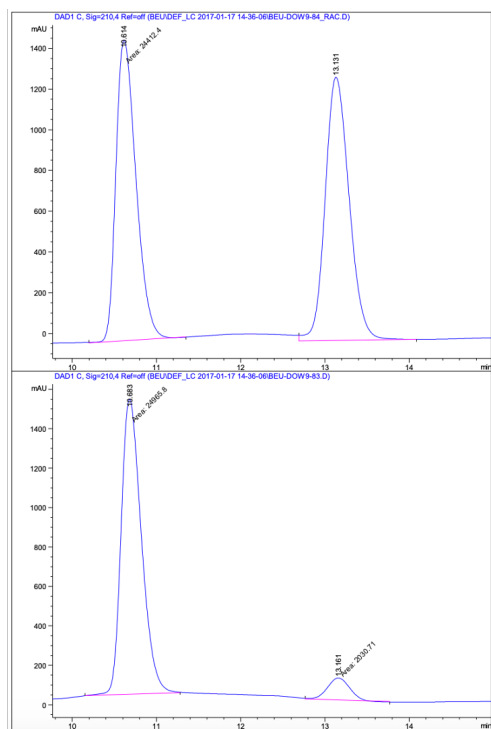
Signal 2: DAD1 C, Sig=210,4 Ref=off

Peak #	RetTime [min]	Type	Width [min]	Area [mAU*s]	Height [mAU]	Area %
1	23.058	BB	0.5263	5523.57617	164.27777	49.7196
2	31.543	BB	0.7464	5585.88477	116.29561	50.2804

Signal 2: DAD1 C, Sig=210,4 Ref=off

Peak #	RetTime [min]	Type	Width [min]	Area [mAU*s]	Height [mAU]	Area %
1	23.201	MM	0.5728	5039.52979	146.64676	13.4138
2	31.814	MM	0.8147	3.25302e4	665.46429	86.5862

Chiral HPLC trace of racemic and enantioenriched II-29 synthesized *via* reaction at -20 °C.



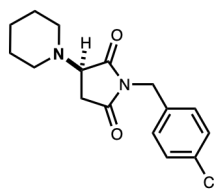
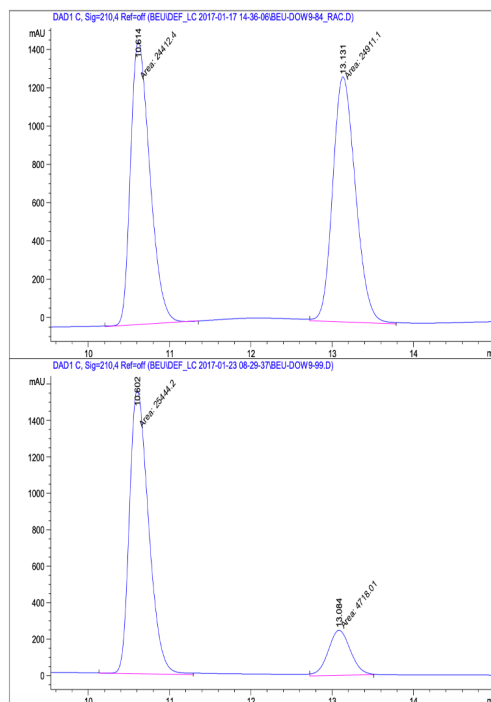
Signal 2: DAD1 C, Sig=210,4 Ref=off

Peak #	RetTime [min]	Type	Width [min]	Area [mAU*s]	Height [mAU]	Area %
1	10.614	MM	0.2755	2.44124e4	1476.93445	48.7928
2	13.131	VB	0.3093	2.56204e4	1292.45898	51.2072

Signal 2: DAD1 C, Sig=210,4 Ref=off

Peak #	RetTime [min]	Type	Width [min]	Area [mAU*s]	Height [mAU]	Area %
1	10.683	MM	0.2780	2.49658e4	1496.76892	92.4779
2	13.161	MM	0.3043	2030.71130	111.20616	7.5221

Chiral HPLC trace of racemic and enantioenriched II-29 synthesized *via* reaction at -40 °C.



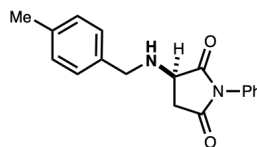
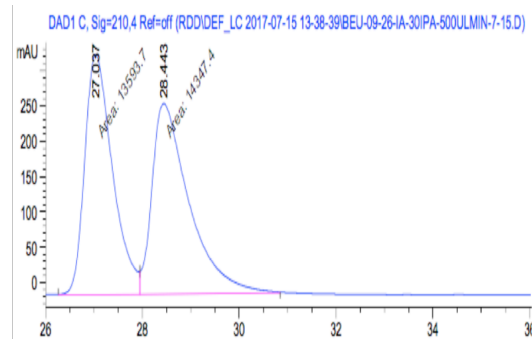
Signal 2: DAD1 C, Sig=210,4 Ref=off

Peak #	RetTime [min]	Type	Width [min]	Area [mAU*s]	Height [mAU]	Area %
1	10.614	MM	0.2755	2.44124e4	1476.93445	48.7928
2	13.131	VB	0.3093	2.56204e4	1292.45898	51.2072

Signal 2: DAD1 C, Sig=210,4 Ref=off

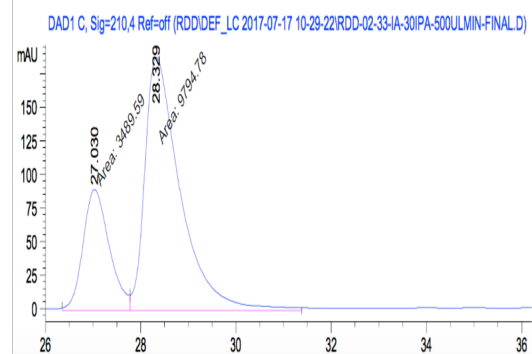
Peak #	RetTime [min]	Type	Width [min]	Area [mAU*s]	Height [mAU]	Area %
1	10.602	MM	0.2725	2.54442e4	1556.49866	84.3579
2	13.084	MM	0.3178	4718.01318	247.41553	15.6421

Chiral HPLC trace of racemic and enantioenriched II-30.



Signal 3: DAD1 C, Sig=210,4 Ref=off

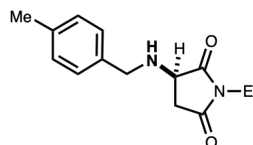
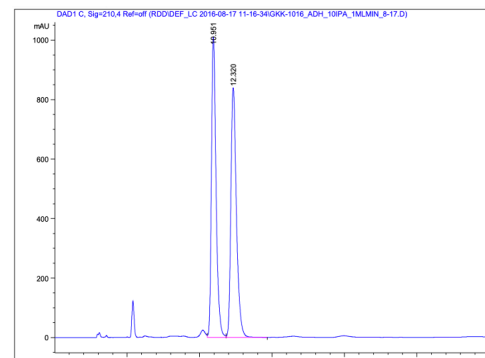
Peak #	RetTime [min]	Type	Width [min]	Area [mAU*s]	Height [mAU]	Area %
1	27.037	MF	0.6661	1.35937e4	340.14880	48.6513
2	28.443	FM	0.8875	1.43474e4	269.42029	51.3487



Signal 3: DAD1 C, Sig=210,4 Ref=off

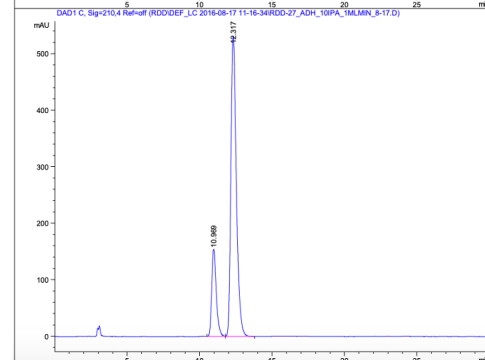
Peak #	RetTime [min]	Type	Width [min]	Area [mAU*s]	Height [mAU]	Area %
1	27.030	MF	0.6436	3489.58740	90.36543	26.2684
2	28.329	FM	0.8633	9794.77637	189.09468	73.7316

Chiral HPLC trace of racemic and enantioenriched II-31.



Signal 2: DAD1 C, Sig=210,4 Ref=off

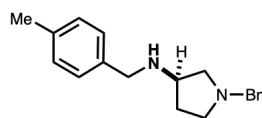
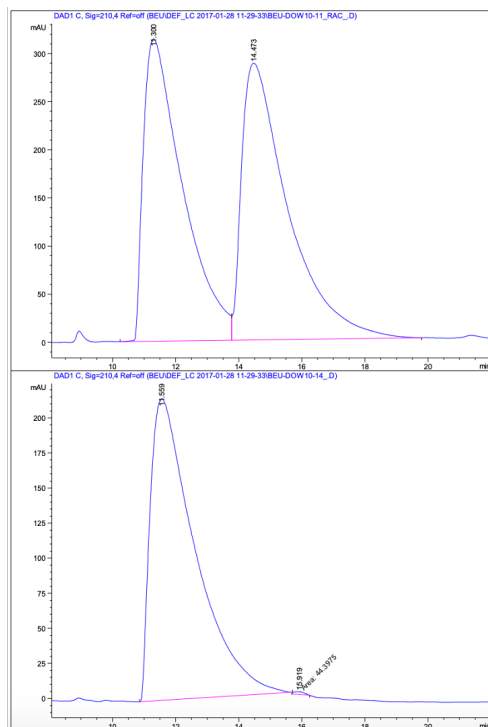
Peak #	RetTime [min]	Type	Width [min]	Area [mAU*s]	Height [mAU]	Area %
1	10.951	VV	0.3361	2.23300e4	1009.49506	50.0033
2	12.320	VB	0.4045	2.23271e4	838.82086	49.9967



Signal 2: DAD1 C, Sig=210,4 Ref=off

Peak #	RetTime [min]	Type	Width [min]	Area [mAU*s]	Height [mAU]	Area %
1	10.969	BV	0.3317	3358.74561	154.44734	19.4415
2	12.317	VB	0.3995	1.39174e4	531.48181	80.5585

Chiral HPLC trace of racemic and enantioenriched II-34.



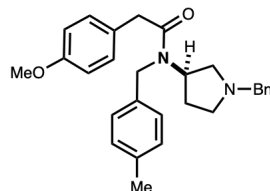
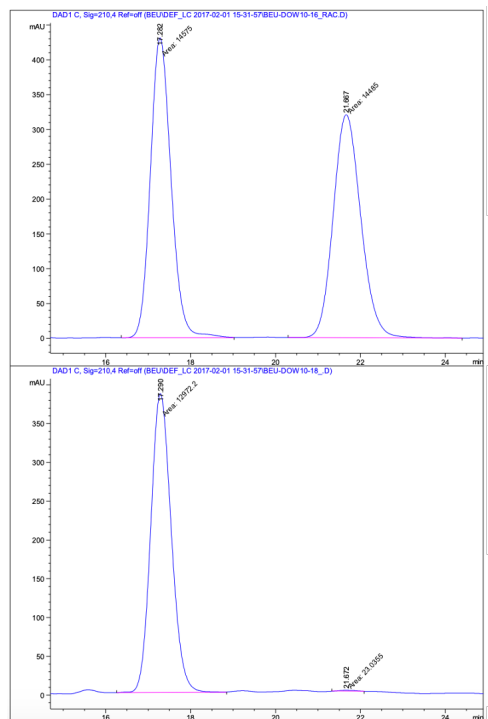
Signal 1: DAD1 C, Sig=210,4 Ref=off

Peak #	RetTime [min]	Type	Width [min]	Area [mAU*s]	Height [mAU]	Area %
1	11.300	BV	1.2625	2.71527e4	314.12094	48.1202
2	14.473	VB	1.4896	2.92742e4	287.57574	51.8798

Signal 1: DAD1 C, Sig=210,4 Ref=off

Peak #	RetTime [min]	Type	Width [min]	Area [mAU*s]	Height [mAU]	Area %
1	11.559	BB	1.3959	2.11996e4	215.09189	99.7910
2	15.919	MM	0.3771	44.39747	1.96218	0.2090

Chiral HPLC trace of racemic and enantioenriched II-35.



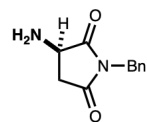
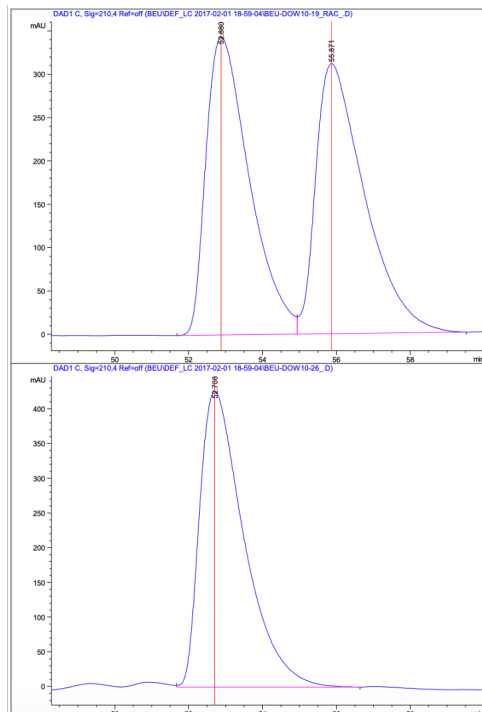
Signal 2: DAD1 C, Sig=210,4 Ref=off

Peak #	RetTime [min]	Type	Width [min]	Area [mAU*s]	Height [mAU]	Area %
1	17.282	MM	0.5642	1.45750e4	430.52969	50.1547
2	21.667	MM	0.7541	1.44850e4	320.14590	49.8453

Signal 2: DAD1 C, Sig=210,4 Ref=off

Peak #	RetTime [min]	Type	Width [min]	Area [mAU*s]	Height [mAU]	Area %
1	17.290	MM	0.5608	1.29722e4	385.51501	99.8227
2	21.672	MM	0.4016	23.03553	9.55973e-1	0.1773

Chiral HPLC trace of racemic and enantioenriched II-36.



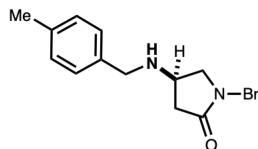
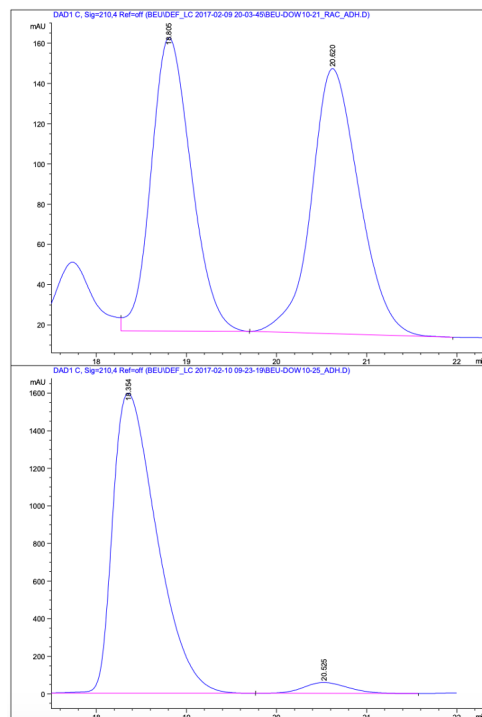
Signal 2: DAD1 C, Sig=210,4 Ref=off

Peak #	RetTime [min]	Type	Width [min]	Area [mAU*s]	Height [mAU]	Area %
1	52.880	BV	1.2273	2.80466e4	343.96411	49.5273
2	55.871	VB	1.2949	2.85820e4	311.37842	50.4727

Signal 2: DAD1 C, Sig=210,4 Ref=off

Peak #	RetTime [min]	Type	Width [min]	Area [mAU*s]	Height [mAU]	Area %
1	52.708	VB	1.2689	3.54968e4	426.52151	100.0000

Chiral HPLC trace of racemic and enantioenriched II-37.



Signal 2: DAD1 C, Sig=210,4 Ref=off

Peak #	RetTime [min]	Type	Width [min]	Area [mAU*s]	Height [mAU]	Area %
1	18.805	VB	0.4777	4496.20557	145.84627	48.1582
2	20.620	BB	0.5626	4840.10938	131.76305	51.8418

Signal 2: DAD1 C, Sig=210,4 Ref=off

Peak #	RetTime [min]	Type	Width [min]	Area [mAU*s]	Height [mAU]	Area %
1	18.354	BB	0.5225	5.42645e4	1596.57056	96.4660
2	20.525	BB	0.5319	1987.94116	58.00003	3.5340

Appendix B

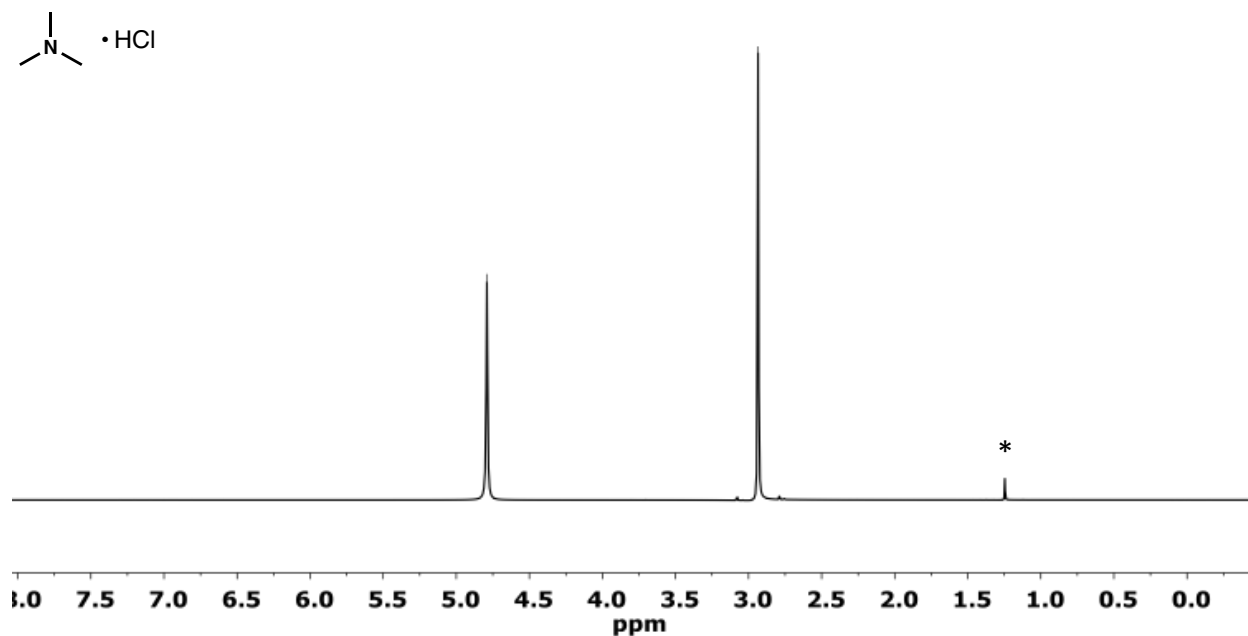
Supplementary to Chapter 3

Data included in this appendix appear in the following publication:

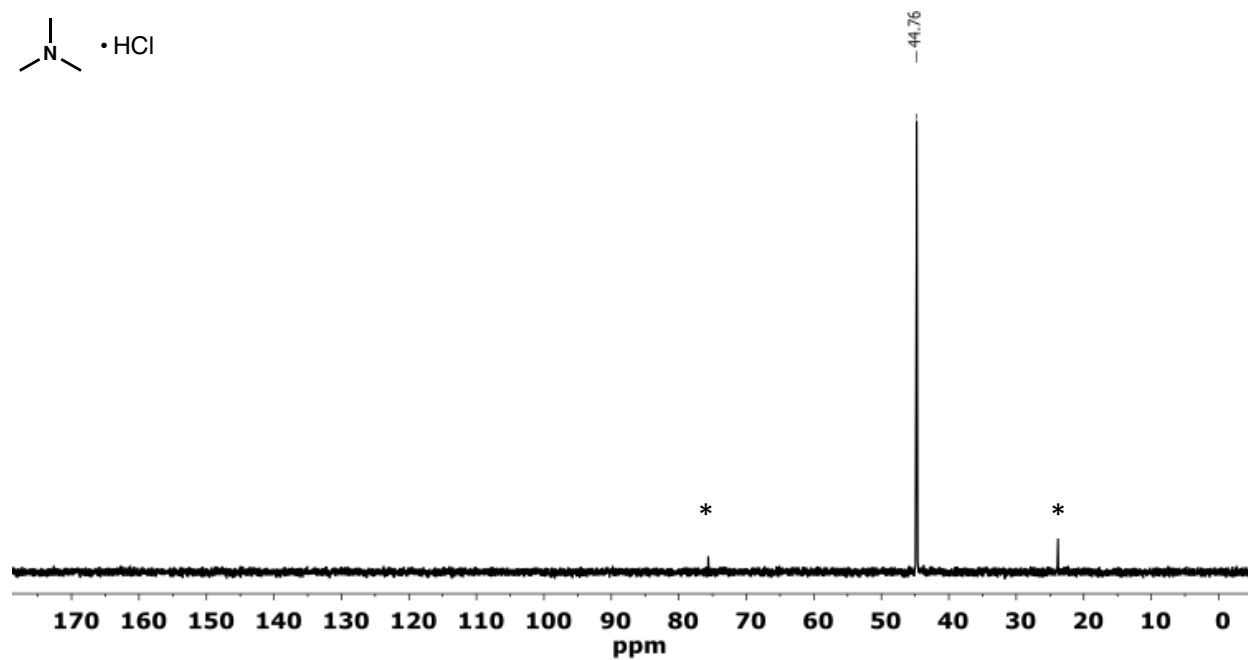
Christopher J. Barger, Rachel D. Dicken, Victoria L. Weidner, Alessandro Motta, Tracy L. Lohr, and Tobin J. Marks, La[N(SiMe₃)₂]₃-Catalyzed Deoxygenative Reduction of Amides with Pinacolborane. Scope and Mechanism. *J. Am. Chem. Soc.* **2020**, *142* (17), 8019-8028.

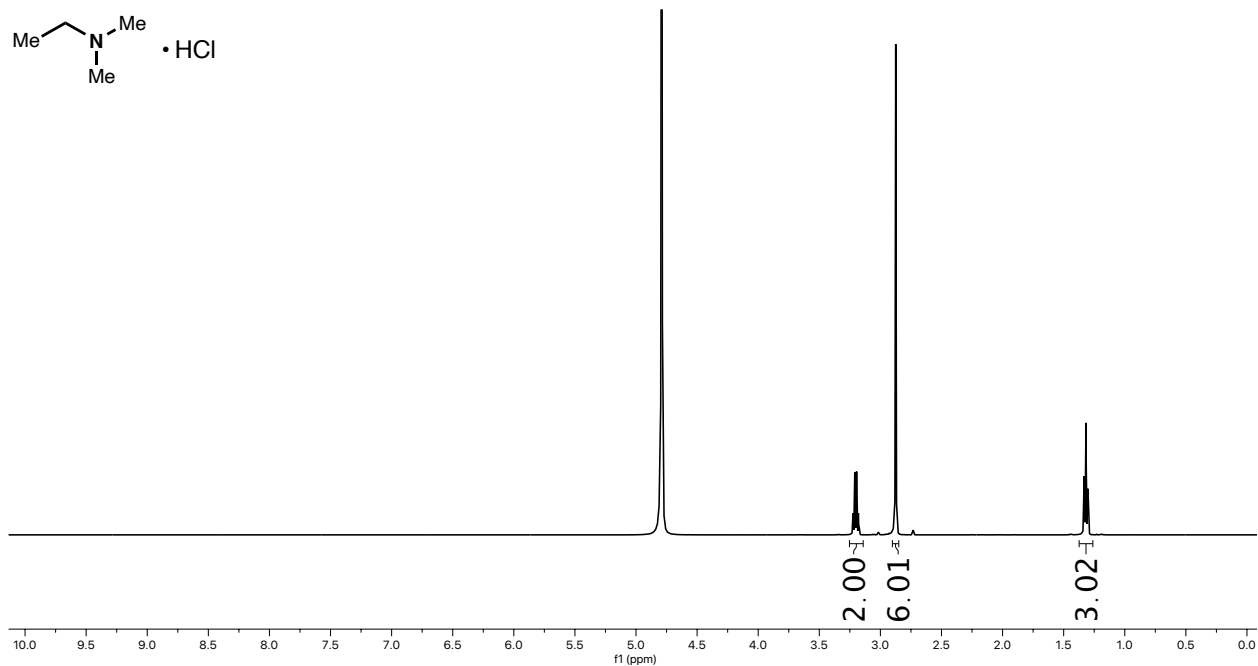
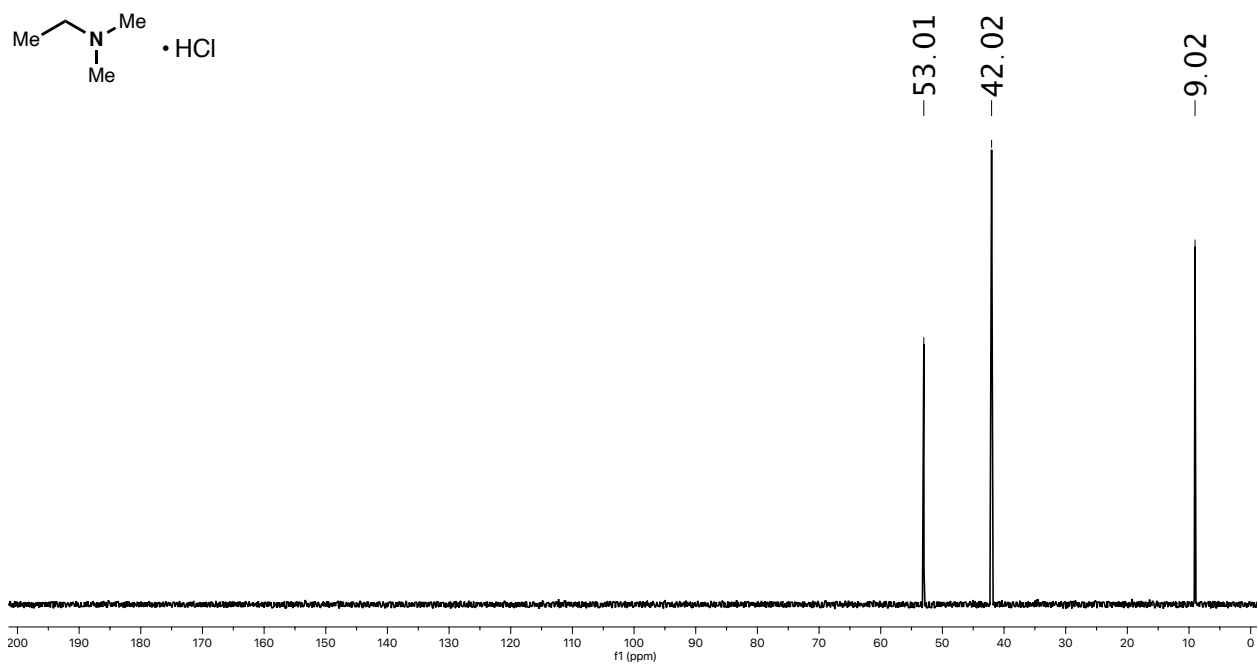
B1. NMR Spectra

^1H NMR spectrum of III-6 (500 MHz, D_2O). * = residual $\text{O}(\text{Bpin})_2$.

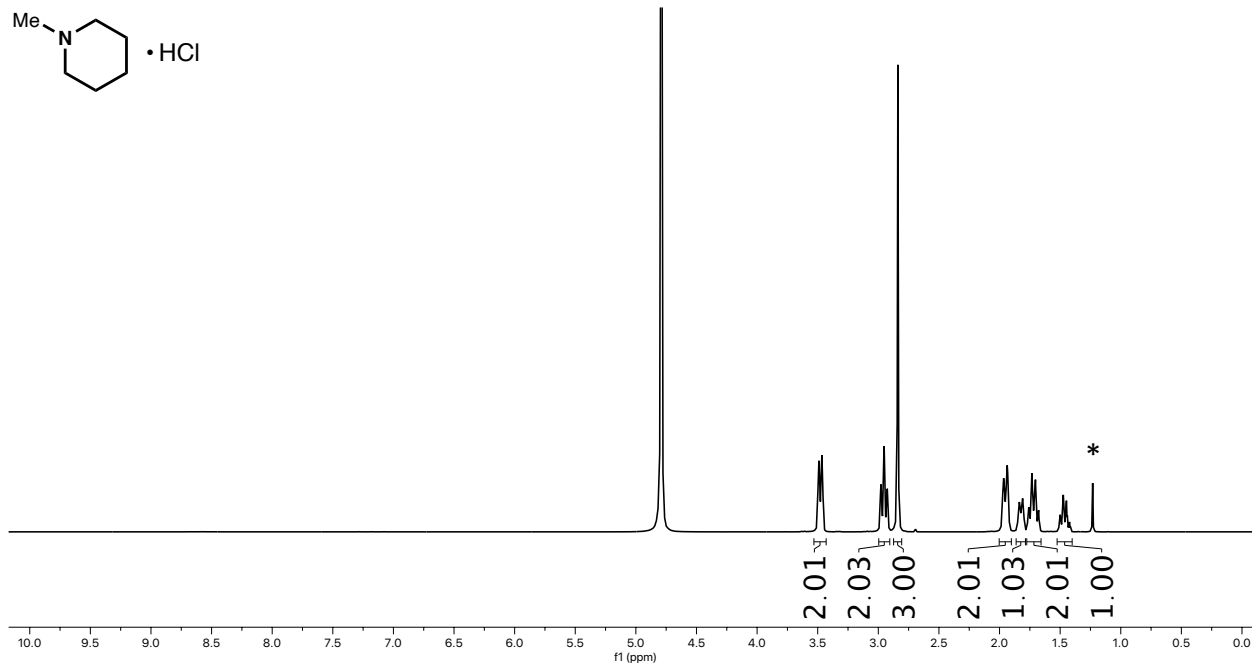


^{13}C NMR spectrum of III-6 (126 MHz, D_2O). * = residual $\text{O}(\text{Bpin})_2$.

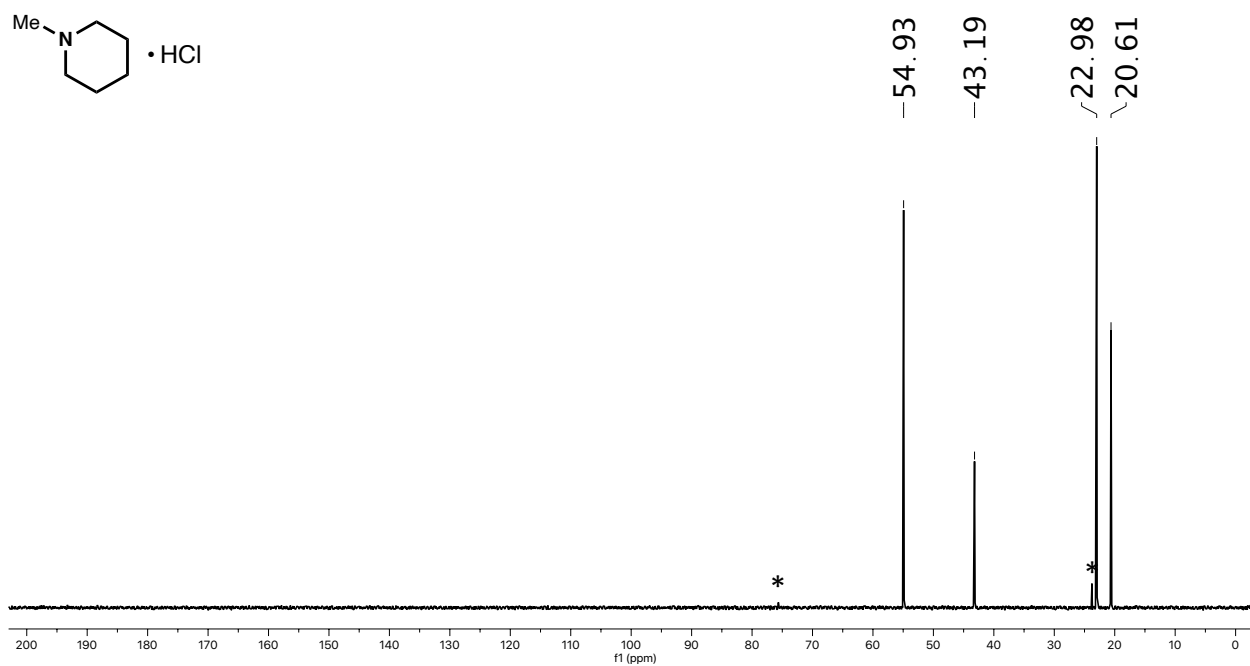


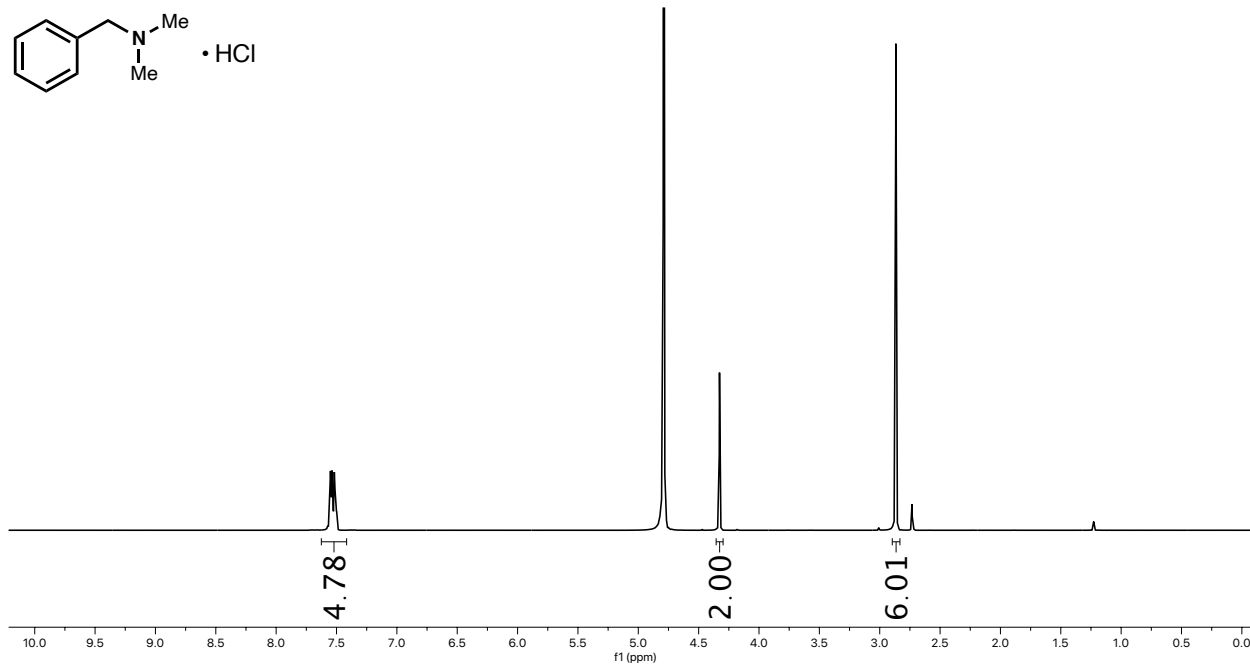
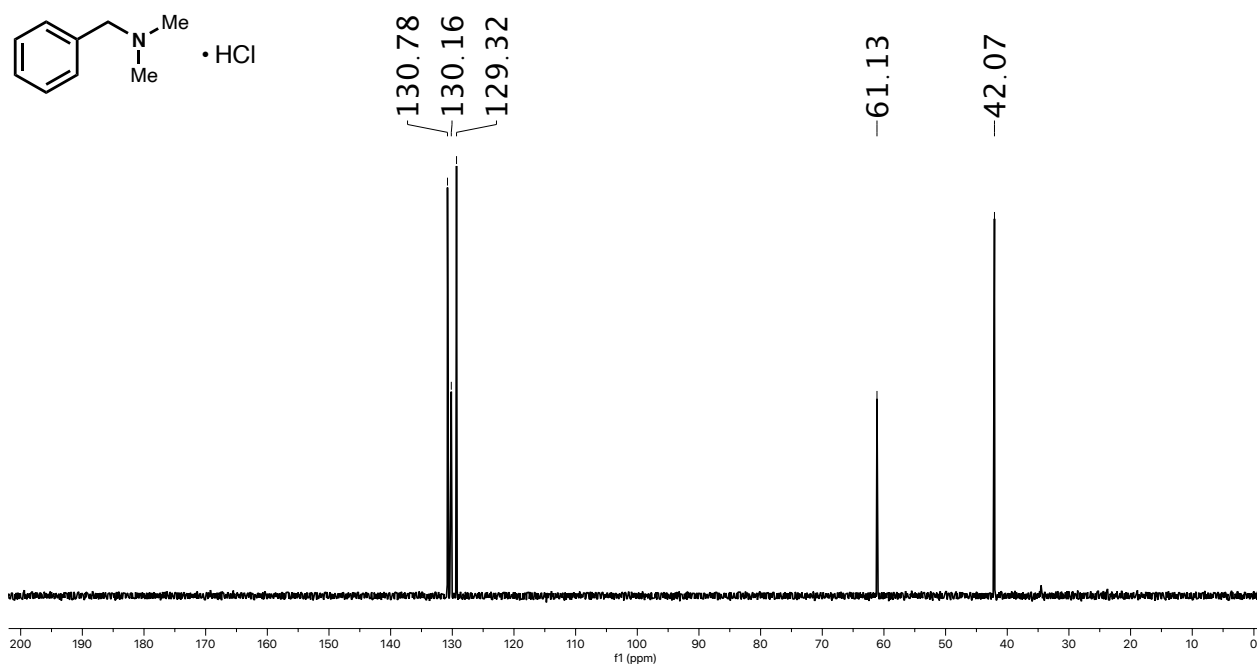
¹H NMR spectrum of III-7 (500 MHz, D₂O).**¹³C NMR spectrum of III-7 (126 MHz, D₂O).**

¹H NMR spectrum of III-8 (500 MHz, D₂O). * = residual O(Bpin)₂.

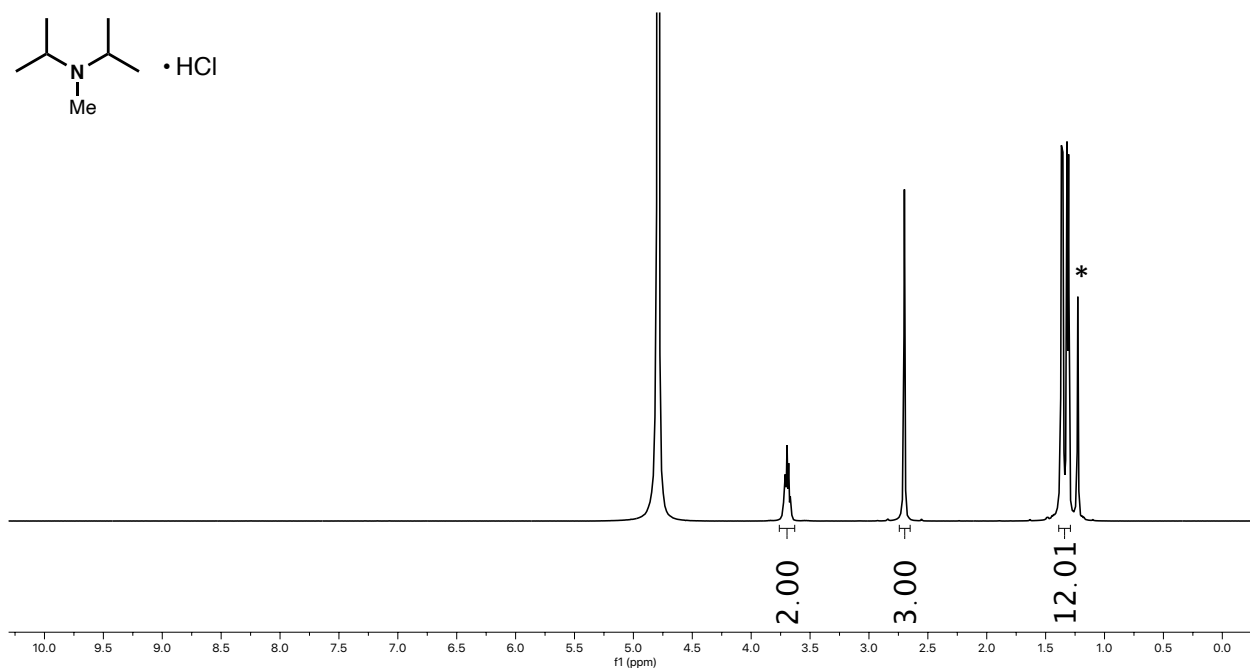


¹³C NMR spectrum of III-8 (126 MHz, D₂O). * = residual O(Bpin)₂.

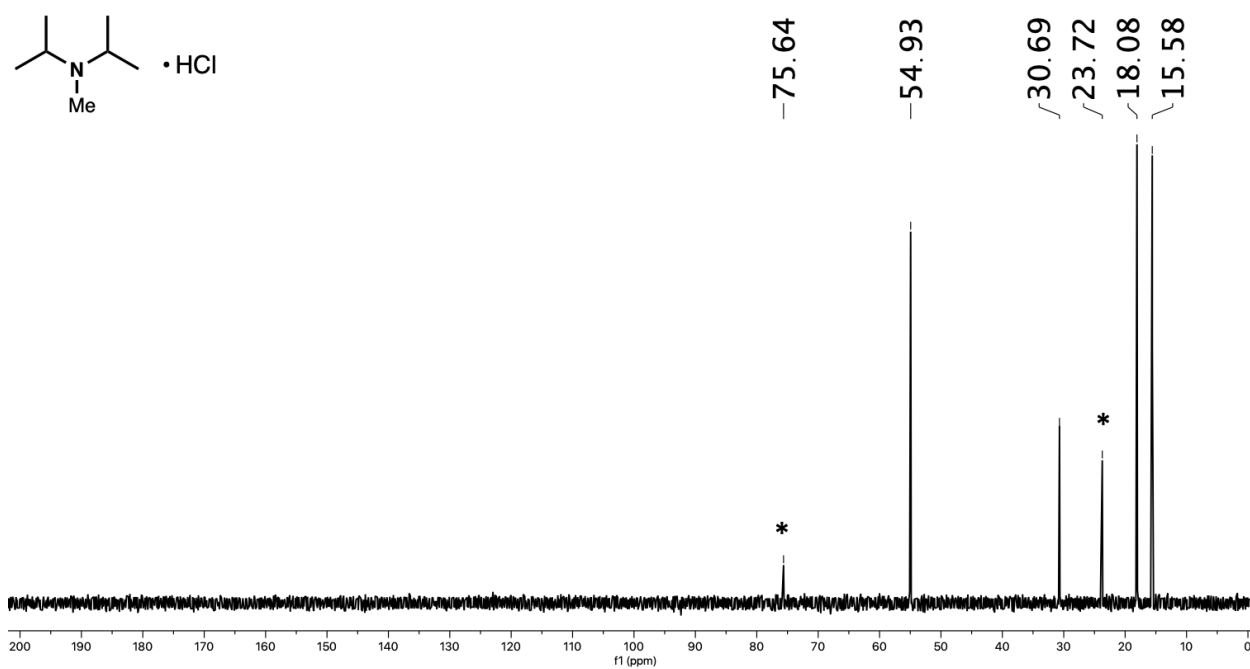


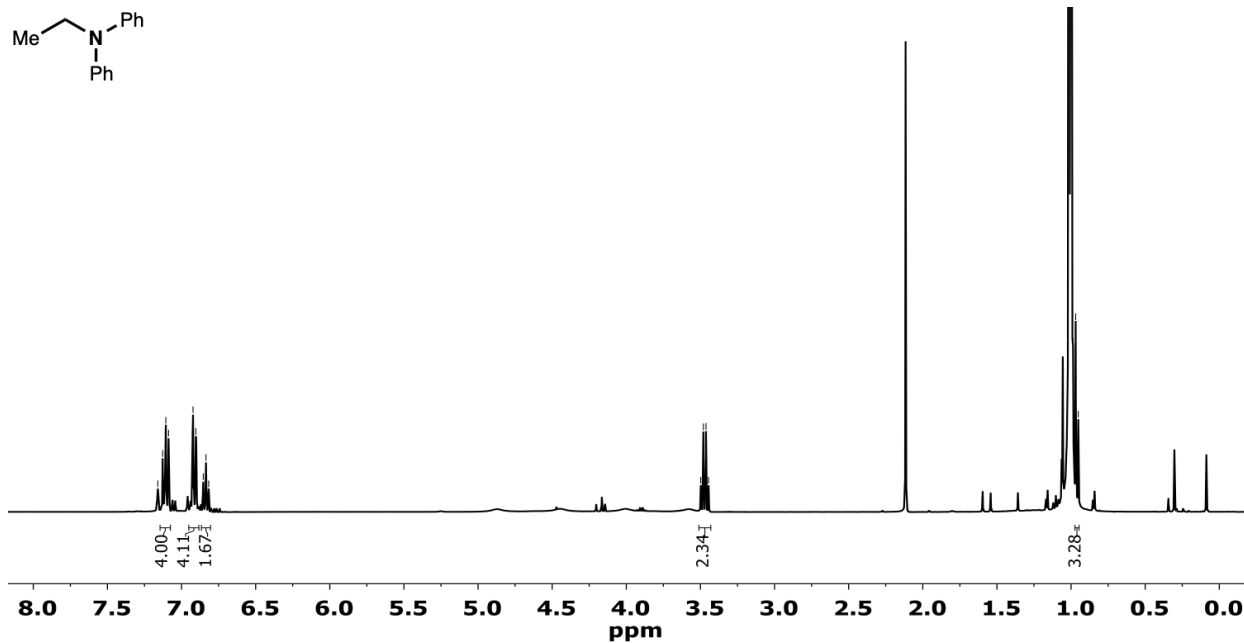
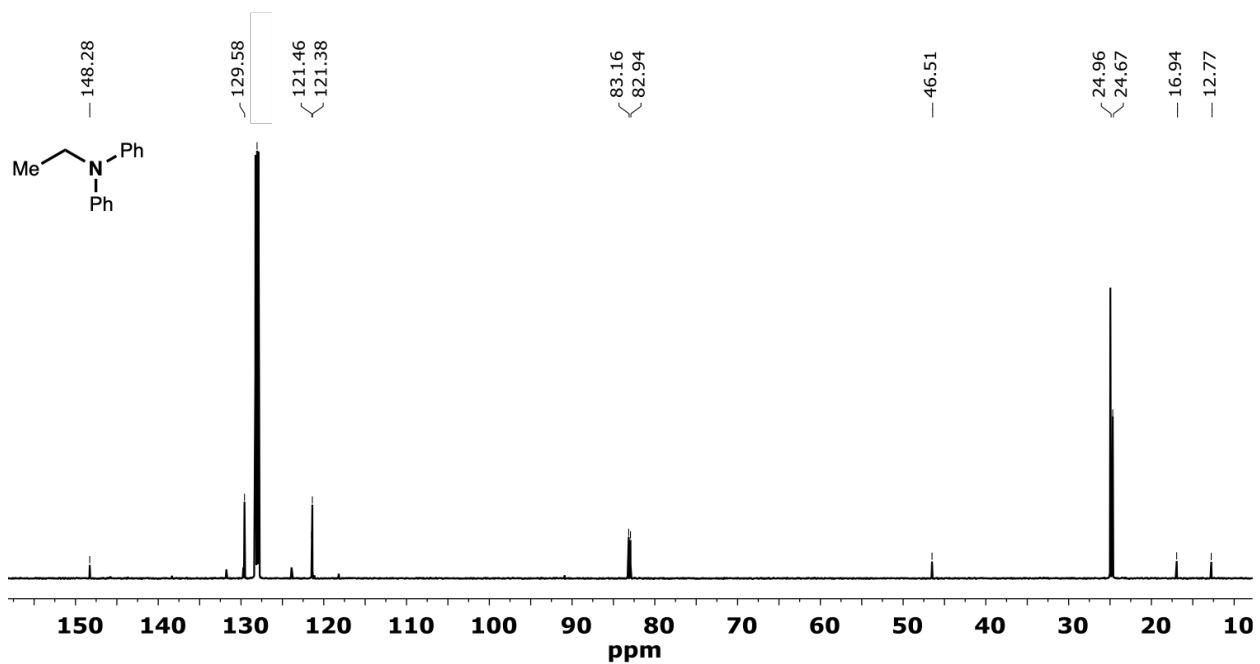
^1H NMR spectrum of III-9 (500 MHz, D_2O). **^{13}C NMR spectrum of III-9 (126 MHz, D_2O).**

¹H NMR spectrum of III-10 (500 MHz, D₂O). * = residual O(Bpin)₂.

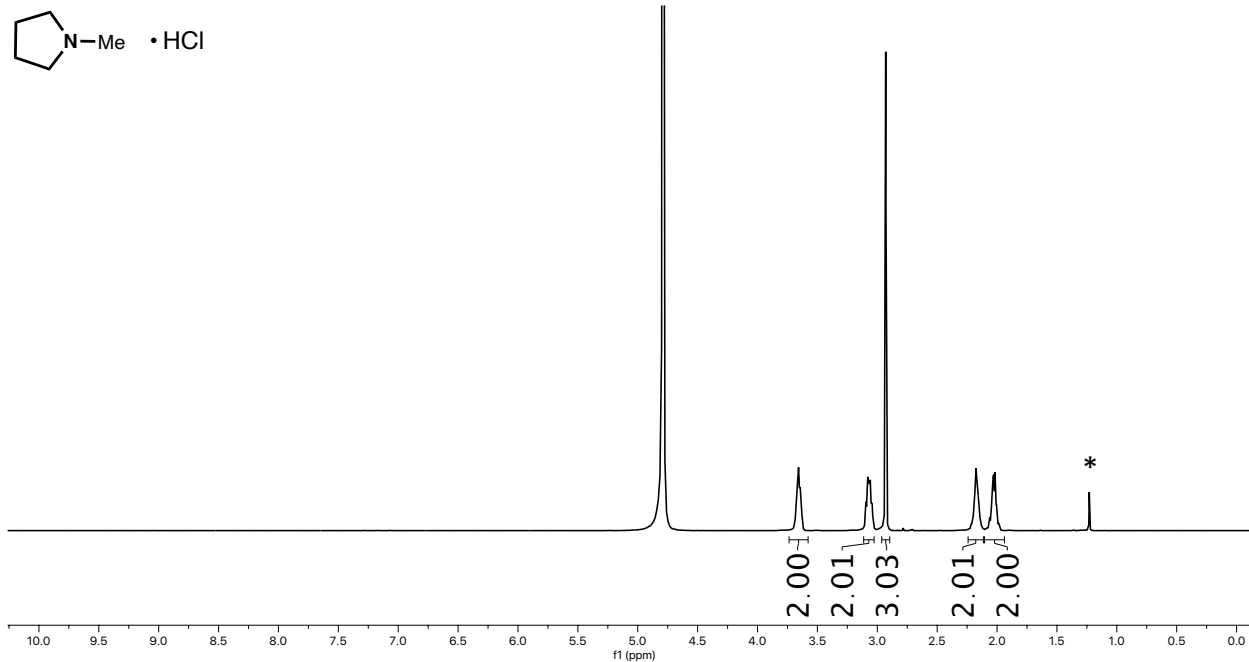


¹³C NMR spectrum of III-10 (126 MHz, D₂O). * = residual O(Bpin)₂.

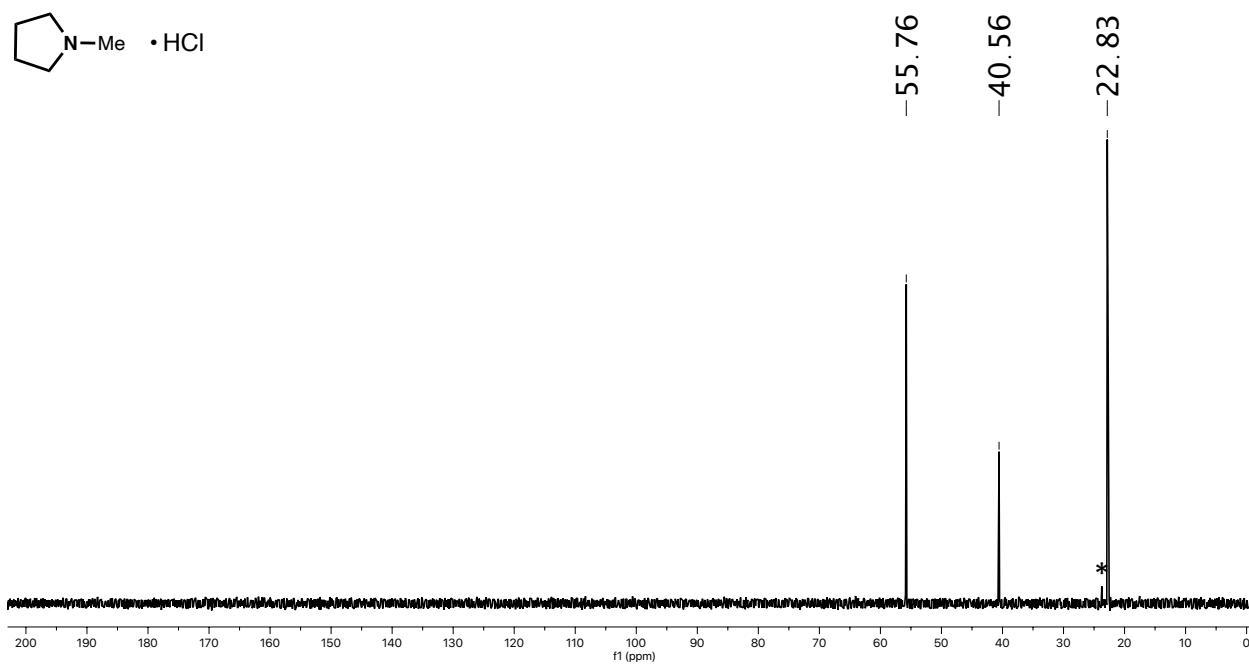


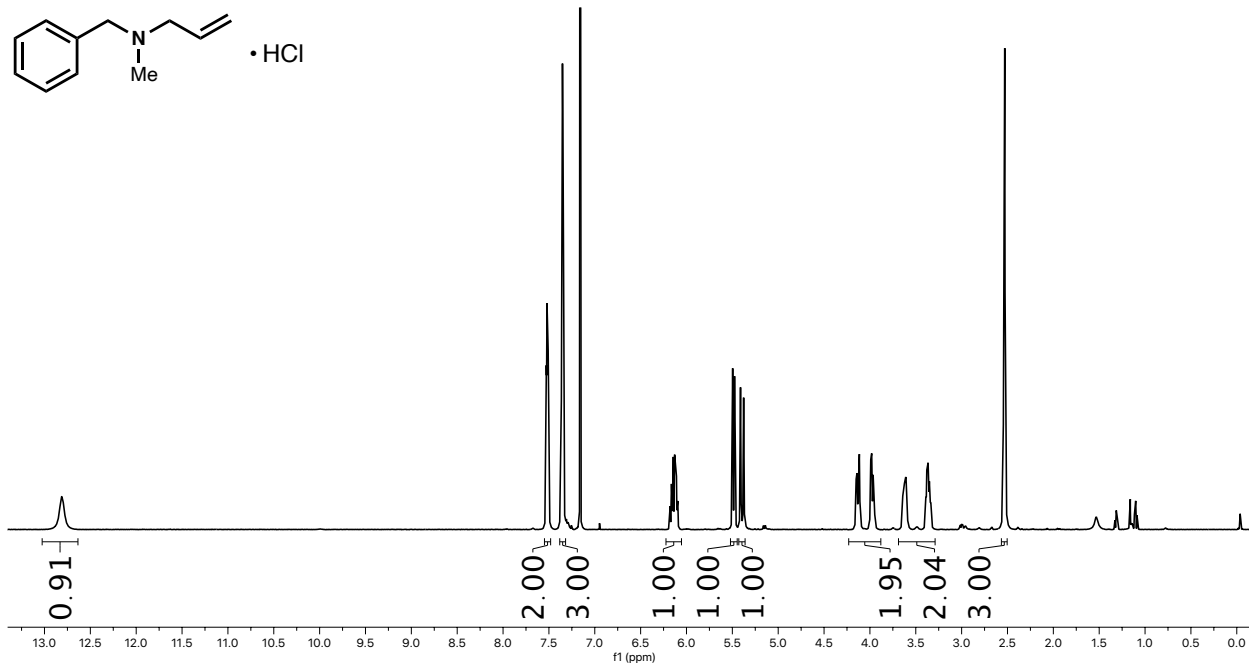
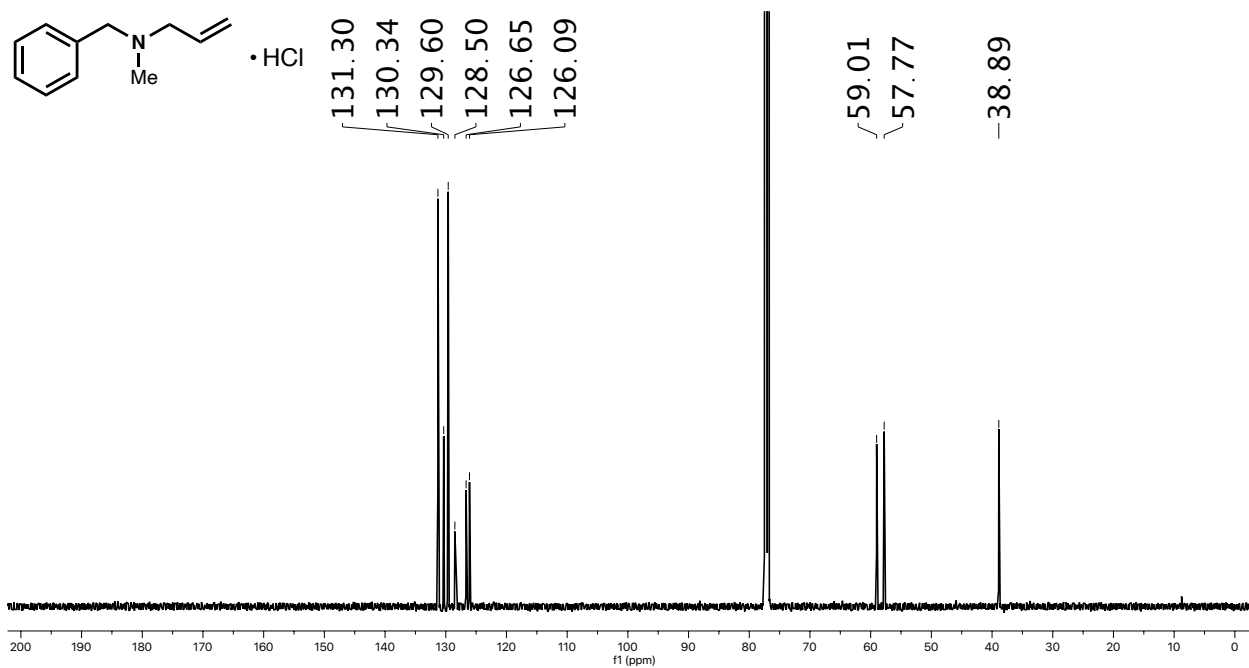
^1H NMR spectrum of III-11 (500 MHz, C_6D_6). **^{13}C NMR spectrum of III-11 (126 MHz, C_6D_6).**

¹H NMR spectrum of III-12 (500 MHz, D₂O). * = residual O(Bpin)₂.

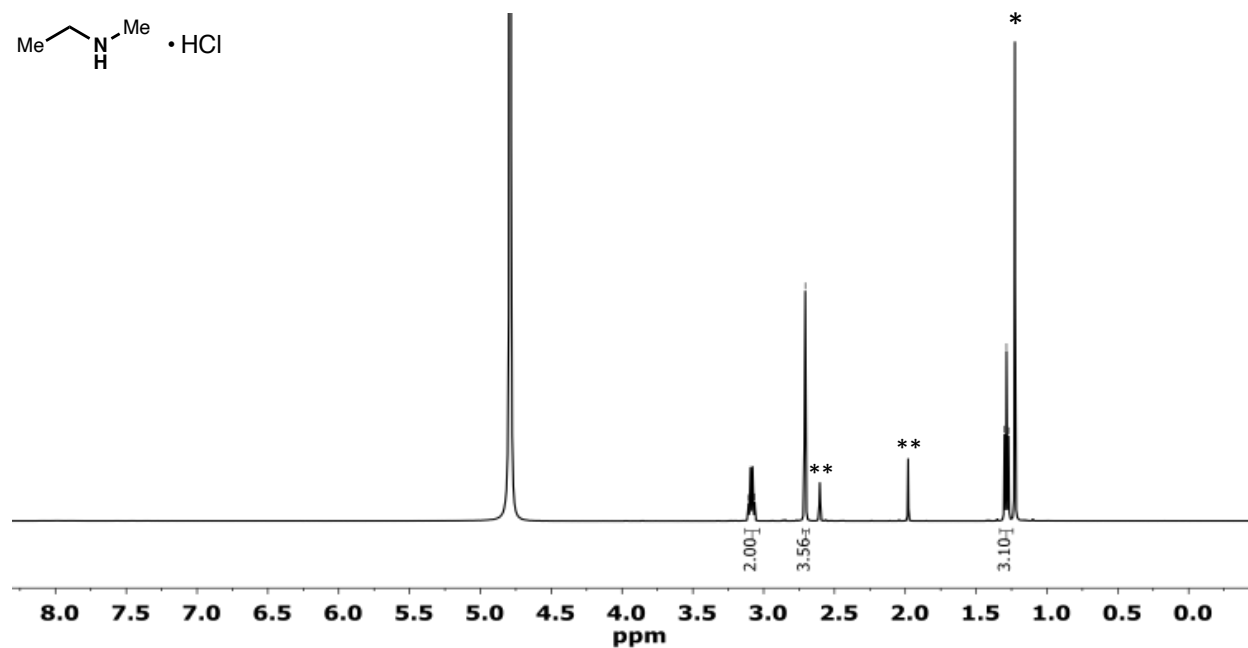


¹³C NMR spectrum of III-12 (126 MHz, D₂O). * = residual O(Bpin)₂.

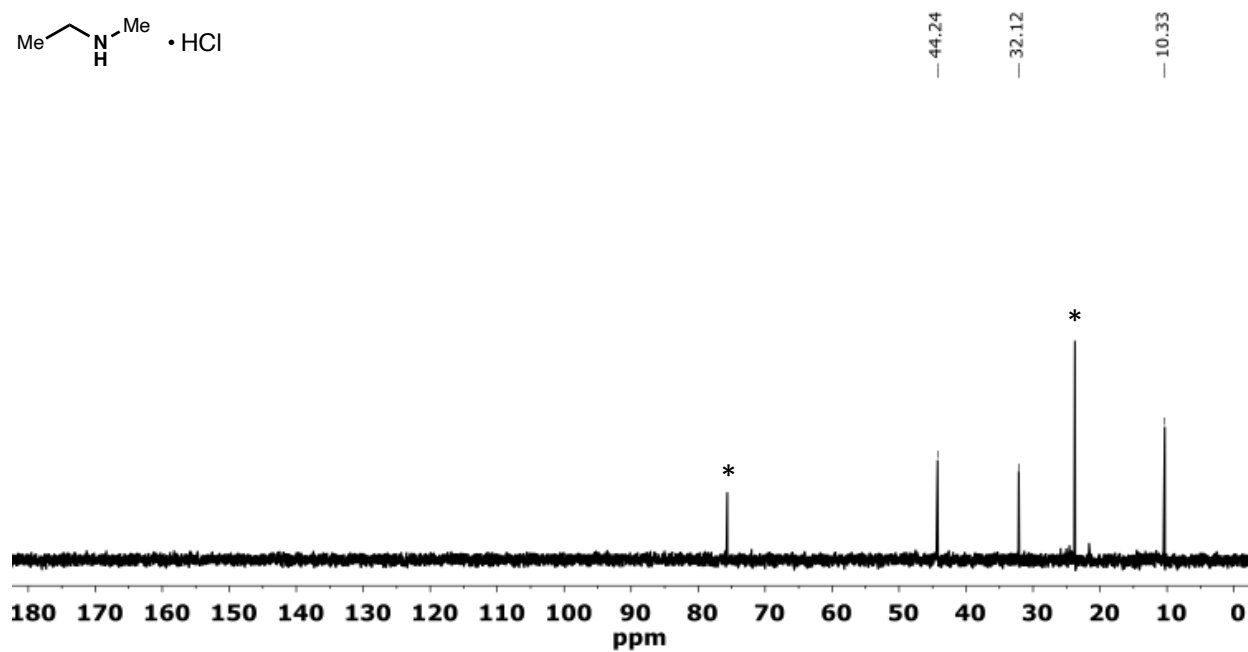


¹H NMR spectrum of III-13 (500 MHz, Chloroform-*d*).**¹³C NMR spectrum of III-13 (126 MHz, Chloroform-*d*).**

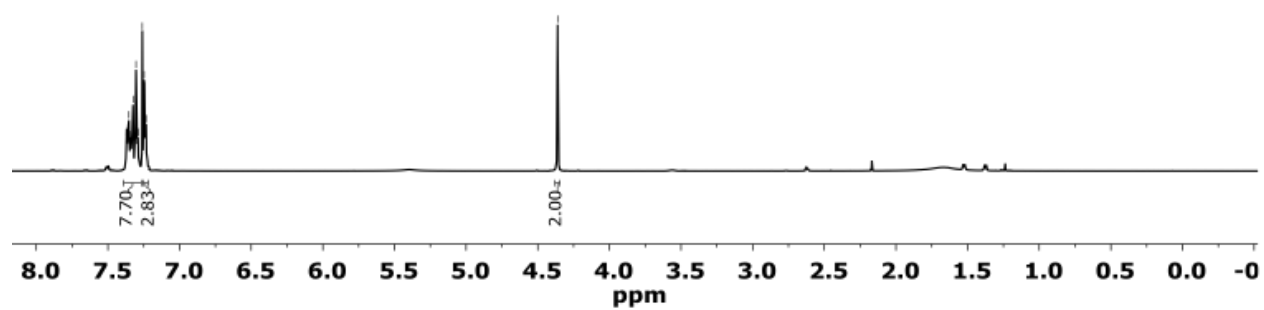
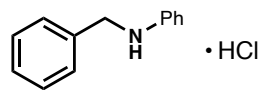
^1H NMR spectrum of III-14 (500 MHz, D_2O). * = residual $\text{O}(\text{Bpin})_2$, ** = trace starting material.



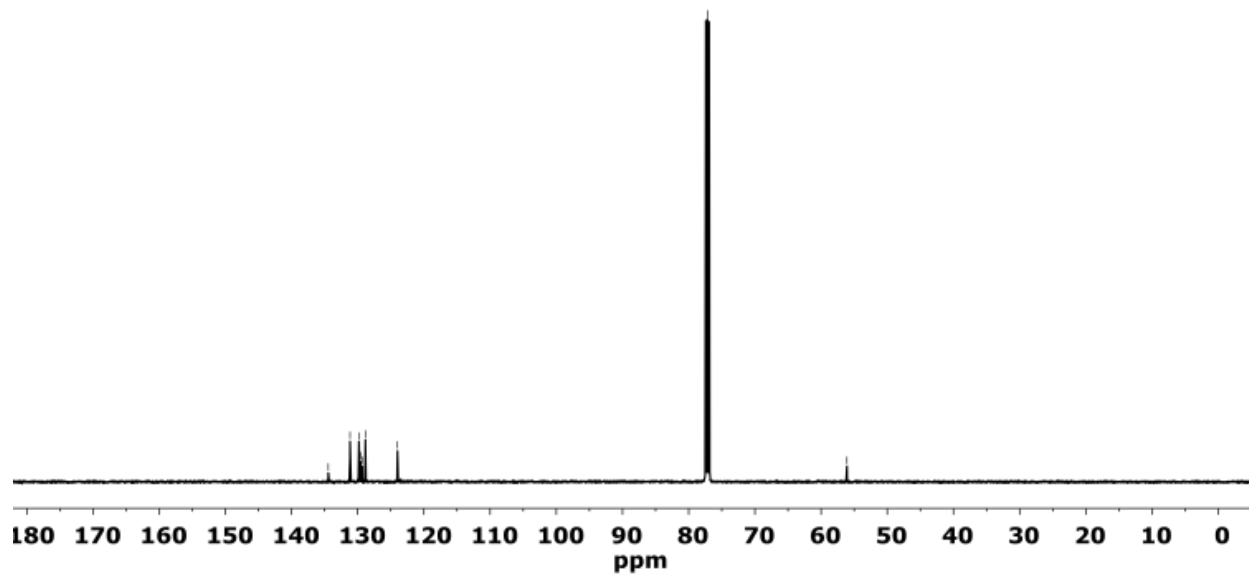
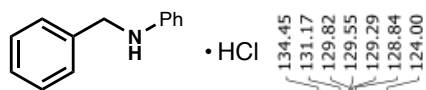
^{13}C NMR spectrum of III-14 (126 MHz, D_2O). * = residual $\text{O}(\text{Bpin})_2$.

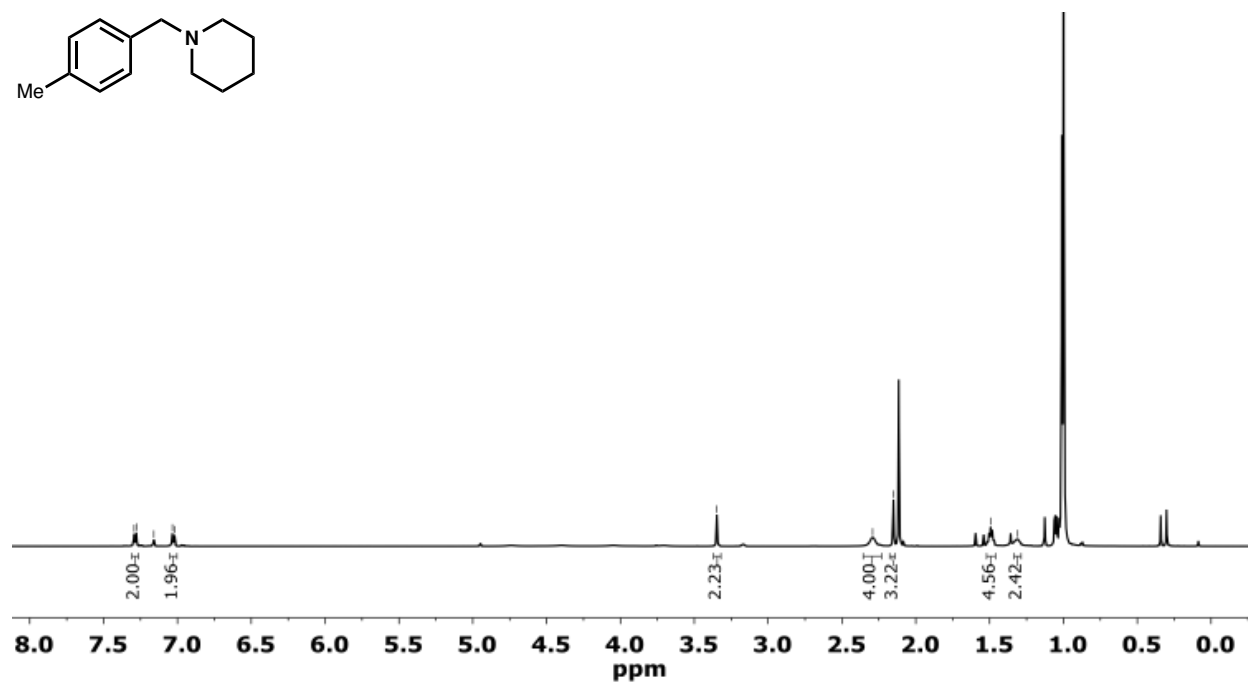
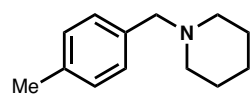
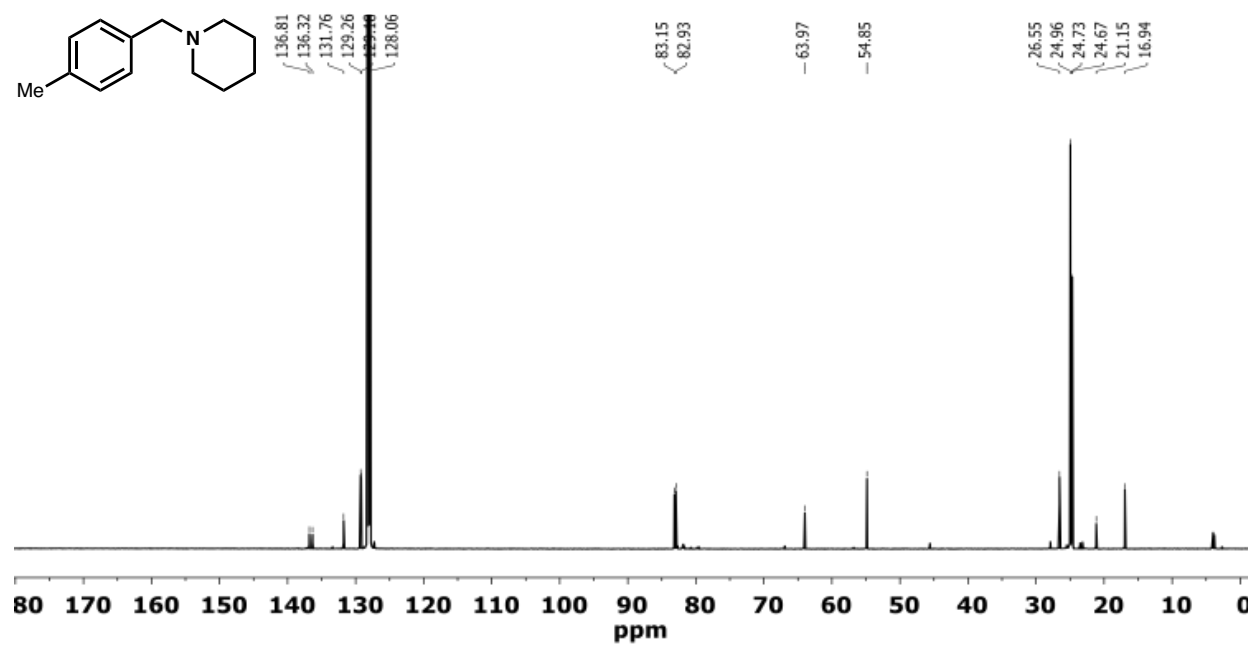
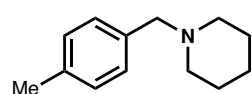


^1H NMR spectrum of III-15 (500 MHz, Chloroform-*d*).

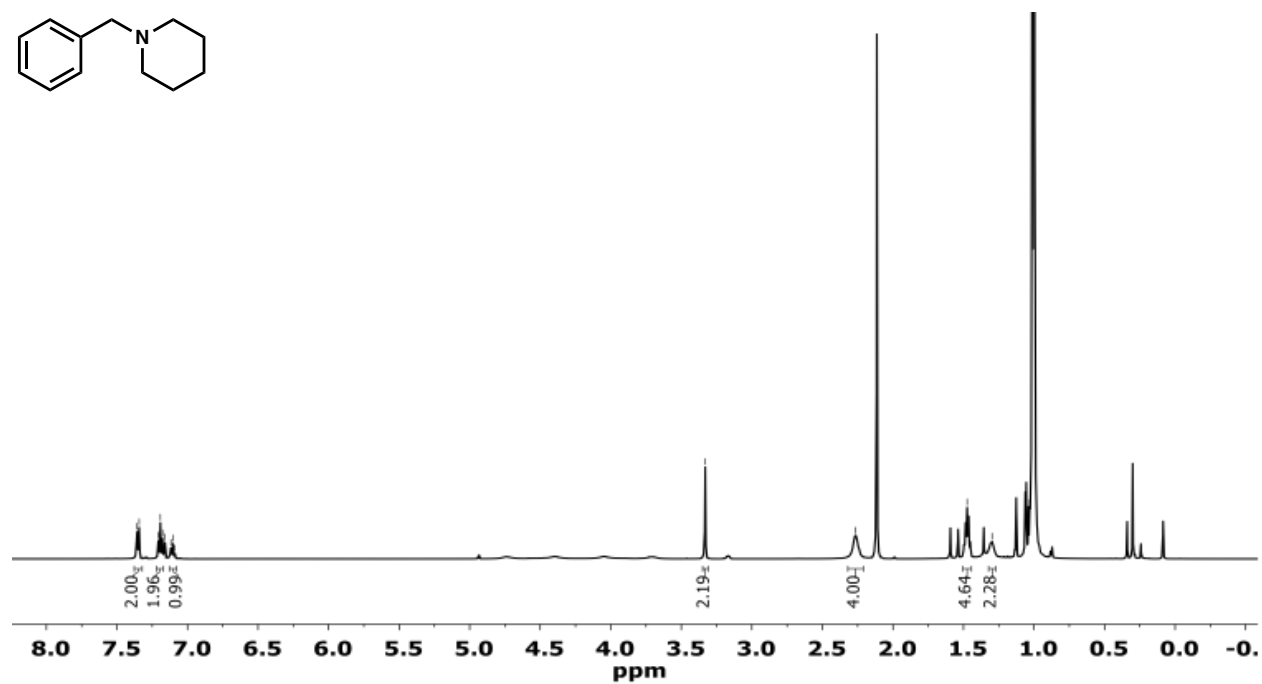
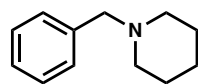


^{13}C NMR spectrum of III-15 (126 MHz, Chloroform-*d*).

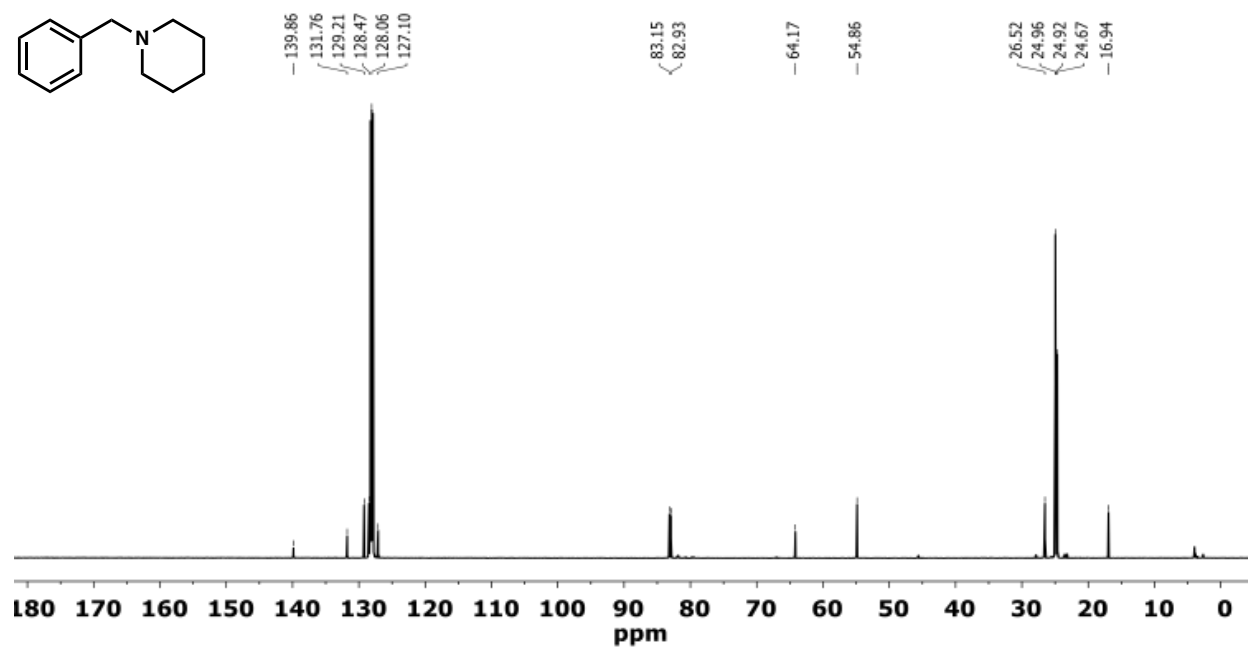
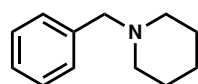


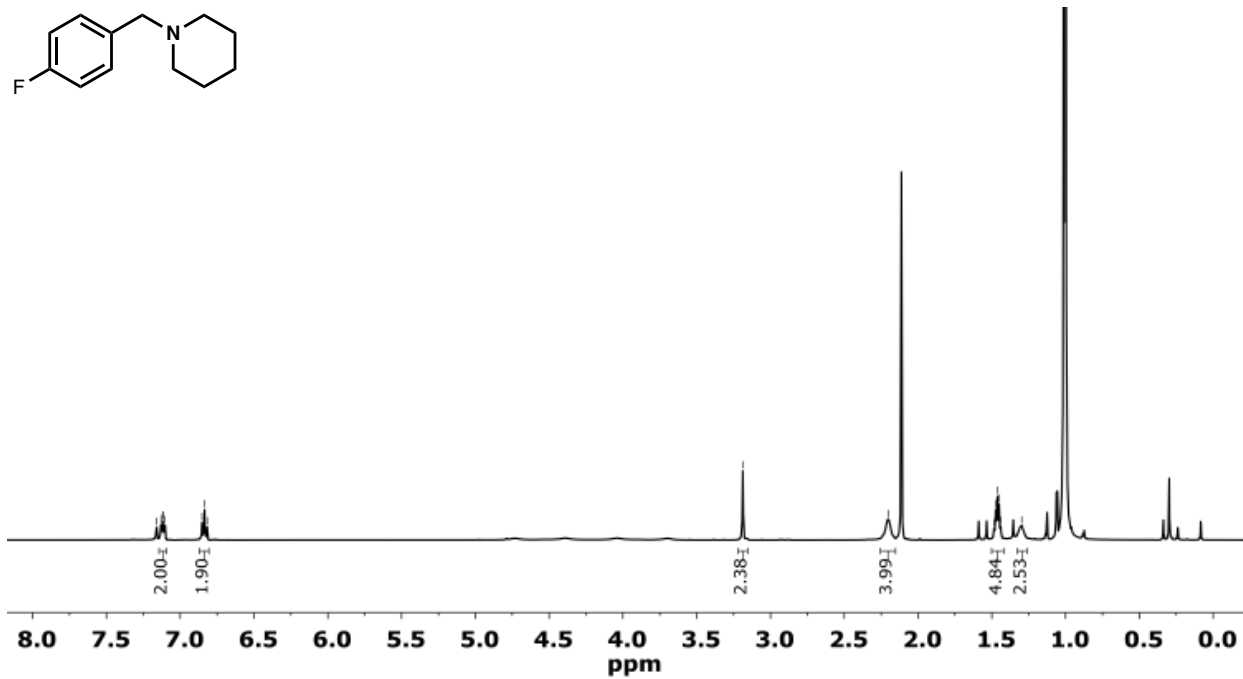
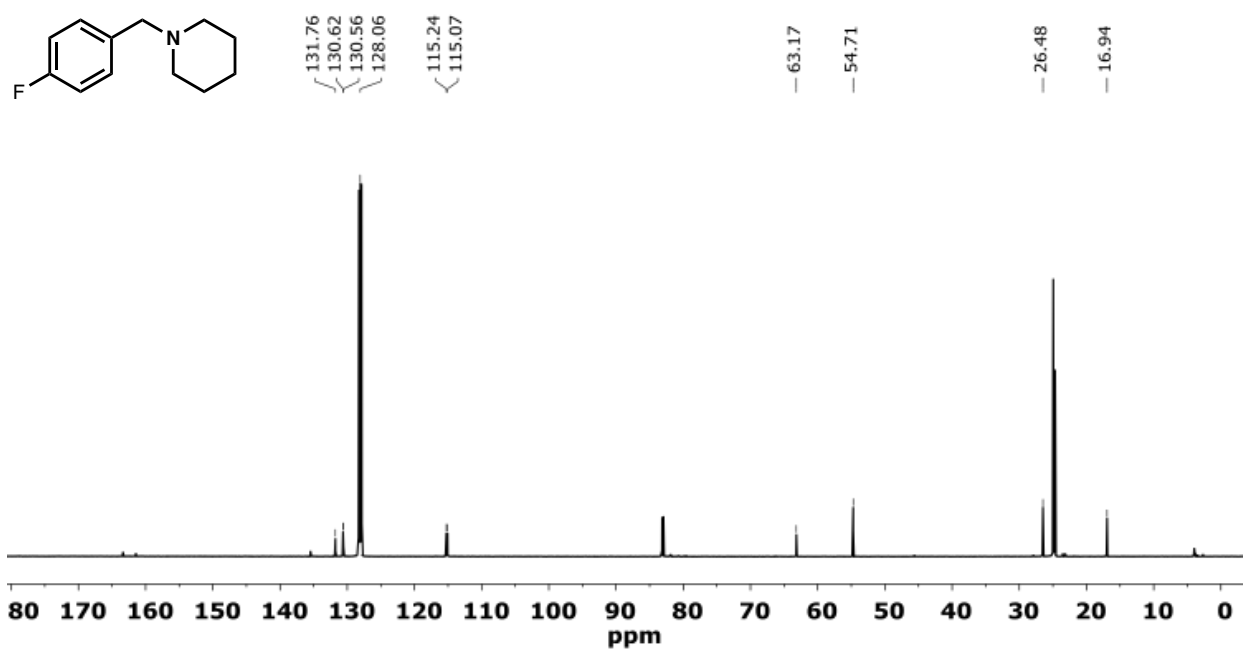
^1H NMR spectrum of III-17 (500 MHz, C_6D_6). **^{13}C NMR spectrum of III-17 (126 MHz, C_6D_6).**

^1H NMR spectrum of III-18 (500 MHz, C_6D_6).

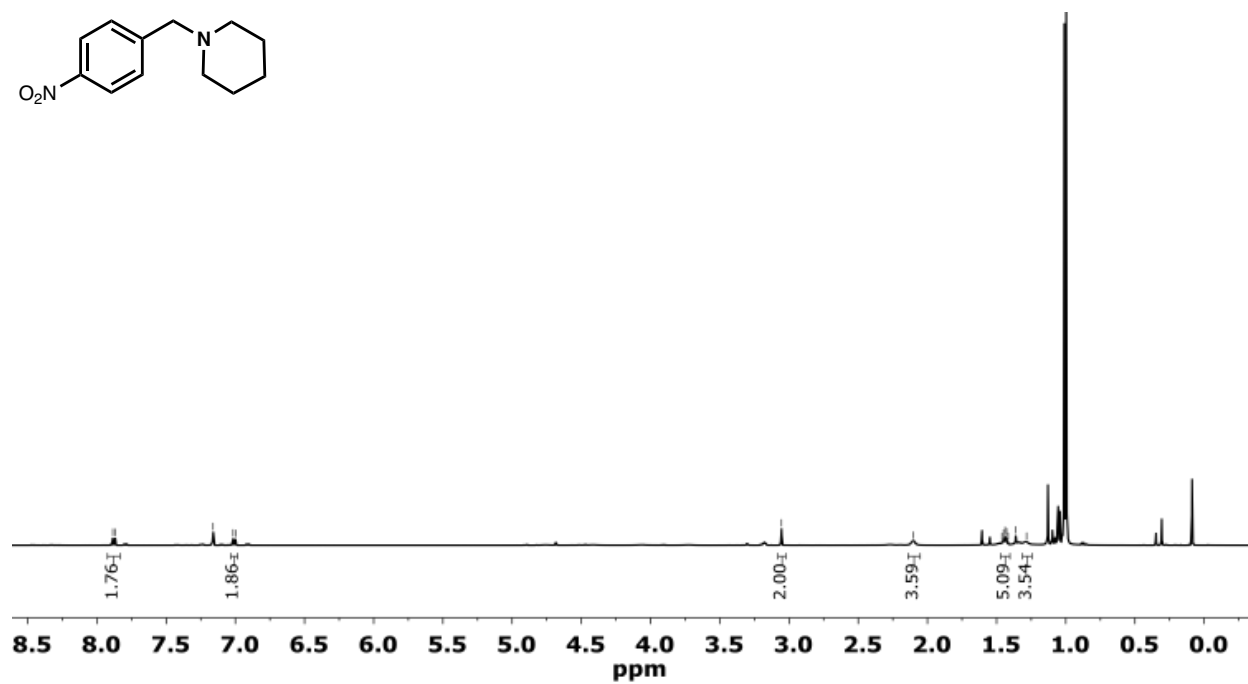


^{13}C NMR spectrum of III-18 (126 MHz, C_6D_6).



^1H NMR spectrum of III-19 (500 MHz, C_6D_6). **^{13}C NMR spectrum of III-19 (126 MHz, C_6D_6).**

^1H NMR spectrum of III-20 (500 MHz, C_6D_6).



^{13}C NMR spectrum of III-20 (126 MHz, C_6D_6).

